

อิทธิพลของเรขาคณิต เงื่อนไขควงรอยร้าวและแรงกระทำต่อปัจจัยความเข้มของรอยร้าวในตัวกลาง
ไพโอโซ อิเล็กทริกเชิงเส้น ไร้ขอบเขตสามมิติ



นายบุญชนะ จันสะหว่าง

จุฬาลงกรณ์มหาวิทยาลัย

CHULALONGKORN UNIVERSITY

บทคัดย่อและแฟ้มข้อมูลฉบับเต็มของวิทยานิพนธ์ตั้งแต่ปีการศึกษา 2554 ที่ให้บริการในคลังปัญญาจุฬาฯ (CUIR)
เป็นแฟ้มข้อมูลของนิสิตเจ้าของวิทยานิพนธ์ ที่ส่งผ่านทางบัณฑิตวิทยาลัย

The abstract and full text of theses from the academic year 2011 in Chulalongkorn University Intellectual Repository (CUIR)
are the thesis authors' files submitted through the University Graduate School.

วิทยานิพนธ์นี้เป็นส่วนหนึ่งของการศึกษาตามหลักสูตรปริญญาวิศวกรรมศาสตรมหาบัณฑิต

สาขาวิชาวิศวกรรมโยธา ภาควิชาวิศวกรรมโยธา

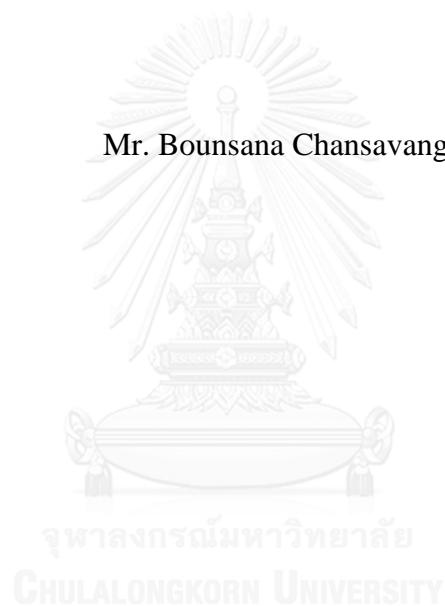
คณะวิศวกรรมศาสตร์ จุฬาลงกรณ์มหาวิทยาลัย

ปีการศึกษา 2558

ลิขสิทธิ์ของจุฬาลงกรณ์มหาวิทยาลัย

INFLUENCE OF GEOMETRY, CRACK-
FACE CONDITIONS AND LOADING ON INTENSITY FACTORS OF CRACKS I
N 3D LINEAR PIEZOELECTRIC MEDIA

Mr. Bounsana Chansavang



A Thesis Submitted in Partial Fulfillment of the Requirements
for the Degree of Master of Engineering Program in Civil Engineering

Department of Civil Engineering

Faculty of Engineering

Chulalongkorn University

Academic Year 2015

Copyright of Chulalongkorn University

Thesis Title INFLUENCE OF GEOMETRY, CRACK-FACE
CONDITIONS AND LOADING ON
INTENSITY FACTORS OF CRACKS IN 3D
LINEAR PIEZOELECTRIC MEDIA

By Mr. Bounsana Chansavang

Field of Study Civil Engineering

Thesis Advisor Associate Professor Jaroon Rungamornrat, Ph.D.

Thesis Co-Advisor Weeraporn Phongtinnaboot, Ph.D.

Accepted by the Faculty of Engineering, Chulalongkorn University in
Partial Fulfillment of the Requirements for the Master's Degree

..... Dean of the Faculty of Engineering
(Professor Bundhit Eua-arporn, Ph.D.)

THESIS COMMITTEE

..... Chairman
(Professor Teerapong Senjuntichai, Ph.D.)

..... Thesis Advisor
(Associate Professor Jaroon Rungamornrat, Ph.D.)

..... Thesis Co-Advisor
(Weeraporn Phongtinnaboot, Ph.D.)

..... Examiner
(Assistant Professor Watanachai Smittakorn, Ph.D.)

..... External Examiner
(Yasothon Sapsathiarn, Ph.D.)

บุญชนะ จันสะหว่าง : อิทธิพลของเรขาคณิต เงื่อนไขผิวรอยร้าวและแรงกระทำต่อปัจจัยความเข้มของรอยร้าวในตัวกลางไพเอโซ อิเล็กทริกเชิงเส้น ไรซ์ขอบเขตสามมิติ (INFLUENCE OF GEOMETRY, CRACK-FACE CONDITIONS AND LOADING ON INTENSITY FACTORS OF CRACKS IN 3D LINEAR PIEZOELECTRIC MEDIA) อ.ที่ปรึกษาวิทยานิพนธ์หลัก: รศ. ดร.จรรยา รุ่งอมรรัตน์, อ.ที่ปรึกษาวิทยานิพนธ์ร่วม: ดร. วีรพร พงศ์ติณบุตร, 150 หน้า.

วิทยานิพนธ์ฉบับนี้นำเสนอผลการศึกษเกี่ยวกับอิทธิพลของเรขาคณิตรอยร้าว เงื่อนไขขอบเขตที่ผิวรอยร้าว เงื่อนไขแรงกระทำระยะไกล และค่าการนำไฟฟ้าของตัวกลางในรอยร้าว ที่มีต่อตัวประกอบความเข้มของรอยร้าวในตัวกลางไพเอโซอิเล็กทริกเชิงเส้น ในการศึกษาใช้ รอยร้าวผิวทรงกลม รอยร้าวผิวทรงกระบอก รอยร้าวอุโมงค์ และรอยร้าวรูปวงกลมคู่ เป็นรอยร้าวตัวแทนสำหรับศึกษาบทบาทของพารามิเตอร์ต่างๆที่เกี่ยวข้อง โดยใช้ระเบียบวิธีวิเคราะห์แบบสมมาตรกาลอดินเชิงเอกฐานต่ำในการหาตัวแปรไม่ทราบค่าบนผิวรอยร้าว และรูปแบบการประมาณเฉพาะร่วมกับสูตรสำเร็จในการเพิ่มความถูกต้องในการประมาณสนามที่บริเวณใกล้ขอบรอยร้าวและการคำนวณค่าตัวประกอบความเข้มบริเวณขอบรอยร้าว ผลที่ได้จากการศึกษาเชิงตัวเลขแสดงให้เห็นว่า ความโค้ง มุมขยายโค้ง และอัตราส่วนรูปร่างรอยร้าวมีอิทธิพลอย่างมีนัยสำคัญต่อค่าตัวประกอบความเข้ม นอกจากนี้ยังพบว่าค่าตัวประกอบความเข้มของความเค้นแบบที่ 1 ของรอยร้าว โค้งแบบไฟฟ้าซึมผ่านได้ ซึมผ่านไม่ได้ และซึมผ่านได้บางส่วน มีพฤติกรรมแตกต่างกันโดยสิ้นเชิงเมื่อเทียบกับรอยร้าวระนาบภายใต้แรงกระทำเชิงกล ยิ่งไปกว่านั้น ค่าตัวประกอบความเข้มของความเค้นแบบที่ 1 ของรอยร้าว โค้งแบบไฟฟ้าซึมผ่านไม่ได้และซึมผ่านได้บางส่วน ขึ้นอยู่กับสนามไฟฟ้าที่กระทำ ผลที่ได้นี้มีลักษณะตรงกันข้ามกับกรณีของรอยร้าวระนาบซึ่งค่าตัวประกอบความเข้มของความเค้นแบบที่ 1 มีค่าเท่ากันและไม่ขึ้นอยู่กับสนามไฟฟ้าที่กระทำ นอกจากนั้นเมื่อเพิ่มค่าการนำไฟฟ้าของตัวกลางในรอยร้าว ค่าตัวประกอบความเข้มของรอยร้าว โค้งแบบไฟฟ้าซึมผ่านได้ ซึมผ่านไม่ได้ และซึมผ่านได้บางส่วนมีค่าไม่เหมือนกัน และผลเฉลยของกรณีไฟฟ้าซึมผ่านได้บางส่วนขึ้นอยู่กับค่าการนำไฟฟ้าของตัวกลางในรอยร้าวอย่างชัดเจน

ภาควิชา วิศวกรรมโยธา

สาขาวิชา วิศวกรรมโยธา

ปีการศึกษา 2558

ลายมือชื่อนิสิต

ลายมือชื่อ อ.ที่ปรึกษาหลัก

ลายมือชื่อ อ.ที่ปรึกษาร่วม

5670500921 : MAJOR CIVIL ENGINEERING

KEYWORDS: PIEZOELECTRIC MATERIALS / CRACKS / INFINITE DOMAIN / WEAKLY SINGULAR / SGBEM

BOUNSANA CHANSAVANG: INFLUENCE OF GEOMETRY, CRACK-FACE CONDITIONS AND LOADING ON INTENSITY FACTORS OF CRACKS IN 3D LINEAR PIEZOELECTRIC MEDIA. ADVISOR: ASSOC. PROF. JAROON RUNGAMORN RAT, Ph.D., CO-ADVISOR: WEERAPORN PHONGTINNABOOT, Ph.D., 150 pp.

This thesis presents extensive results to demonstrate the influence of the crack geometry, crack-face boundary conditions, remote loading conditions and permittivity of a medium inside the crack gap on the intensity factors of cracks in linear piezoelectric media. A spherical cap crack, a cylindrical crack, a tunnel crack and a pair of identical penny-shaped cracks are chosen as representative cracks in the present study to fully explore the role of all parameters. In simulations, the weakly singular SGBEM is used to determine the unknown crack-face data and special local interpolations are employed along with the explicit formula to enhance the near-front approximation and directly extract intensity factors along the crack front. Results from a numerical study indicate that the curvature, the crack subtended angle and the crack aspect ratio significantly influence the value of the intensity factors. It is also observed that K_I of impermeable, permeable and semi-permeable non-planar cracks exhibit completely different behavior from that of planar cracks when the mechanical load increases. Moreover, K_I for both impermeable and semi-permeable non-planar cracks depends strongly on the applied electric field. These findings are in contrast with results in the case of planar cracks where K_I of impermeable, permeable and semi-permeable cracks are identical and independent of the electric field. In addition, as the permittivity inside the crack gap increases, the stress intensity factors of impermeable, permeable and semi-permeable non-planar cracks are not identical and the semi-permeable solution strongly depends on the permittivity of a medium inside the crack gap.

Department: Civil Engineering

Field of Study: Civil Engineering

Academic Year: 2015

Student's Signature

Advisor's Signature

Co-Advisor's Signature

ACKNOWLEDGEMENTS

Firstly, I would like to express my sincere gratitude to my advisor, Associate Professor Dr. Jaron Rungamornrat and my thesis co-advisor, Dr. Weeroporn Phongtinnaboot for the continuous support to my master study and related research, for their endurance, incentive, and vast knowledge. Their exhortation helped me throughout the research and the development of this thesis. I could not have imagined having a better advisor and mentor for my master study.

Besides my advisor, I would like to thank the rest of my thesis committee: Professor Dr Teerapong Senjuntichai, Assistant Professor Dr. Watanachai Smittakorn, and Dr. Yasothorn Sapsathiam not only for their insightful comments and encouragement, but also for the challenging questions which turned to be an incentive for me to widen my research from various perspectives.

My sincere thanks also go to Chulalongkorn University scholarship for ASEAN Countries 2013 program, which provided me an opportunity to study master degree in Chulalongkorn University and also the financial support for this study

I thank my fellow lab mates in for the stimulating discussions, for the sleepless nights we worked together before deadlines, and for all the fun we have had in the last four years. Also I thank my friends in the following institution: Department of Civil engineering, libraries and canteens.

Last but most importantly, I would like to express my deepest gratitude to family: my parents, my older brothers and my cousins, as well as to my close friends for their psychological support throughout the development of this thesis and for all my life in general.

CONTENTS

	Page
THAI ABSTRACT	iv
ENGLISH ABSTRACT.....	v
ACKNOWLEDGEMENTS	vi
CONTENTS.....	vii
LIST OF FIGURES	xi
LIST OF TABLES	xvi
LIST OF ABBREVIATIONS.....	xviii
CHAPTER 1 INTRODUCTION	1
1.1 General.....	1
1.2 Literature and review	3
1.2.1 Influence of parameters on intensity factors	3
1.3 Objective of research	8
1.4 Scope of research.....	8
1.5 Methodology and procedures	9
1.6 Significance	9
CHAPTER 2 THEORETICAL CONSIDERATIONS	10
2.1 Problem Descriptions.....	10
2.2 Basic equations	11
2.3 Boundary conditions Boundary conditions	11
2.4 Near-tip generalized stress field of linear piezoelectric material	13
CHAPTER 3 SOLUTION TECHNIQUE	15
3.1 Introduction of SGBEM	15
3.2 Determination of stress and electric intensity factors.....	18
3.3 Mesh generations	19
3.4 Convergence check.....	21
3.4.1 Convergence of spherical cap crack in infinite medium under tensile remote loadings	22

	Page
3.4.2 Convergence of cylindrical cracks in infinite medium under tensile remote loadings	24
3.4.3 A pair of penny-shaped cracks	27
3.4.4 Tunnel crack	31
3.5 Verification	34
CHAPTER 4 NUMMERICAL RESULT AND DISCUSSIONS	37
4.1 Influence of geometry on four crack-face boundary conditions.....	37
4.1.1 Influence of crack-subtended angle for non-planar cracks.	38
4.1.1.1 Influence of half subtended angle for penny-shaped crack folded in a half circular ball (spherical cap crack)	38
4.1.1.2 Influence of half subtended angle for penny-shaped crack folded in cylindrical under remote tensile loading	42
4.1.1.3 Comparison between spherical cap crack and cylinder crack	52
4.1.2 Influence of curvature for non-planar cracks.	54
4.1.2.1 Influence of curvature on penny-shaped crack folded in circular ball (spherical cap crack).....	54
4.1.2.2 Influence of curvature on penny-shaped crack folded in a cylindrical (cylindrical crack).....	57
4.1.2.3 Comparison between spherical cap crack and cylinder crack	66
4.1.3 Influence of geometry by varying aspect ratio of tunnel crack	68
4.1.4 Interacting of two penny-shaped crack in vertical directions.....	70
4.1.5 Interacting of two penny-shaped crack in horizontal directions	74
4.2 Influence of remote tensile mechanical load on four crack-face boundary conditions	77
4.2.1 Influence of remote tensile mechanical load on spherical cap and cylindrical crack	77
4.2.1.1 Influence of remote tensile mechanical load on spherical cap crack.....	77
4.2.1.2 Influence of remote tensile mechanical load on cylindrical crack.....	81
4.2.1.3 Comparison between spherical cap crack and cylinder crack	90

	Page
4.2.2 Influence of remote tensile mechanical load on tunnel crack	91
4.2.3 Influence of remote tensile mechanical load on a pair of penny-shaped crack	94
4.2.3.1 Influence of remote tensile mechanical load on two penny-shaped crack in vertical direction	94
4.2.3.2 Influence of remote tensile mechanical load on two penny-shaped crack in horizontal direction	97
4.3 Influence of remote electrical load on four crack-face boundary conditions	99
4.3.1 Influence of remote electrical load on spherical cap and cylindrical crack	99
4.3.1.1 Influence of remote electrical load on spherical cap crack	99
4.3.1.2 Influence of remote electrical load on cylindrical crack	102
4.3.1.3 Comparison between spherical cap crack and cylinder crack.....	111
4.3.2 Influence of remote electrical load on tunnel crack	113
4.3.3 Influence of remote electrical load on two pair of penny-shaped cracks.....	116
4.3.3.1 Influence of remote electrical load on two penny-shaped crack in vertical direction.....	116
4.3.3.2 Influence of remote electrical load on two penny-shaped crack in horizontal direction.....	119
4.4 Influence of permittivity on four crack-face boundary conditions	121
4.4.1 Influence of permittivity on spherical cap and cylindrical crack	121
4.4.1.1 Influence of permittivity on spherical cap crack	121
4.4.1.2 Influence of permittivity on cylindrical crack	125
4.4.1.3 Comparison between spherical cap and cylinder cracks	134
4.4.2 Influence of permittivity of tunnel crack.....	135
4.4.3 Influence of permittivity of two penny-shaped crack in vertical direction.....	137

	Page
4.4.4 Influence of permittivity of two penny-shaped crack in horizontal direction.....	141
CHAPTER 5 CONCLUSIONS	143
5.1 Influence of geometry on intensity factors	143
5.2 Influence of mechanical loading on intensity factors	145
5.3 Influence of electrical loading (electric field) on intensity factors.....	145
5.4 Influence of permittivity inside the crack gap on intensity factors.....	146
REFERENCES	147
VITA.....	150



LIST OF FIGURES

Figure 2.1 Schematic of a linear piezoelectric body containing a crack infinite medium.	10
Figure 2.2 The coordinate system with notation utilized in near-tip generalized stress field along the crack front	13
Figure 3.1 Schematic of an isolated crack in three-dimensional, generally anisotropic infinite domain	16
Figure 3.2 Schematic of an isolated crack in a three-dimensional, generally anisotropic, piezoelectric unbounded domain.....	18
Figure 3.3 The elements employed in the discretization of various geometries (a) 9-nodes quadrilateral crack tip elements, (b) standard 8-nodes quadrilateral elements and (c) standard 6-nodes triangle elements (e) an example of mesh transition	21
Figure 3.4 (a) schematic of a spherical cap crack in infinite domain and (b) three meshes utilized in computation.....	23
Figure 3.5 (a) schematic of a cylindrical crack in infinite domain and (b) three meshes utilized in computation and coordinate of each meshes.....	26
Figure 3.6 (a) schematic of a pair of penny-shaped cracks in vertical direction in infinite domain and (b) a pair of penny-shaped cracks in horizontal direction and (c) three meshes utilized in computation.	29
Figure 3.7 (a) schematic of a tunnel crack in infinite domain, (b),(c) and (d) are three meshes utilized in computation such as 24, 72 and 144 elements.	32
Figure 3.8 (a) schematic of a penny-shaped crack in infinite domain, (b) the body subjected to remote tensile mechanical and electrical load	34
Figure 3.9 three mesh utilized in analysis, (a) Coarse mesh, (b) Medium mesh and (c) Fine mesh.....	35
Figure 4.1 Schematic of a penny-shaped crack folded in circular ball (a spherical cap crack) in a piezoelectric infinite medium	39
Figure 4.2 (a), (b) and (c) are dependent of normalized stress and electric [K_I , K_{II} , K_{IV}] intensity factors on the crack subtended angle for spherical cap crack in infinite medium.	42

- Figure 4.3** (a) Schematic of a penny-shaped crack folded in cylindrical pipe (a cylindrical crack) in a piezoelectric infinite medium (b) three different points on the mesh coordinate of cylindrical crack 43
- Figure 4.4** Dependent of normalized stress intensity factors K_I on the crack subtended angle for cylindrical crack in infinite medium. Results are reported on (a) all points, the (b) top, (c) middle and (d) bottom points..... 46
- Figure 4.5** Dependent of normalized stress intensity factors K_{II} on the crack subtended angle for cylindrical crack in infinite medium. Results are reported on (a) all points, the (b) top, (c) middle and (d) bottom points..... 49
- Figure 4.6** Dependent of normalized stress intensity factors K_{III} on the crack subtended angle for cylindrical crack in infinite medium. Results are reported on the middle point 49
- Figure 4.7** Dependent of normalized electric intensity factors K_{IV} on the crack subtended angle for cylindrical crack in infinite medium. Results are reported on (a) all points, the (b) top, (c) middle and (d) bottom points..... 52
- Figure 4.8** (a), (b) and (c) are dependent of normalized stress and electric [K_I , K_{II} , K_{IV}] intensity factors on the curvature for spherical cap crack in infinite medium. Results are reported as average values..... 57
- Figure 4.9** Dependent of normalized stress intensity factors [K_I] on the curvature for cylindrical crack in infinite medium. Results are reported on (a) all points, the (b) top, (c) middle and (d) bottom points..... 60
- Figure 4.10** Dependent of normalized stress intensity factors [K_{II}] on the curvature for cylindrical crack in infinite medium. Results are reported on (a) all points, the (b) top, (c) middle and (d) bottom points 63
- Figure 4.11** Dependent of normalized stress intensity factors [K_{III}] on the curvature for cylindrical crack in infinite medium. Results are reported on the middle point 63
- Figure 4.12** Dependent of normalized electric intensity factors [K_{IV}] on the curvature for cylindrical crack in infinite medium. Results are reported on (a) all points, the (b) top, (c) middle and (d) bottom points 66
- Figure 4.13** (a) Schematic of tunnel crack in a piezoelectric infinite medium and (b),(c) and (d) are the example of the meshes that utilized for the investigation .. 68
- Figure 4.14** (a) and (b) are dependent of normalized stress and electric intensity factors [K_I , K_{IV}] on the aspect ratio for tunnel crack in infinite medium. Results are reported on both the end-radius and half-length points 70

- Figure 4.15** (a) Schematic of two penny-shaped cracks in vertical direction in a piezoelectric infinite medium and (b) are the meshes for one penny-shaped crack that utilized for the investigation 71
- Figure 4.16** (a),(b) and (c) are dependent of normalized stress and electric intensity factors $[K_I, K_{II}, K_{IV}]$ on the interaction for two penny-shaped crack in infinite medium. Results are reported on a penny-shaped cracks..... 74
- Figure 4.17** (a) Schematic of two penny-shaped cracks in horizontal direction in a piezoelectric infinite medium and (b) are the meshes for one penny-shaped crack that utilized for the investigation 75
- Figure 4.18** (a) and (b) are dependent of normalized stress and electric intensity factors $[K_I, K_{IV}]$ on the interaction for two penny-shaped crack in infinite medium. Results are reported on the maximum and minimum values and planar crack along the crack front 77
- Figure 4.19** (a), (b) and (c) are dependent of normalized stress and electric intensity factors $[K_I, K_{II}, K_{IV}]$ on the mechanical load for spherical cap crack in infinite medium. Results are reported as average values 80
- Figure 4.20** Dependent of normalized stress intensity factors $[K_I]$ on the mechanical load for cylindrical crack in infinite medium. Results are reported on values 83
- Figure 4.21** Dependent of normalized stress intensity factors $[K_{II}]$ on the mechanical load for cylindrical crack in infinite medium. Results are reported on (a) all points, (b) top, (c) middle and (d) bottom points 86
- Figure 4.22** Dependent of normalized stress intensity factors $[K_{III}]$ on the mechanical load for cylindrical crack in infinite medium. Results are reported on the middle point 87
- Figure 4.23** Dependent of normalized electric intensity factors $[K_{IV}]$ on the mechanical load for cylindrical crack in infinite medium. Results are reported on (a) all points, (b) top, (c) middle and (d) bottom points 89
- Figure 4.24** (a) the positions at end-radius and half-length points, (b) and (c) are dependent of normalized stress and electric intensity factors $[K_I, K_{IV}]$ on the mechanical load for a tunnel crack in infinite medium. Results are reported on the end-radius and half-length points..... 93
- Figure 4.25** (a), (b) and (c) are dependent of normalized stress and electric intensity factors $[K_I, K_{IV}]$ on the mechanical load for a two penny-shaped crack in infinite medium. Results are reported on one penny-shaped crack 96

- Figure 4.26** (a) and (b) are dependent of normalized stress and electric intensity factors [K_I , K_{IV}] on the mechanical load for a two penny-shaped crack in infinite medium. Results are reported on the maximum and minimum values..... 99
- Figure 4.27** (a), (b) and (c) are dependent of normalized stress and electric intensity factors [K_I , K_{II} , K_{IV}] on the electrical load for spherical cap crack in infinite medium. Results are reported as average values..... 102
- Figure 4.28** Dependent of normalized stress intensity factors [K_I] on the electrical load for cylindrical crack in infinite medium. Results are reported on (a) all points, (b) top, (c) middle and (d) bottom points 105
- Figure 4.29** Dependent of normalized stress intensity factors [K_{II}] on the electrical load for cylindrical crack in infinite medium. Results are reported on (a) all points, (b) top, (c) middle and (d) bottom points..... 107
- Figure 4.30** Dependent of normalized stress intensity factors [K_{III}] on the electrical load for cylindrical crack in infinite medium. Results are reported on the middle point 108
- Figure 4.31** Dependent of normalized electric intensity factors [K_{IV}] on the electrical load for cylindrical crack in infinite medium. Results are reported on (a) all points, (b) top, (c) middle and (d) bottom points 111
- Figure 4.32** (a), (b), (c) and (d) are dependent of normalized electric intensity factors [K_I , K_{IV}] on the electrical load for tunnel crack in infinite medium. Results are reported on the end-radius and half-length points 116
- Figure 4.33** (a), (b) and (c) are dependent of normalized stress and electric intensity factors [K_I , K_{II} , K_{IV}] on the electrical load for two penny-shaped cracks in infinite medium. Results are reported on one penny-shaped crack 119
- Figure 4.34** (a) and (b) are dependent of normalized stress and electric intensity factors [K_I , K_{IV}] on the electrical load for two penny-shaped cracks in infinite medium. Results are reported on the maximum and minimum values..... 121
- Figure 4.35** (a), (b) and (c) are dependent of normalized stress and electric intensity factors [K_I , K_{II} , K_{IV}] on the permittivity for spherical cap cracks in infinite medium. Results are reported as average values..... 124
- Figure 4.36** (a), (b), (c) and (d) are dependent of normalized stress intensity factors [K_I] on the permittivity for a cylindrical cracks in infinite medium. Results are reported on all points, the top, middle and bottom points..... 127
- Figure 4.37** Dependent of normalized stress intensity factors [K_{II}] on the permittivity for a cylindrical cracks in infinite medium. Results are reported on (a) all points, (b) top, (c) middle and (d) bottom points 130

- Figure 4.38** Dependent of normalized stress intensity factors [K_{III}] on the permittivity for a cylindrical cracks in infinite medium. Results are reported on the middle point 131
- Figure 4.39** Dependent of normalized electric intensity factors [K_{IV}] on the permittivity for a cylindrical cracks in infinite medium. Results are reported on (a) all points, (b) top, (c) middle and (d) bottom points 133
- Figure 4.40** (a) and (b) are dependent of normalized electric intensity factors [K_I , K_{IV}] on the permittivity for a tunnel crack in infinite medium. Results are reported on the end-radius and half-length points..... 137
- Figure 4.41** (a, a.1) (b) and (c) dependent of normalized stress and electric intensity factors [K_I , K_{II} , K_{IV}] on the permittivity for a two penny-shaped cracks in vertical direction in infinite medium. Results are reported on one penny-shaped crack..... 140
- Figure 4.42** (a) and (b) are dependent of normalized electric intensity factors [K_I , K_{IV}] on the permittivity for two penny-shaped cracks in horizontal direction in infinite medium. Results are reported on the maximum and minimum values along the crack front 142

LIST OF TABLES

Table 3.1 Property of transversely isotropic piezoelectric materials, PZT-4 gained from Li et al., (2011). The axis of material symmetry is directed along the x_3 -axis direction.	22
Table 3.2 The convergence of normalized stress and electric intensity factors $[K_I, K_{II}, K_{IV}]$ for a spherical cap crack under remote uniform tensile stress $\sigma_0 = 50$ MPa and uniform electric field $E_0 = 2.5$ MV/m for impermeable and permeable models	24
Table 3.3 The convergence of normalized stress and electric intensity factors $[K_I, K_{II}, K_{IV}]$ for a spherical cap crack under remote uniform tensile stress $\sigma_0 = 50$ MPa and uniform electric field $E_0 = 2.5$ MV/m for Semi-permeable and energetically consistent models	24
Table 3.4 The convergence of normalized stress and electric intensity factors $[K_I, K_{II}, K_{IV}]$ for a cylindrical crack under remote uniform tensile stress $\sigma_0 = 50$ MPa and uniform electric field $E_0 = 2.5$ MV/m for impermeable and permeable models	27
Table 3.5 The convergence of normalized stress and electric intensity factors $[K_I, K_{II}, K_{IV}]$ for a cylindrical crack under remote uniform tensile stress $\sigma_0 = 50$ MPa and uniform electric field $E_0 = 2.5$ MV/m for Semi-permeable and energetically consistent models	27
Table 3.6 The convergence of normalized stress and electric intensity factors $[K_I, K_{II}, K_{IV}]$ for a pair of penny-shaped crack in vertical direction under remote uniform tensile stress $\sigma_0 = 50$ MPa and uniform electric field $E_0 = 2.5$ MV/m for impermeable and permeable models.....	30
Table 3.7 The convergence of normalized stress and electric intensity factors $[K_I, K_{II}, K_{IV}]$ for a pair of penny-shaped cracks in vertical direction under remote uniform tensile stress $\sigma_0 = 50$ MPa and uniform electric field $E_0 = 2.5$ MV/m for Semi-permeable and energetically consistent models	30
Table 3.8 The convergence of normalized stress and electric intensity factors $[K_I, K_{IV}]$ for two penny-shaped cracks in horizontal direction under remote uniform tensile stress $\sigma_0 = 50$ MPa and uniform electric field $E_0 = 2.5$ MV/m for impermeable and permeable models.....	31
Table 3.9 (3.9) The convergence of normalized stress and electric intensity factors $[K_I, K_{IV}]$ for two penny-shaped cracks in horizontal direction under remote uniform	

tensile stress $\sigma_0 = 50$ MPa and uniform electric field $E_0 = 2.5$ MV/m for Semi-permeable crack and Energetically consistent crack	31
Table 3.10 The convergence of normalized stress and electric intensity factors $[K_I, K_{IV}]$ for a tunnel crack under remote uniform tensile stress $\sigma_0 = 50$ MPa and uniform electric field $E_0 = 2.5$ MV/m for impermeable and permeable models ...	33
Table 3.11 The convergence of normalized stress and electric intensity factors $[K_I, K_{IV}]$ for a tunnel crack under remote uniform tensile stress $\sigma_0 = 50$ MPa and uniform electric field $E_0 = 2.5$ MV/m for Semi-permeable crack and Energetically consistent crack.....	33
Table 3.10 The verification of normalized stress and electric intensity factors $[K_I, K_{IV}]$ for a penny-shaped crack under remote uniform tensile stress $\sigma_0 = 5$ MPa and uniform electric field $E_0 = 0.5$ MV/m for impermeable and permeable models	35
Table 3.11 The verification of normalized stress and electric intensity factors $[K_I, K_{IV}]$ for a penny-shaped crack under remote uniform tensile stress $\sigma_0 = 5$ MPa and uniform electric field $E_0 = 0.5$ MV/m for semi-permeable and energetically consistent models	36
Table 4.1 the entire parameters, typical value and range that used to investigate stress and electric intensity factors on four crack-face boundary conditions	37

LIST OF ABBREVIATIONS

ξ	Point located on the surface
σ_{iJ}	Stress components
k_{im}	Dielectric permittivity of piezoelectric material
k_C	Dielectric permittivity of the medium inside the crack gap
ϕ	Electric potential
ε_{ij}	Strain components
ΔU	Vector of nodal quantities associated with the jump of the generalized displacement
Z	Unit vector
X	Interior point within the domain
u_K	Generalized displacement vectors
u_i	Mechanical displacement vectors in the i - direction
U_J^P	Generalized displacement fundamental solution
U	Vector of nodal quantities of the generalized displacement
t_i	Mechanical traction in the i –direction
t_J	Generalized surface traction
T	Vector of nodal quantities of the generalized traction
S_C^+	Upper crack surfaces
S_C^-	Lower crack surfaces
S_{iJ}^P	Generalized stress fundamental solution
n_i	Outward unit normal vector in the i -direction
G_{iK}^J	Weakly singular kernels
e_{mij}	Piezoelectric constants
E_{iJKm}	Generalized moduli
E_{ijkm}	Elastic constants
E_i	Electric fields in the i - direction
D_i	Electric induction vectors in the i - direction

CHAPTER 1

INTRODUCTION

In this chapter we first summarize and describe the motivations of the proposed research and the background review to demonstrate the historical development and statements of relevant works in this area. Then we address the objectives, the scope of work, the methodology and the significance of the proposed research.

1.1 General

During World War I piezoelectric material was employed as an essential part in various equipment and tools such as sonars, ultrasonic submarine detectors, transducers, hydrophones to return echo and etc. Such applications largely received an attention from many electromechanical material investigators to conduct further study. Nevertheless, these various applications were not extensively revealed to the public during that period. Presently, however, piezoelectric material has been significantly widespread and played an important role in economic development. It has been one of the major components for commercial, engineering and industrial works, all of which involve automotive, electronic, consumer, medical and military product. Examples include an actuator (e.g. ultrasonic equipment, ultrasonic cleaner, ultra precision positioner, ink jet print head, controlling helicopter rotor blades, disc drives, cigarette lighters and jewelry cleaners), a sensor (e.g. contact microphone, sonar, nondestructive testing device, airbag sensor, air flow sensor, keyless door entry, seat belt buzzers, knock sensors, depth finders, fish finders and musical instruments), a signal transmitter (e.g. Remote car opener, cellular phone, audible alarms, fuel atomizer and humidifiers), an audio frequency (e.g. microphones, earphones, beepers and buzzers in wireless application) and a medical instrument (e.g. hearing aid, the scanning probe microscopies, disposable patient monitors, foetal heart monitors, ultrasonic imaging, MRI machines and liver arm application). Piezoelectric material has been regarded as a smart material and commonly accepted among electromechanical material scientists that it exhibits coupling effect avail between electric and mechanic field when subject to some kind of mechanic stress. It also generates electric potential called the direct piezoelectric effect (brother Pierre Curie and Curie (1880)) In other word, they will produce electric field when subject to mechanic loading and vice versa. It also exhibits the converse piezoelectric effect Lippmann (1881). In addition, it leads to deformation when subject to electric field. The word “piezoelectric” means electricity resulting from pressure. It is derived from the Greek word “Piezo” or “Piezein” which means to squeeze or press and “electric” or “electron” which stands for amber or an ancient of electric charge. Nevertheless, there are properties of piezoelectric material of which the major drawbacks are breakability, responsive to collapse, low fracture viscosity, high inclination to expand crack throughout the applications and usage abatement.

Piezoelectric material is a brittle body and utilized frequently in the part of applications, aiming especially to reduce the size of various equipment in electronic applications which directly withstand temperature change during the manufacture process. These issues lead to the crack in the body of piezoelectric material. If a fracture appears in such material, it will pander the stress concentration. Moreover, it also

induces stagnancy and breakage within material along the crack region, and eventually this will generate the peak failure. Such problem currently gives rise to further research essential to gain a deeper understanding about the crack behaviors in piezoelectric material. This is particularly because of the complicated affinity of the electro-mechanical aspect with enigmatic anisotropic inside piezoelectric materials and of a variety of electric and mechanical loading conditions. Such problems become a rather complicate issue and mainly unreachable as well. In addition, if dislocation and various flaw problem are additionally diagnosed, the predicament will be more complicate. Since this material is significantly exploited in a large number of various aspects, it is therefore essential to investigate the stress and electric intensity factors of the embed crack in piezoelectric materials.

To imitate the behavior of the crack, various expedient assumptions must be incorporated. For the last three decades, facile mathematical simulations which have been basic upon linear constitutive law, has received a great attention from scientists who and increasingly interested and utilized by many investigators to several crack behaviors in many cases involving crack problems in piezoelectric material. Furthermore, such simulations are also the linear piezoelectric assumption which has carried out as well-set and adequate to predict the response throughout practical application. In linear piezoelectric context, to analyze a body embed no crack has been well-created in comparison with a body containing crack in which is mainly sophistication of electric and elastic field which give rise to complexity in the vicinity of the crack, Particularly the singularity along the crack front. In a previous investigation mostly have only studied and investigated simple crack geometries constituting planar, such as the penny-shaped crack, elliptical crack and straight crack and inclined straight crack under loading conditions (Park & Sun, 1993; Xu & Rajapakse, 2001; Wang & Jiang, 2002; Chen & Lim, 2005; Chiang & Weng, 2007)). This is not sufficient to gain insight into the behaviors of the cracks clearly. Moreover, many modeling of crack behaviors was restricted with specious parametric prediction in the geometries of the cracks, in particular curvilinear of the cracks in non-planar cracks (i.e., spherical cap and cylindrical cracks) and consideration of a various crack subtended angle of the surface in non-planar cracks such as spherical cap and cylindrical cracks, the aspect ratio of tunnel crack, and the interaction of two penny-shaped cracks in vertical and horizontal directions which have currently not been widespread considered in infinite domain. Besides, there is less diagnosis of changed permittivity for planar and non-planar cracks (e.g., spherical cap crack, cylindrical crack, tunnel crack and a pair of penny-shaped cracks in vertical and horizontal directions) on crack-face assumptions (i.e., impermeable, permeable, semi-permeable and energetically consistent models) which implied that the remaining electric quantity or electric induction current inside the crack gap including the crack surface that affected to non-zero stress and electric intensity factors, along the crack front in those geometries and less diagnosis of various loading conditions (i.e., remote tensile mechanical and electrical loads) associated with various electric boundary conditions. The main objective is to investigate the behavior of the piezoelectric material containing various cracks in infinite medium with affected relevant parameters to non-zero stress and electric intensity factors with various electric boundary conditions such as permeable, impermeable, Simi-permeable and energetically consistent boundary conditions. In the present, influence of geometry, crack-face condition and loading on

intensity factors of cracks in 3D linear piezoelectric media is becoming more interesting and essential to conduct further research.

The approach to investigate the fracture behavior, especially the stress and an electric intensity factor in piezoelectric materials is the simulation in arithmetic. Such spacious approach utilized to simulate the crack is upon basic of the Boundary Element Methods (BEMs) which was admitted as a numerical technique that is efficiently capable to compute the crack for fracture analysis in linear homogenous media. Later this technique is developed as weakly singular, SGBEM (Rungamornrat & Mear, 2008).

1.2 Literature and review

In this part, a brief background and the present work related to the current investigation is discussed. The major purpose is to exhibit the study of crack behaviors in piezoelectric media to illustrate the gap of perception and the derivation of the present work. For this part of literature exploration, the parametric influential study would be discussed. This includes geometries, permittivity, loading conditions and electric boundary conditions aspect and etc.

1.2.1 Influence of parameters on intensity factors

Many investigators attempt to study the crack behaviors in a large number of different methods and various conditions to obtain required unknown quantities in the body containing the various cracks in piezoelectric medium. (Kogan et al., 1996) In the three-dimensional problem, they have applied spheroidal piezoelectric inclusion or penny-shaped crack subject to axisymmetric, in-plane and out of plane shear (remote loading) in transversely isotropic piezoelectric (PZT-4, PZT-5H) infinite medium under electrical permeable boundary condition via the harmonic function (analytical solution) to investigate the stress and induction intensity factor. (Gao & Fan, 1999) They have examined and found that the uniform electric loads have no influence on the field singularities and obtain the field intensity factor in two-dimensional problem under transversely isotropic piezoelectric infinite medium with electric impermeable BC. They have also employed the elliptical hole subjected to uniform remote loads using the potential approach (analytical solution). (Chen & Shioya, 2000) By employing the potential theory (analytical solution) beneath the electric impermeable BC in the three-dimensional problem, the penny-shaped crack subjected to axisymmetric arbitrary shear loading “uniform shear and point loading” at the crack surface is employed in transversely isotropic piezoelectric (PZT-4, PZT-5, PZT-7A, PZT-6B, BaTiO₃) finite medium to obtain the complex stress intensity factor. In addition, mode II and mode III are also derived in an exact manner, for the case of the uniform loading in comparison with Kogan et al. (1996). (Davì & Milazzo, 2001) They have obtained the generalized stress intensity factors and the generalized relative crack displacement and compared with exact solution by using the horizontal crack “inclined crack with angle in a rectangular solid” applied to normal far-field stress and normal electric displacement (remote loading) via the boundary element method (numerical solution) in two-dimensional transversely isotropic piezoelectric (PZT-4) infinite medium with electric impermeable BC. Again, the investigation of Jiang and Sun (2001) under electric impermeable BC in the three-dimensional and transversely isotropic piezoelectric

(PZT-4) infinite medium is utilized in association with a half-penny-shaped crack. This is for half space problem under arbitrarily axisymmetric loading conditions. In addition, semicircular crack (applied at crack surface) is carried out by using the Henkel integral transform and dual integral equation. (Yang & Lee, 2002) they have applied the potential theory, Henkel transform and Fourier series to gain the Fredholm integral equation under the electric impermeable BC in three-dimensional transversely isotropic piezoelectric (PZT-6B) finite domain associated with a penny shaped crack under non-axisymmetric in-plane and a pair of concentrated normal mechanical and electrical loads (at the crack surface). (Gruebner et al., 2003) In three-dimensional, transversely isotropic piezoelectric (PZT-4) finite domain, the mixed electric BC (limited permeable or Semi-permeable, permeable, impermeable) is discussed. The finite element method is employed in association with the Griffith crack in the piezoelectric block subject to external electromechanical load at the surface of the block. (Landis, 2004) In three-dimension transversely isotropic piezoelectric (PZT-5H) infinite medium under the standard infinitesimal deformation theory with the electrical consistent BC, the Griffith crack with electromechanical loading (at the crack faces) is employed to demonstrate that the energy release rate computed near the crack tip is equivalent to the total energy release rate in which this result is compared with the electric impermeable BC. (Denda & Mansukh, 2005) They have applied the multiple straight crack (e.g., two inclined cracks in an infinite body under uniaxial tension, two aligned parallel cracks in an infinite body under uniaxial tension, and two collinear cracks in an infinite body under uniaxial tension (all at remote loading)), on the mixed mode BCs (electric impermeable and permeable BC) in two-dimensional orthogonal piezoelectric infinite medium by employing much simpler linear solution procedure by Boundary element method (BEM) in association with the Green's function approach. Also (Groh & Kuna, 2005) under the problem of two-dimensional transversely isotropic piezoelectric (PZT-4, PZT-5H, BaTiO₃), infinite medium is investigated in association with the electric impermeable BC by using the kinked crack subject to electrical loading. In addition, Crack perpendicular is employed to an interface under electromechanical loading. Moreover, Griffith crack is applied under shear load and uniaxial load (all at remote loading) via the universal boundary element method, sub-domain technique and fundamental solution using Fourier series. For Ou and Chen (2007), based on Stroh's theorem (Stroh, 1958) and the compact formulations under the electric Semi-permeable in two-dimensional transversely isotropic piezoelectric (PZT-4, PZT-5H, PZT-6B) infinite medium, they have applied the conducting crack "a center crack" under mechanical and electrical loading (remote loading). In the same year, (Qin et al., 2007) the electric impermeable is diagnosed in three-dimensional transversely isotropic piezoelectric (PZT-4, PZT-6B) infinite medium by employing a planar crack (Rectangular crack) under mechanical and electrical loads, Elliptical crack under mechanical and electrical loads (all at remote) via the Finite-part integral and boundary element method associated with body force method. For (Nam & Watanabe, 2008) in two-dimensional transversely isotropic piezoelectric (PZT-4) infinite medium under the mixed BC (permeable and impermeable BC) via the finite element method, they have utilized a notch-like crack filled with a dielectric inclusion under electromechanical loading (remote loading). Moreover, (Solis et al., 2009) they have investigated the stress and electric intensity factor by utilizing three types of crack. The first one is the elliptical crack under electric and mechanical load. The second one is the prismatic

plate with central crack subject to uniform normal traction and electric displacement at two opposite faces. The last is prismatic plate with two edge cracks. All these three types of crack are subject to uniform normal traction and uniform electric displacement at the two opposite faces parallel to the crack via the boundary element method in three-dimensional transversely isotropic piezoelectric (PZT-4) finite and infinite medium under the electric impermeable and permeable BC. The result of this investigation is also compared with other results. (Kuna, 2010) has applied the theoretical fundamentals of linear piezoelectric fracture mechanics under the mixed modes BC (impermeable, permeable, conducting and limited permeable “Semi-permeable”) in two-dimensional anisotropic piezoelectric (PZT-5H, PZT-4) switching domain by utilizing Griffith crack under a constant remote stress with perpendicular poling and electric field (remote loading). (Fang et al., 2011) in the electric impermeable BC via the complex variable method (analytical solution) in two-dimensional transversely isotropic piezoelectric (PZT-5H, PZT-4, BaTiO₃) infinite medium, the elliptical inclusion with an interfacial crack subjected to arbitrary singularity loads (point charge and anti-plane concentrated force) and remote anti-plane mechanical and in-plane electrical loads (remote loading) is employed. (Zhou et al., 2012) in three-dimensional transversely isotropic piezoelectric (BaTiO₃-CoFe₂O₄) infinite medium via the generalized Almansi’s theorem and the Schmidt method (analytical solution) under the electric limit-permeable BC (Semi-permeable), they have utilized the rectangular limited-permeable crack and two three-dimensional limited-permeable rectangular crack assumed a distributed normal stress loading (applied the crack surface). At the same time, (Zhao et al., 2012) The conventional displacement discontinuity method associated with green’s function method is employed on the electric impermeable BC in three-dimensional transversely isotropic piezoelectric (BaTiO₃) infinite medium with the vertical crack (the rectangular crack) subjected to the uniform mechanical and electric loading (at crack surface), besides; (Sladek et al., 2012) They have investigated in two-dimensional transversely isotropic piezoelectric (PZT-4) in an inhomogeneous finite strip under the mixed boundary condition “permeable and impermeable”, the central interface crack of two dissimilar piezoelectric materials under a pure mechanical load at the crack surface is employed via a mesh less method based on the local Petro Galerkin approach associated with Quasi-static governing equations. (Li et al., 2013) under the electric impermeable BC in two-dimensional transversely isotropic piezoelectric (PZT-4 and PZT-5) infinite domain via the scaled boundary finite element method, the Infinite plate with central-inclined crack under remote tension and electric displacement load, Infinite plate with a branched crack under a uniform tension or a uniform electric displacement load and Finite plate with a central-inclined crack under a uniform tension or a uniform electric displacement load is used. (Hu & Chen, 2013) the cracked piezoelectric strip under in-plane mechanical and electric impact loadings (remote loading) is discussed under the electric impermeable BC in two-dimensional transversely isotropic piezoelectric infinite medium via the Fourier and Laplace transform to a singular integral equation. (Nan & Wang, 2013) the electrical mixed mode BC (permeable and impermeable) is employed associated with a through-thickness crack of length “2a” under a remote uniform normal stress and an electric displacement (remote loading) beneath two-dimensional transversely isotropic piezoelectric (PZT-5H) infinite medium via the singular integral equation technique whereas the result is found that the effect of surface on the electric displacement

intensity factor depends on the crack face electric boundary condition and influenced by the residual surface stress on the entire crack surface which compared with the theoretical result. (Tran & Mear, 2014) in the two-dimensional multi-field (anisotropic, elastic, isotropic, transversely isotropic “PZT-4” and magnetoelastic) finite and infinite medium under the electric impermeable via a weakly singular, SGBEM, the Straight crack in infinite domain, subjected to either a uniaxial far-field stress or a far-field electric induction, Rectangular plate with a central inclined crack subjected to either uniform tension stress or electric induction (remote loading). The result has indicated that the ‘generalized’ stress intensity factors are examined, highly accurate results are obtained with relatively coarse meshes under comparing with the exact solution and available result associated with different method. Also (Chen et al., 2014) a Semi-infinite conducting crack under mechanical impact loading (at crack surface) under two-dimensional transversely isotropic piezoelectric (PZT-4, PZT-6B, PZT-7A and PZT-8) Semi-infinite medium under electric impermeable BC via the integral transform method, the Wiener-Hopf technique assembled with the universal function. Fan et al. (2014), the extended displacement discontinuity integral equation method (analytical solution) and developed an extended displacement discontinuity boundary element method is employed with the electric impermeable BC in three-dimensional transversely isotropic piezoelectric (PZT-6B) infinite medium under the penny-shaped crack under a uniform electric and mechanical loading, non-uniform loading (at the crack surface)

The various parameters (e.g., geometry, loading conditions, permittivity in the crack gap, various geometries and four crack-face boundary conditions) have an influence to fracture in the piezoelectric medium. Many investigators have conducted researches on this topic. (Kogan et al., 1996) they have considered stress component in x and y -axis subjected to anti-symmetric (out of plane shear and in-plane shear) by varying the range of latitude ($\omega = 0$ to 80) to diagnose the quantities (load ratio) on the boundary of a spherical hole inside the piezoelectric-ceramics PZT-4 at $\vartheta=0$ and $\vartheta=0$, respectively. (Yang & Lee, 2002) The singular mechanical and electric fields and all mode-I field intensity factors are examined. For the first case, the stress intensity factor is considered in different ratio of the crack radius to layer thickness ($a/h = 0.0$ to 1.0) for PZT-6B ceramic under axisymmetric loads (case1 to case4). The second case is to investigate the change of normalized SIF ($\varepsilon_0=1.0 \times 10^{-5}$ & $a=10\text{mm}$) with the applied electric field ($E_0 = -20$ to 10×10^5 V/m) of the load case2. For the third case of non-axisymmetric loads, the polar angle ($\theta=0$ to 90 degree, a/h is constant and vary r_0) on the face is considered by varying the polar angle of the crack ($\theta = -200$ to 200 degree) to demonstrate the stress IF and the ratio of $r_0 = b/a$ (a/h is constant and vary θ) is represented to diagnose the SIF of the load case1 by varying θ . (Gruebner et al., 2003) According to the distinct permittivity (0.5 , 1.0 and 2.5) in various BC (e.g., impermeable, permeable and semi-permeable) are discussed by varying electrical load (-0.01 to 0.01 C/m²) to demonstrate the stress intensity factor mode-I and mode-IV and the case of the energy release rate J and J^M with the mechanical load ($\sigma_{22}^{ext} = 10\text{MPa}$). In this research, the investigation is to demonstrate that the influence of the permeability of the crack on electric and mechanical fields near the crack tip is considered, and that the influence on the stress intensity factors and energy release rate will be discussed and compared with the CT specimen. Furthermore, (Ou & Chen, 2007) they have found that the normal crack opening displacement jump (NCODJ) is

always extremely small, whereas the electric potential drop (EPD) across the crack is very large and the energy release rate (ERR) influences the permittivity. In this investigation, they considered the permittivity ($\varepsilon_a = 10^{-8}, 1, 2.5, 20000 \varepsilon_0$) by varying the distinct valued electric field (-0.5 to 0.5 MV/m) to demonstrate the influence of permittivity upon normalized crack opening displacement jump (NCODJ) and electric potential drop (EPD) of PZT-5H and PZT-4 with $a = 1\text{mm}$ and $\sigma_{22}^{\infty} = 20\text{MPa}$. Moreover, the normalized crack tip ERR against the applied electric field (-0.5 to 0.5 MV/m) for a central crack in PZT-4 and PZT-5H is subject to different mechanical loading levels ($1, 5, 10, 20, 50$ Mpa) and the influence of the permittivity ($\varepsilon_a = 10^{-8}, 1, 2.5, 20000 \varepsilon_0$) of medium inside crack gap on the crack tip ERR of PZT-5H, PZT-4 and PZT-6B is investigated. According to Qin et al. (2007), the different ratio ($a/b = 1, 2, 3$ and 4) with the position along the crack front ($\pm b$) of the rectangular crack ($x/a = 0.0$ to 1) is carried out. Besides, the aspect ratio of the elliptical crack ($a/b = 1, 4/3, 3/2$ and 2) with varying the angle φ (position) of the elliptical crack also considered to obtain the result of dimensionless intensity factor mode-I and mode-IV in which this result is compared with the exact and Chen's result. As (Kuna, 2010) mentioned, the relative permittivity is diagnosed by varying the remote electric field (-1 to 1 MV/m) to demonstrate the total and mechanical EER (semi-permeable) of the Griffith's crack in PZT-5H subject to the mechanical load (20MPa). The result can be found that experimental fracture investigations are relatively poor when compared the method because of many influential factors. For (Fang et al., 2011) the result is that the energy release rate (ERR) increases with an increment of the ellipse aspect ratio. It is positive but can be negative when both mechanical and electric fields are applied. This effect has been obtained from the shear modulus ratio ($\lambda = 0.1$ to 20) with different loading (case1: $\varepsilon = 0.5, \tau_{xz}^{\infty} = \tau^{\infty}, \tau_{yz}^{\infty} = \tau^{\infty} = 0$ and case2: $\varepsilon = 0.5, \tau_{xz}^{\infty} = 0, \tau_{yz}^{\infty} = \tau^{\infty}$, distinct aspect ratio ($\varepsilon = 0.1$ to 0.9) with different loading ($\lambda = 0.5, \tau_{xz}^{\infty} = \tau_{yz}^{\infty} = \tau^{\infty}$), the permittivity of PZT- 65/35, PZT-5H, PZT-4, BATIO3 with the constant $\lambda = 0.5, \varepsilon = 0.5$ by varying the angle of the elliptical crack ($\beta = 0$ to 180 degree). To enhance their computational, the different matrix piezoelectric constants is varied $e_{15}^{(2)}$ ($5, 10, 20$) with the load cases (case1: $E_x^{\infty} = E^{\infty}, E_y^{\infty} = 0, \lambda = 0.5, d_{11}^{(2)} = 0.5d_{11}^{(1)}$ and case2: $E_x^{\infty} = 0, E_y^{\infty} = E^{\infty}, \lambda = 0.5, d_{11}^{(2)} = 0.5d_{11}^{(1)}$). The aspect ratio is varied in the range $\varepsilon = 1, 0.2, 0.5, 0.7, 0.9$ with the load ($E_x^{\infty} = E_y^{\infty} = E^{\infty}$). The permittivity of PZT- 65/35, PZT-5H, PZT-4, BATIO3 with the load ($E_x^{\infty} = E_y^{\infty} = E^{\infty}, \varepsilon = 0.5$) is varied with the angle of the elliptical crack ($\beta = 0$ to 180 degree). Besides, the loading coefficient $e_{15}^{(2)}$ (0.06 to 0.10) matrix piezoelectric constant $e_{15}^{(2)}$ (6 to 16) with the conditions $\beta = \pi/2, \varepsilon = 0.5$ and $E_x^{\infty} = E_y^{\infty} = E^{\infty}, \tau_{xz}^{\infty} = \tau_{yz}^{\infty} = \tau^{\infty}, E^{\infty} = 0.1\tau^{\infty}, \varepsilon = 0.5$, respectively, indicates the normalized ERR by varying different angle. According to (Zhou et al., 2012), various BC (permeable and semi-permeable) is considered to indicate the stress intensity factors K_x along the crack edge with the conditions ($D_0/\varepsilon_0 = 1.0 \times 10^8, B_0/\mu_0 = 1.0 \times 10^5$ with $l_1 = l_2$) versus position ($y/l_2 = 0.0$ to 1.0). Moreover, the stress intensity factor K_x & K_y along the crack edge $x = l_1$ and $y = l_2$ with the condition ($D_0/\varepsilon_0 = 1.0 \times 10^8, B_0/\mu_0 = 1.0 \times 10^5$) is investigated by

varying ($y/l_2 = 0.0$ to 5.0) and ($y/l_2 = 0.0$ to 1.0) of various lengths l_2 respectively. In this case, the result revealed that the effects on the rate of the rectangular crack edge length on the stress intensity factors along the rectangular crack are large in comparison with Zhu's result and the electrical permeable BC. (Hu & Chen, 2013)) have found that the geometry of the cracked strip and the electric loading significantly influence the singular field distributions around the crack tip. For this investigation, they considered different angle ($\theta = 0, 25$ and 50 degree) by varying ($TVs/c = 0$ to 1), to obtain not only the dynamic hoop stress intensity factors while ($LE = +0.5, h_1/c=1, h_2/c=3$), but also the aspect ratio of the crack (h_1/c and h_2/c). The result was discussed to determine the maximum value of the normalized hoop stress intensity factors versus angles (-180 to 180 degree). Moreover, the different electrical loading ($LE = -1.0$ to $+1.0$) is carried out to indicate the dynamic HSIF, whereas the angle and the various lengths are constant ($\theta = 25, h_2=3h_1=3c$). Besides, the aspect ratios of the crack (h_1/c and h_2/c) are varied to reveal the dynamic stress intensity factor $K_I(t)$ versus electric loading the normalized time.

Clearly described above, a large number of studies related to theoretical modeling and analysis of cracks in piezoelectric media has been well recognized in the literature. However, work related to the investigation of the influence of various factors such as the crack geometry, crack-face conditions, loading conditions, properties of piezoelectric media and properties of a medium inside the crack gap on the fracture data along the crack front is still available only for certain scenarios and a limited range of parameters. Further studies are still required to provide more complete information and enhance fundamental understanding of the fracture behavior in piezoelectric materials.

1.3 Objective of research

The key objective of the proposed research is to fully investigate the influence of crack geometry, crack-face boundary conditions, loading conditions and permittivity inside the crack gap on the stress and electric intensity factors of cracks in piezoelectric media.

1.4 Scope of research

The proposed work is limited to (i) a three-dimensional, infinite medium made of a homogenous, transversely isotropic, linearly piezoelectric material and obeying the classical theory of linear piezoelectricity, (ii) a medium that is free of the body force and electric body charge, and (iii) the poling direction is directed along the axis of material symmetry. The influence of four parameters, (1) the geometry of cracks which is characterized by four representative cracks including a spherical cap crack, a cylindrical crack, a tunnel crack and a pair of two identical penny-shaped cracks, (2) the crack-face boundary conditions including the impermeable, permeable, semi-permeable, and energetically consistent conditions, (3) the electrical and mechanical remote loading conditions, and (4) the dielectric permittivity of the medium inside the crack gap, on the values and distribution of the intensity factors along the crack front are investigated.

1.5 Methodology and procedures

The key task of the present study is the efficient and accurate determination of the stress and electric intensity factors of cracks in piezoelectric media for various crack configurations and under various crack-face and loading conditions. To achieve this crucial task, following methodology and procedures are proposed.

(1) The boundary value problem is formulated based on a classical theory of linear piezoelectricity. A method of boundary integral equations is utilized to obtain the final governing integral equations.

(2) An existing numerical technique, based on a weakly singular symmetric Galerkin boundary element method (SGBEM) proposed by Rungamornrat and Mear (2008) and Phongtinnaboot et al. (2011), is utilized to determine the unknown crack-face data such as the relative crack-face generalized displacement.

(3) The stress and electric intensity factors along the crack front are post-processed from the relative crack-face generalized displacement using the existing formula proposed by Rungamornrat and Mear (2008)

(4) Results for certain cases are compared with available benchmark solutions to validate the numerical technique employed.

(5) The convergence of numerical solutions is fully investigated via a series of meshes with different levels of refinement. Sufficiently fine meshes are then chosen in the numerical study for investigating various parameters.

In the parametric study, various scenarios covering the range of all parameters of interest are considered to provide a set of data sufficient for concluding final findings.

1.6 Significance

Extensive results obtained from the present investigation should directly offer fundamental and in depth understandings of the influence of various factors such as models used to simulate the crack-face conditions, crack geometry and loading conditions on the value and distribution of stress and electric intensity factors along the crack front. For instance, the sensitivity of the adopted crack-face condition and the corresponding parameters on predicted results should at least provide a useful guideline in the selection of a mathematical model suitable for a given scenario.

CHAPTER 2

THEORETICAL CONSIDERATIONS

This chapter briefly presents the clear problem statement, the basic field equations used to formulate the boundary value problem of cracks in linear piezoelectric media, various models for simulating the crack-face boundary conditions, and characteristics of the near-tip generalized stress field. In addition, the standard definition of the stress and electric intensity factors is also provided at the end of this chapter.

2.1 Problem Descriptions

In this section, we consider an infinite domain containing a planar and non-planar cracks in three-dimensional problem in which this material is linear, homogenous transversely anisotropic piezoelectric. In this particular case, the body force and electric charge is assumed to disappear at the beginning. In this case, to investigate the stress and electric intensity factors, along the crack front, we discuss only loading on crack surface and remote loading associated with various electric boundary conditions such as electrical impermeable, electric permeable, semi-permeable and energetically consistent boundary conditions indicated in Figure 2.1.

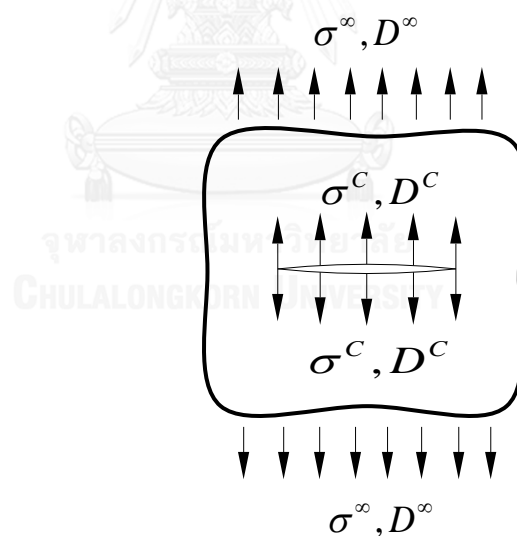


Figure 2.1 Schematic of a linear piezoelectric body containing a crack infinite medium.

In the current investigations, the various influence parameters are utilized to examine the non-zero stress and electric intensity factor. The geometries such as planar and non-planar cracks are first utilized to investigate various parameters including influence of geometry on four crack-face models. The permittivity inside the crack gap is varied in the wide range on four crack-face models. The loading conditions such as applied remote tensile mechanical and electrical load are also varied in the wide range and the various boundary conditions (viz. impermeable, permeable, semi-permeable and energetically consistent models) are investigated in all cases.

2.2 Basic equations

In this section, we firstly propose a set of basic field equations governing a body constituting a linear piezoelectric material. In the piezoelectric problem, providing that the body force field and the body electric charges do not appear in the beginning, a set of field equations governing a piezoelectric body, including conservation of forces and electric charges, strain-displacement and electric field-electric potential relations and constitutive model for linear piezoelectricity can be presented below. The conservation of forces and electric charges is governed by

$$\frac{\partial \sigma_{ij}}{\partial x_i} = 0 \quad ; \quad \frac{\partial D_i}{\partial x_i} = 0 \quad (2.1)$$

The strain-displacement and electric field-electric potential relations are given by

$$\varepsilon_{ij} = \frac{1}{2}(u_{i,j} + u_{j,i}) \quad ; \quad E_i = -\phi_{,i} \quad (2.2)$$

The constitutive model for linear piezoelectricity follows

$$\sigma_{ij} = E_{ijkl} \varepsilon_{kl} + e_{mij} \phi_{,m} \quad ; \quad D_i = e_{ikm} \varepsilon_{km} - k_{im} \phi_{,m} \quad (2.3)$$

where $\sigma_{ij}, D_i, \varepsilon_{ij}, E_i$ and u_i are components of the stress tensor, electric induction vector, strain tensor, electric field and displacement vector, respectively; besides, K_{im} is dielectric permittivity; ϕ is the electric field and e_{mij} is piezoelectric constants.

2.3 Boundary conditions

In this section, the essential conditions must be diagnosed including the basic field equation, the boundary conditions on the crack surfaces and outer boundary such as the mechanical and the electric conditions. Such conditions are significant information that must suitably be assigned in the analysis of piezoelectric media containing fracture. This information, particularly the boundary conditions on the crack surfaces, has a major influence on both the main data and behavior of the crack surface. For this investigation the outer boundary is considered in association with the uncoupled mechanical-electric boundary conditions, whereas the boundary conditions at the crack surface are considered in two groups. The first one is associated with uncoupled mechanical-electrical boundary conditions (i.e. Permeable and impermeable assumptions) and the second one with the fully mechanical-electrical boundary conditions (i.e. semi-permeable and energetically consistent assumptions). The four types of cracks are summarized in this investigation as following:

For permeable crack, Parton (1967) was the first to propose the definition of the boundary condition, that there is an electric current inside the crack gap. For this special case, it means that both the electric induction and electric potential normal to the crack surface are continuous on the both sides of the crack surface. This implies that both the

jump of the electric potential across crack surface and the electric potential drop across the crack surface vanish. Accordingly, the entire data for this case can be briefly summarized that the jump in the mechanical displacement Δu_i and the surface electric charge t_4^+ are unknown in the beginning whereas the jump in the electric potential and the sum of the surface electric charges disappear ($\Delta u_4 = 0$ and $(\Sigma t_4 \equiv t_4^+ + t_4^- = 0)$) and the mechanical tractions t_i^- and t_i^+ are imposed.

For impermeable crack, this boundary condition was firstly proposed by Deeg (1980) that there is no electric current inside the crack gaps. This means that on the both sides of the crack surface (upper and lower surfaces), the electric induction normal to the crack surface was supposed to disappear while the electric potential was unknown in the beginning. The known data for this case can be summarized that the generalized tractions t_i^+ and t_i^- , are completely imposed, whereas the jump in the generalized displacement across the crack surfaces, represented by $\Delta u_j \equiv u_j^+ + u_j^-$, are unknown a priori.

For semi-permeable crack, it is commonly known that the impermeable and permeable cracks are extreme cases. In this boundary condition is the mixed modes between impermeable and permeable boundary conditions, considering the permittivity inside the crack gap. It means that the vacuum inside the crack gap can partially induce electric induction. This derivation of this boundary is from Hao and Shen (1994)'s boundary condition which can be concluded that the mechanical traction t_i^+ and t_i^- are prescribed and the sum of the surface electric charges disappear ($\Sigma t_4 = 0$) whereas the jump of generalized displacement are unknown in the beginning and must be satisfied the following extra condition:

$$t_4^+ \Delta u_i n_i^+ = k_c \Delta u_4 \quad (2.4)$$

Where K_c is the dielectric permittivity of the medium inside the crack gap

For the energetically consistent crack, this boundary condition is a more realistic assumption from Landis (2004) in resolving the investigation of McMeeking (2004). The result can be found that energetically consistent model is equivalent to each other by increasing the traction on the crack surfaces in which Semi-permeable model is not considered. In this particular case from the discussion of the energetically consistent model, the non-zero-mechanical traction t_i^+ and t_i^- which tend to pull the upper and lower crack surfaces can be separated into two parts $\sigma_i^+ + \tau_i^+$ and $\sigma_i^- + \tau_i^-$, where $\{\sigma_i^+, \sigma_i^-\}$ and $\{\tau_i^+, \tau_i^-\}$ represent the normal and shear tractions respectively. In this crack, $\{\tau_i^+, \tau_i^-\}$ are completely imposed and the sum of the surface electric charges and the sum of the normal mechanical tractions disappears (i.e., $\Sigma t_4 = 0$ and $\Sigma \sigma_i \equiv \sigma_i^+ + \sigma_i^- = 0$), whereas the jump in the generalized displacement Δu_j , the mechanical normal traction σ_i^+ and the surface electric charge t_4^+ are unknown and satisfy the relation.

$$\sigma_j^+ = (1/2)k_c n_j^+ (\Delta u_4)^2 / (\Delta u_i n_i^+)^2 \quad (2.5)$$

2.4 Near-tip generalized stress field of linear piezoelectric material

Analogous to the work of *Westergaard, Irwin, Sedona and Williams (1975)* who were among the first group to carry out the near-tip field investigation of the crack body in infinite domain, it is possible to derive closed-form expressions for the stresses in the body in linear piezoelectric material with respect to the coordinate system. We determine a polar coordinate (r, θ) and standard coordinate system (x_1, x_2, x_3) with the origin at the crack front x_c where the plane $x_1 - x_2$ normal to the crack front at x_c . The plane $x_2 - x_3$ and $x_1 - x_3$ is the tangent plane at the point x_c at the crack front (as shown in the figure below) and the orthonormal base vector (e_1, e_2, e_3) is in the same direction of (x_1, x_2, x_3) respectively. It can be illustrated that the stress field in any linear piezoelectric cracked body is offered by:

$$\sigma_{ij}(x_c; r, \theta) = \sum_{n=1}^4 \left\{ \frac{K_n(x_c, f_{co})}{\sqrt{2\pi r}} \sigma_{ij}^{(n)}(\theta) + \sum_{m=0}^{\infty} A_m(x_c, f_{co}) r^{\frac{m}{2}} \sigma_{ij}^m(\theta) \right\} \quad (2.6)$$

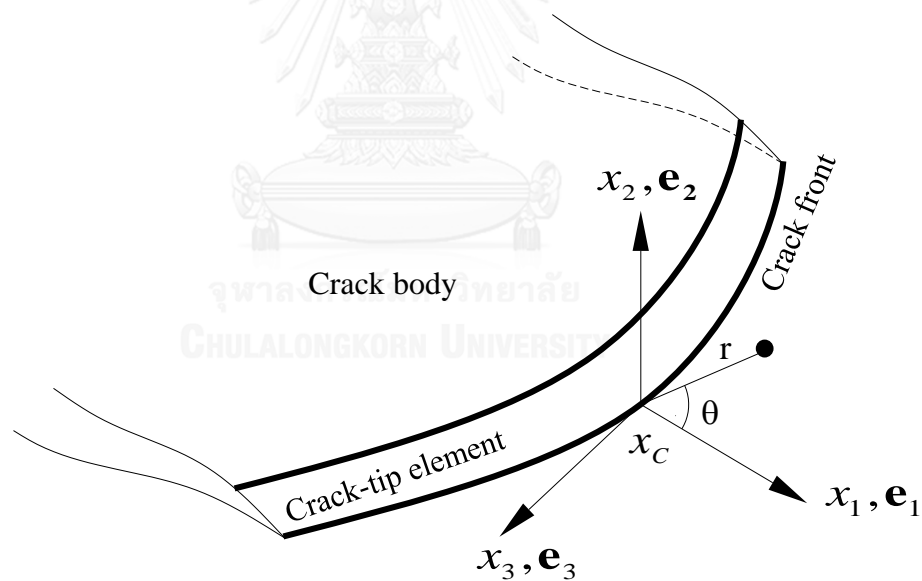


Figure 2.2 The coordinate system with notation utilized in near-tip generalized stress field along the crack front

where σ_{ij} represents the generalized (Mechanic and electric stress) stress tensor ($i=1,2,3$ and $J=1,2,3,4$) and $D_i = \sigma_{i4}$ are components of the electric induction vector. K_n and A_m are constant in which depend primarily on position x_c and the conditional function f_{co} where f_{co} is the function with respect to loadings, boundary conditions, geometries and material properties. $\sigma_{ij}^{(n)}$ is the stress function which depends only on θ (independent of radius r) in the first term and depends on the modes. For the higher-

order terms, $\sigma_{ij}^{(m)}$ denotes the stress function with respect to θ for the m -term and depending on geometries. In this particular case, the solution for the above equation (2.6) contains a first term that is proportional $1/\sqrt{r}$. If and only if the radius $r \rightarrow 0$ the first term approaches to infinity or called the singular at that point, but the other higher term remains finite or approach to zero called non-singular. Inasmuch, the generalized stress near the crack front varies with $1/\sqrt{r}$. The stress $\sigma_{ij}^{(n)}$ and $\sigma_{ij}^{(m)}$ in equation (2.6) can be simply gained by asymptotic analysis for each proper problems. Unfortunately this is still not the perfect analysis for the analytical of boundary value problems. When the perfect stress field can be assigned, the stress function $\sigma_{ij}^{(n)}$ and $\sigma_{ij}^{(m)}$ in equation (2.6) can be found by the procedure of standard series expansion.

There are four types of loading that a crack can be experienced. Mode-I denoted as K_I or K_I where the principal loads are applied normally to the crack plane and tend to open the crack. Mode-II denoted as K_2 or K_{II} represents in-plane shear loading and tends to slide one crack surface with respect to the other plane. Mode-III denoted as K_3 or K_{III} represents out-of-plane shear and Mode-IV denoted as K_4 or K_{IV} represents electrical intensity factor on a crack body, or a combination of two or three modes. Each mode of loading offers the $1/\sqrt{r}$ singularity at the crack front. The stress and electric intensity factors (or generalized stress) at a point x_c are determined by taking The limit $r \rightarrow 0^+$, after the stress function of the left hand side of the equation (2.6) are known as shown:

$$\begin{bmatrix} K_1 \\ K_2 \\ K_3 \\ K_4 \end{bmatrix} = \lim_{x_1 \rightarrow 0^+} \sqrt{2\pi x_1} \begin{bmatrix} \sigma_{22} \\ \sigma_{12} \\ \sigma_{23} \\ \sigma_{24} \end{bmatrix} \quad (2.7)$$

Where the stress field $[\sigma]$ in the right hand side of equation (2.7) depends on the local coordinate system (x_1, x_2, x_3) and can be obtained from each proper problems.

CHAPTER 3

SOLUTION TECHNIQUE

This section discusses the technique and procedure used to obtain the solution of the boundary value problem stated in Chapter II. A brief introduction to the weakly singular SGBEM adopted in the present study is presented first and then the post-process for the stress and electric intensity factors along the crack front is addressed. In addition, the generation of meshes used in the numerical study, convergence check and verification of the numerical technique are also included.

3.1 Introduction of SGBEM

From the mechanic computational aspect (fracture problem), to analyze fracture problems in infinite domain can be analyzed from two main groups, such as analytical and numerical technical groups. We can derive closed form for the fracture problem only for the case that the problem is not very sophisticated, for example two-dimensional problems and simple geometries and etc. In such case the analysis is required. Solving the crack problems via the numerical technic is particularly reasonable for a complex or more complex problem such a three-dimensional problem or that of which geometries are complicated. In the numerical technique, there are many approaches such as finite difference method (FDM), finite element method (FEM) and boundary element method (BEM) and so on. These are considered as common methods to investigate the data along the crack front in the fracture problems.

The difference between the finite element method (FEM) or finite different method (FDM), and the boundary element method (BEM) is that the finite element method is efficient for large scale and complex problem of fracture and is in the symmetric of sparse coefficient matric form. However, this method demands discretization in the whole domain, which means that the final governing integral equation involves the entire variables of the domain that is no need for crack problem. Moreover, the generation of mesh also requires in whole domain (involved crack surfaces) which needs to be considered as three-dimensional problem; hence, this method is not popular in use in infinite domain problem. The finite element method (FEM) can also be more difficult in practice.

In the group of boundary element method (BEM), on the other hand, the data appears only as unknown variable on the crack surface into the governing integral equation. This means that the dimension of the problem can be reduced. The BEM group is more effective in the area in which the FEM has difficulties. They can be classified in many techniques for instance boundary element method (BEM) which based upon collocation technic (e.g. to satisfy integral equation at each point). The form of metrics is also the dense non-symmetric form. However, the BEM (based on collocation technique) is not suitable when the domain becomes larger and non-linear or non-homogeneous. It is then difficult to develop the governing equation as it is related to kernel which appears in governing integral equation, or we must implement the strong form of the governing integral equation.

Another feature of the BEM group is the symmetric Galerkin boundary element method (SGBEM) which is based on symmetric Galerkin approximation or in weak form integral equation, which is to satisfy integral equation as average point. Notably, this technique have separated singular kernel in the final governing formulation as many forms, such as Hyper singular SGBEM (which needs C^1 element which is a high smoothness required for the shape function), strongly singular SGBEM (which needs C^1 element) and weakly singular SGBEM (which needs C^0 element in which the slope can be discontinuous and require only the continuous of function values essential for the shape function). According to the weakly singular, SGBEM have many advantages, inasmuch this method will be employed here.

To obtain an integral equation applied for constituting fundamental of weakly singular, SGBEM must impose the stress and electric intensity factors along the crack front. We need a boundary integral equation (BIE) in term of complete boundary value problem including the whole data at the crack. The stress field along the crack front and the relative crack face can be employed to separate the stress and electric intensity factors in the equation (2.7). In this section, we can briefly summarize a series of boundary integral equation significant for weakly singular, SGBEM. We consider a crack body in the infinite domain in which the material is linear homogenous, transversely anisotropic piezoelectric media. The upper and lower crack surfaces denoted by S_c^+ and S_c^- , respectively, and the outward unit normal vector n^+ and n^- normal to the upper and the lower crack surface is determined in figure 3.1 below. The traction on the crack surface is supposed known a priori.

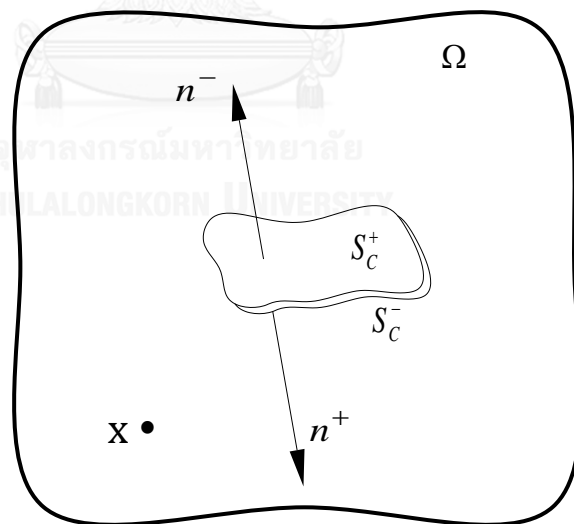


Figure 3.1 Schematic of an isolated crack in three-dimensional, generally anisotropic infinite domain

Eventually, The complete weakly singular, weak-form boundary integral equation for the generalized surface traction is assigned which was developed and

offered by Rungamornrat and Mear (2008). It should be noted that each term contains weakly singular of $\mathcal{O}(1/r)$. The final equation of weak form is shown below:

$$\begin{aligned}
-\frac{1}{2} \int_S \tilde{v}_K(\mathbf{y}) t_K^*(\mathbf{y}) dS(\mathbf{y}) &= \int_{S_C^+} D_i \tilde{v}_K(\mathbf{y}) \int_{S_C^+} C_{mJ}^{iK}(\xi - \mathbf{y}) D_m v_J(\xi) dS(\xi) dS(\mathbf{y}) \\
&+ \int_{S_C^+} D_i \tilde{v}_K(\mathbf{y}) \int_{S_C^+} G_{iK}^J(\xi - \mathbf{y}) t_J(\xi) dS(\xi) dS(\mathbf{y}) \\
&+ \int_{S_C^+} \tilde{v}_K(\mathbf{y}) \int_{S_C^+} H_{iK}^J(\xi - \mathbf{y}) n_i(\mathbf{y}) t_J(\xi) dS(\xi) dS(\mathbf{y})
\end{aligned} \tag{3.1}$$

where \tilde{v}_K represent a test function $\tilde{v}_K(\mathbf{y}) = \Delta \tilde{v}_K(\mathbf{y})$, $y \in S_C^+$, $t_K^*(\mathbf{y})$ represent the generalized traction by $t_K^*(\mathbf{y}) = 2t_K^+(\mathbf{y})$, $y \in S_C^+$; v_J denote the generalized jump of displacement; D_m is a surface differential operator assigned by $D_m = n_i \varepsilon_{ism} \partial / \partial \xi_s$. Where ε_{ism} represent alternating symbol.

A specific solution of the unknown singular functions G_{mJ}^P and C_{mJ}^{IK} can be established by solving a system of partial differential equations. A method of Radon transforms which is analogous to the method utilized in work of Rungamornrat and Mear (2008) is applied. Finally, the implemented solution is expressly displayed in term of a linear integral as below:

$$G_{mJ}^P((\xi - \mathbf{x})) = \frac{1}{8\pi^2 r} (\varepsilon_{abm} E_{aJdc}) \oint_{z,r=0} z_b z_c (\mathbf{z}, \mathbf{z})_{DP}^{-1} ds(\mathbf{z}) \tag{3.2}$$

$$C_{mJ}^{IK}((\xi - \mathbf{x})) = \frac{1}{8\pi^2 r} (A_{mJdN}^{iKsM}) \oint_{z,r=0} z_s z_d (\mathbf{z}, \mathbf{z})_{MN}^{-1} ds(\mathbf{z}) \tag{3.3}$$

where $z.r = 0$ denote the line integral evaluated over a unit circle in the plane; A_{mJdN}^{iKsM} is the material-dependent constants can be presented by:

$$A_{mJdN}^{iKsM} = \varepsilon_{pam} \varepsilon_{pbt} \left(E_{bKNd} E_{aJMs} - \frac{1}{4} E_{aJKb} E_{dNMs} \right) \tag{3.4}$$

And $H_{ij}^P(\xi - \mathbf{x})$ is given which is independent of the generalized elastic moduli defined by:

$$H_{ij}^P(\xi - \mathbf{x}) = -\frac{\delta_{JP}(\xi_i - x_i)}{4\pi r^3} \quad (3.5)$$

where δ_{JP} is represented as a generalized Kronecker delta symbol; $\delta_{JP}(\xi_i - x_i)$ is a Dirac-delta functional distribution centered at point X. The outstanding product of an equation (3.1) is the weakly singular kernels contain only $\{C_{mJ}^{iK}, G_{iK}^J, H_{iK}^J n_i\}$ of $\mathcal{O}(1/r)$

3.2 Determination of stress and electric intensity factors

According to the definition, the mode-I, mode-II and mode-III stress intensity factors [K_1 , K_2 and K_3] and mode-IV electric intensity factor K_4 are determined in equation (2.7). To implement the perfect analysis in contact with boundary value problems and estimate the stress and electric intensity factors, the complete integral equation for instance equation (3.1) can obtain the nodal values of the jump in the generalized displacements on the crack surfaces. This can be employed to evaluate the stress along crack front (since the crack-face nodal is recognized). Nevertheless, it might be complicate to carry out such an approach in a fashion which would permit the stress and electric intensity factors to be exactly assigned.

For this difficulty, we look for an alternative to the definition of equation (2.7) to permit the stress and electric intensity factors appeared in term of the crack-face displacement information straightforwardly.

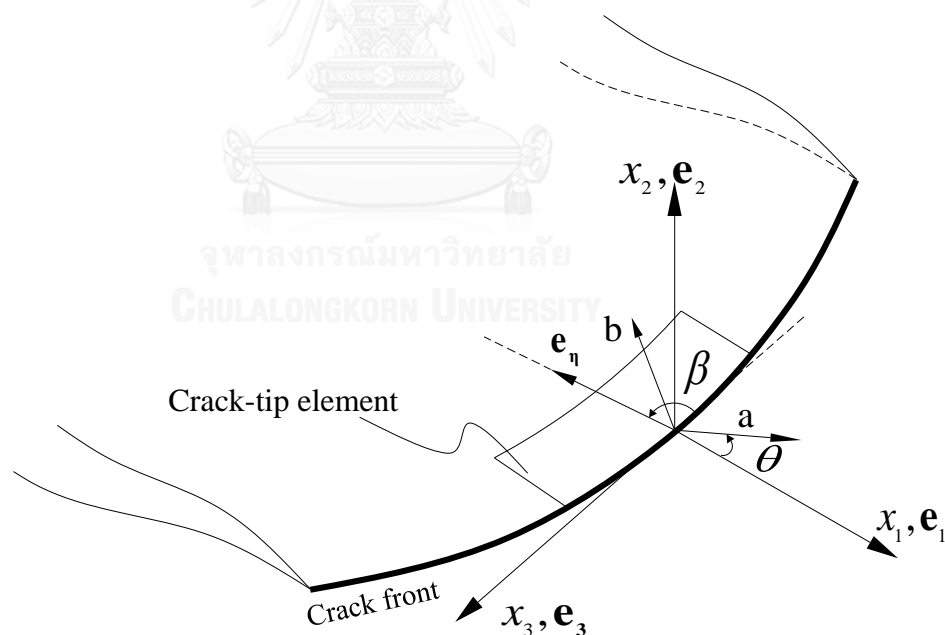


Figure 3.2 Schematic of an isolated crack in a three-dimensional, generally anisotropic, piezoelectric unbounded domain

Here we indicate only the final alternative expression (Barnett and Asaro (1972) and Xu (2000)) which provides the stress and electric intensity factors in term of the jump of the displacement on the crack surface as shown:

$$k_J(\mathbf{x}_C) = \frac{\sqrt{2\pi}}{4} B_{JP}(\mathbf{x}_C) \lim_{x_1 \rightarrow 0} \left(\frac{\Delta u_p(\mathbf{x})}{\sqrt{-x_1}} \right) \quad (3.6)$$

$$B_{JP}(\mathbf{x}_C) = \frac{1}{2\pi} \int_0^{2\pi} [(a,a)_{JP} - (a,b)_{JM} (b,b)_{MN}^{-1} (b,a)_{NP}] d\phi \quad (3.7)$$

Where $k_I=K_{II}$, $k_2=K_I$, $k_3=K_{III}$ and $k_4=K_{IV}$, ϕ denote the angle between a and e_I as shown in figure 3.2 and the latter association, a and b are orthonormal vectors contained in the plane $x_3 = 0$. Noted that equation (3.6) & (3.7) is carried out related to the local coordinate system (x_1, x_2, x_3) .

The equation (3.6) still has a disadvantage (i.e., the equation includes taking limit). Later, to avoid this drawback, the other approach is offered inasmuch the stress and electric intensity factors can be obtained directly in term of the crack front nodal information (also see Rungamornrat and Mear 2008) as shown:

$$K_J(\mathbf{x}_C) = \sqrt{\frac{\pi}{2J \sin \beta}} B_{JP}(\mathbf{x}_C) u_p^*(\mathbf{x}_C) \quad (3.8)$$

$$u_p^*(\mathbf{x}_C) = \sum_{i=1}^9 u_{p(i)}^e \psi_i(\xi_C, -1) \quad (3.9)$$

$$J = \left\| \frac{\partial r_C}{\partial \eta}(\xi_C, -1) \right\| \quad (3.10)$$

$$e_\eta = \frac{1}{\eta} \frac{\partial r_C}{\partial \eta}(\xi_C, -1) \quad (3.11)$$

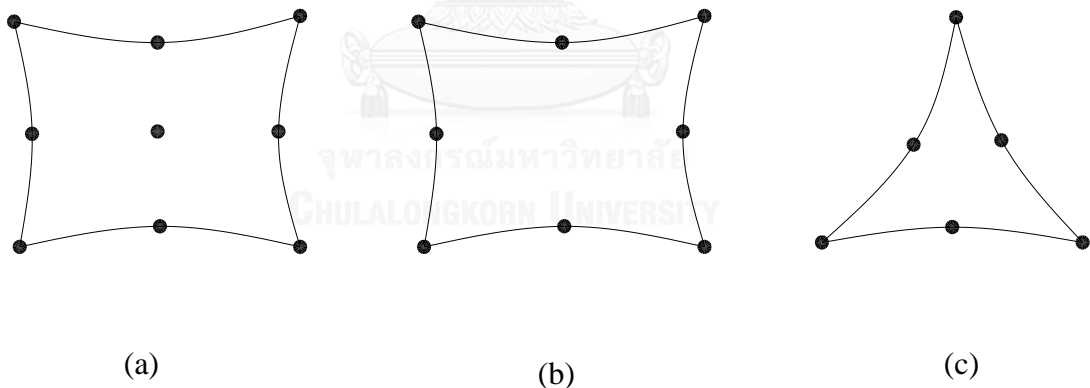
β is an angle satisfying $\sin \beta = -e_\eta \cdot e_I$, $(\xi_C, -1)$ are the natural coordinates of \mathbf{X}_C (determined with respect to the computational element illustrated in figure 3.2), $u_{p(i)}^e$ are the component of $u_{(i)}^e$ related to the local coordinate system (x_1, x_2, x_3) and $r_C(\xi, \eta) = x(\xi, \eta) - \mathbf{X}_C$. Emphasize that the quantities u_p^* represented in equation (3.8), in reality only involve the nodal information along the crack front (where the “special” degrees of freedom are utilized) once $\psi_i(\xi_C, -1) = 0$; this for the nodes is not on the crack front.

3.3 Mesh generations

To imitate the crack behaviors on the boundary of the various geometries and the crack surfaces, the stress and electric intensity factors is imposed by weakly singular, SGBEM. This technique requires sufficient and fine mesh generation for

implementation. The aspect ratio of distorted elements has suitably reduced the size to avoid exceeded distortion. Also a finer implementation is employed in the area where fields are estimated at sophisticated vicinity for instance the area near the crack front, the mesh with smooth transition is utilized to relate the meshes. Furthermore, in the discretization, to obtain the unknown variable data along the crack surface appeared in the governing integral equation, the crack-tip element is utilized as shown in figure 3.3(d) as the 9-nodes quadrilateral crack-tip elements illustrated in figure 3.3 (a) which is more flexible and utilized along the crack front; Moreover, the crack-tip element have two advantage features; the first one is the corresponding shape functions can capture the first three term of asymptotic fields and the other is extra degree of freedom introduced along the crack front to directly capture to the strength of singularity or in other word, the first feature enables relatively large crack-tip elements be used along the crack front and the second feature provides a direct mean to assign the mixed-modes intensity factors without carrying extrapolations. Another crack elements is the quadrature element such as standard 8-nodes quadrilateral elements shown in figure 3.3(b) and standard 6-nodes triangle elements illustrated in figure 3.3(c) which is utilized to connect the inner meshes.

Since the domain becomes very large and the sector of the mesh is increased, i.e. the angle between each sector is reduced with respect to coordinate system, the transition will be employed to ensure the exact computation, the mesh transition must be implemented to other fashion indicated in figure 3.3(e).



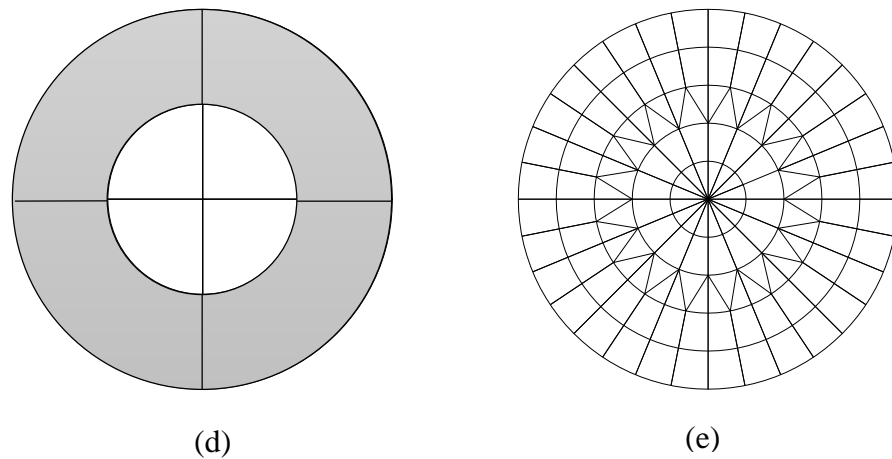


Figure 3.3 The elements employed in the discretization of various geometries (a) 9-nodes quadrilateral crack tip elements, (b) standard 8-nodes quadrilateral elements and (c) standard 6-nodes triangle elements (e) an example of mesh transition

3.4 Convergence check

The major purpose is to ensure and verify the mesh generation that we have created in the previous section to be the finest meshes, and the mesh should be converged to the acceptable unchanged values. We will investigate the stress and electric intensity factor along the crack front on four distinct type of boundary conditions (i.e., permeable, impermeable, semi-permeable and energetically consistent models) under various geometry cracks. Examples include penny-shaped crack folded in circular ball or Spherical cap crack and penny-shaped crack folded in cylindrical or cylindrical crack, tunnel crack, two penny-shaped crack in vertical direction and two penny-shaped cracks in horizontal direction subjected to any kind of loading conditions (i.e., electrical and Mechanical loads) in a three-dimensional linear transversely anisotropic piezoelectric material by using weakly singular symmetric Galerkin boundary element method (SGBEM). The series of mesh generations will be utilized at least three meshes refinement with explicit distinct levels in each problem which depends primarily on the difficulty of the geometries and the considered domain size. The result of this converged implementation is very gainful for each mesh of the problem and this will become the exact benchmark in the next step.

To implement the convergence of analysis, a collection of meshes is employed. The mesh refinement is used depending on the crucial level of region on the crack surface. Particularly, in vicinity of the crack front, the nine-node crack-tip elements are adopted to approximate, and the remaining regions on the crack surfaces are utilized eight-nodes and six-nodes-elements. The direction of symmetric axis is defined as x_3 -axis. The piezoelectric material utilized in this study is transversely isotropic and the generalized moduli are analogous to PZT-4 illustrated in table 4.1 below:

Table 3.1 Property of transversely isotropic piezoelectric materials, PZT-4 gained from Li et al., (2011). The axis of material symmetry is directed along the x_3 -axis direction.

Elastic constants ($\times 10^9 Pa$)	E_{1111}	139
	E_{1122}	77.8
	E_{1133}	74.3
	E_{3333}	113
	E_{1313}	25.6
Piezoelectric constants (C/m^2)	E_{1143}	-6.98
	E_{3343}	13.8
	E_{1341}	13.4
Dielectric Permittivity ($\times 10^{-9} C/(Vm)$)	$-E_{1441}$	6.0
	$-E_{3443}$	5.47

3.4.1 Convergence of spherical cap crack in infinite medium under tensile remote loadings

Here we consider a non-planar cracks containing in a transversely isotropic piezoelectric infinite medium which is made of PZT-4 as shown in figure 3.3 (a) and (b). The geometries are determined as the penny-shaped crack folded in a half of circular ball or spherical cap crack with the radius of penny-shaped crack a , the radius of the spherical cap cracks R and the half-subtended angle θ . These geometries will be employed to investigate intensity factors along the crack front in several cases, e.g., the half subtended angle, curvilinear of crack surface, remote tensile mechanical load, remote electrical load and the permittivity inside the crack gap.

Where $a = l$ is determined as a radius of the penny-shaped crack, the θ present the half subtended angle of the crack surface ($\theta = 90$) and R is imposed the radius of the crack ($R=l$). The material symmetric axis and the poling direction are the same of the x_3 -axis. In this case, we employ three meshes which are explicitly different levels. The finest meshes contain 144 elements, whereas the medium meshes contains 64 elements and the coarsest mesh contain 8 elements, respectively, as shown in the figure.3.3 (b). The piezoelectric medium of the crack is beneath the remote uniaxial tension $\sigma_0 = 50$ MPa, uniform electric field $E_0 = 2.5$ MV/m in the x_3 - direction. In this exploration, the permittivity is supposed as $5 \times 8.85 \times 10^{-12}$ C/Vm.

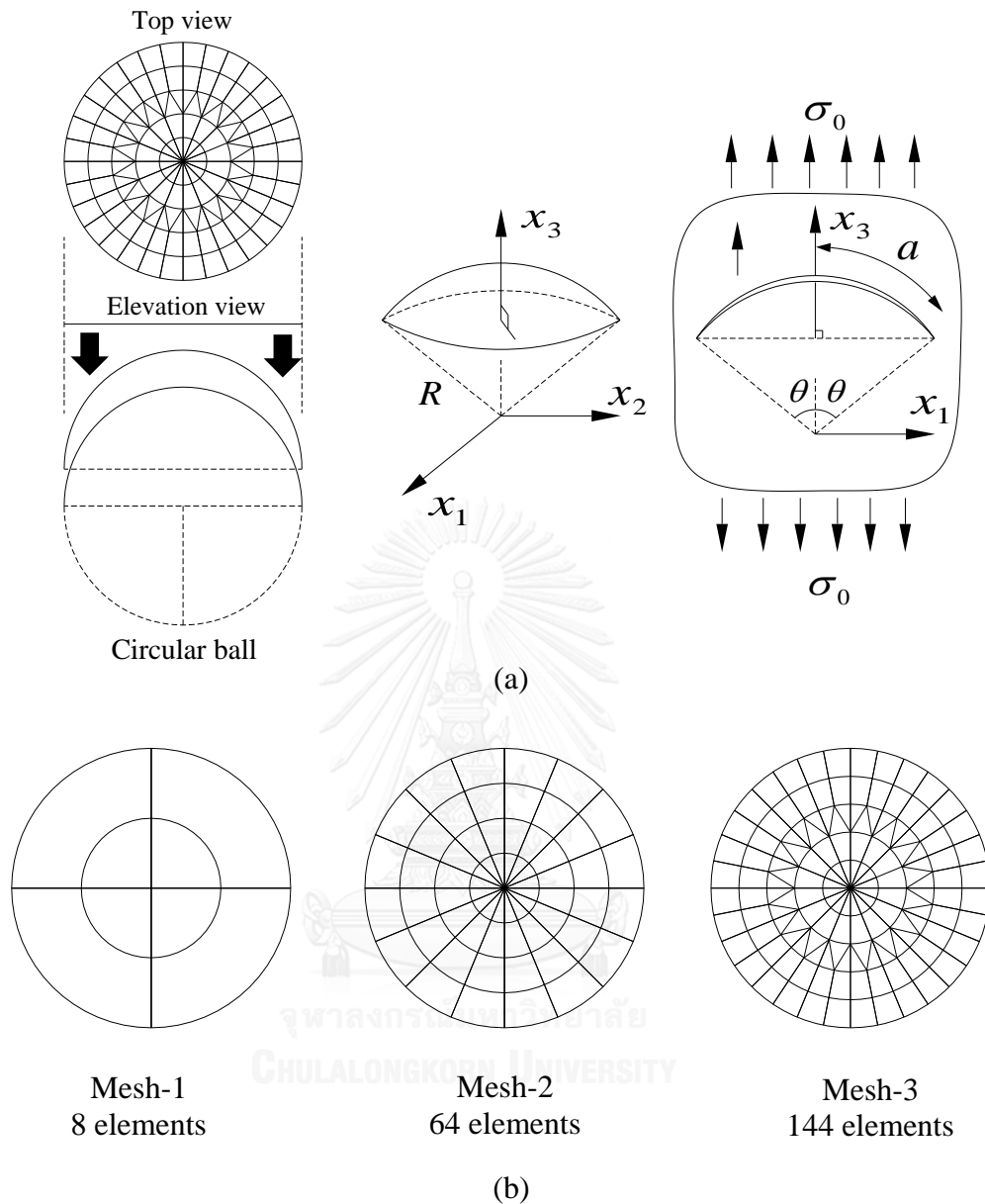


Figure 3.4 (a) schematic of a spherical cap crack in infinite domain and (b) three meshes utilized in computation.

From the numerical results for stress and electric intensity factors $[K_I, K_{II}, K_{IV}]$ normalized by the results gained from the finest mesh (144 elements) as listed in the table 3.2 and 3.3, it can be found that the non-zero intensity factors computed from three meshes are in good agreement. More specifically, the disparity of the obtained results from the coarsest and the medium meshes compared with the fine mesh is less than 6.7640% and 0.5232% respectively for all crack face models (i.e., impermeable, permeable, semi-permeable and energetically consistent models). It should be remarked that the coarsest mesh comprises only 8 elements along the crack front, and the rest elements is for the region of crack surface.

Table 3.2 The convergence of normalized stress and electric intensity factors $[K_I, K_{II}, K_{IV}]$ for a spherical cap crack under remote uniform tensile stress $\sigma_0 = 50$ MPa and uniform electric field $E_0 = 2.5$ MV/m for impermeable and permeable models

Mesh	Impermeable crack			Permeable crack		
	K_I / K^{ref}	K_{II} / K^{ref}	K_{IV} / K^{ref}	K_I / K^{ref}	K_{II} / K^{ref}	K_{IV} / K^{ref}
Coarse(1)	0.9600	0.9989	0.9868	0.9512	0.9938	0.9863
Medium(2)	0.9979	1.0009	0.9999	0.9972	1.0005	0.9999
Fine(3)	1.0000	1.0000	1.0000	1.0000	1.0000	1.0000
% (1)&(3)	4.0004%	0.1143%	1.3246%	4.8842%	0.6188%	1.3723%
%(2)&(3)	0.2144%	0.0850%	0.0081%	0.2762%	0.0476%	0.0071%

Table 3.3 The convergence of normalized stress and electric intensity factors $[K_I, K_{II}, K_{IV}]$ for a spherical cap crack under remote uniform tensile stress $\sigma_0 = 50$ MPa and uniform electric field $E_0 = 2.5$ MV/m for Semi-permeable and energetically consistent models

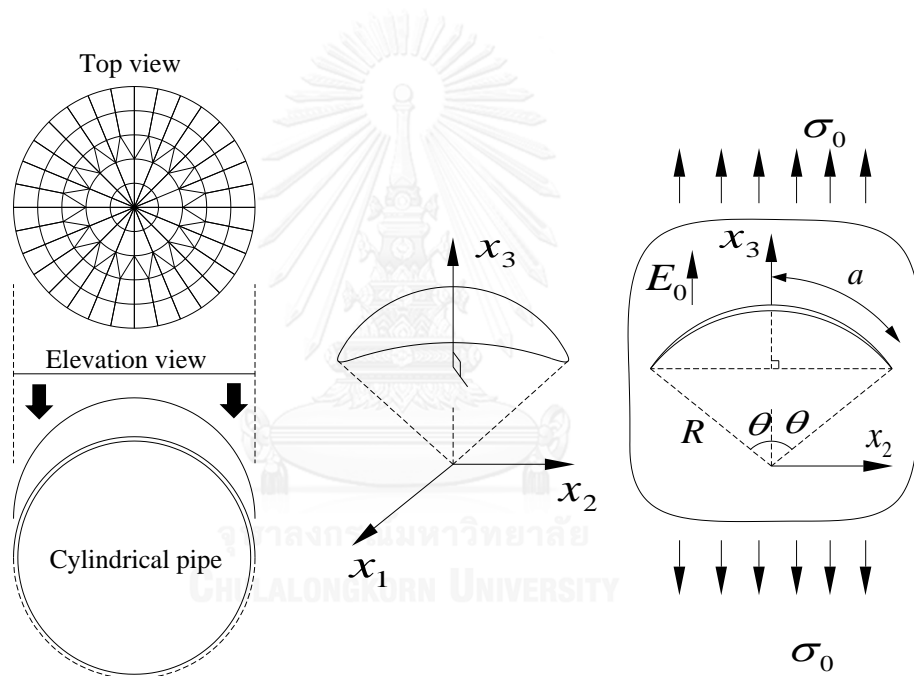
Mesh	Semi-permeable crack			Energetically consistent crack		
	K_I / K^{ref}	K_{II} / K^{ref}	K_{IV} / K^{ref}	K_I / K^{ref}	K_{II} / K^{ref}	K_{IV} / K^{ref}
Coarse(1)	0.9495	0.9937	0.9324	0.9517	0.9969	0.9400
Medium(2)	0.9970	1.0005	0.9948	0.9966	1.0007	0.9961
Fine(3)	1.0000	1.0000	1.0000	1.0000	1.0000	1.0000
% (1)&(3)	5.0485%	0.6332%	6.7640%	4.8272%	0.3138%	6.0011%
%(2)&(3)	0.3027%	0.0469%	0.5232%	0.3405%	0.0732%	0.3922%

3.4.2 Convergence of cylindrical cracks in infinite medium under tensile remote loadings

Similarly, in this case we consider a cylindrical crack with the radius of penny-shaped crack a , radius of cylindrical cracks R and the half-subtended angle θ embed in a transversely isotropic piezoelectric infinite medium which is made of PZT-4 as shown in figure 3.4 (a) and (b). These geometries will be utilized to explore the intensity factors in the three points (i.e., top, middle and bottom points) along the crack front in

several cases, e.g., the half subtended angle, curvilinear of crack surface, remote tensile mechanical load, remote electrical load and the permittivity inside the crack gap.

Where the radius of the penny-shaped crack is defined as $a = l$, the θ is imposed as the half subtended angle of the crack surface ($\theta = 90^\circ$) and R indicates the radius of cylindrical crack ($R=l$). The material symmetric axis and the poling direction are identical to the x_3 -axis. In this special case, we similarly employ three meshes which are explicit different level similar to the spherical cap crack. The finest meshes contains 144 elements, whereas the medium meshes contains 64 elements and the coarsest mesh contain 8 elements, respectively, as identically shown in figure.3.3 (b). The piezoelectric medium of the cylindrical crack is upon the remote uniaxial tension $\sigma_0 = 50$ MPa, uniform electric field $E_0 = 2.5$ MV/m in the x_3 -direction. In this exploration, the permittivity is assumed as $5 \times 8.85 \times 10^{-12}$ C/Vm



(a)

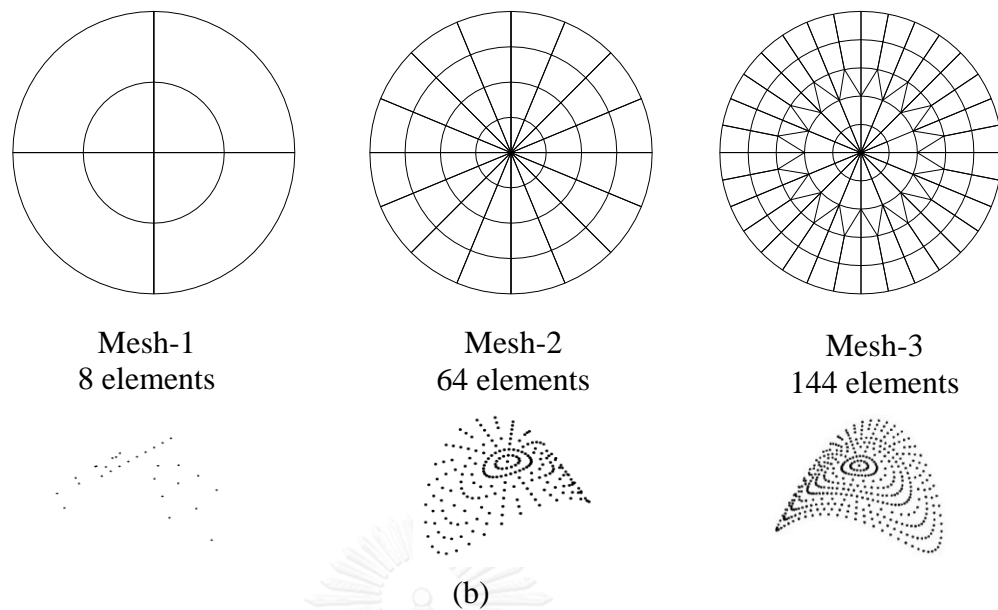


Figure 3.5 (a) schematic of a cylindrical crack in infinite domain and (b) three meshes utilized in computation and coordinate of each meshes.

Similarly, from the numerical results for stress and electric intensity factors $[K_I, K_{II}, K_{IV}]$ normalized by the harvests obtained from the finest mesh as reported in the table 3.4 and 3.5, it is found that the stress and electric intensity factors provided from three meshes (i.e., coarse, medium and fine meshes) are well accepted. In particular, the discrepancy of the given results from the medium meshes correlated with the fine mesh is less than 0.2381% respectively for all crack face models (i.e., impermeable, permeable, semi-permeable and energetically consistent models). It should be noted again that the coarsest mesh comprises only 8 elements along the crack front.

Table 3.4 The convergence of normalized stress and electric intensity factors $[K_I, K_{II}, K_{IV}]$ for a cylindrical crack under remote uniform tensile stress $\sigma_0 = 50$ MPa and uniform electric field $E_0 = 2.5$ MV/m for impermeable and permeable models

Mesh	Impermeable crack			Permeable crack		
	K_I / K^{ref}	K_{II} / K^{ref}	K_{IV} / K^{ref}	K_I / K^{ref}	K_{II} / K^{ref}	K_{IV} / K^{ref}
Coarse(1)	0.7301	0.9859	0.9688	0.7882	0.9852	1.0085
Medium(2)	1.0024	1.0001	1.0006	0.9997	1.0002	0.9998
Fine(3)	1.0000	1.0000	1.0000	1.0000	1.0000	1.0000
% (1)&(3)	26.9892%	1.4128%	3.1240%	21.1765%	1.4797%	0.8523%
%(2)&(3)	0.2381%	0.0106%	0.0587%	0.0315%	0.0172%	0.0179%

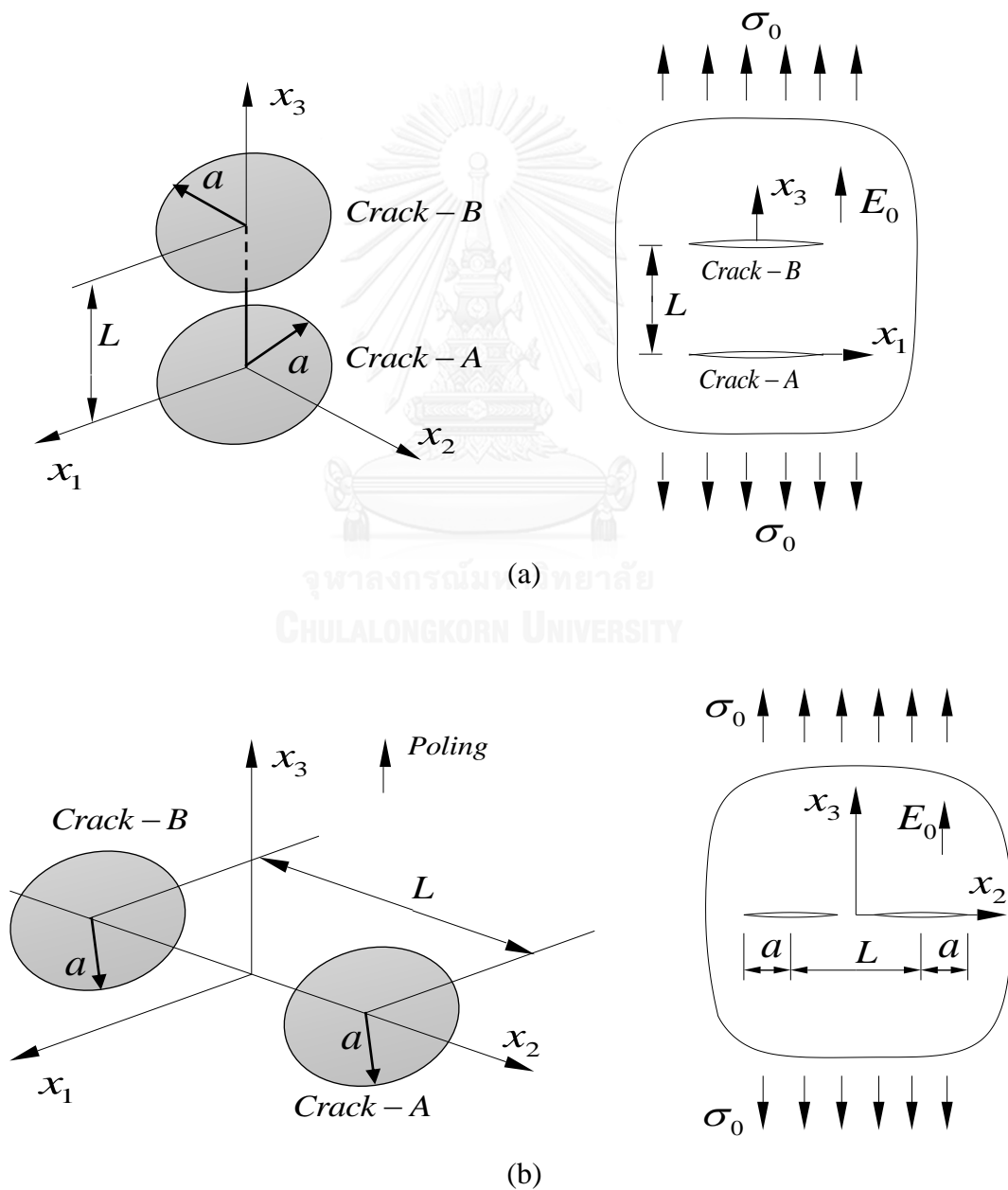
Table 3.5 The convergence of normalized stress and electric intensity factors $[K_I, K_{II}, K_{IV}]$ for a cylindrical crack under remote uniform tensile stress $\sigma_0 = 50$ MPa and uniform electric field $E_0 = 2.5$ MV/m for Semi-permeable and energetically consistent models

Mesh	Semi-permeable crack			Energetically consistent crack		
	K_I / K^{ref}	K_{II} / K^{ref}	K_{IV} / K^{ref}	K_I / K^{ref}	K_{II} / K^{ref}	K_{IV} / K^{ref}
Coarse(1)	0.7874	0.9799	0.9222	0.7369	0.9874	0.9465
Medium(2)	0.9998	1.0001	0.9993	0.9993	1.0002	1.0002
Fine(3)	1.0000	1.0000	1.0000	1.0000	1.0000	1.0000
% (1)&(3)	21.2552%	2.0061%	7.7769%	26.3120%	1.2648%	5.3509%
%(2)&(3)	0.0184%	0.0149%	0.0712%	0.0705%	0.0185%	0.0244%

3.4.3 A pair of penny-shaped cracks

Next, we consider a pair of penny-shaped cracks, i.e., two penny-shaped crack in vertical direction and two penny-shaped crack in horizontal direction with radius a , and the distance of the two cracks L embed in a transversely isotropic piezoelectric infinite medium made of PZT-4 as indicated in figure 3.5 (a) and (b). These geometries will be utilized to explore other cases for instance interacting of both cracks, remote tensile mechanical load, remote electrical load and the permittivity inside the crack gap.

Where a is a radius of the penny-shaped crack ($a = 1$) and the L represent the distance of two cracks ($L=0.5$ and $L=2.25$ for two penny-shaped crack in both vertical and horizontal direction, respectively). The material symmetric axis and the poling direction are the same, which is the x_3 -direction. In this crack, we employ three meshes from explicitly different levels. The finest meshes contain 144 elements per a crack, whereas the medium meshes contains 64 elements and the coarsest mesh contain 8 elements, respectively, as shown in the figure 3.5. The piezoelectric medium of the spherical crack is under remote uniaxial tension $\sigma_0 = 50$ MPa, uniform electric field $E_0 = 2.5$ MV/m in the x_3 -direction. In this exploration, the permittivity is $5 \times 8.85 \times 10^{-12}$ C/Vm



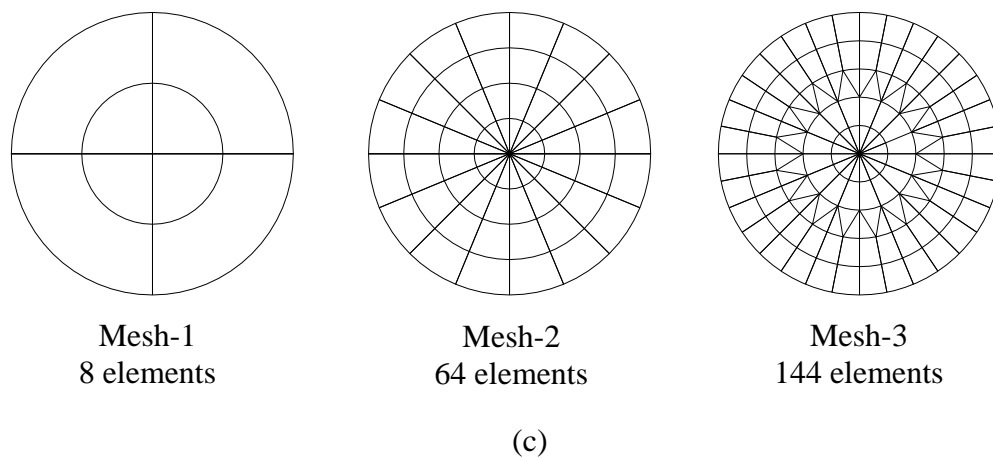


Figure 3.6 (a) schematic of a pair of penny-shaped cracks in vertical direction in infinite domain and (b) a pair of penny-shaped cracks in horizontal direction and (c) three meshes utilized in computation.

For the two penny-shaped crack in vertical direction, results from the numerical results for stress and electric intensity factors [K_I , K_{II} , K_{IV}] given from the finest mesh (144 elements) recorded in the table 3.6 and 3.7 indicate that the stress and electric intensity factors of one penny-shaped cracks obtained from three meshes are good convergence. To be precise, the disparity of the gained results from the coarsest and the medium meshes compared with the fine mesh are less than 2.8575% and 0.2892%, respectively, for all crack-face models.

Another cracks are two penny-shaped crack in horizontal direction. In this case, the numerical results for stress and electric intensity factors [K_I , K_{IV}] given from the finest mesh (144 elements) recorded in the table 3.8 and 3.9 show that the stress and electric intensity factors offer from three meshes are good acceptable. The disparity of the gained results from the coarsest and the medium meshes compared with the fine mesh are less than 1.2875% and 0.0561%, respectively, for all crack-face models.

Table 3.6 The convergence of normalized stress and electric intensity factors [K_I, K_{II}, K_{IV}] for a pair of penny-shaped crack in vertical direction under remote uniform tensile stress $\sigma_0 = 50$ MPa and uniform electric field $E_0 = 2.5$ MV/m for impermeable and permeable models

Mesh	Semi-permeable crack			Energetically consistent crack		
	K_I / K^{ref}	K_{II} / K^{ref}	K_{IV} / K^{ref}	K_I / K^{ref}	K_{II} / K^{ref}	K_{IV} / K^{ref}
Coarse(1)	0.9937	1.0286	0.9940	0.9938	1.0258	0.9938
Medium(2)	1.0005	1.0029	1.0005	1.0005	1.0027	1.0005
Fine(3)	1.0000	1.0000	1.0000	1.0000	1.0000	1.0000
% (1)&(3)	0.6329%	2.8575%	0.6016%	0.6201%	2.5820%	0.6201%
%(2)&(3)	0.0518%	0.2892%	0.0479%	0.0521%	0.2653%	0.0521%

Table 3.7 The convergence of normalized stress and electric intensity factors [K_I, K_{II}, K_{IV}] for a pair of penny-shaped cracks in vertical direction under remote uniform tensile stress $\sigma_0 = 50$ MPa and uniform electric field $E_0 = 2.5$ MV/m for Semi-permeable and energetically consistent models

Mesh	Semi-permeable crack			Energetically consistent crack		
	K_I / K^{ref}	K_{II} / K^{ref}	K_{IV} / K^{ref}	K_I / K^{ref}	K_{II} / K^{ref}	K_{IV} / K^{ref}
Coarse(1)	0.9938	1.0264	0.9940	0.9937	1.0266	0.9939
Medium(2)	1.0005	1.0027	1.0005	1.0005	1.0027	1.0005
Fine(3)	1.0000	1.0000	1.0000	1.0000	1.0000	1.0000
% (1)&(3)	0.6238%	2.6441%	0.6042%	0.6290%	2.6616%	0.6065%
%(2)&(3)	0.0520%	0.2708%	0.0512%	0.0519%	0.2728%	0.0511%

Table 3.8 The convergence of normalized stress and electric intensity factors [K_I, K_{IV}] for two penny-shaped cracks in horizontal direction under remote uniform tensile stress $\sigma_0 = 50$ MPa and uniform electric field $E_0 = 2.5$ MV/m for impermeable and permeable models

Mesh	Impermeable crack		Permeable crack	
	K_I / K^{ref}	K_{IV} / K^{ref}	K_I / K^{ref}	K_{IV} / K^{ref}
Coarse(1)	0.9871	0.9875	0.9872	0.9872
Medium(2)	1.0006	1.0007	1.0006	1.0006
Fine(3)	1.0000	1.0000	1.0000	1.0000
% (1)&(3)	1.2875%	1.2520%	1.2758%	1.2758%
%(2)&(3)	0.0561%	0.0654%	0.0594%	0.0594%

Table 3.9 (3.9) The convergence of normalized stress and electric intensity factors [K_I, K_{IV}] for two penny-shaped cracks in horizontal direction under remote uniform tensile stress $\sigma_0 = 50$ MPa and uniform electric field $E_0 = 2.5$ MV/m for Semi-permeable crack and Energetically consistent crack

Mesh	Semi-permeable crack		Energetically consistent crack	
	K_I / K^{ref}	K_{IV} / K^{ref}	K_I / K^{ref}	K_{IV} / K^{ref}
Coarse(1)	0.9872	0.9873	0.9872	0.9873
Medium(2)	1.0006	1.0006	1.0006	1.0006
Fine(3)	1.0000	1.0000	1.0000	1.0000
% (1)&(3)	1.2788%	1.2673%	1.2831%	1.2705%
%(2)&(3)	0.0585%	0.0623%	0.0577%	0.0617%

3.4.4 Tunnel crack

Finally, we consider a tunnel crack with the half-length L and end-radius a containing in a transversely isotropic piezoelectric infinite medium as shown in figure 3.6. The material properties such as PZT-4 is utilized. In this case, the poling direction is similar to that of the symmetry axis of material as x_3 -axis. The geometry will be utilized to investigate other cases, for instance the aspect ratio (L/a), remote tensile mechanical load, remote electrical load and the permittivity inside the crack gap

Where a is the end-radius of tunnel crack (a is defined as 1), the L represent the half-length of tunnel cracks (L is determined as 5). In this crack, we employ three

meshes with explicitly different levels. As shown in the figure.3.5, the finest meshes contain 144 elements, whereas the medium meshes contains 72 elements and the coarsest mesh contain 24 elements respectively. The piezoelectric medium of the spherical crack is under remote uniaxial tension $\sigma_0 = 50$ MPa, uniform electric field $E_0 = 2.5$ MV/m in the x_3 -direction. In this exploration, the permittivity is $5 \times 8.85 \times 10^{-12}$ C/Vm

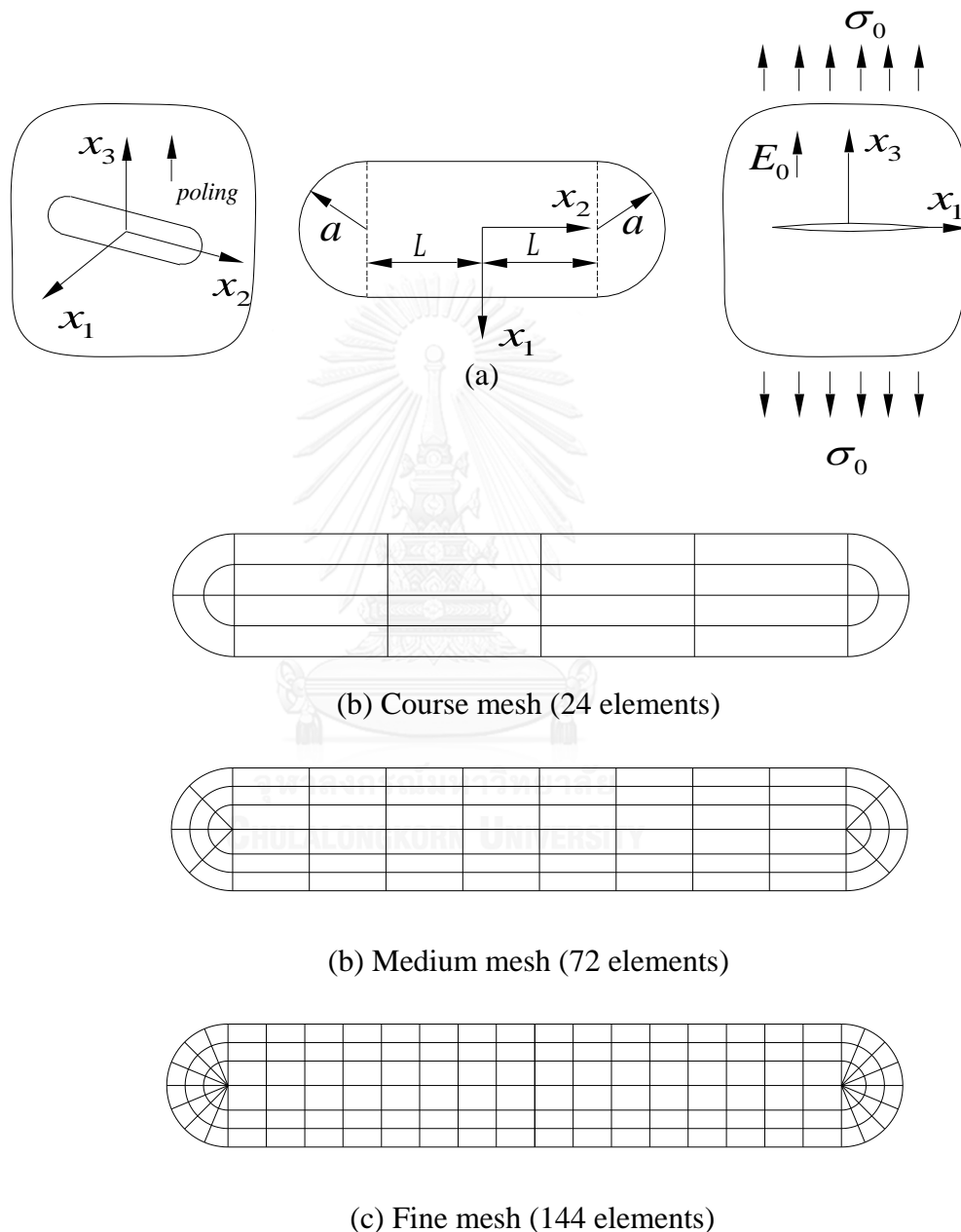


Figure 3.7 (a) schematic of a tunnel crack in infinite domain, (b),(c) and (d) are three meshes utilized in computation such as 24, 72 and 144 elements.

Finally, from the numerical results for stress and electric intensity factors $[K_I, K_{IV}]$ normalized by the results obtained from the finest mesh as shown in the table 3.8 and

3.9, it can be found that the non-zero intensity factors $[K_I, K_{IV}]$ given from three meshes are acceptable. In particular, the discrepancy of the provided results from the coarsest and the medium meshes compared with the fine mesh is 1.8861% and 0.2364%, respectively, for all crack face models (i.e., impermeable, permeable, semi-permeable and energetically consistent models). It should be remarked again, that the coarsest mesh includes only 24 elements in the region along the crack front, whereas the rest are in the remaining crack surface.

Table 3.10 The convergence of normalized stress and electric intensity factors $[K_I, K_{IV}]$ for a tunnel crack under remote uniform tensile stress $\sigma_0 = 50$ MPa and uniform electric field $E_0 = 2.5$ MV/m for impermeable and permeable models

Mesh	Impermeable crack		Permeable crack	
	K_I / K^{ref}	K_{IV} / K^{ref}	K_I / K^{ref}	K_{IV} / K^{ref}
Coarse(1)	1.0185	1.0189	1.0186	1.0186
Medium(2)	1.0022	1.0024	1.0022	1.0022
Fine(3)	1.0000	1.0000	1.0000	1.0000
% (1)&(3)	1.8529%	1.8861%	1.8633%	1.8633%
%(2)&(3)	0.2181%	0.2364%	0.2241%	0.2241%

Table 3.11 The convergence of normalized stress and electric intensity factors $[K_I, K_{IV}]$ for a tunnel crack under remote uniform tensile stress $\sigma_0 = 50$ MPa and uniform electric field $E_0 = 2.5$ MV/m for Semi-permeable crack and Energetically consistent crack

Mesh	Semi-permeable crack		Energetically consistent crack	
	K_I / K^{ref}	K_{IV} / K^{ref}	K_I / K^{ref}	K_{IV} / K^{ref}
Coarse(1)	1.0186	1.0187	1.0186	1.0187
Medium(2)	1.0022	1.0023	1.0022	1.0023
Fine(3)	1.0000	1.0000	1.0000	1.0000
% (1)&(3)	1.8607%	1.8719%	1.8568%	1.8691%
%(2)&(3)	0.2226%	0.2297%	0.2208%	0.2285%

3.5 Verification

The stress and electric intensity factors, along the crack front, in the infinite domain of three-dimensional, transversely anisotropic piezoelectric material resulting from the weakly singular, SGBEM under various boundary condition (i.e., impermeable, permeable, semi-permeable and energetically consistent models) will be verified and compared with the existing benchmark solutions in the literatures in order to guarantee the accuracy of the current approach.

In this work, we consider the penny-shaped crack with radius a containing in transversely isotropic piezoelectric unbound domain. The poling axis are directed along with x_3 -direction (the axis of material symmetry which is perpendicular on the crack surface) as indicated in figure 3.8 (a). The body is subjected to remote tensile mechanical and electrical loading $\sigma_0 = 5$ MPa and $E_0 = 0.5$ MV/m as shown in figure 3.8 (b). the material properties that used for this verification is PZT-4 and the three different meshes such as the coarse mesh (8 elements), the medium mesh (24 elements) and the fine mesh (64 elements) are utilized as illustrated in figure 3.9 (a),(b) and (c), respectively.

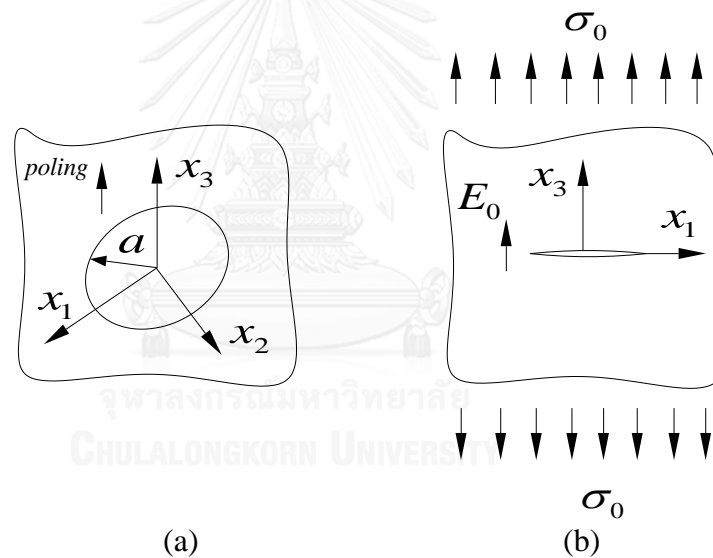
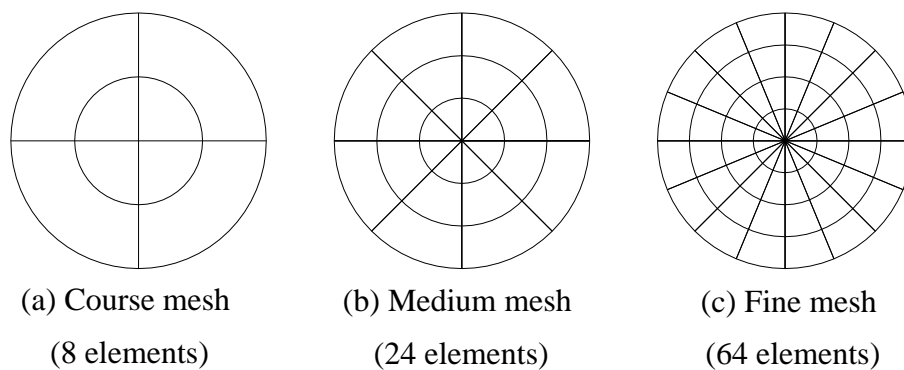


Figure 3.8 (a) schematic of a penny-shaped crack in infinite domain, (b) the body subjected to remote tensile mechanical and electrical load



(a) Course mesh
(8 elements)

(b) Medium mesh
(24 elements)

(c) Fine mesh
(64 elements)

Figure 3.9 three mesh utilized in analysis, (a) Coarse mesh, (b) Medium mesh and (c) Fine mesh

The result $[K_I, K_{IV}]$ obtained from penny-shaped crack under four models are good agreement with exact solution such as K_I, K_{IV} (*exact*) are proposed by Chen et al (2000) for permeable and Li and Lee (2004) for permeable and semi-permeable models whereas K_I, K_{IV} (*exact*) for energetically consistent models are offered by Li et al (2011). The numerical result as indicated in table 3.10 and 3.11 show that the error for impermeable is less than 0.561%, for permeable 0.549%, for semi-permeable 0.551% and for energetically consistent models is less than 0.550%. Moreover, it manifest that even the coarse mesh can obtain the excellent results under various boundary conditions.

Table 3.12 The verification of normalized stress and electric intensity factors $[K_I, K_{IV}]$ for a penny-shaped crack under remote uniform tensile stress $\sigma_0 = 5$ MPa and uniform electric field $E_0 = 0.5$ MV/m for impermeable and permeable models

Mesh	Impermeable crack		Permeable crack	
	K_I / K^{Exact}	K_{IV} / K^{Exact}	K_I / K^{Exact}	K_{IV} / K^{Exact}
Coarse(1)	5.6102	8.1242	5.6109	1.4177
Medium(2)	5.6428	8.1707	5.6432	1.4259
Fine(3)	5.6335	8.1568	5.6338	1.4235
Exact	5.6419	8.1680	5.6419	1.4256
Exact & (1)	0.5610%	0.5363%	0.5493%	0.5493%
Exact & (2)	-0.0158%	-0.0331%	-0.0240%	-0.0240%
Exact & (3)	0.1494%	0.1375%	0.1439%	0.1438%

Table 3.13 The verification of normalized stress and electric intensity factors [K_I, K_{IV}] for a penny-shaped crack under remote uniform tensile stress $\sigma_0 = 5$ MPa and uniform electric field $E_0 = 0.5$ MV/m for semi-permeable and energetically consistent models

Mesh	Semi-permeable crack		Energetically consistent crack	
	K_I / K^{Exact}	K_{IV} / K^{Exact}	K_I / K^{Exact}	K_{IV} / K^{Exact}
Coarse(1)	5.6108	2.4130	3.4658	1.5960
Medium(2)	5.6432	2.4269	3.4859	1.6052
Fine(3)	5.6451	2.4277	3.4871	1.6058
Exact	5.6419	2.4263	3.4852	1.6049
Exact & (1)	0.5511%	0.5465%	0.5553%	0.5509%
Exact & (2)	-0.0228%	-0.0264%	-0.0201%	-0.0236%
Exact & (3)	-0.0567%	-0.0595%	-0.0549%	-0.0577%

CHAPTER 4

NUMMERICAL RESULT AND DISCUSSIONS

Extensive results on intensity factors are obtained to exhibit preciseness and efficacy of the weakly singular SGBEM. Spacious numerical simulations are implemented on crack in a three-dimensional, linear transversely anisotropic piezoelectric infinite medium under four distinct types of electrical boundary conditions on the crack surface (viz. impermeable, permeable, semi-permeable and energetically consistent boundary conditions). The five different cracks are computed here, i.e., the penny-shaped crack folded in a half circular ball (spherical cap crack), the penny-shaped crack folded in a cylinder (cylindrical crack), tunnel crack, two penny-shaped cracks in vertical direction and two penny-shaped cracks in the horizontal direction containing in a piezoelectric infinite medium subject to tensile remote electrical and mechanical loading conditions.

4.1 Influence of geometry on four crack-face boundary conditions

It still remains uncertain which of the four-type electric boundaries (i.e., impermeable, permeable, semi-permeable and energetically consistent models), is physical methodical and more naturalistic. Accordingly, this uncertainty becomes the motivation for current investigations to predicate the four-types of the crack-face electric boundary conditions on non-zero intensity factors of piezoelectric medium embed isolated crack in infinite domain. The numerical approximated results of planar and non-planar cracks are then diagnosed.

In this investigation, we utilize the planar and non-planar geometries such as a spherical cap crack, a cylindrical crack, a tunnel crack, two penny-shaped cracks in a vertical direction and two penny-shaped crack in the horizontal direction to investigate the influence of various parameters on stress and electric intensity factors. The parameters utilized in entire explorations are based on the table below:

Table 4.1 the entire parameters, typical value and range that used to investigate stress and electric intensity factors on four crack-face boundary conditions

Parameters	Typical value	Range
<u>1.Spherical and cylindrical crack</u>		
- Permittivity ϵ_c	$\epsilon_c = 5 \times 8.85 \times 10^{-12} \text{C/Vm}$	$2, 2.5, 3, \dots, 10\epsilon_c$
- Electric field E_0	$E_0 = 2.5 \text{ MV/m}$	$-4.5, -4, \dots, 4.5 \text{ MV/m}$
- Mechanical load σ_0	$\sigma_0 = 50 \text{ MPa}$	$10, 20, \dots, 100 \text{ MPa}$
- Half-subtended angle θ	$\theta = 45$	$-5 \text{ to } 90 \text{ degree}$
- Boundary conditions	4 BCs	(No)
- Curvature μ	(No)	$\mu = 1 \text{ to } \mu = 18$
<u>2.Tunnel crack</u>		
Permittivity ϵ_c	$\epsilon_c = 5 \times 8.85 \times 10^{-12} \text{C/Vm}$	$2, 2.5, 3, \dots, 10\epsilon_c$
Electric field E_0	$E_0 = 2.5 \text{ MV/m}$	$-4.5, -4, \dots, 4.5 \text{ MV/m}$
Mechanical load σ_0	$\sigma_0 = 50 \text{ MPa}$	$10, 20, \dots, 100 \text{ MPa}$

Aspect ratio L/a	5	0.5,1,1.5,...,10
Boundary conditions	4 BCs	(No)
<u>3.two penny-shaped crack in vertical direction</u>		
Permittivity ϵ_c	$\epsilon_c = 5 \times 8.85 \times 10^{-12} \text{C/Vm}$	2,2.5,3,..., 10 ϵ_c
Electric field E_0	$E_0 = 2.5 \text{ MV/m}$	-4.5.-4 ..., 4.5MV/m
Mechanical load σ_0	$\sigma_0 = 50 \text{ MPa}$	10,20,...,100 MPa
Aspect ratio L/a	0.5	0.25,0.5,0.75,1 ...,10
Boundary conditions	4 BCs	(No)
<u>4.two penny-shaped crack in horizontal direction</u>		
Permittivity ϵ_c	$\epsilon_c = 5 \times 8.85 \times 10^{-12} \text{C/Vm}$	2,2.5,3,..., 10 ϵ_c
Electric field E_0	$E_0 = 2.5 \text{ MV/m}$	-4.5.-4 ..., 4.5MV/m
Mechanical load σ_0	$\sigma_0 = 50 \text{ MPa}$	10,20,...,100 MPa
Aspect ratio L/a	2.25	2.25,2.5,2.75,3...,10
Boundary conditions	4 BCs	(No)

4.1.1 Influence of crack-subtended angle for non-planar cracks.

In this section, the non-planar crack such as spherical cap and cylindrical cracks is utilized to investigate the influence of the crack subtended angle on stress intensity factor along the crack front, which can be indicated in the following subsection.

4.1.1.1 Influence of half subtended angle for penny-shaped crack folded in a half circular ball (spherical cap crack)

At the outset, we consider a penny-shaped crack, folded in a half of circular ball or a spherical cap crack containing in a transversely isotropic piezoelectric infinite medium which is made of PZT-4. In this case, the finest mesh (144 elements) chosen in the convergence sections (3.4.1) is employed. The symmetric axis of material and the poling direction are similarly directed by the x_3 -axis. The crack is adopted to investigate the intensity factors along the crack front which can be concluded in the following (i) the crack- subtended angle θ can be varied from [5,10,15,...90 degree], (ii) the remote uniaxial tension is fixed $\sigma_0 = 50 \text{ MPa}$, (iii) the uniform electric field is defined as $E_0 = 2.5 \text{ MV/m}$ in the x_3 -direction and (iv) and the permittivity containing the crack gap is determined as $\epsilon_c = 5\epsilon_0$ where $\epsilon_0 = 5 \times 8.85 \times 10^{-12} \text{ C/Vm}$ is the permittivity of the air. The geometry is illustrated in the figure 4.1.

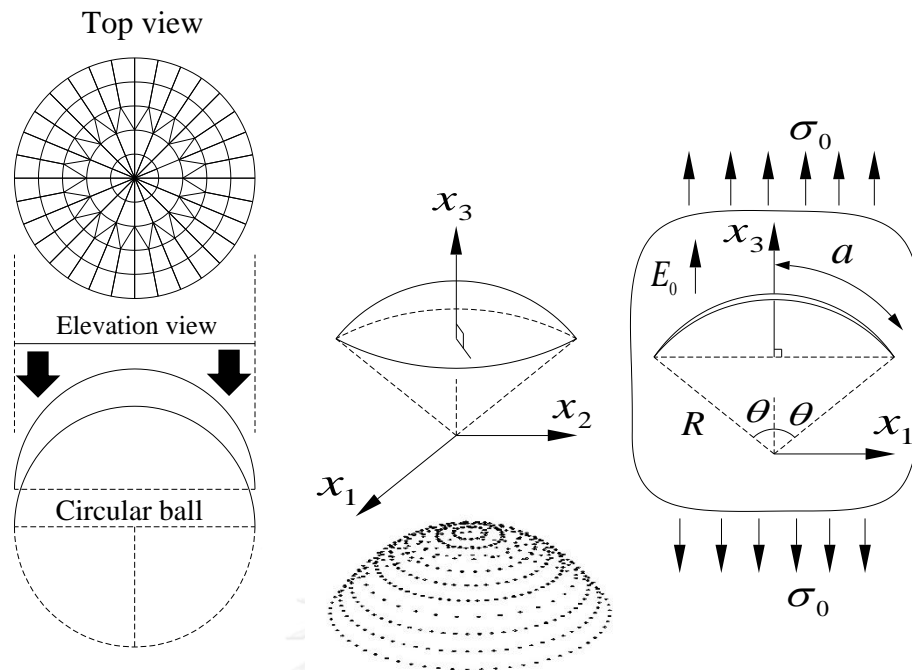


Figure 4.1 Schematic of a penny-shaped crack folded in circular ball (a spherical cap crack) in a piezoelectric infinite medium

where a is a radius of the penny-shaped crack and is varied from $a = 0.087266462599717$ ($\theta = 5$) to $a = 1.570796326794900$ ($\theta = 90$), θ represents the half-subtended angle of the crack surface whereas the radius R indicates the radius of spherical cap crack after folding (R is defined as 1).

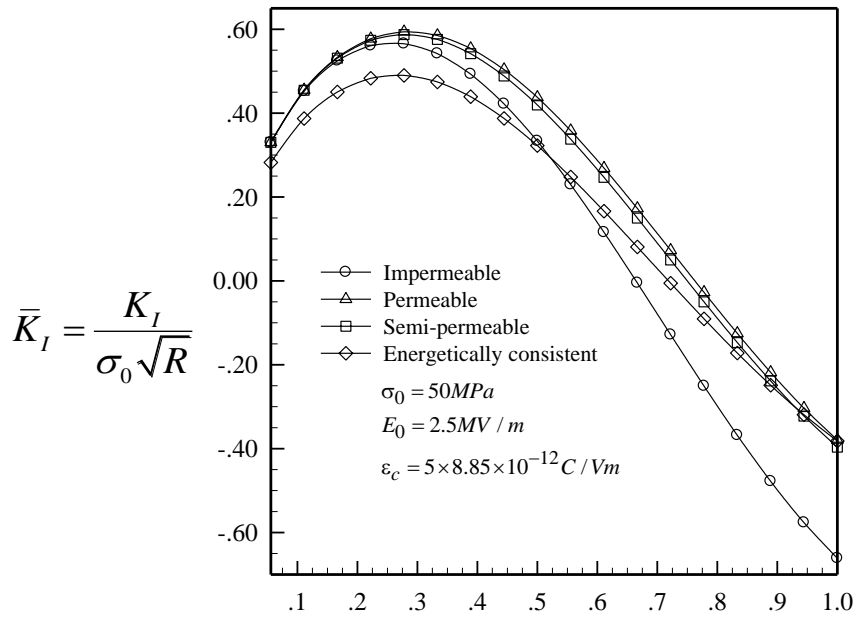
The influence of the half-subtended angle on intensity factors along the crack front obtained from the spherical cap crack by employing the finest mesh (144 elements) are considered as reported in the figure 4.2 (a), (b) and (c) respectively. Results indicate that when the half-subtended angle increases, the stress intensity factor K_{III} expressly vanishes. The magnitude of the stress and electric intensity factors [K_I , K_{II} , K_{IV}] of four crack-face models (i.e., permeable, impermeable, semi-permeable and energetically consistent models) are different values at the entire range. It can be discussed the detail as follow:

The numerical results of stress intensity factors K_I are reported in figure. 4.2 (a). It is found that when the half-subtended angle of the crack surface increases, the value of the stress intensity factor K_I of four models (i.e., impermeable, permeable, semi-permeable and energetically consistent models) increases at the range $\theta = 5$ to $\theta = 25$ degree (the peak magnitude) and decreases when the crack subtended angle increase. It can be observed further that the three models (i.e., impermeable, permeable and semi-permeable models) are nearly identical when half-subtended angle is relatively small at the range $\theta = 5$ to $\theta = 15$ degree and that those three models become clearly distinct when crack subtended angle is sufficiently large. Besides, Results also indicate that the energetically consistent model is lower than other three models in the

beginning and that one approach to the permeable model at the end. Moreover, it is found that the permeable and semi-permeable models show the same behaviors of distributions at the entire range. Furthermore, results reveal that the upper bound is permeable model whereas the lower bound is switched of energetically consistent and impermeable models at $\theta = 45$ degree. This can be concluded that when the half subtended angle becomes large ($\theta = 25$ to 90), it has influence not only to the values of the stress intensity factor K_I of four models but also to the bounds of four crack-face models.

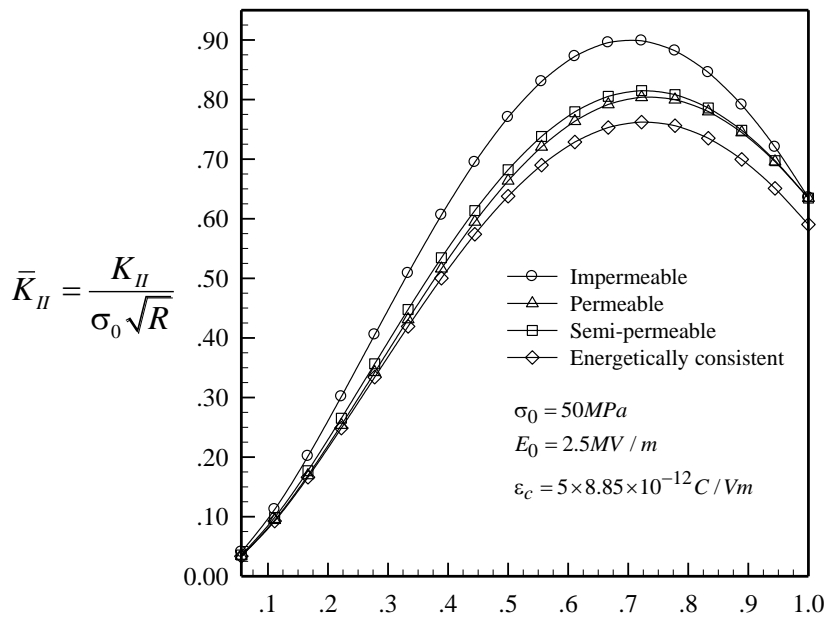
Influence of half subtended angle of spherical cap crack on stress intensity factor K_{II} can achieve results illustrated in figure. 4.2 (b). It is found that when the half-subtended angle θ increases, the magnitude of K_{II} on four crack-face models increase to the peak magnitude at $\theta = 65$ degree and decreases to the end of distributions ($\theta = 65$ to 90). It is obvious that four crack-face models are expressly not identical. However, results reveal that the bounds of four crack-face models are not switched, which means that the impermeable model is upper bound and the energetically consistent model is lower bound. Moreover, the effects also found that when half-subtended angle is small at $\theta = 5$ degree (starting point), the four models are nearly identical whereas the energetically consistent model is different from other three models at the end point. This can be summarized that as the half subtended angle is larger, it has a significant influence on the values of stress intensity factor K_{II} .

Eventually, Influence of half subtended angle of non-planar crack on electric intensity factors K_{IV} on four crack-face models are obtained as illustrated in figure. 4.2 (c). It is seen that when half subtended angle increases, the four crack-face models (i.e., impermeable, semi-permeable, energetically consistent and permeable models) differently increase the magnitude. It can be observed further from figure that the maximum values of the impermeable and permeable models are different from the semi-permeable and energetically consistent models, e.g. the impermeable and permeable models have the maximum values at the point $\theta = 60$ degree whereas the semi-permeable and energetically consistent models have the peak values at $\theta = 35$ degree. Moreover, results also reveal that when the crack subtended angle increase, the lower bound is switched of permeable and energetically consistent models at $\theta = 60$ degree whereas the impermeable model retains the upper bound at the entire range of distributions. Moreover, it is also found that when the crack subtended angle is sufficiently large at $\theta = 90$ degree, the semi-permeable and energetically models are nearly identical to permeable model. This can be summarized that when half-subtended angle is large, it has influence to value of electric intensity factor K_{IV} and the lower bound of four crack models, respectively.



$$\bar{\theta} = \frac{\theta}{\pi / 2}$$

(a)



$$\bar{\theta} = \frac{\theta}{\pi / 2}$$

(b)

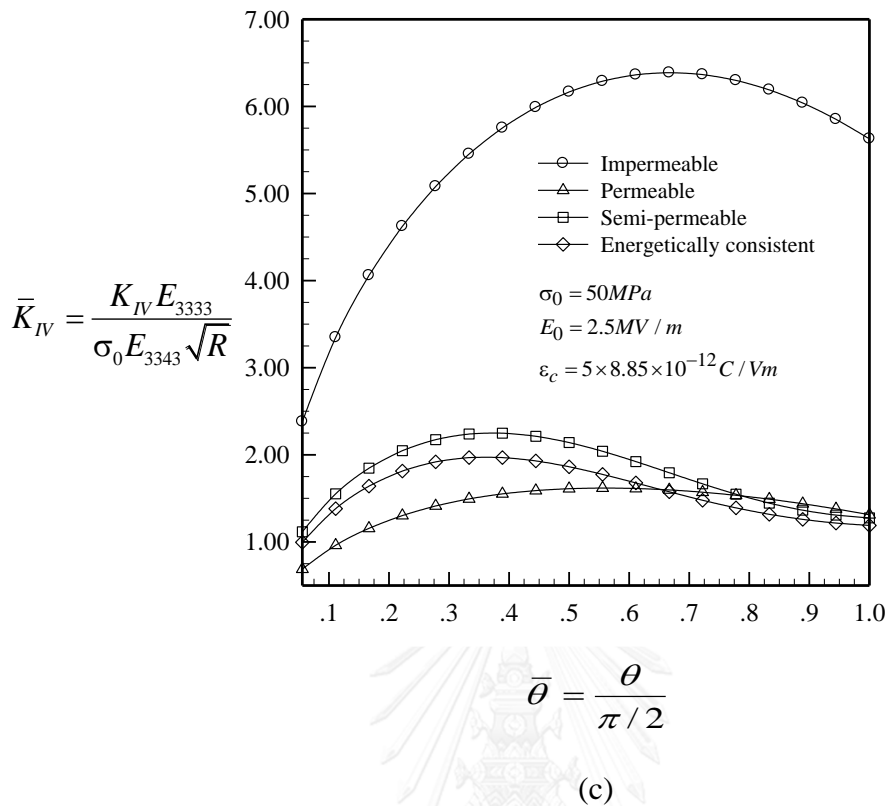


Figure 4.2 (a), (b) and (c) are dependent of normalized stress and electric [K_I , K_{II} , K_{IV}] intensity factors on the crack subtended angle for spherical cap crack in infinite medium.

4.1.1.2 Influence of half subtended angle for penny-shaped crack folded in cylindrical under remote tensile loading

In this case, we implement analogously to the case of spherical cap crack by considering a penny-shaped crack folded in a half of cylindrical or a cylindrical crack embed in a transversely isotropic piezoelectric infinite medium which made of PZT-4 illustrated in the figure 4.3(a). In this special case, we apply the finest mesh (144 elements) similar to the convergence section 3.4.2. The poling directions are analogous to the symmetric axis of material of x_3 -axis. The parameters of this investigations can be concluded in the following (i) the half subtended angle θ vary from [5,10,15...90], (ii) the remote uniaxial tension is fixed $\sigma_0 = 50 \text{ MPa}$, (iii) the uniform electric field is defined $E_0 = 2.5 \text{ MV/m}$ directed in x_3 -direction, (iv) and the dielectric permittivity inside the crack gap is fixed $\epsilon_c = 5\epsilon_0$ where $\epsilon_0 = 8.85 \times 10^{-12} \text{ C/Vm}$ is the permittivity of the air.

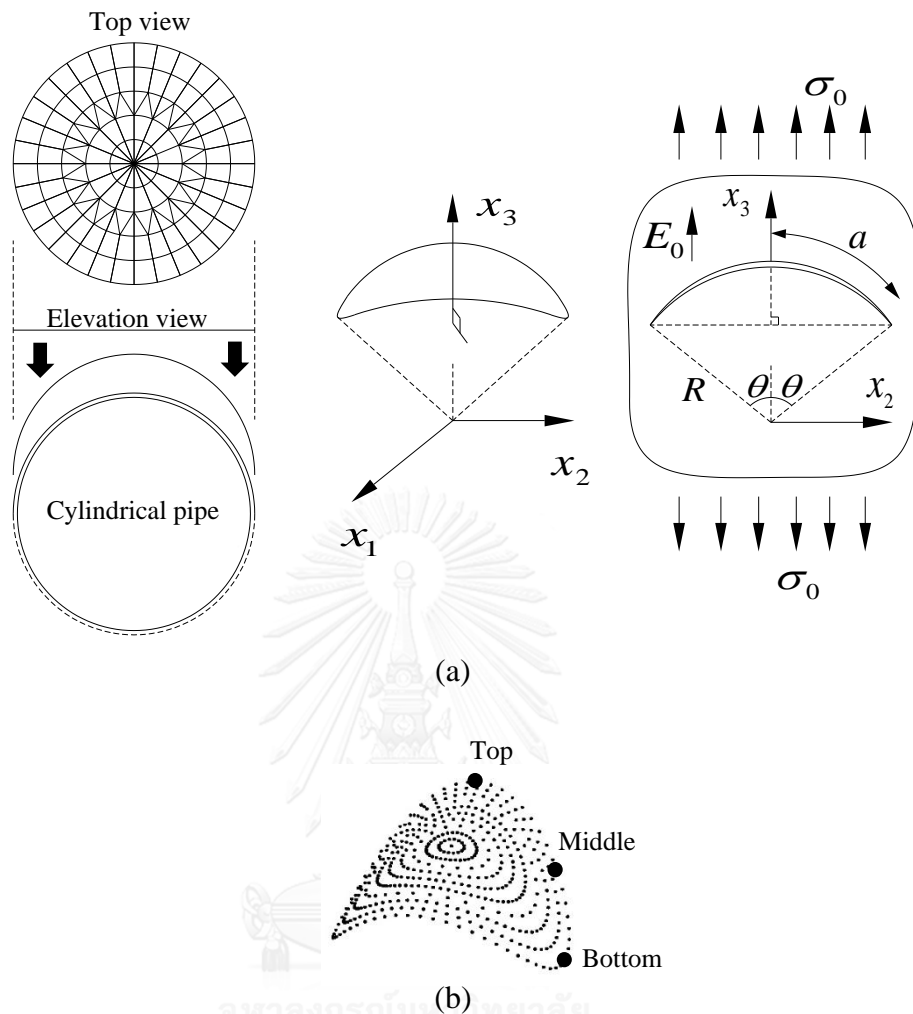
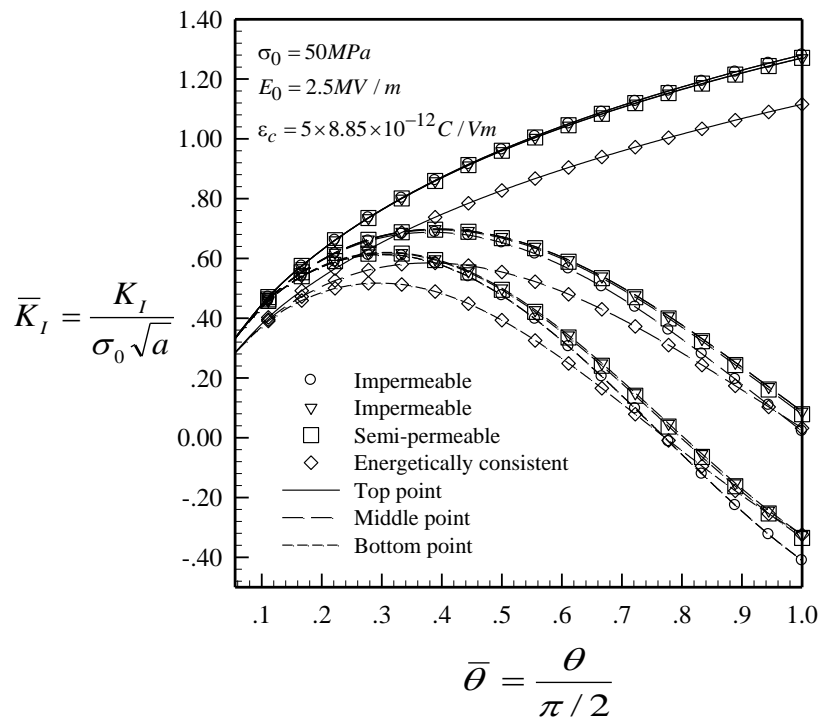


Figure 4.3 (a) Schematic of a penny-shaped crack folded in cylindrical pipe (a cylindrical crack) in a piezoelectric infinite medium (b) three different points on the mesh coordinate of cylindrical crack

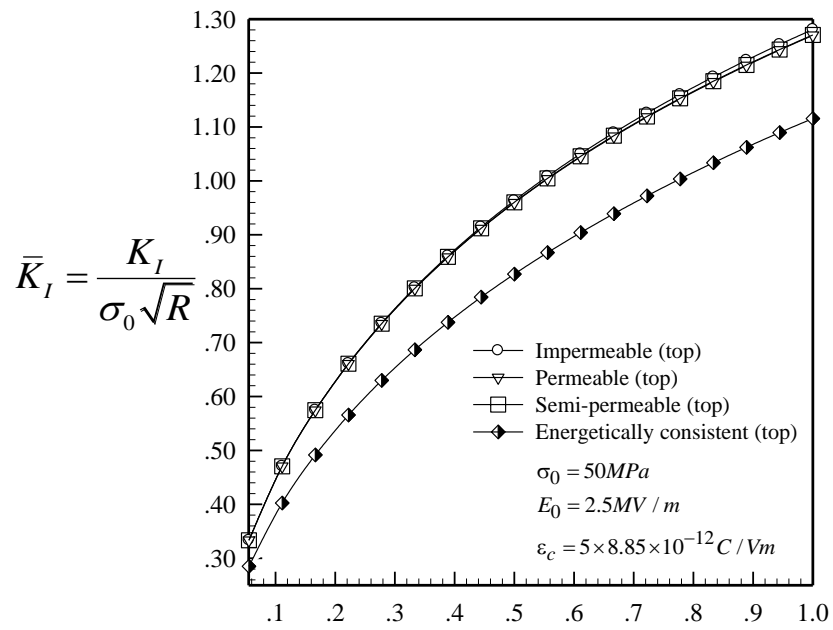
The stress and electric intensity factors $[K_I, K_{II}, K_{IV}]$ are obtained from the three different points such as top, middle and bottom points of four crack-face models (i.e., impermeable, permeable, semi-permeable and energetically consistent models) as shown in figure 4.3 (b) whereas the stress intensity factor K_{III} only appears at the middle point (a point at the middle zone). When the half-subtended angle θ increases, the results show that the normalized stress and electric $[K_I, K_{II}, K_{IV}]$ are different the magnitude and are different trends depending on the positions (i.e., top, middle and bottom points) which can be discussed as follow:

Results indicated in figure 4.4(a), 4.4(b) and 4.4(c) are completely obtained. The normalized stress K_I of four models at the three different points (e.g., top, middle and bottom points) reveals that when the crack subtended angle increases, the magnitude K_I of the top point increase and are greater than the middle and bottom points respectively. It can be observed further that the peak magnitude of middle and bottom points are respectively occurred at $\theta = 35$ and $\theta = 25$ degree whereas the top point is

strongly increase at the entire range without the peak magnitude. Moreover, the upper bounds of three different points are strongly changed depending on the positions along the crack front. For example, it is impermeable model for the top point and permeable model for both middle and bottom points throughout the range of distribution, whereas the lower bound is energetically consistent model for the top point, and that again are switched between energetically consistent and impermeable models at the middle and bottom points. More specifically, those switching points are completely different such as the switching point of middle and bottom points are occurred at $\theta = 85$ and at $\theta = 70$ degree, respectively. Furthermore, it is obvious that the impermeable model depends strongly on the increase of crack-subtended angle; this means that at the top point K_I is greater than both permeable and semi-permeable models whereas the impermeable model is lower than those two models at the middle and bottom points. Besides, results indicate that not only the three crack-face models (i.e., impermeable, permeable and semi-permeable models) of three different points are nearly identical when half-subtended angle is relative small ($\theta = 5$ to $\theta = 20$ degree) but also the energetically consistent model expressly approaches to the permeable model only at the bottom point at $\theta = 90$ degree. It can then be concluded that when the half-subtended angle increases, not only the three crack models are identical when half-subtended angle is small but also the switching point of the lower bounds at middle and bottom points become also different. Results also reveal that the upper bounds are also changed depending on the positions along the crack front. Besides, the energetically consistent models are significantly approached to permeable model only at bottom point.

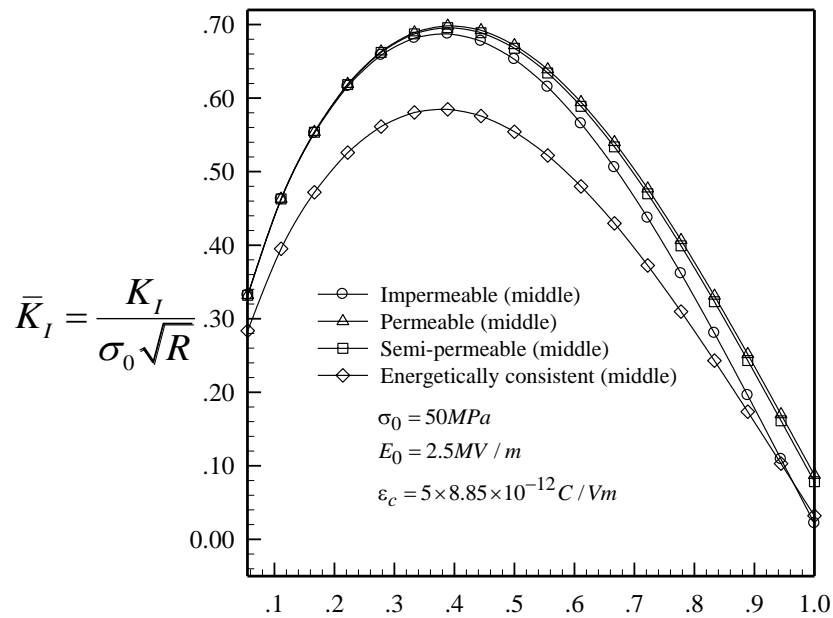


(a)



$$\bar{\theta} = \frac{\theta}{\pi / 2}$$

(b)



$$\bar{\theta} = \frac{\theta}{\pi / 2}$$

(c)

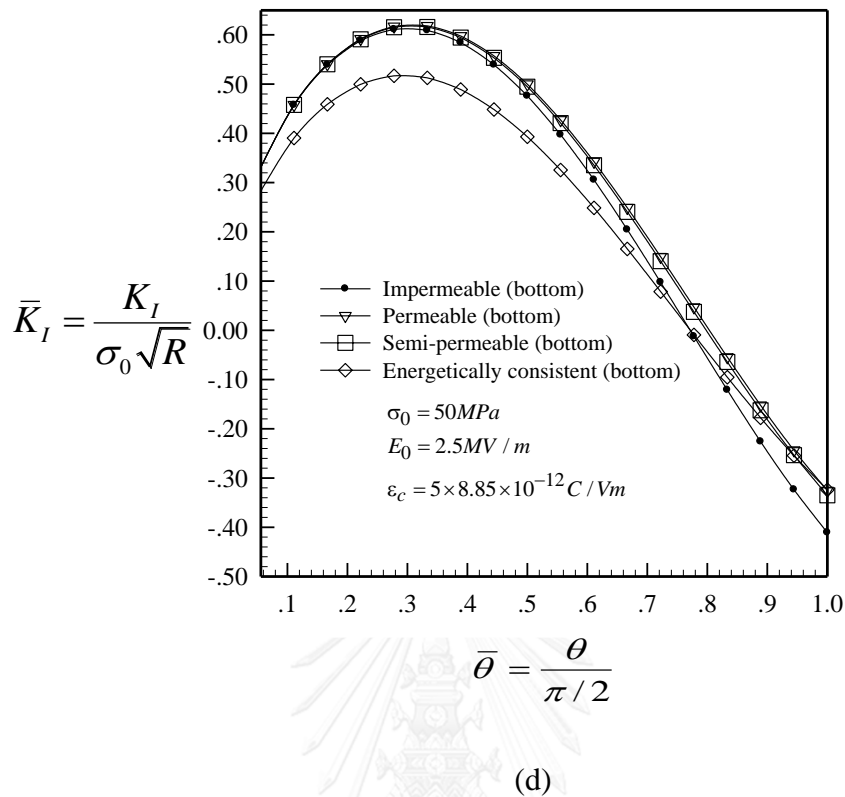
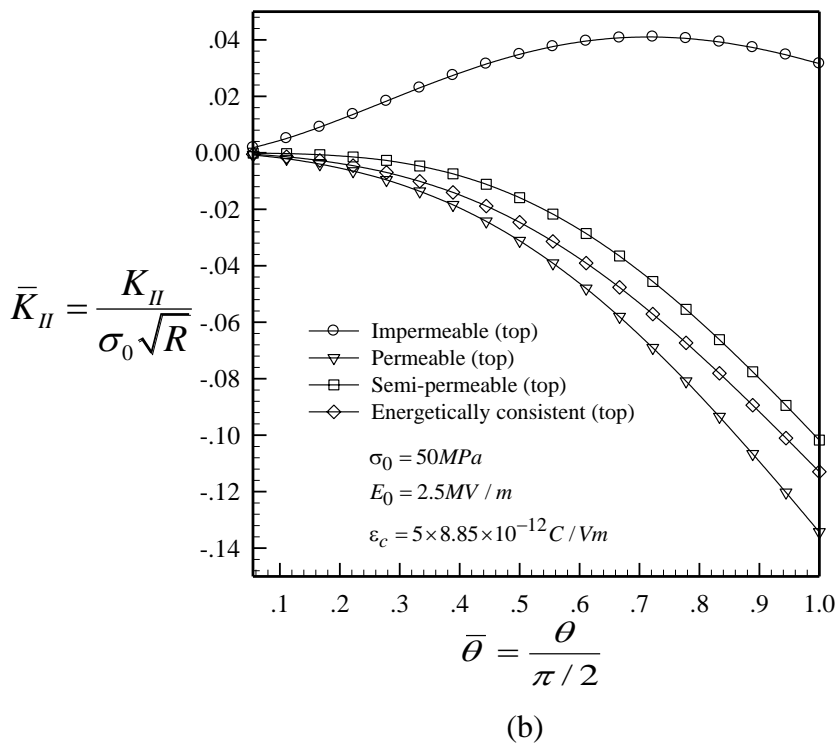
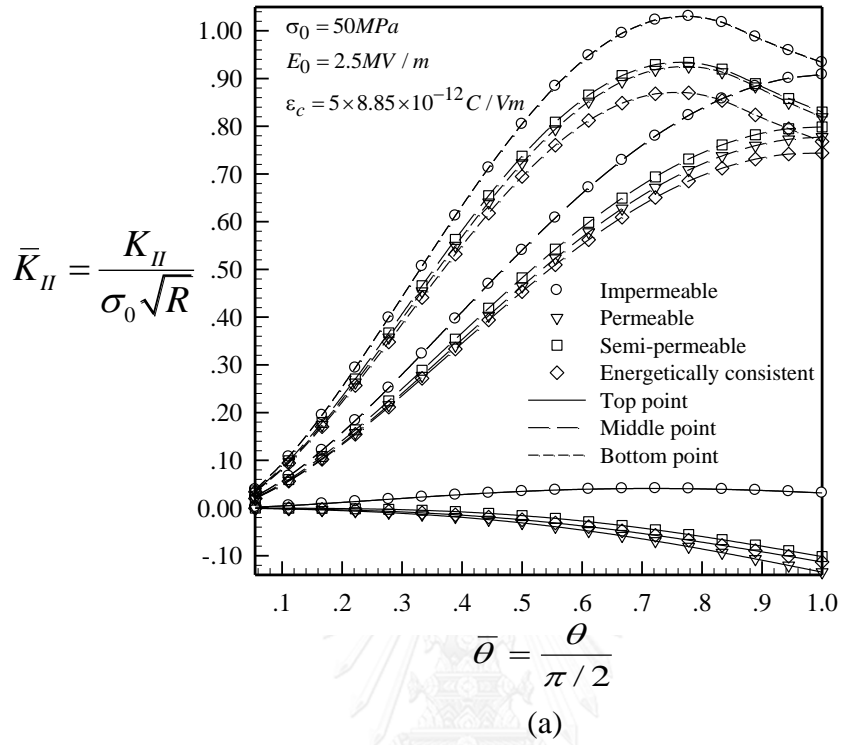


Figure 4.4 Dependent of normalized stress intensity factors K_I on the crack subtended angle for cylindrical crack in infinite medium. Results are reported on (a) all points, the (b) top, (c) middle and (d) bottom points

The harvest reported in the figure 4.5(a),(b),(c) and (d) of a penny-shaped crack folded in a cylindrical pipe (a cylindrical crack) on four crack-face models indicate that when the half-subtended angle increases, the stress intensity factors K_{II} at various positions (i.e., top, middle and bottom points) are unequivocally different. It is also found that the magnitude of K_{II} at the top point is less than both middle and bottom point as indicated in the figure 4.5(a) which can be discussed in detail as follows. As half-subtended angle increase, figure 4.5(b), (c) and (d) show that the distributions of K_{II} on four crack-face models (i.e., impermeable, permeable, semi-permeable and energetically consistent models) in three distinct points (i.e., top, middle and bottom points) variously increase. It can be observed further that the maximum values of K_{II} differently occur, for example, at $\theta = 70$ degree it occurs at the bottom point, at $\theta = 65$ degree is occurred only for the impermeable model on the top point (for the permeable, semi-permeable and energetically consistent models of K_{II} completely decrease) and K_{II} of four models at the middle point strongly increase. Results also show that the bounds of each position (i.e., top, middle and bottom points) is not changed. For example, at both middle and bottom points, the upper bound and the lower bounds are impermeable and energetically consistent models respectively. Nevertheless, at the top point, the lower bound is permeable model. This can be concluded that when crack-subtended angle increases, it influences not only the value of intensity factors K_{II} but

also the bounds of four crack-face models; more specifically, the difference of both upper and lower bounds at the top and the two points (i.e., middle and bottom points).



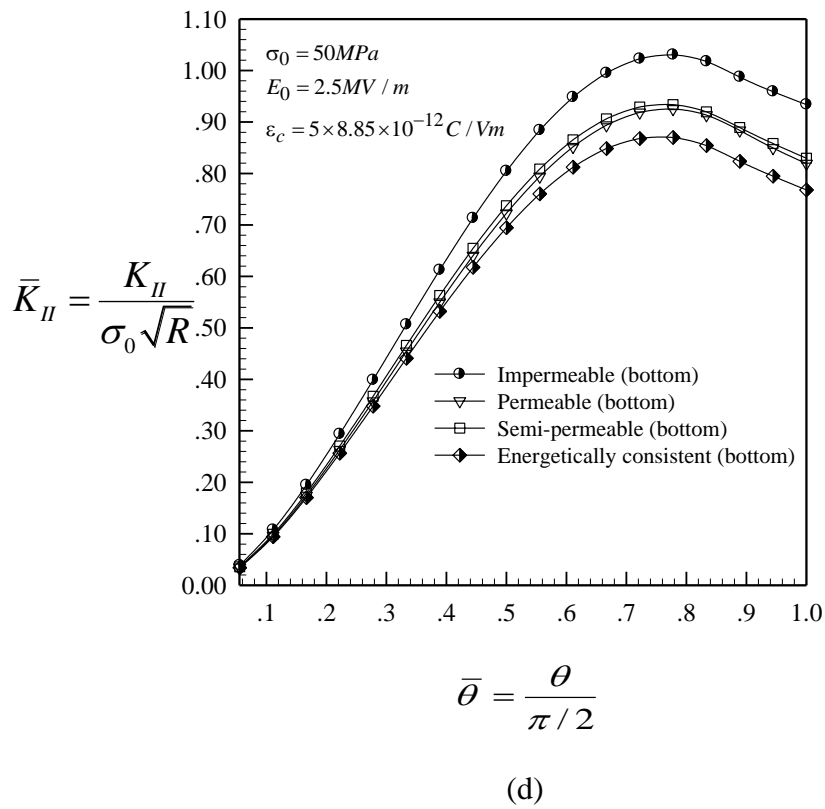
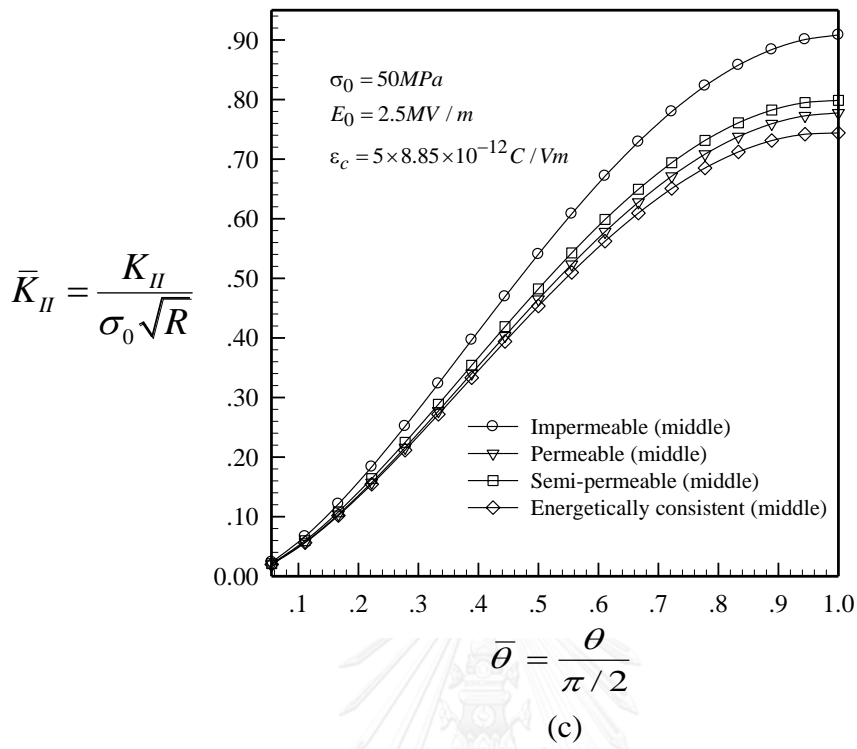


Figure 4.5 Dependent of normalized stress intensity factors K_{II} on the crack subtended angle for cylindrical crack in infinite medium. Results are reported on (a) all points, the (b) top, (c) middle and (d) bottom points

The stress intensity factors K_{III} obtained only at a middle point (at middle zone between top and bottom points) of a quarter (1/4) along the crack front are investigated as mentioned in figure 4.6. It indicates that when the crack-subtended angle increases, the four crack-face models (i.e., impermeable, permeable, semi-permeable and energetically consistent models) strongly decrease to different minimum values, for example, at $\theta = 80$ degree for impermeable and $\theta = 85$ for permeable, semi-permeable and energetically consistent models; however, the distributions are in negative values. Moreover, results manifest that the bounds including upper and lower bound are respectively impermeable and permeable models at the entire range. Besides, the numerical results K_{III} appear only at the middle zone between the top and bottom points whereas the top and bottom points completely disappear. This can be concluded that when half-subtended angle of cylindrical crack increases, it has influence the value of stress intensity factors K_{III} with different minimum values and also give rise to the negative value of four crack-face models.

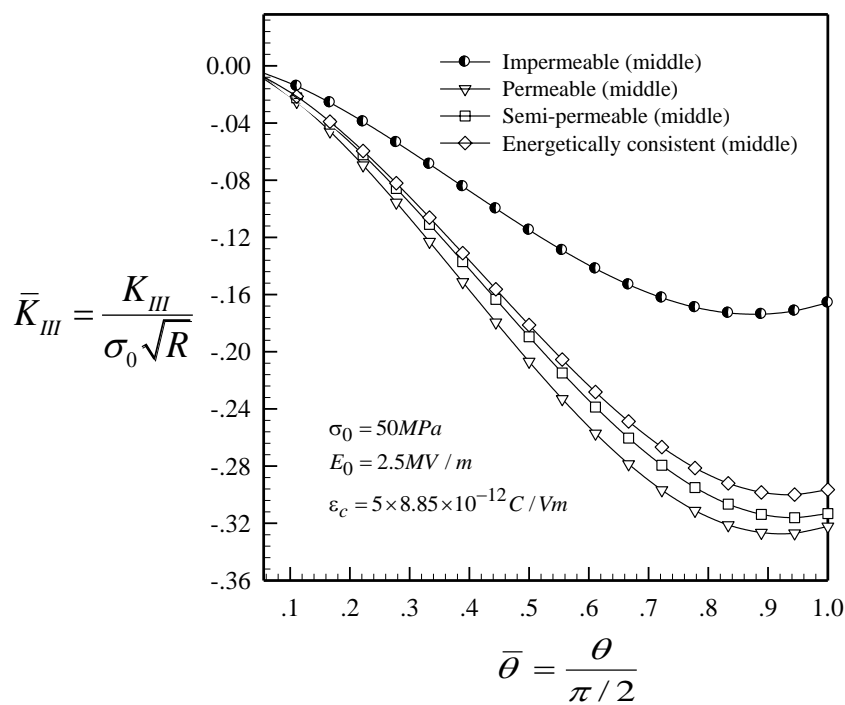
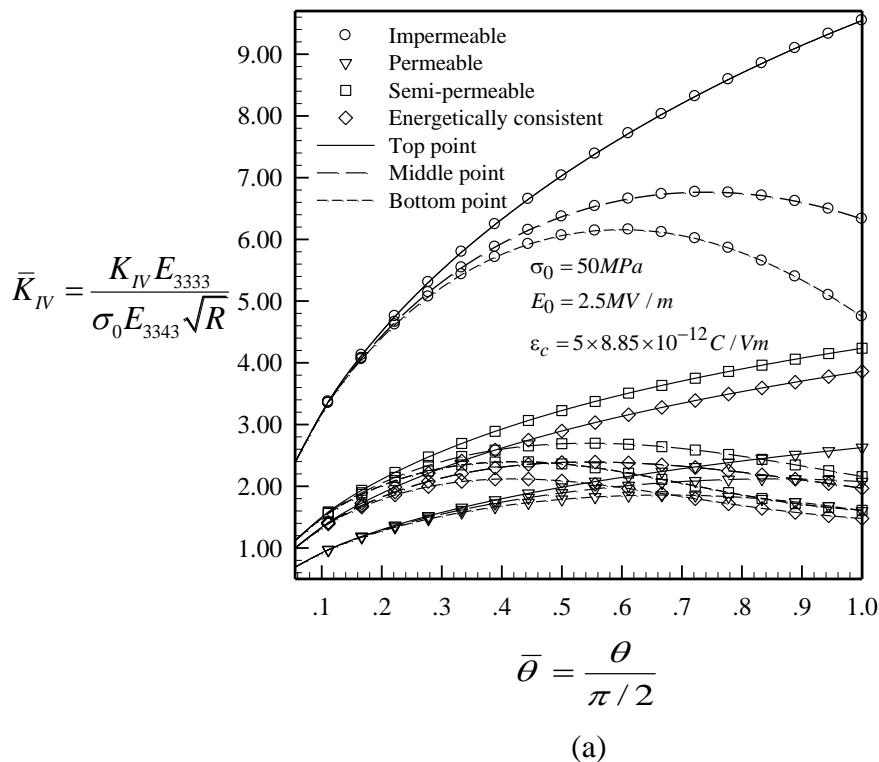
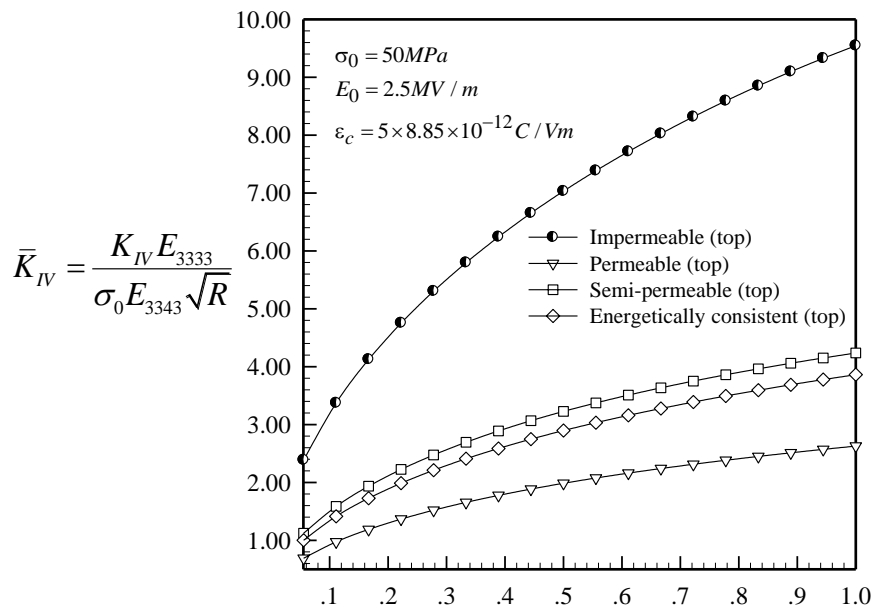


Figure 4.6 Dependent of normalized stress intensity factors K_{III} on the crack subtended angle for cylindrical crack in infinite medium. Results are reported on the middle point

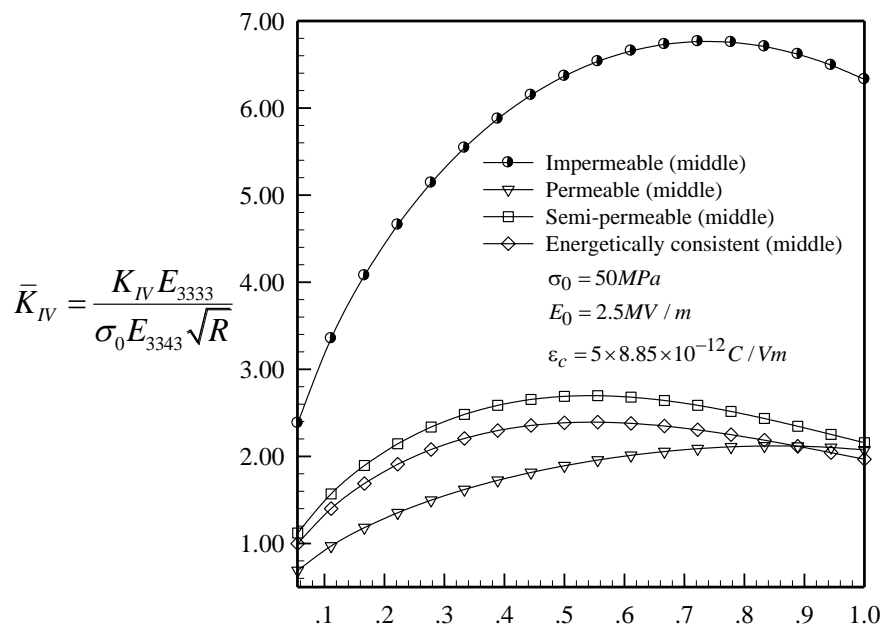
The numerical results of electric intensity factors K_{IV} of a penny-shaped crack folded in a cylindrical pipe (a cylindrical crack) are eventually obtained from various points such as top, middle and bottom points as displayed in the figure 4.7(a). Results indicate that as the half-subtended angle increase, the electric intensity factors K_{IV} are completely different and increase to the differential peak magnitude depending on the

positions (i.e., top, middle and bottom points) and the four crack-face models, for example, the peak magnitude of impermeable models, the two models (i.e., semi-permeable and energetically consistent models) and permeable model of middle points are occurred at $\theta = 65$, at $\theta = 50$ and at $\theta = 75$ degree, respectively. Results reveal further from figure 4.7 (b),(c) and (d) that the impermeable model of three different points are upper bound at the entire range whereas the lower bounds is switched of permeable and energetically consistent models which is different from the lower bound at the top point (lower bound is completely permeable). It can be observed further that the switching points of lower bound at both middle and bottom points are completely different, for instance, the bottom point is at $\theta = 60$ degree whereas at the middle point is shifted to $\theta = 85$ degree. Besides, results also report that when the half-subtended angle is large, the semi-permeable model at both middle and bottom points are converged to permeable models at the end distribution at $\theta = 90$ degree which is distinct from the beginning $\theta = 5$ degree. Throughout above discussions of electric intensity factors K_{IV} illustrated in the figure 4.7(a) to 4.7(d), it can be summarized that as the half-subtended angle increases, it significantly influences both the value electric intensity factors K_{IV} and the bounds of four crack-face models at three different points, i.e., the lower bounds at the middle and bottom point.





(b)



(c)

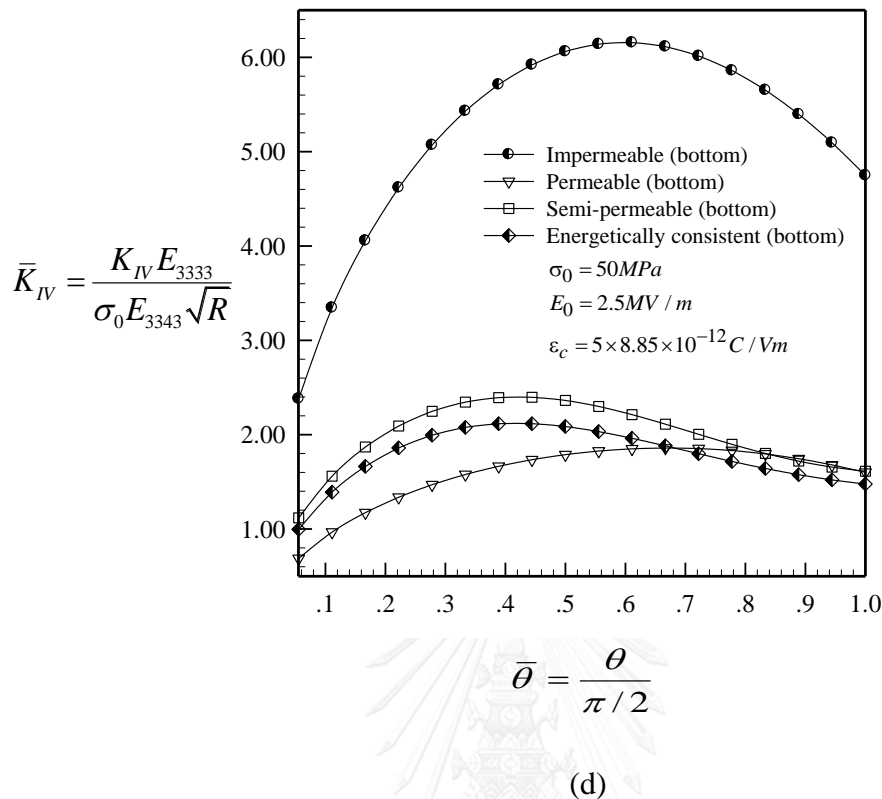


Figure 4.7 Dependent of normalized electric intensity factors K_{IV} on the crack subtended angle for cylindrical crack in infinite medium. Results are reported on (a) all points, the (b) top, (c) middle and (d) bottom points

4.1.1.3 Comparison between spherical cap crack and cylinder crack

From the above discussion, the difference and similarity of the numerical results obtained from both spherical cap and cylindrical cracks can be concluded in the following:

For the spherical cap crack, It can be found that as the crack subtended angle increase from [5, 10, 15, ..., 90] with the constant loading, K_I of four models are completely different and are dependent on the crack subtended angle. For example, the magnitude of four models increases to the peak points when the crack subtended angle is relative small and the magnitude of those four models decreases when the crack subtended angle is sufficiently large. Results also indicate further that the three models (i.e., impermeable, permeable and semi-permeable models) are identical and independent on the boundary conditions. For example, when the crack subtended angle is small in the beginning and those three models are completely different when the crack subtended angle is large. In addition, the energetically consistent model is lower than those three models (i.e., impermeable, permeable and semi-permeable modes) at the beginning range and it approaches to permeable model at the end range. Besides, it is seen again that the increasing crack subtended angle has an influence only to the lower bound by switching of energetically consistent and impermeable model corresponding to turning point. On the contrary, the stress intensity factors K_I obtained from other non-

planar cracks (i.e., cylindrical crack) at three different points (i.e., top, middle and bottom points) are provided when the crack subtended angle increases. It can be found again that all the behaviors and trends are very identical and analogous to the spherical cap crack only at the bottom points. However, the other remaining points (i.e., middle and top points) exhibit less identical behaviors respectively. In addition to the similarity of both cracks (i.e., spherical cap and cylindrical cracks on the bottom point), the upper bound at the top point is impermeable model which is different from upper bound at both middle and bottom points. Again, the lower bound at the top point is energetically model which is completely distinct from lower bound of both middle and bottom points by switching of lower bounds). Moreover, the behavior of impermeable model the top point is different from the remaining points (i.e., middle and bottom points)

The numerical results obtained from the stress intensity factors K_{II} of spherical cap crack can be concluded as follows. It can be found that when the crack subtended angle increases, the magnitude of four models (i.e., impermeable, permeable, semi-permeable and energetically consistent models) strongly depends on the crack subtended angle, for example, they simultaneously increase to the maximum point at the beginning range and those four models will be decreased when the crack subtended angle is sufficiently large. Moreover, the increasing crack subtended angle has no influence to the bounds of four crack models. Identically, the stress intensity factors K_{II} obtained from the cylindrical crack at three different points (i.e., top, middle and bottom points) are proposed to compare the K_{II} of spherical cap crack. It is found again that when the crack subtended angle increases, the magnitude K_{II} of three different points are completely different values depending on different points. It exhibits only the behavior of the bottom point which is very identical with the behavior of spherical cap crack. Apart from, the similarity of the spherical cap crack, it has no the maximum points both K_{II} at the middle point and also three models at the top points i.e., permeable, semi-permeable and energetically consistent models (accept impermeable). Moreover, it is also found that the lower bound at the top point is permeable model which is different from the lower bound of both middle and bottom points. Overall, it can be concluded that the increasing crack subtended angle has an influence not only to magnitude K_{II} of both cracks but also to the bounds of four models of cylindrical crack, especially the bounds at the top point.

The difference between spherical cap crack and cylindrical crack is the stress intensity factor K_{III} in which the cylindrical crack appears only the middle point (a point of the middle zone is located between the top and bottom points). It can be concluded that when the crack subtended angle increases, the magnitude of four models becomes completely different and tend to decrease the magnitude to the different minimum values when the crack subtended angle is sufficiently large; however, it is negative intensity factors. This meant that the crack surface has influence to the magnitude but not to the bound of four models.

Different to the stress intensity factors $[K_I, K_{II}]$ is the electric intensity factor K_{IV} of non-planar cracks. The results of the spherical cap crack can be summarized as follow. It can be found that increasing the crack subtended angle, the magnitude of four crack-face models are complete different and are dependent on the crack subtended angle. Results also show that the maximum points of the magnitude of the two models (i.e., semi-permeable and energetically consistent models) are not identical to that of impermeable and permeable models. Moreover, the lower bound of four models are

switching of permeable and energetically consistent models. In addition, energetically consistent model approaches the permeable model. Identically, the electric intensity factor K_{IV} obtained from the cylindrical crack is offered to correlate the spherical cap crack. When the increasing crack subtended angle, the magnitude of four models become completely different and dependent on the crack subtended angle at the three different points (i.e., top, middle and bottom points). Moreover, behaviors and the trends of the normalized K_{IV} at the bottom points of cylindrical crack are very identical to that of spherical cap crack. In addition to the parity of both cracks, it is seen that when the crack subtended angle increases, the lower bound of the top point is permeable model which is different from the middle and bottom points. Furthermore, the turning point of lower bound of both spherical cap and cylindrical cracks at the bottom point is clearly identical.

4.1.2 Influence of curvature for non-planar cracks.

This section, we investigate the influence on the curvature of the crack surface. The stress and electric intensity factors will be obtained by using the non-planar crack i.e., spherical cap crack and cylindrical crack, which can be seen as follow.

4.1.2.1 Influence of curvature on penny-shaped crack folded in circular ball (spherical cap crack)

To demonstrate the influence of curvature on four crack-face boundary conditions, the investigation is similar to the previous section 3.4.1 in which we consider a penny-shaped crack folded in a half of circular ball or spherical cap crack. The geometry is illustrated in the figure 4.1 which is embed in a transversely isotropic piezoelectric infinite medium. The material properties is assumed as PZT-4. The symmetric axis of material and the poling direction are analogous to the x_3 -axis. To investigate influence of the intensity factors along the crack front, the data can be concluded as follow: (i) the $\mu = \pi R/2a$ is varied from [1, 1.0588, 1.250, ..., 18] (ii) radius of a penny-shaped crack for creating the spherical cap crack is defined as 1, (iii) the radius of spherical cap crack varies from $R = 0.636619772367581$ (the half-subtended angle is now equal to 90 degree) till $R = 11.459155902616500$ (the half-subtended angle is now at 5 degree), and (iv) the remote uniaxial tension is fixed $\sigma_0 = 50$ MPa, (v) the uniform electric field is fixed $E_0 = 2.5$ MV/m and (vi) the permittivity inside the crack gap is fixed $\varepsilon_c = 5\varepsilon_0$ where $\varepsilon_0 = 8.85 \times 10^{-12}$ C/Vm is the permittivity of the air.

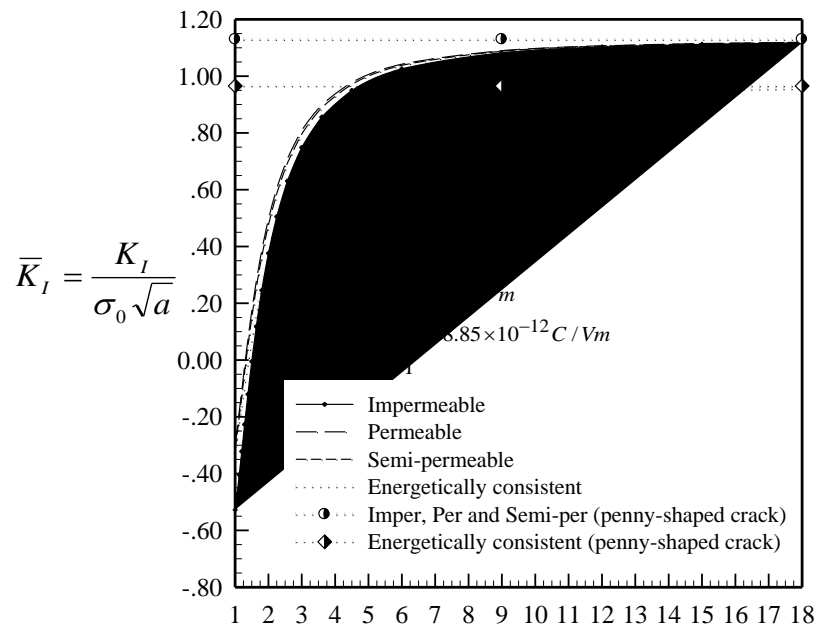
The non-zero stress and electric intensity factors [K_I, K_{II}, K_{IV}] obtained on four crack-face models (i.e., impermeable, permeable, semi-permeable and energetically consistent models) come from as average value of the point along the crack front as shown in the figure 4.8(a),(b) and (c). Results reveal that as the curvature becomes flat crack, the stress and electric intensity factors [K_I, K_{IV}] are strongly increased when the curvature is sufficiently large. On the contrary, the stress K_{II} is increased at large curvature and decreased when the curvature becomes small or nearly the flat crack. This can be discussed as follows.

According to the numerical results of stress intensity factors K_I on four crack-face models (i.e., impermeable, permeable, semi-permeable and energetically consistent models), it can be seen that the stress intensity factors K_I are strongly

increased when the curvature is sufficiently large and that one are converged to the flat crack when the curvature is reduced. This means that the crack opening is strongly inhibited by curvature of the surface at the range $\mu=1$ to $\mu=6$ as indicated in the figure 4.8(a). Moreover, results show that the lower bounds are switched between the impermeable and energetically consistent model at $\mu=2$, whereas the upper bound is dominated by permeable models. In addition, the three models (i.e., permeable, semi-permeable and energetically consistent models) are nearly identical in the beginning and the energetically consistent model gradually develops lower than the permeable and semi-permeable models when the curvature is small. It can be observed further that the impermeable model are converged to the permeable and semi-permeable models at the end point. It should be noted that at $\mu=1$ to 1.5 , K_I of four models are negative values. From their distribution, it can be summarized that when the curvature is sufficiently large, it influences not only the values of intensity factors but also the lower bound of four crack models.

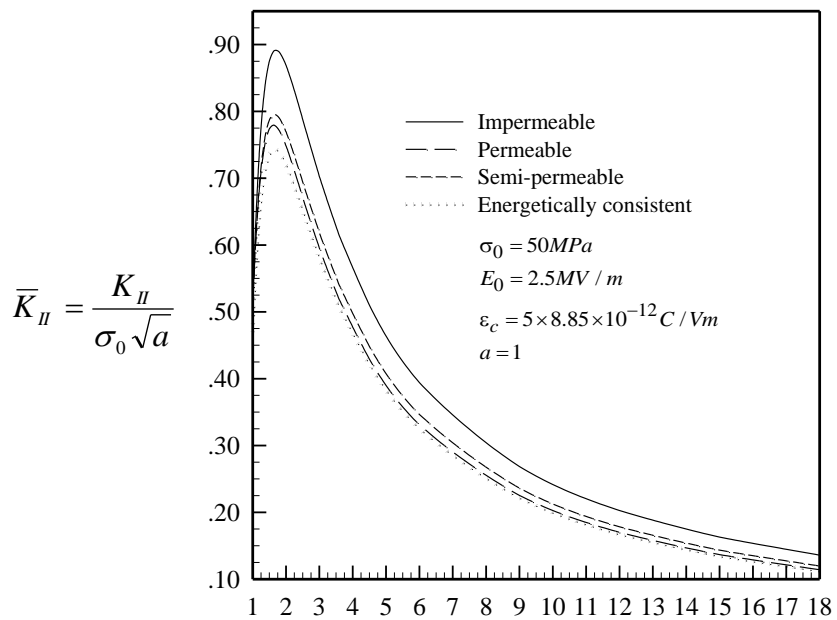
The numerical results of the stress intensity factor K_{II} obtained in the figure 4.8(b) are investigated on four crack-face model. It shows that when the crack-face model is reduced to the flat crack, the value of stress intensity factors K_{II} is increased to the maximum value at $\mu=1.6364$. Provided that, the curvature is sufficiently large and the magnitude gradually decreased when the curvature begins to reduce at the range $\mu=1.6364$ to $\mu=18$. Besides, it can be demonstrated that the upper bound is impermeable model whereas the lower bound is energetically consistent model. This can be implied that when the curvature is reduced, it has influence upon the magnitude of stress intensity factor K_{II} corresponding to the maximum value.

Finally, the electric intensity factors K_{IV} are discussed in association with four crack-face boundary conditions (BCs) shown in the figure 4.8(c). Results manifest that when the curvature becomes flat crack, the distribution of stress intensity factors K_{IV} on four crack-face models become completely different. This means that when the curvature is sufficiently large, the value of K_{IV} significantly tend to increase corresponding to the flat of curvature at the range $\mu=1$ to $\mu=6$. Moreover, the upper bound is impermeable crack whereas the lower bounds are switched of energetically consistent and permeable models. More specifically, this means that when $\mu=0$ to $\mu=1.5$, the lower bound is energetically consistent model whereas the permeable models become the lower bound at the range $\mu=1.5$ to $\mu=18$ as observed in the figure 4.8c. This can be conclude that as the curvature of crack-face model are reduced to the flat crack, the magnitudes of four crack-face BCs and the bounds play a significant role and that affects the lower bound of four crack-face models.



$$\mu = \frac{\pi R}{2a}$$

(a)



$$\mu = \frac{\pi R}{2a}$$

(b)

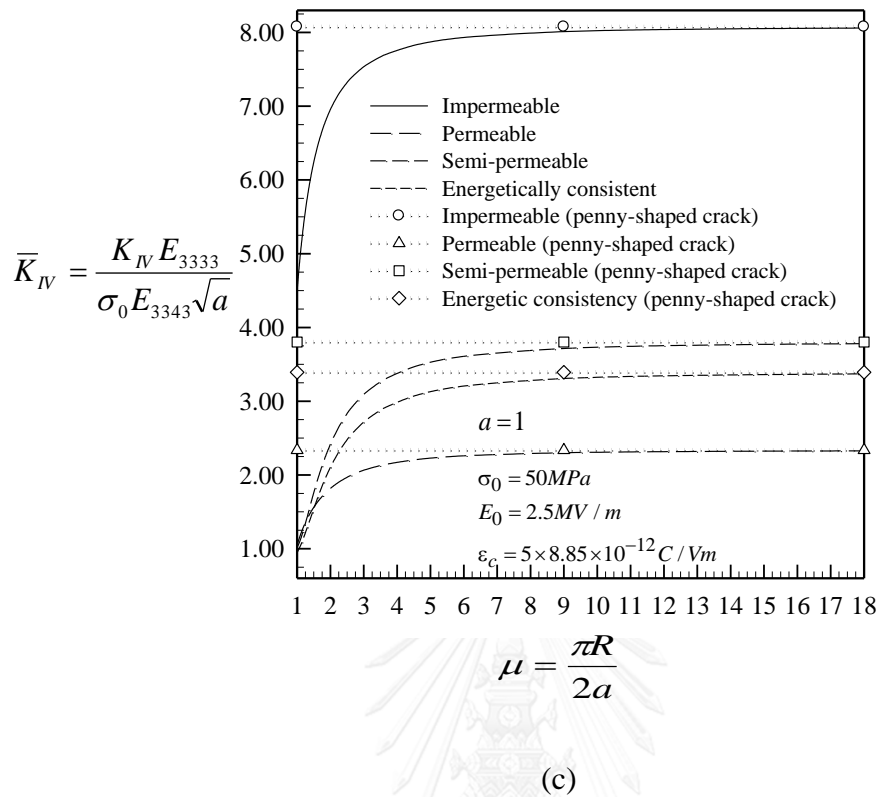


Figure 4.8 (a), (b) and (c) are dependent of normalized stress and electric [K_I , K_{II} , K_{IV}] intensity factors on the curvature for spherical cap crack in infinite medium. Results are reported as average values

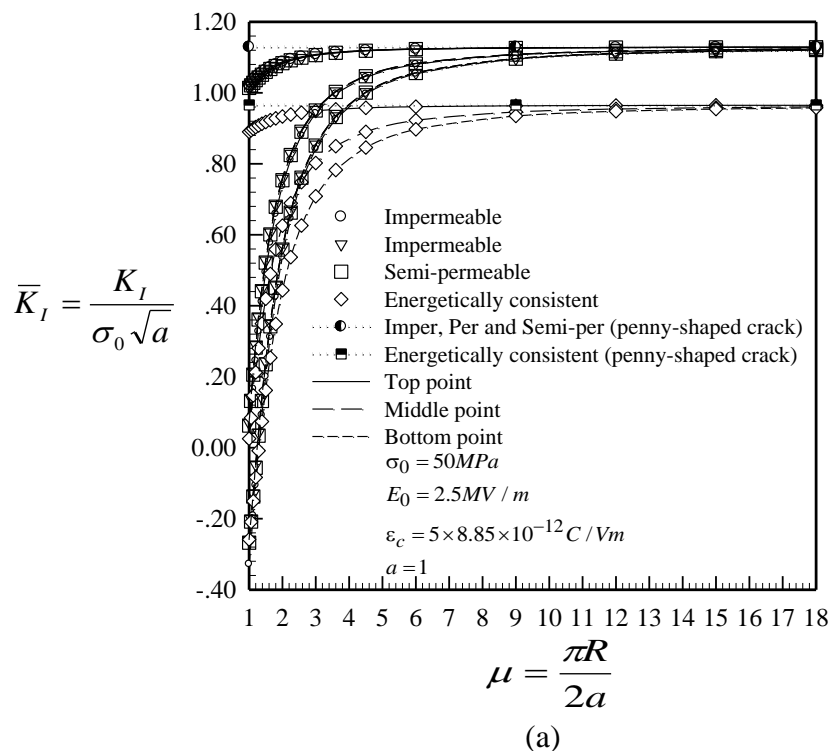
4.1.2.2 Influence of curvature on penny-shaped crack folded in a cylindrical (cylindrical crack)

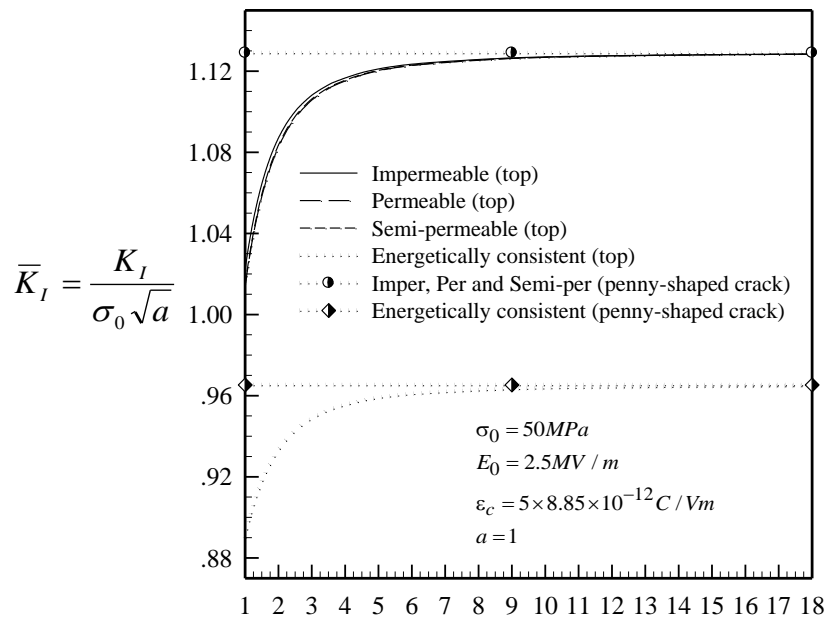
Consider a penny-shaped crack folded in a cylindrical (a cylindrical crack), the geometry is illustrated in the figure 4.3 which is embed in a transversely isotropic piezoelectric infinite medium. The material properties constitutes as PZT-4. The finest mesh from the convergence section 3.4.2 is utilized for the cylindrical crack. The symmetric axis of material and the poling direction analogous to the x_3 -axis., the data for obtaining the intensity factors can be concluded as follow (i) the $\mu = \pi R/2a$ is varied from [1 to 18] (ii) radius of a penny-shaped crack for creating the cylindrical crack is fixed as 1, (iii) the radius of cylindrical crack is varied from $R = 0.636619772367581$ (the half-subtended angle is equal to 90 degree) till $R = 11.459155902616500$ (the half-subtended angle is now at 5 degree). (iv) the remote uniaxial tension is fixed $\sigma_0 = 50\text{MPa}$, (v) the uniform electric field is fixed $E_0 = 2.5\text{MV/m}$ similar to the x_3 -direction, (vi) and the permittivity inside the crack gap is fixed $\epsilon_c = 5\epsilon_0$ where $\epsilon_0 = 8.85 \times 10^{-12}\text{C/Vm}$ is the permittivity of the air.

The numerical results of stress and electric intensity factors [K_I, K_{II}, K_{IV}] and K_{III} (only at middle point) of cylindrical crack offered from three different points (top, middle and bottom points) of a quarter (1/4) along the crack front are reported in figure 4.9(a), 4.10(a) and 4.11(a). It can be seen that when the curvature is reduced to planar

crack, the value of K_I , K_{II} and K_{IV} are explicitly different depending on the positions which can be discussed in detail in the following:

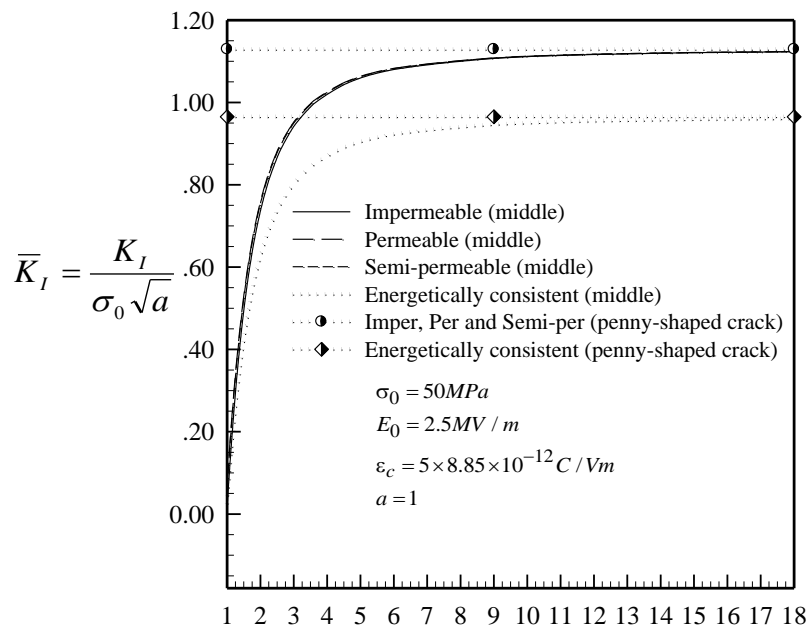
Results of stress intensity factors K_I reported in figure 4.9(b), (c) and (d) indicate that the magnitude of three different points strongly increase; nevertheless, the value of magnitude which is near the planar crack are different, for example, for the middle and bottom points are approximately occurred at $\mu=9$ whereas for the top point is approximately occurred at $\mu=4.5$. Apart from, the three models (i.e., impermeable, permeable and semi-permeable models) at three points (i.e., top, middle and bottom points) are nearly identical when the curvature is sufficiently large. On the contrary, the energetically consistent model is obviously less than other three models. Furthermore, results manifest that the bound of four crack-face models at three distinct points along the crack front are clearly different, for example, the upper bound at both middle and bottom point are identically permeable whereas at the top point is impermeable. Again, the lower bound at both top and middle point is obviously energetically consistent model, whereas the lower bound at bottom points are obviously switched between impermeable and energetically consistent model when half-subtended angle is sufficiently large corresponding to the turning point at $\mu = 1.2857$. This can be concluded that when the curvature converged to planar crack, it influences not only value of mode-I stress IF but also the bounds of four crack-face boundary condition possess both upper and lower bound.





$$\mu = \frac{\pi R}{2a}$$

(b)



$$\mu = \frac{\pi R}{2a}$$

(c)

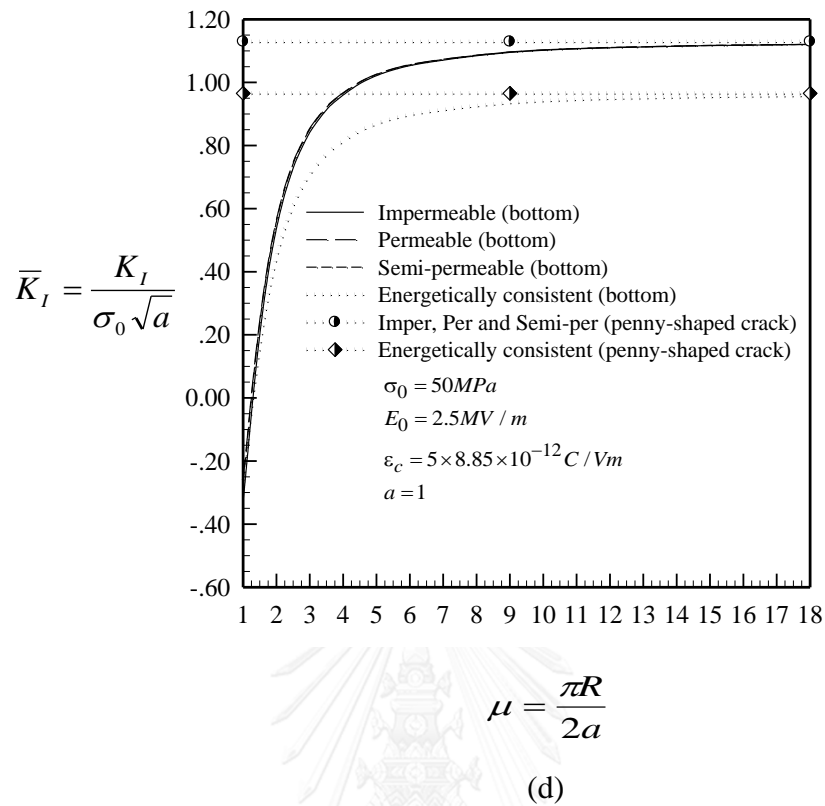
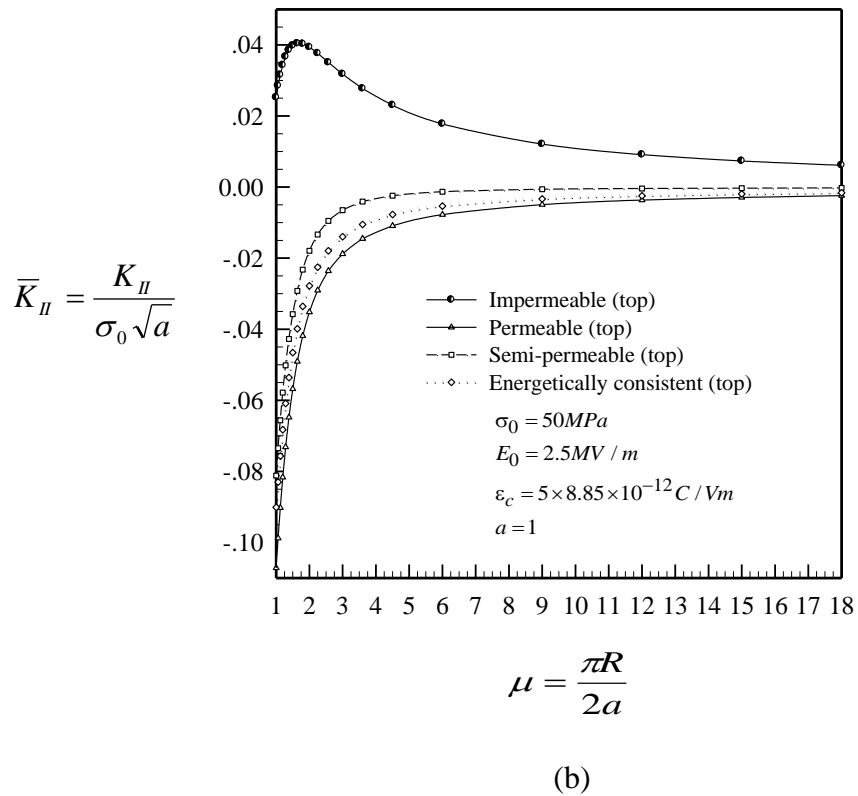
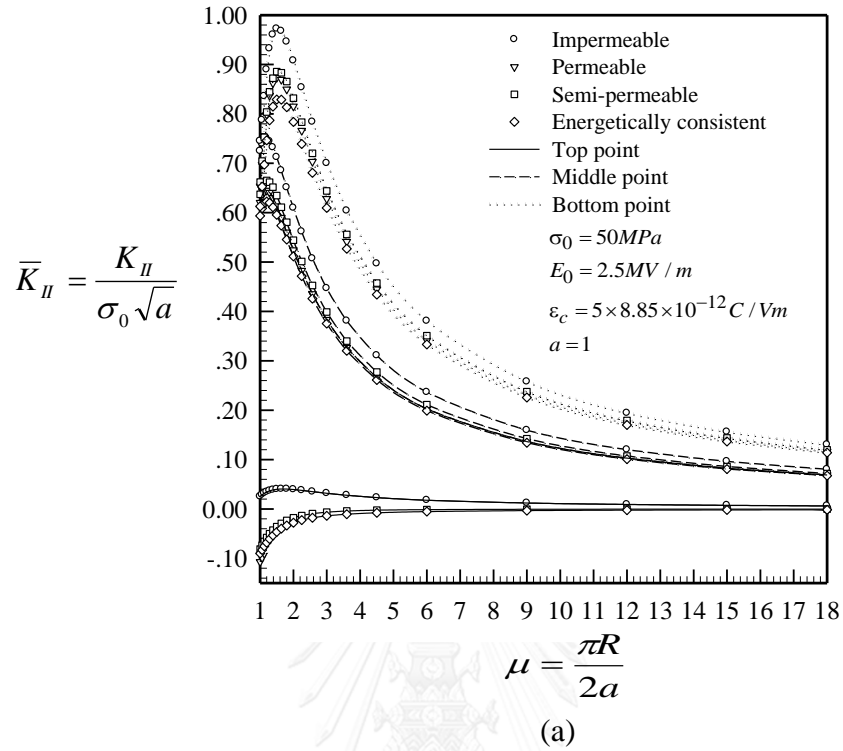
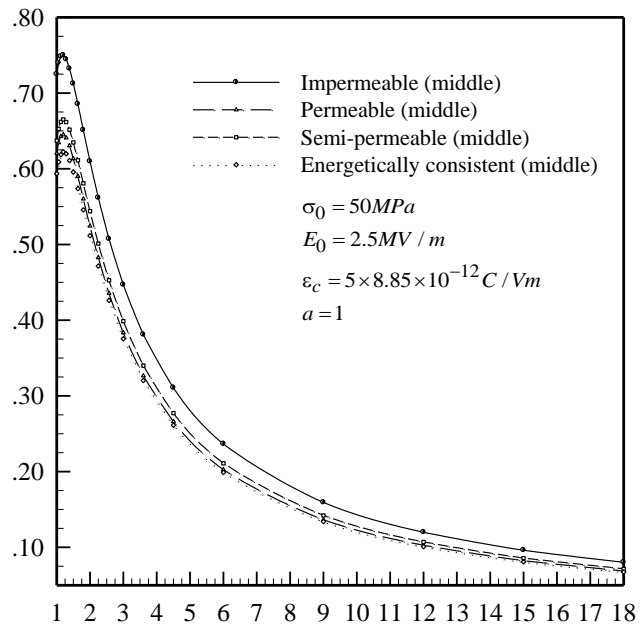


Figure 4.9 Dependent of normalized stress intensity factors [K_I] on the curvature for cylindrical crack in infinite medium. Results are reported on (a) all points, the (b) top, (c) middle and (d) bottom points

For the results of stress intensity factors K_{II} on four crack-face models (i.e., impermeable, permeable, semi-permeable and energetically consistent models) are again similar to the spherical cap crack only some point. The value of stress K_{II} at three different points (i.e., top, middle and bottom points) will be mentioned in figure 4.10 (a). According to the result, provided that the curvature is reduced to flat crack, the values of stress K_{II} at three different points obviously increase when the curvature is large corresponding to the maximum point. For example, it occurs in the bottom point at $\mu = 1.3846$ and in the middle point at $\mu = 1.2$, whereas only the impermeable of the top point occurs $\mu = 1.6364$ as reported in figure 4.10(b),(c) and (d) respectively. It can be observed further that the distribution of stress K_{II} at the top point are explicitly different from both the middle and bottom points. More specifically, the three crack models (i.e., permeable, semi-permeable and energetically consistent model) at the top point have no maximum value. Moreover, results also indicate that the upper bounds of four models at three distinct points are identically impermeable, whereas the lower bounds change depending on the point along the crack front. For example, the lower bound of both middle and bottom point are energetically consistent, at the same time it is dominated by permeable at the top point. It can be concluded that as the curvature converged to flat crack, it has influence to the maximum points of stress intensity factor and to the lower bounds of four models.



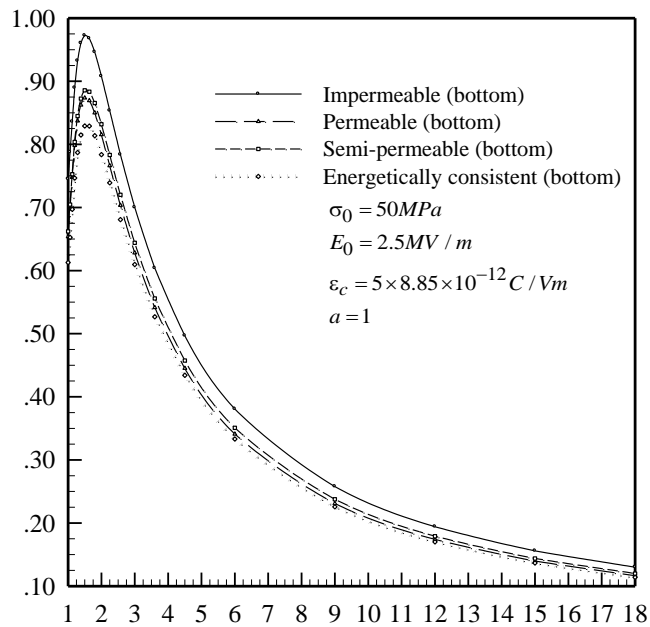
$$\bar{K}_{II} = \frac{K_{II}}{\sigma_0 \sqrt{a}}$$



$$\mu = \frac{\pi R}{2a}$$

(c)

$$\bar{K}_{II} = \frac{K_{II}}{\sigma_0 \sqrt{a}}$$



$$\mu = \frac{\pi R}{2a}$$

(d)

Figure 4.10 Dependent of normalized stress intensity factors $[K_{II}]$ on the curvature for cylindrical crack in infinite medium. Results are reported on (a) all points, the (b) top, (c) middle and (d) bottom points

It is obvious that the stress intensity factors K_{III} obtained from four crack-face models (i.e., impermeable, permeable, semi-permeable and energetically consistent models) at both the top and the bottom points vanished, whereas at a middle (a point at middle zone) of a quarter (1/4) along the crack front as reported in figure 4.11 the magnitude indicates that when the curvature converged to planar crack, the three models (viz. permeable, semi-permeable and energetically consistent models) extremely increase with high slope at the range $\mu=1$ to $\mu=3.6$ approximately and then the slope will lower to the end point, whereas the impermeable model strongly decrease to the minimum point at $\mu=1.2857$ and then start increasing to the end distribution which means that the impermeable model can be increased and decreased. It can be observed further that the three models started at the same point and gradually exhibited the difference when the curvature becomes flat. Besides, the upper and lower bounds are impermeable and permeable models respectively. This can be concluded that as the curvature becomes flat, it affects the magnitude of four crack-face models or, more specifically, the impermeable model.

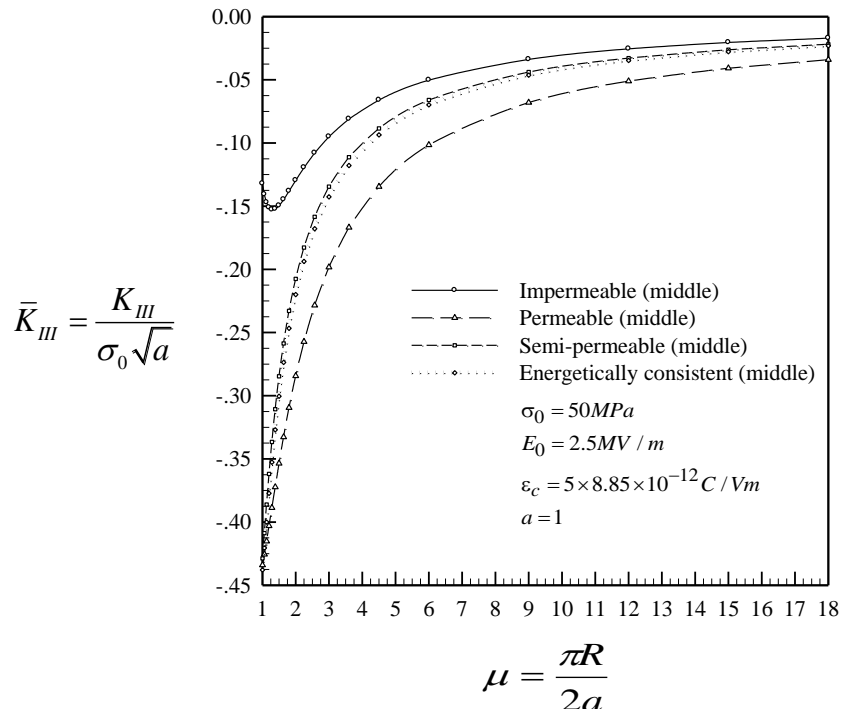
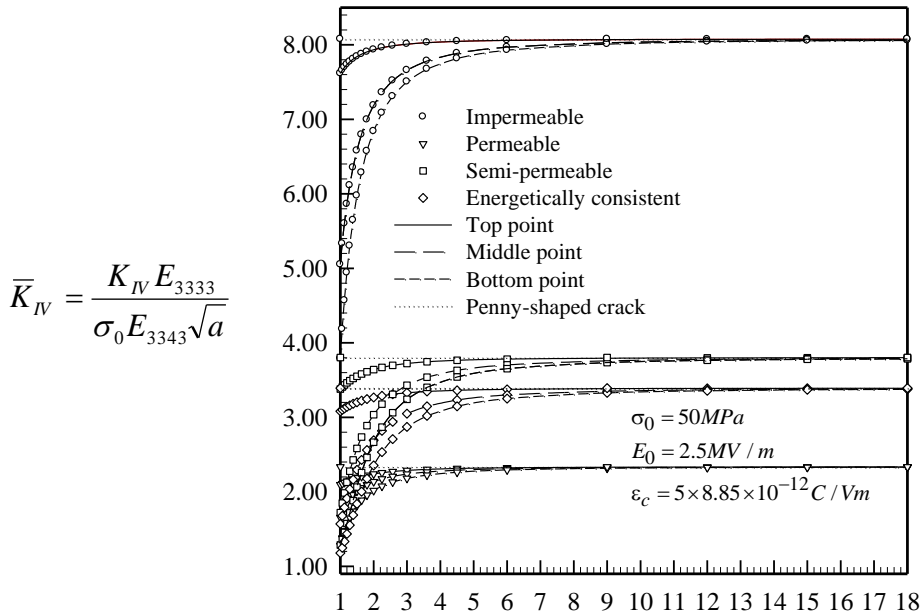


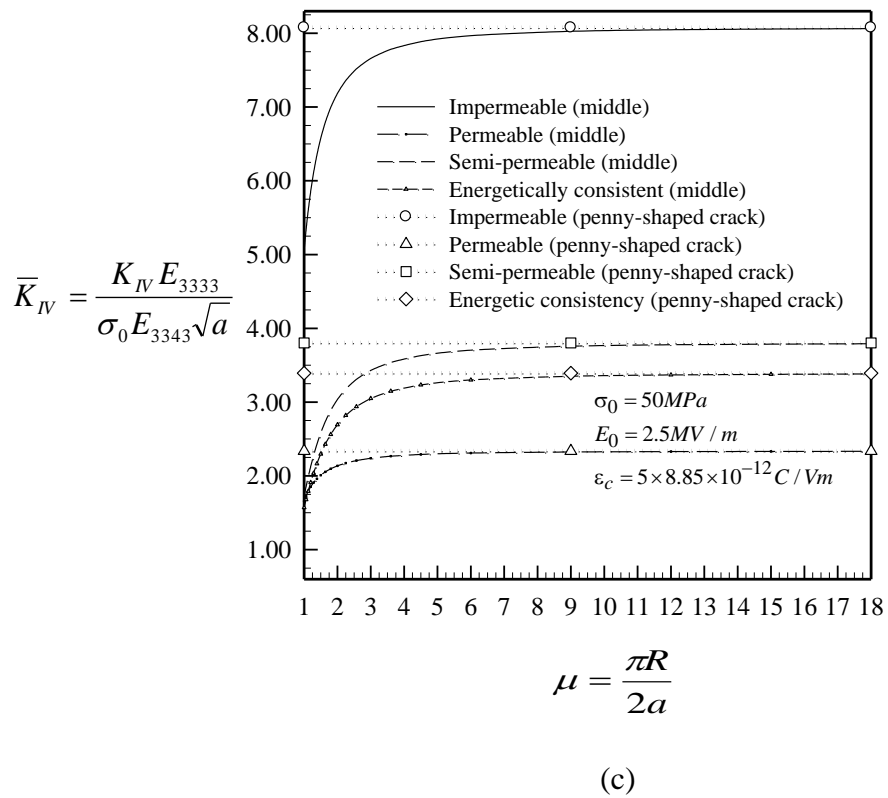
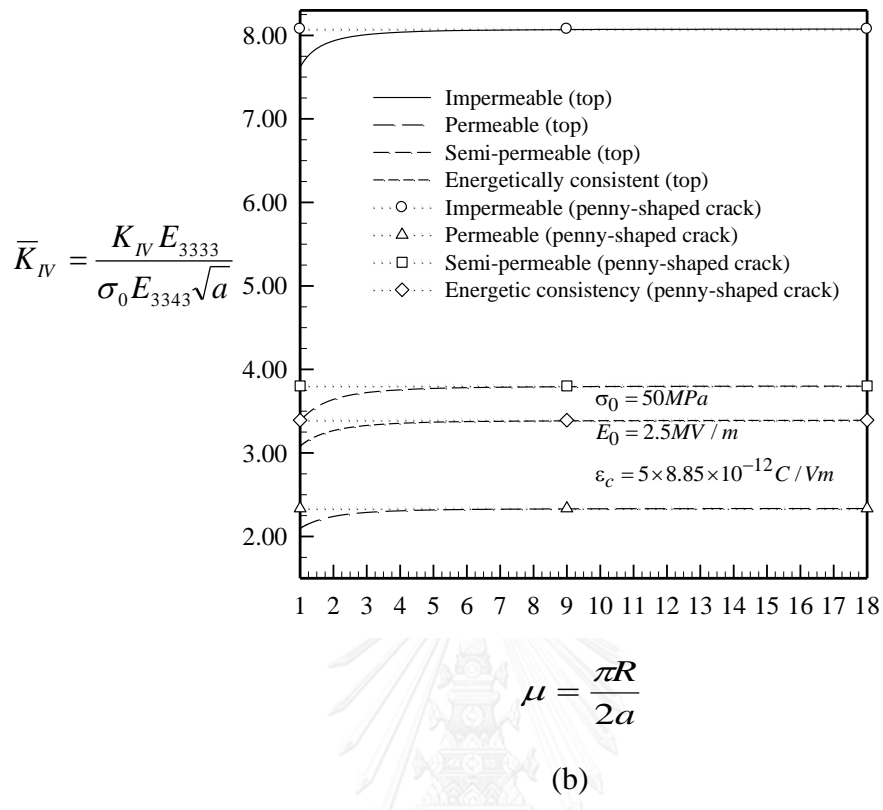
Figure 4.11 Dependent of normalized stress intensity factors $[K_{III}]$ on the curvature for cylindrical crack in infinite medium. Results are reported on the middle point

Finally, the influence of the electric intensity factors K_{IV} of cylindrical crack obtained from three different point (i.e., top, middle and bottom points) reported in figure 4.12(a) indicates that as the curvature converged to planar crack, the value of electric IFs of four crack face boundary conditions (BCs) again become different and strongly increases with different range of high slop for example, the magnitude value of middle and bottom points are occurred at $\mu=9$ whereas for the top point is occurred at $\mu=9$ approximately. This would be discussed in details as follows; figure 4.12(b), (c) and (d) show that the values of electric IFs of four models (i.e., impermeable, permeable, semi-permeable and energetically consistent models) are nearly similar to planar crack at the top point and gradually show the distinct value at the middle and bottom points. It can be observed further that the bounds of four models change, for instance at the top point, the upper and lower bound form as impermeable and permeable models respectively. Moreover, the middle and bottom points illustrated that the upper bounds clearly form identically as impermeable (analogous to the upper bound of the top point), whereas the lower bound significantly switches between energetically consistent and permeable model corresponding to turning point, for example the turning point of lower bound at middle point occurs at $\mu=1.1250$ and at $\mu=1.3846$ for the bottom point. It can be concluded that the turning points at a quarter (1/4) along the crack front change depending on the curvature, and that when the curvature of surface change, it affects not only to the magnitude of electric IFs but to lower bound at three different points.



$$\mu = \frac{\pi R}{2a}$$

(a)



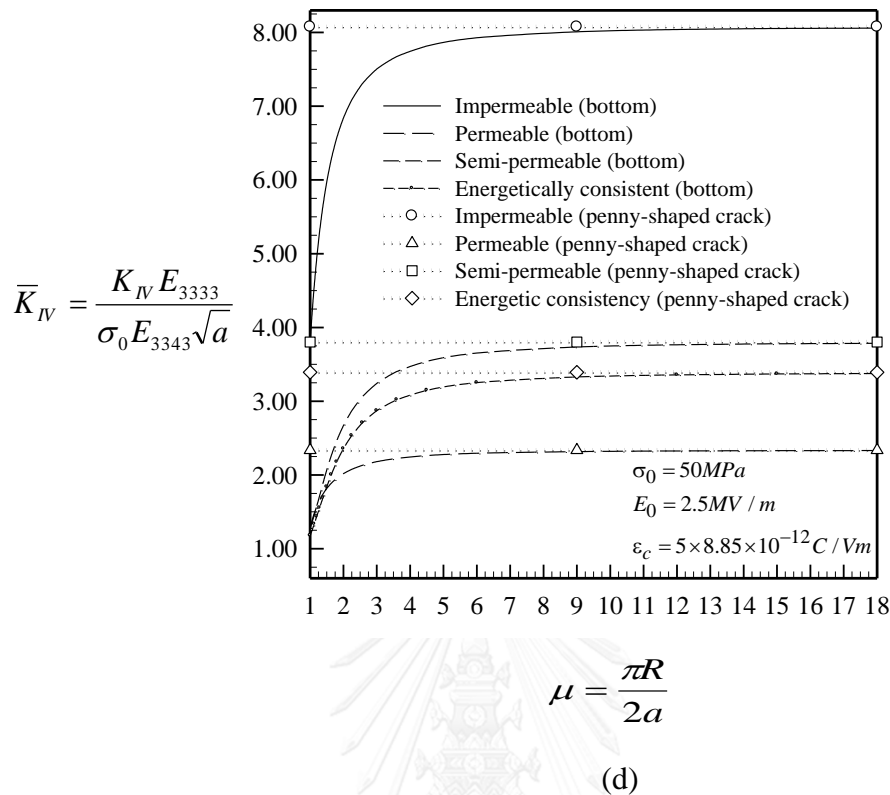


Figure 4.12 Dependent of normalized electric intensity factors [K_{IV}] on the curvature for cylindrical crack in infinite medium. Results are reported on (a) all points, the (b) top, (c) middle and (d) bottom points

4.1.2.3 Comparison between spherical cap crack and cylinder crack

Considering the result mentioned above, the difference and similarity of the numerical results obtained from both spherical cap and cylindrical crack of four crack-face models can be summarized as follows.

Results of spherical cap crack is proposed. It implies that with the reducing curvature of the crack, the magnitude K_I of four models are strongly dependent of the large curvature but the four models are independent on the boundaries. Moreover, when the curvature is reduced to flat crack, only the energetically consistent model is dependent on the curvature whereas other three models are not. In addition the reducing curvature of the crack also affects the lower bond of four models (the lower bound is switched of impermeable and energetically consistent models). Similarly, the stress intensity factors K_I on four models at three different points (i.e., top, middle and bottom points) of cylindrical crack are obtained to compare the influence of curvature of spherical cap crack. Here we find that with the reducing curvature of the crack, the magnitude K_I of three different points become clearly different among four models. Moreover, the behaviors and the trends at the top point are very identical to the spherical cap crack. Apart from the similarity of the spherical cap crack, the results show that the

upper bounds at the top point of cylindrical crack are impermeable, whereas the lower bounds at both top and middle points are similarly energetically consistent models.

The stress intensity factor K_{II} obtained from spherical cap crack on four crack models (i.e., impermeable, permeable, semi-permeable and energetically consistent models). It is found that with the reducing curvature of the crack surface, the magnitudes of four crack models are strongly dependent of large curvature. For example, they increase to the maximum value when the curvature is large but decrease when the curvature reduces to flat crack. Moreover, the reducing curvature of the crack surface does not affect the bounds of four crack models. Identically, comparison between spherical cap and cylindrical cracks becomes more interesting when the stress intensity factors K_{II} are obtained of four models at the three different points (i.e., top, middle and bottom points). It is found that as the curvature of the crack surface reduces, the magnitude of normalized stress K_{II} at three different points becomes clearly distinct. Similarly, the similarity of spherical cap crack to cylindrical crack is focused only on the top point of cylindrical crack. Apart from the similarity of both cracks, from the numerical results offered from cylindrical crack, it can be observed further that when the curvature of the crack reduces, the dependent of K_{II} for the rest points (i.e., middle and top points) are nearly identical to spherical cap crack (or similar to the bottom point of cylindrical crack) at the large curvature of crack surface. Moreover, the reducing curvature of the crack surface influences only the lower bound of the stress intensity factors K_{II} obtained from the three different points. For example, the lower bound of both middle and bottom points are energetically consistent whereas it is permeable models for the top point.

The difference between spherical cap crack and cylindrical crack is the appearance of stress intensity factors K_{III} only at the middle points of cylindrical crack. It can be found that with the reducing curvature of the crack surface, the magnitude of four models are strongly depend on the curvature of crack surface, i.e., the impermeable model has the minimum points at the large curvature of crack surface.

The electric intensity factors K_{IV} obtained from the two non-planar cracks (i.e., spherical cap and cylindrical cracks) on four models. The results of spherical cap cracks indicate that with the reducing curvature of the crack, the magnitudes of four models are strongly dependent when the curvature of crack surface is large. Moreover, when the curvature of crack surface is sufficiently large, the three models (i.e., permeable, semi-permeable and energetically consistent models) are independent of boundaries different from the impermeable model. On the contrary, the four models are dependent of boundaries when the curvature is largely reduced. In addition, the reducing curvature of the crack also affects the lower bound of four models by switching of permeable and energetically consistent models. Again, providing that the load condition remains the same, in which the electric intensity factors K_{IV} obtained from cylindrical crack at three different points (i.e., top, middle and bottom points) on four crack-face models, the magnitude K_{IV} of three different points are dependent of crack subtended angle. Apart from the same behavior of both cracks (i.e., spherical cap crack and cylindrical crack only at the top point), the bound of the top points are different from both middle and bottom point. For example, the upper bound and lower bound are impermeable and permeable respectively.

4.1.3 Influence of geometry by varying aspect ratio of tunnel crack

In this case, we consider a tunnel crack with the half-length L and end-radius a containing in a transversely isotropic piezoelectric infinite medium. The material properties such as PZT-4 is utilized. In this case, we utilize the mesh from 72 to 300 elements. The poling direction is similar to the symmetry axis of material of x_3 -axis. The geometry and the meshes are displayed in the figure 4.13 (a),(b),(c) and (d). To investigate intensity factors along the crack front, the parameters of this study can be concluded as follow (i) the aspect ratio of half-length L and end-radius a (L/a) are varied from $[0.5, 1, 1.5 \dots 10]$, (ii) the end-radius is fixed by 1 whereas the half-length are varied from 0.5 to 10, (iii) the remote uniaxial tension is fixed $\sigma_0 = 50$ MPa, (iv) the uniform electric field is fixed $E_0 = 2.5$ MV/m in the x_3 -direction, (v) and the dielectric permittivity inside the crack gap is fixed $\epsilon_c = 5\epsilon_0$ where $\epsilon_0 = 8.85 \times 10^{-12}$ C/Vm is the permittivity of the air in the crack gap.

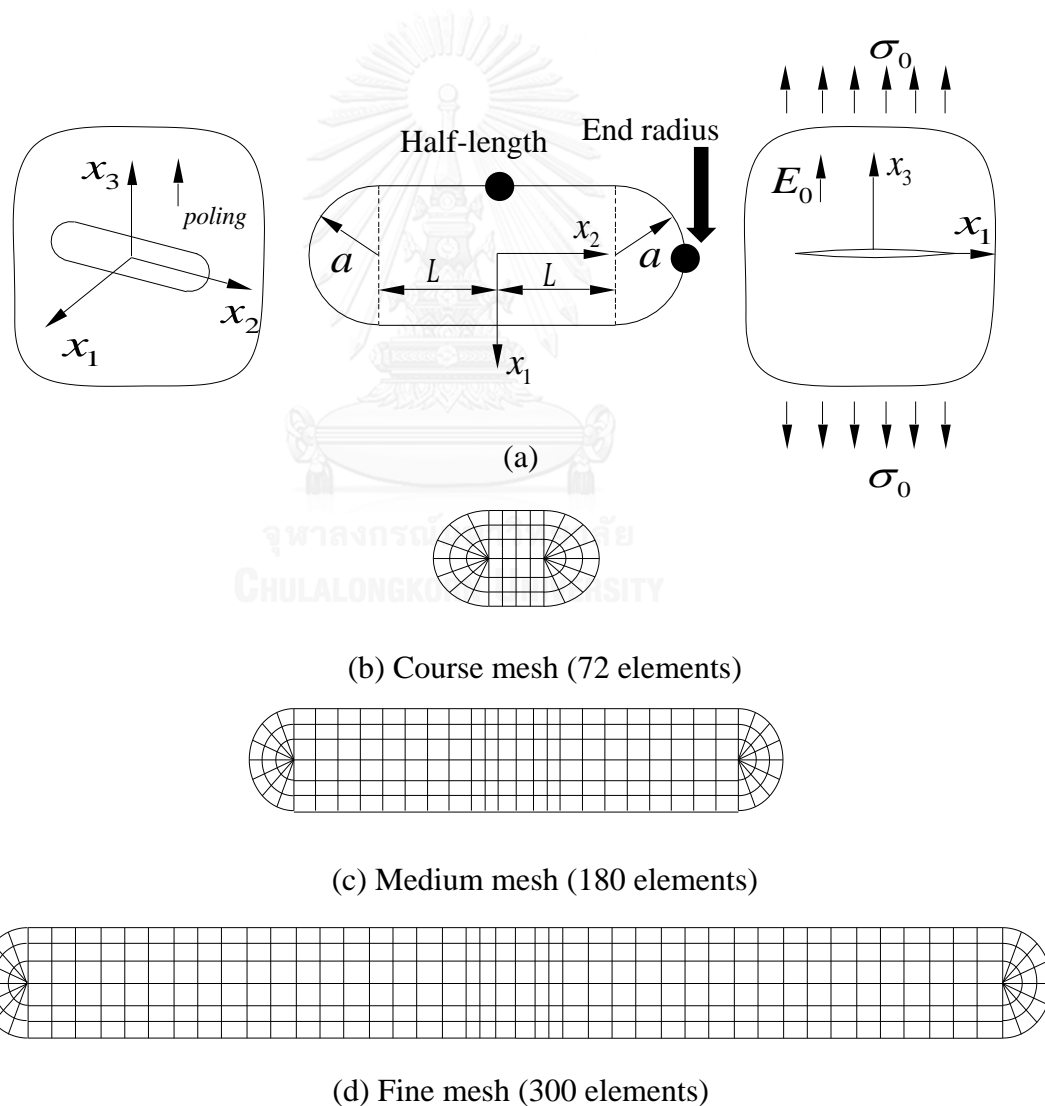
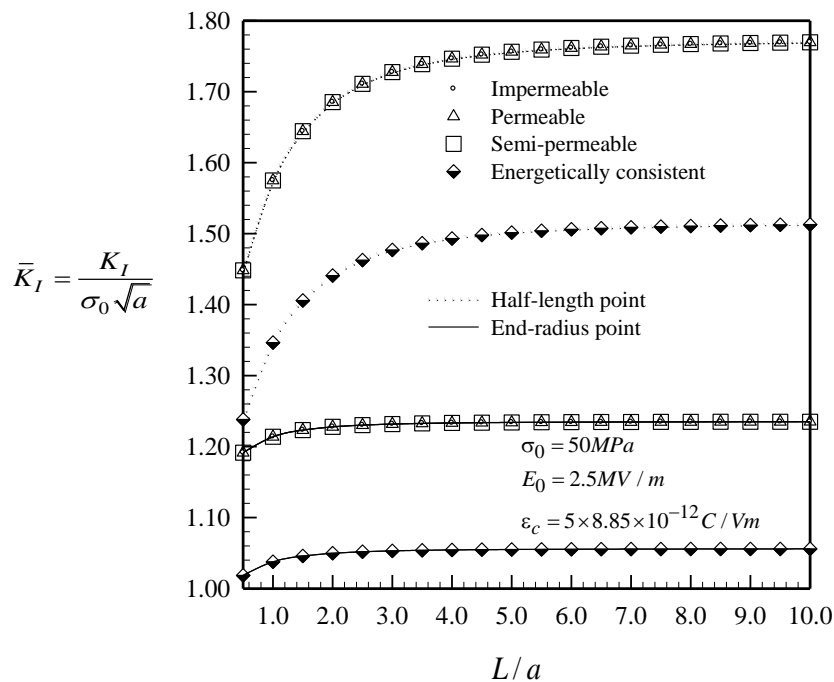


Figure 4.13 (a) Schematic of tunnel crack in a piezoelectric infinite medium and (b),(c) and (d) are the example of the meshes that utilized for the investigation

The influence of the crack aspect ratio L/a of a tunnel crack on the intensity factors along the crack front under four types of crack-face conditions is investigated. The normalized maximum stress and electric intensity factors $[K_I, K_{IV}]$ at two different points (i.e., end-radius and middle of half-length point) on the crack front are shown in figure 4.14 (a) and (b). It can be found that as the half-length point increases, the magnitude of stress and electric intensity factors $[K_I, K_{IV}]$ strongly increases which can be discussed as follows.

Numerical results reported in figure 4.14 (a) indicate that the stress intensity factors K_I of three crack-face models (i.e., impermeable, permeable and semi-permeable models) at any points are completely identical throughout the range of distributions along the crack front ($L/a = 0.5$ to $L/a = 10$), whereas the energetically consistent models are clearly lower than those three models. It can be observed further that the magnitudes of two different points (end-radius and middle of half-length points) are clearly distinct. The result shows that the magnitude of K_I at end-radius point is lower than the magnitude of middle of half-length points, which can be concluded that as the aspect ratio increases, it has an influence only to the magnitude of stress intensity factor K_I .

The electric intensity factor K_{IV} of four crack-face models at two distinct points such as at the end-radius and middle of half-length points along the crack front are shown in figure 4.14 (b). One is found that as the aspect ratio (L/a) increases, the magnitude of four models (i.e., impermeable, permeable, semi-permeable and energetically consistent models) are obviously different throughout the range of distribution, and also that the bounds of electric intensity factor K_{IV} at any points along the crack front and the impermeable and permeable conditions serve as the upper and lower bounds respectively.



(a)

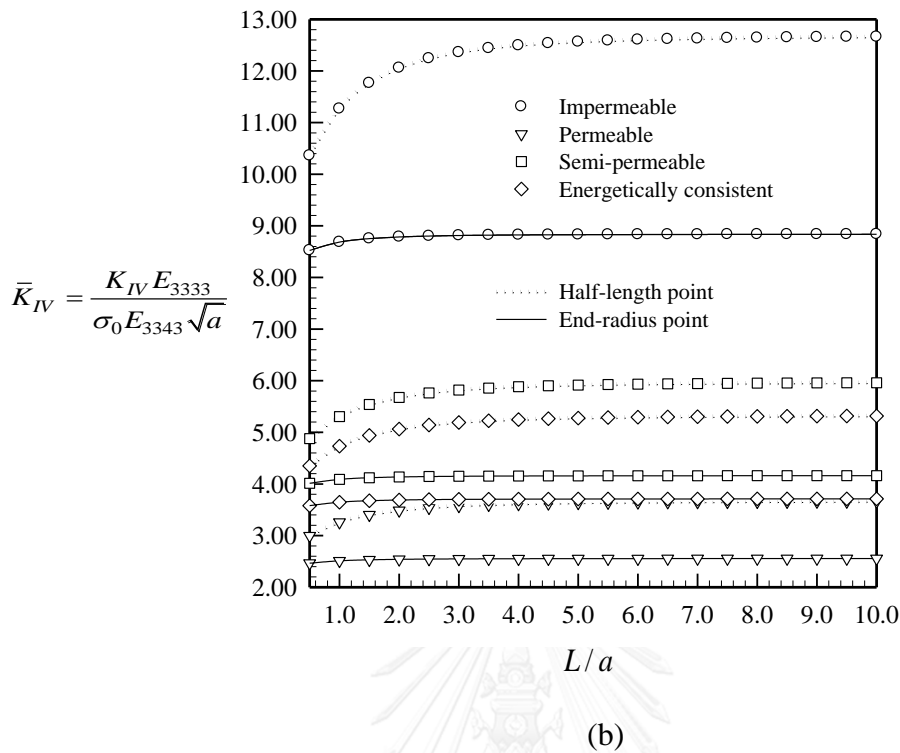


Figure 4.14 (a) and (b) are dependent of normalized stress and electric intensity factors $[K_I, K_{IV}]$ on the aspect ratio for tunnel crack in infinite medium. Results are reported on both the end-radius and half-length points

4.1.4 Interacting of two penny-shaped crack in vertical directions

In this investigation, we consider two penny-shaped cracks with radius a and the distance between the two cracks L , referred to as crack-A and crack-B which are embedded in a transversely isotropic and piezoelectric infinite medium. The material properties such as PZT-4 is employed. In this special case, we utilize the mesh as 144 elements. The poling direction is identical to the symmetric axis of material of x_3 -axis. The geometry and the mesh are displayed as indicated schematically in Figure 4.15 (a) and (b). The parameters used in this exploration can be summarized as follow: (i) the distance between the two cracks L is varied $[0.25, 0.5, 0.75, 1, 2, 3, \dots, 10]$, (ii) the radius of the cracks is defined as 1, (iii) the remote uniaxial tension is fixed as $\sigma_0 = 50$ MPa, (iv) the uniform electric field is fixed $E_0 = 2.5$ MV/m in the x_3 -direction, (v) and the dielectric permittivity inside the crack gap is fixed $\varepsilon_c = 5\varepsilon_0$ where $\varepsilon_0 = 8.85 \times 10^{-12}$ C/Vm is the permittivity of the air in the crack gap.

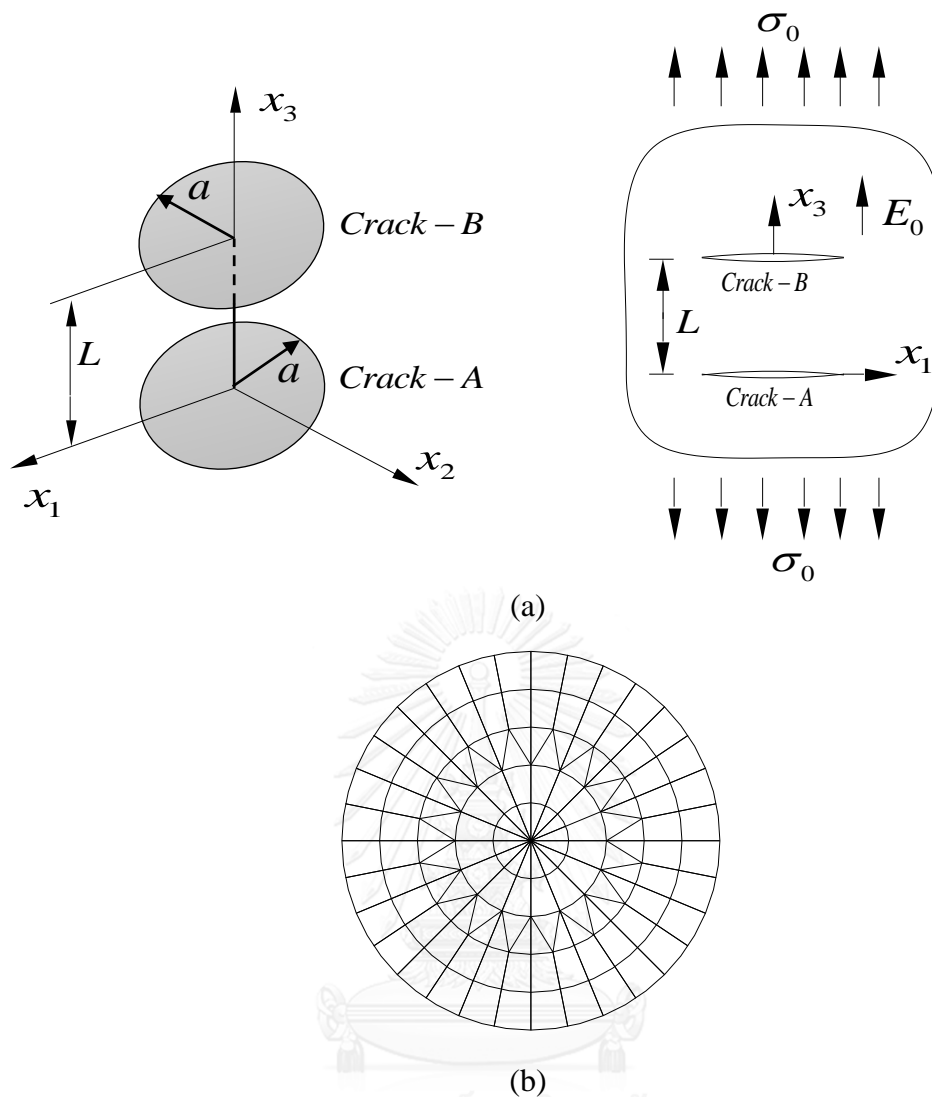


Figure 4.15 (a) Schematic of two penny-shaped cracks in vertical direction in a piezoelectric infinite medium and (b) are the meshes for one penny-shaped crack that utilized for the investigation

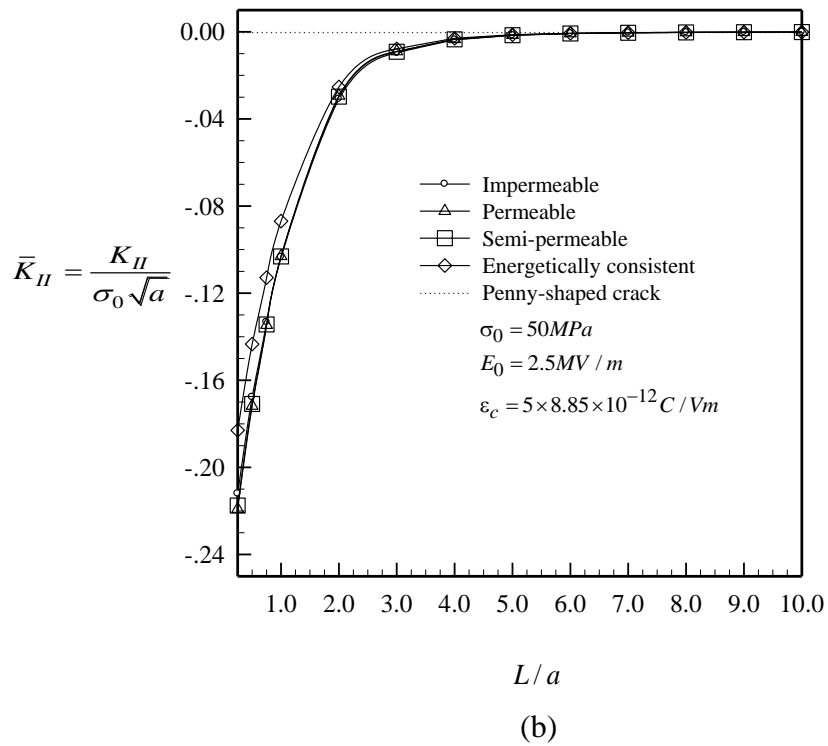
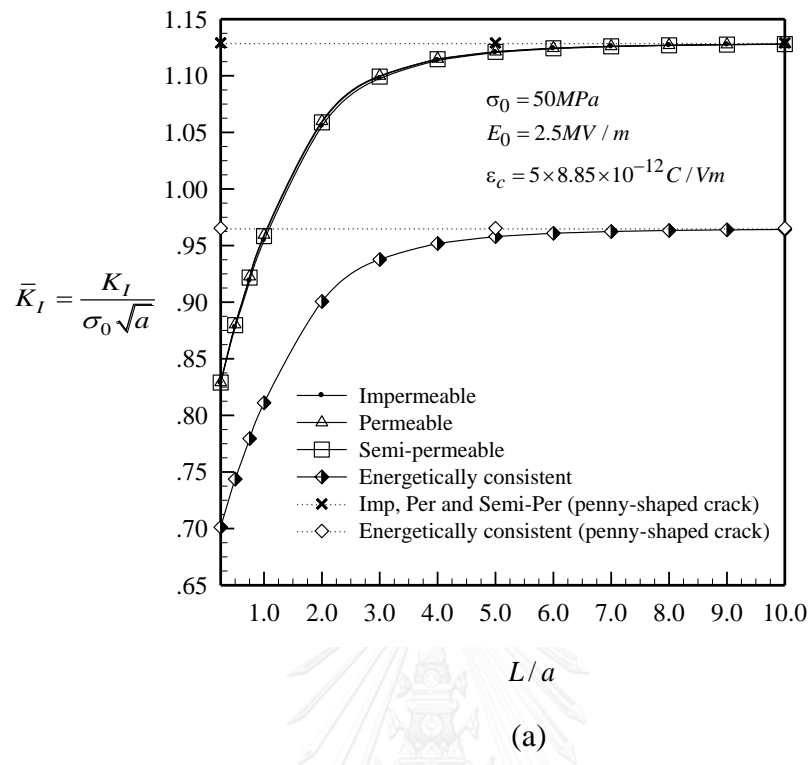
The influence of interacting of two penny-shaped cracks corresponding with L/a on the intensity factors along the crack front under four types of crack-face conditions are investigated. The normalized stress and electric intensity factors [K_I , K_{II} , K_{IV}] at the point on the crack front are reported in figure 4.16 (a), (b) and (c). It can be found that when the distance of two penny-shaped crack increase, the magnitude of the stress and electric intensity factors [K_I , K_{II} , K_{IV}] strongly dependent of the distance of the two cracks in the beginning range of distribution whereas the stress intensity factors K_{III} vanished. It can be discussed as follows:

The numerical results of stress intensity factors K_I reported in figure 4.16 (a) are obtained. It can be found that as the distance (L/a) increases, the four crack-face models strongly increase in the beginning. For example, the stress intensity K_I increasingly and identically drives the values at the range from $L/a=0.25$ to 4 at the three crack models (i.e., impermeable, permeable and semi-permeable models). This means that those three models are independent of boundary conditions and are

significantly distinct from the energetically consistent model by forming as higher magnitude throughout the range of distribution. It can be further explored that the pure penny-shaped crack is formed as the stress intensity factor with constant value which is significantly different from the two penny-shaped cracks of four crack-face boundary conditions. This implies that as the distance of the two cracks in vertical direction (x_3 -direction) increases, it has influence on the magnitude of four crack-face models

The stress intensity factor K_{II} reported in figure 4.16 (b) are investigated on four crack models (i.e., impermeable, permeable, semi-permeable and energetically consistent models). It can be found that as the distance of the two cracks increases, the magnitude of K_{II} strongly increases and are nearly identical at the range of distributions. Moreover, the convergence of four models is converged to penny-shaped crack. Besides, It can be investigated further that the energetically consistent model are greater than other three crack models (i.e., impermeable, permeable and semi-permeable models) at the range $L/a=0.25$ to 4 , whereas the magnitude of pure penny-shaped crack is constant and is greater than two penny-shaped crack model. Accordingly, it can be summarized that as the interacting of the two crack is large, it has an influence to the stress intensity factors K_{II} at the beginning of the range and the effect of the boundary conditions is small throughout distribution.

Finally, the electric intensity factor K_{IV} on four models reported in figure 4.16 (c) are obtained. It can be found that as the distance of the two crack increase, the four crack-face models (i.e., impermeable, permeable, semi-permeable and energetically consistent models) are completely different, and significantly increase in the beginning of the range. For example, the K_{IV} strongly drives the magnitude at the range $L/a=0.25$ to 4 and it is eventually converged to the pure penny-shaped cracks. Moreover, the impermeable model is formed as upper bound whereas the lower bound is formed as permeable model. In addition, it is assured that the results is correct by indicating that the four crack-face models are converged to pure penny-shaped crack. Overall, it can be summarized that as the distance of the two crack increases, it influences the values of electric intensity factors K_{IV} on four models in the beginning of distribution.



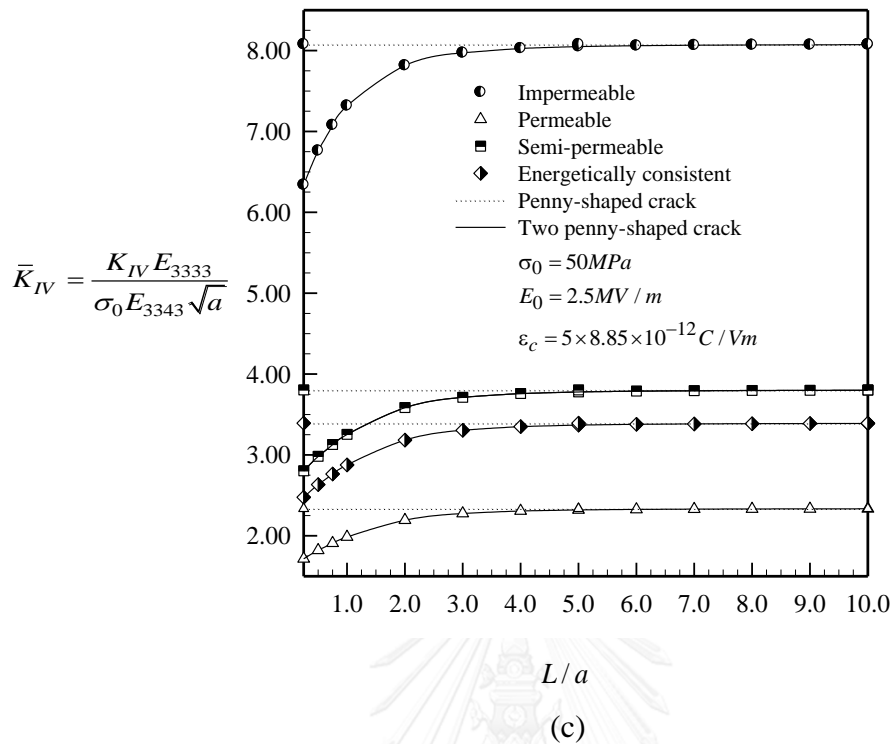


Figure 4.16 (a),(b) and (c) are dependent of normalized stress and electric intensity factors $[K_I, K_{II}, K_{IV}]$ on the interaction for two penny-shaped crack in infinite medium. Results are reported on a penny-shaped cracks

4.1.5 Interacting of two penny-shaped crack in horizontal directions

As for the last investigation we consider two identical penny-shaped cracks with radius a and the distance between the two cracks L , referred to as crack-A and crack-B, which are embedded in a transversely isotropic, piezoelectric infinite medium as indicated in figure 4.17. The material properties such as PZT-4 is utilized. In this final case, we utilize the mesh as 144 elements similar to previous case. The poling direction is identical to the symmetry axis of material of x_3 -axis. The parameters used in this investigation can be summarized as follow: (i) the distance between the two cracks L/a in horizontal direction is varied $[2.25, 2.5, 2.75, 3, 4, 5, \dots, 10]$, (ii) the radius of the cracks is utilized as 1, (iii) the remote uniaxial tension is fixed $\sigma_0 = 50$ MPa, (iv) the uniform electric field is fixed $E_0 = 2.5$ MV/m in the x_3 -direction, (v) and the dielectric permittivity inside the crack gap is fixed $\epsilon_c = 5\epsilon_0$ where $\epsilon_0 = 8.85 \times 10^{-12}$ C/Vm is the permittivity of the air in the crack gap.

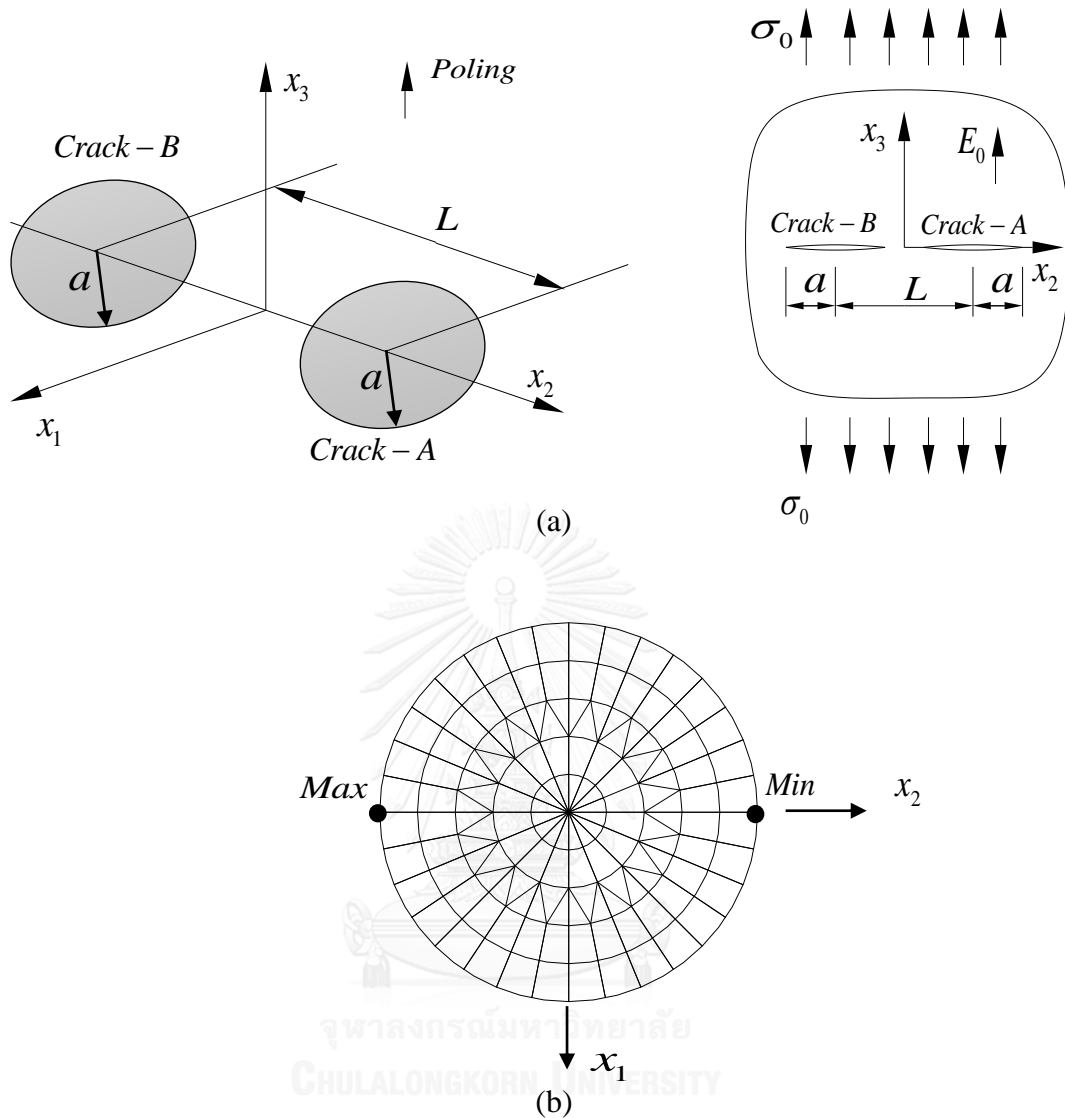


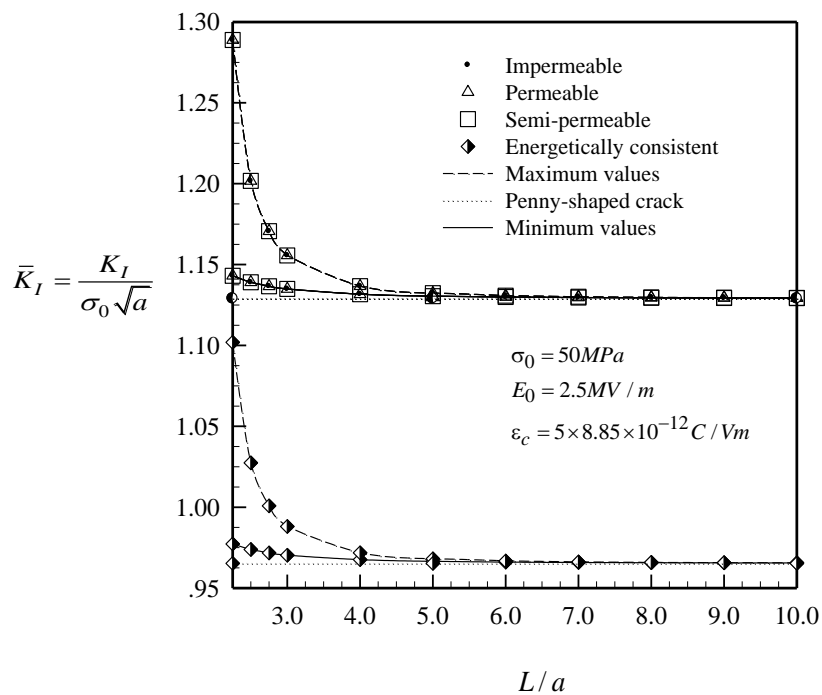
Figure 4.17 (a) Schematic of two penny-shaped cracks in horizontal direction in a piezoelectric infinite medium and (b) are the meshes for one penny-shaped crack that utilized for the investigation

To explore the influence of the interaction between the two penny-shaped cracks corresponding with L/a , the intensity factors along the crack front under four crack-face models are investigated at two different points (i.e., maximum and minimum values) as reported in the figure 4.18 (a) and (b) respectively. Results indicate that as the distance of the two cracks in horizontal direction increases, the values of stress and electric intensity factors $[K_I, K_{IV}]$ tend to decrease. This can be discussed as follows:

The numerical results reported in figure 4.18 (a) are obtained from four crack-face models (i.e., impermeable, permeable, semi-permeable and energetically consistent models). It can be found that as the distance of the two crack increases, the stress intensity factor K_I are strongly decreased at the two points (i.e., maximum and minimum values) providing that the distance L/a is relative small at the range $L/a =$

0.25 to $L/a = 5$. On the other hand, the value of K_I are constant when the distance of the two cracks remains sufficiently large. Moreover, the three models (i.e., impermeable, permeable and semi-permeable models) at two positions are completely identical whereas the energetically consistent models at the two positions are clearly less than those three models. This can be concluded that as the distance increases, it has an influence to the values of K_I at the two positions (i.e., maximum and minimum values).

Eventually, results of electric intensity factors K_{IV} obtained from two different points (e.g., maximum and minimum points) on four crack-face models are shown in figure 4.18 (b). It can be found that as the distance of the two crack increases, the electric intensity factors K_{IV} of four crack-face models (i.e., impermeable, permeable, semi-permeable and energetically consistent models) are completely different. On the other hand, they are strongly decreased when the distance of the two cracks remains small at the range $L/a = 0.25$ to $L/a = 2$. Moreover, the bounds of four crack-face models are not changed which means that the impermeable model serves as upper bound whereas the permeable model serves as lower bound. This implies that it influences the four boundary conditions when the distance L/a increases.



(a)

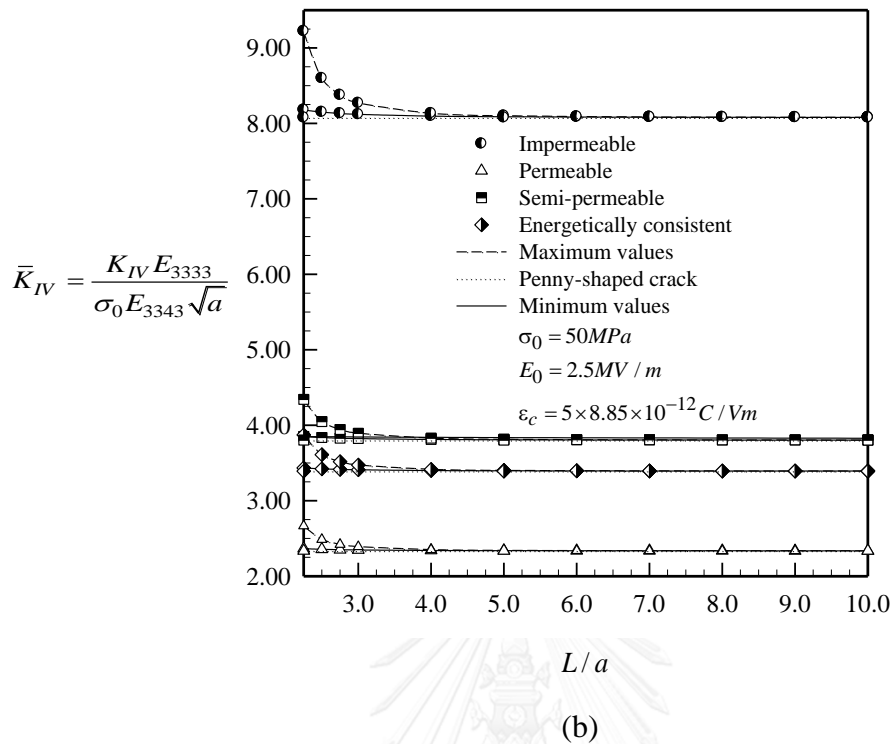


Figure 4.18 (a) and (b) are dependent of normalized stress and electric intensity factors $[K_I, K_{IV}]$ on the interaction for two penny-shaped crack in infinite medium. Results are reported on the maximum and minimum values and planar crack along the crack front

4.2 Influence of remote tensile mechanical load on four crack-face boundary conditions

In this section, the influence of mechanical load is investigated to obtain the stress and electric intensity factors along the crack front. Both planar and non-planar cracks are utilized by using the fine mesh that have verified in the convergence section. The results from those cracks will be carried out in the following sections

4.2.1 Influence of remote tensile mechanical load on spherical cap and cylindrical crack

The two non-planar crack such as spherical cap cracks are employed to study the influence of mechanical load on intensity factors along the crack front. Each crack will be implemented in the following.

4.2.1.1 Influence of remote tensile mechanical load on spherical cap crack

We consider a spherical cap crack embedded in a transversely isotropic piezoelectric infinite medium. The crack geometry and the material properties of piezoelectric medium are similar to those diagnosed in the section 4.1.1.1; However, the key

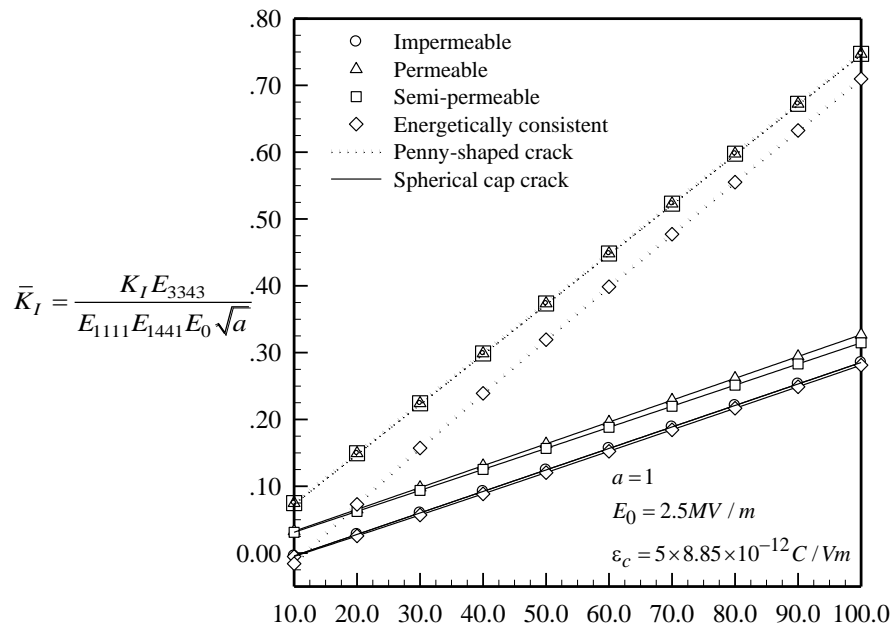
differences from the previous case are that (i) the half subtended angle of the surface (θ) is fixed as 45 degree, (ii) the applied uniaxial remote stress is varied from [10,20,30,..., 100] MPa, (iii) The applied electric field E_0 is fixed at 2.5 MV/m which is identical as that of the previous example, and (iv) the dielectric permittivity inside the crack gap is fixed $\varepsilon_c = 5\varepsilon_0$ where $\varepsilon_0 = 8.85 \times 10^{-12}$ C/Vm is the permittivity of the air in the crack gap. Numerical results of intensity factors computed from the fine mesh 144 elements (see Figure. 4.1) are reported in figures. 4.19 (a), (b) and (c) respectively. It is found that the increasing mechanical load σ_0 tends to increase the magnitude of the stress and electric intensity factors [K_I, K_{II}, K_{IV}], for all crack-face models. In addition, the rate of increase of K_{II} is more rapid than that two models and this can be discussed as follows.

Figure 4.19(a) shows that, as the mechanical load increases, K_I of the permeable models is the upper bound whereas the energetically consistent models are the lower bound and nearly identical to impermeable models. Moreover, it can be found that the stress intensity factor K_I of the semi-permeable crack varies from the same point of the permeable models when the mechanical load is relatively small and it gradually shows the difference as the applied remote stress increases. However, it should be noted again that, when the applied mechanical stress is small, the stress intensity factor K_I of the energetically consistent models is nearly identical to the impermeable model. Besides, it can be observed further that when the applied mechanical load increases, the three models (i.e., impermeable, permeable, semi-permeable models) of planar crack are completely identical which is significantly different from spherical cap crack and those three models serve as upper bound, whereas the energetically consistent model are obviously less than those three models and serves as lower bound. This can be concluded that when the mechanical load increases, the K_I of both planar and non-planar cracks become clearly different as discussed above.

The results of a non-planar crack upon the stress intensity factor K_{II} can be described in figures 4.19 (b). We found that the increasing applied mechanical load tends to increase the magnitude of the stress intensity factor K_{II} whereas the planar crack is obviously vanished. Furthermore, the stress intensity factor K_{II} under four models of electrical boundary conditions (i.e., impermeable, permeable, semi-permeable and energetically consistent models) is not identical. It can be observed further that the upper bound serves as impermeable models while the energetically consistent as lower bound. In addition, when the mechanical load is small, the semi-permeable and permeable models are nearly identical but the permeable model is converged to the energetically consistent models when the mechanical load is sufficiently large. It can be conclude that the increasing applied mechanical load has an influence only to permeable model.

Finally, the result of non-planar crack on the intensity factor K_{IV} on four models can be reported in figures 4.19 (c). It is found that when the applied mechanical load increases, the electrical intensity factors K_{IV} tend to increase as well. Moreover, the impermeable model is the upper bound of the entire range, whereas the lower bound is switched of energetically consistent and permeable models corresponding to turning point at $\sigma_0 = 30$ MPa (as the turning point of planar crack occurred at $\sigma_0 = 20$ MPa). However, when the applied mechanical is sufficiently large, it can be observed further that K_{IV} of both the semi-permeable and energetically consistent models share identical trends and approach to the impermeable model. It can be summarized that the turning

points of both planar and non-planar cracks (the penny-shaped and the spherical cap cracks) of lower bounds are completely different whereas the trends of both cracks are nearly identical.



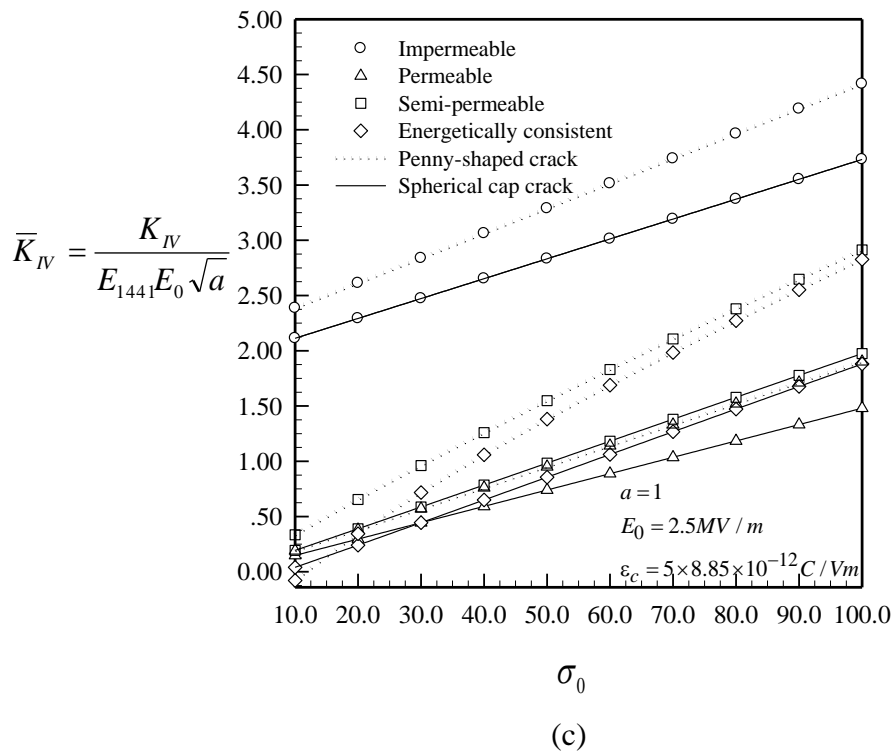
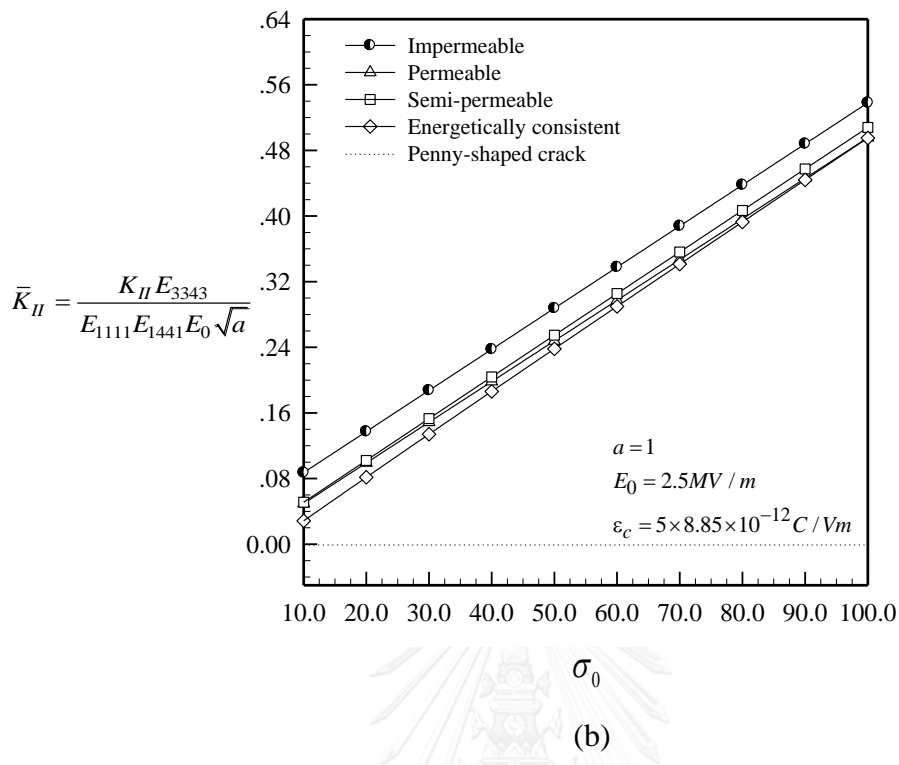
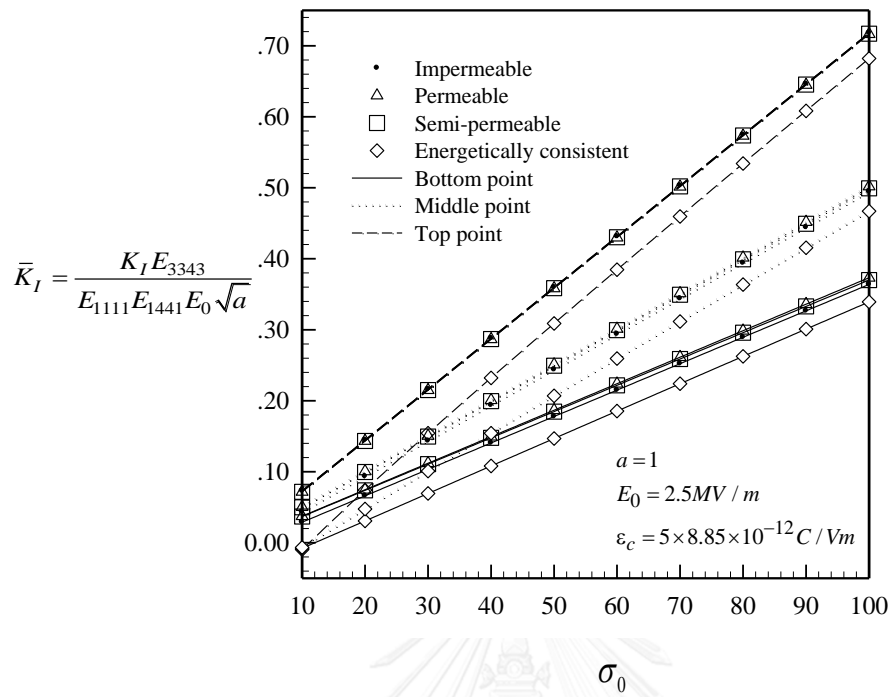


Figure 4.19 (a), (b) and (c) are dependent of normalized stress and electric intensity factors $[K_I, K_{II}, K_{IV}]$ on the mechanical load for spherical cap crack in infinite medium. Results are reported as average values

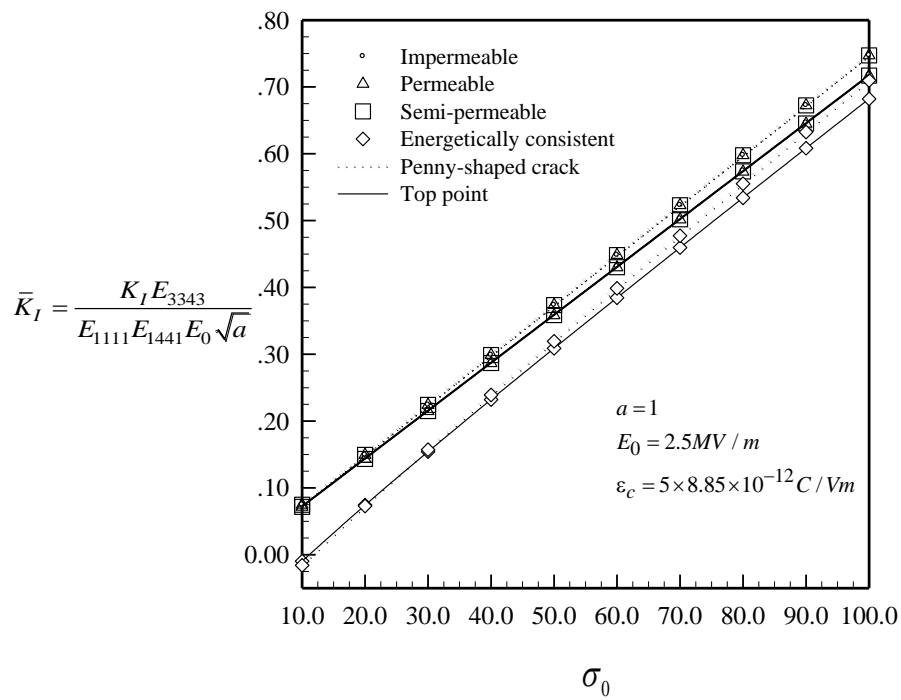
4.2.1.2 Influence of remote tensile mechanical load on cylindrical crack

As an example of non-planar cracks, we consider a cylindrical crack containing in a transversely isotropic piezoelectric infinite medium. The crack geometry and the material properties of piezoelectric medium are similar as those diagnosed in the previous sections 4.1.1.2. However, the key differences from the previous case are similar to those of spherical cap crack and this would be explained as follows, (i) the half subtended angle of the surface θ is fixed as 45 degree, (ii) the applied uniaxial remote stress is varied from [10,20,30,..., 100] MPa, (iii) the applied electric field E_0 is fixed at 2.5 MV/m which is identical as that of the previous example, and (iv) and the dielectric permittivity inside the crack gap is fixed $\varepsilon_c = 5\varepsilon_0$ where $\varepsilon_0 = 8.85 \times 10^{-12}$ C/Vm is the permittivity of the air in the crack gap. Numerical results of intensity factors computed from the fine mesh 144 elements (see Figure. 4.1) are obtained from three different points (i.e., top, middle and bottom points) reported in figures. 4.20 (a), 4.21 (a), 4.22 and 4.3(a) respectively. It can be found that the increasing mechanical load σ_0 leads to the increase of the magnitude of the stress and electric intensity factors $[K_I, K_{II}, K_{IV}]$ for all three points except the K_{III} , K_{II} of middle points and the top point respectively, and this can be discussed below.

Figure 4.20 (b), (c) and (d) shows that, as the mechanical load increase, K_I of all points are clearly less than the penny-shaped crack. The upper bounds of top point serve as three models (i.e., impermeable, permeable and semi-permeable models) similar to the penny-shaped crack, at both middle and bottom point they serve as permeable. It can be found that the lower bounds of three distinct points and planar crack are completely and identically formed as the energetically consistent. Moreover, the stress intensity factor K_I of the three models (i.e., impermeable, permeable and semi-permeable models) is completely identical and analogous to those models of planar crack, whereas only K_I of the semi-permeable and permeable are nearly identical at both top and bottom points. However, it should be noted again that, when the applied mechanical stress is small, the stress intensity factor K_I at the bottom point of the permeable and semi-permeable models is nearly identical and shows the difference as the mechanical load increases. This can be concluded that when the mechanical load increases, the K_I of both planar cracks are the same as the top point and are strongly different at both middle and bottom points as discussed above.



(a)



(b)

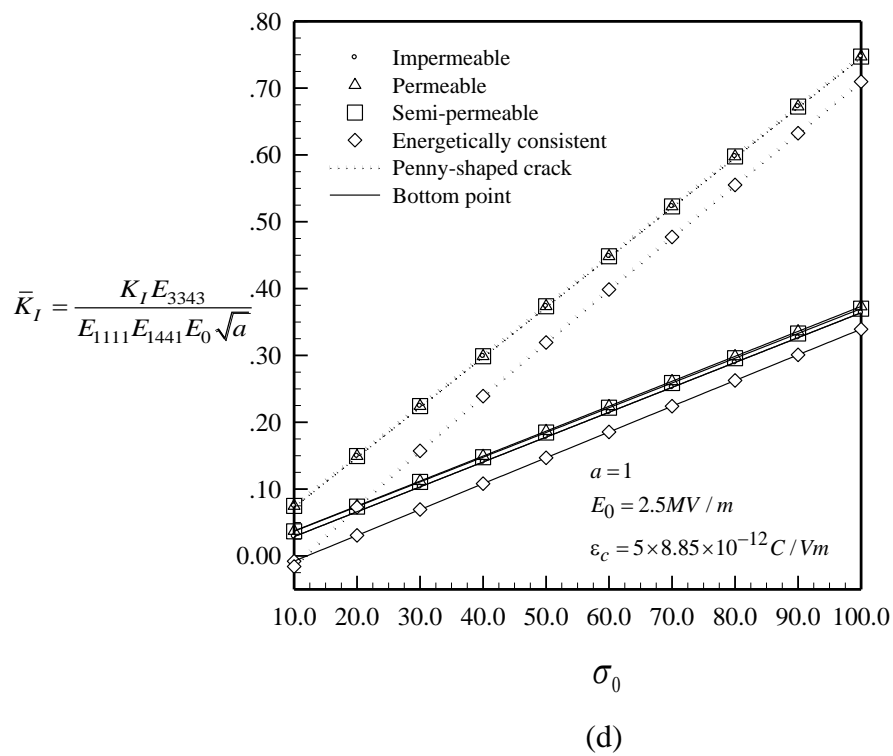
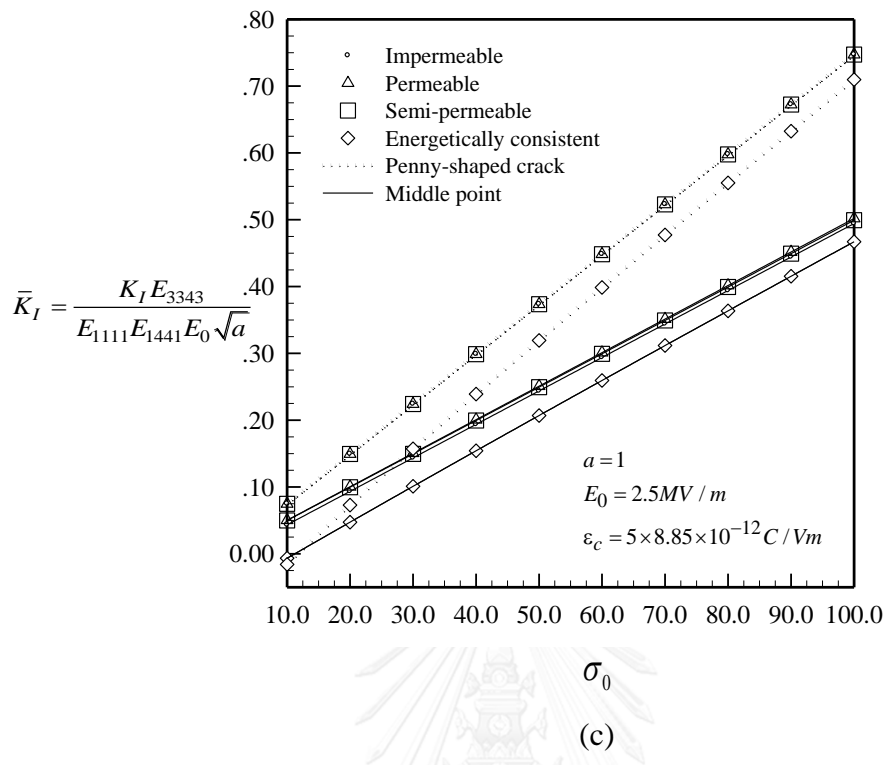
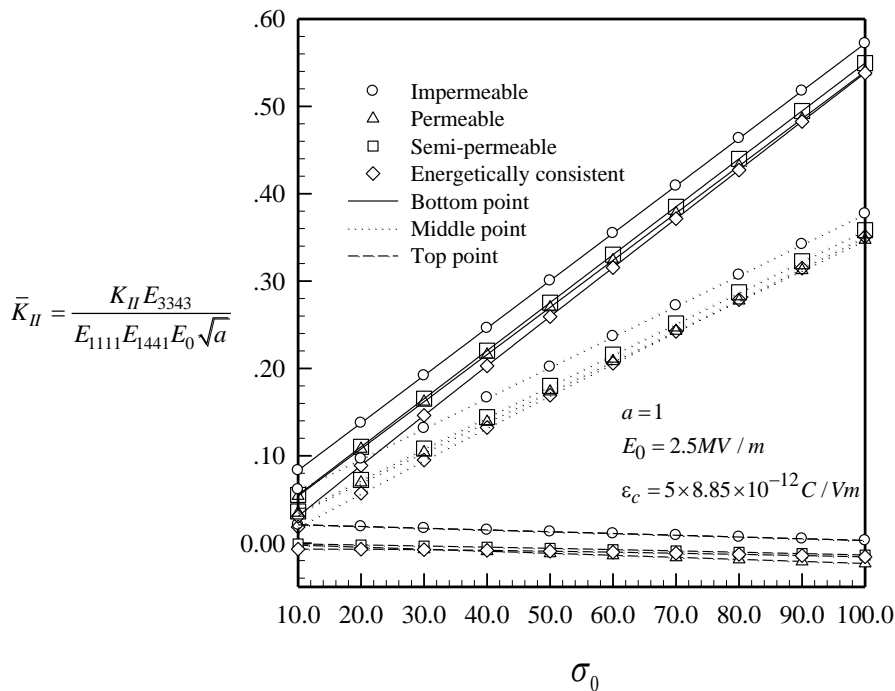
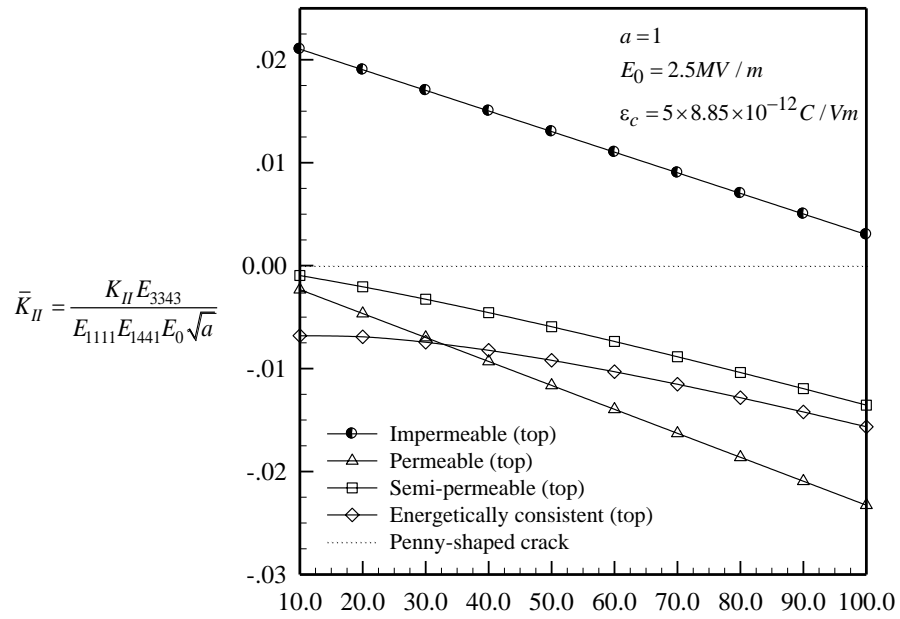


Figure 4.20 Dependent of normalized stress intensity factors [K_I] on the mechanical load for cylindrical crack in infinite medium. Results are reported on values

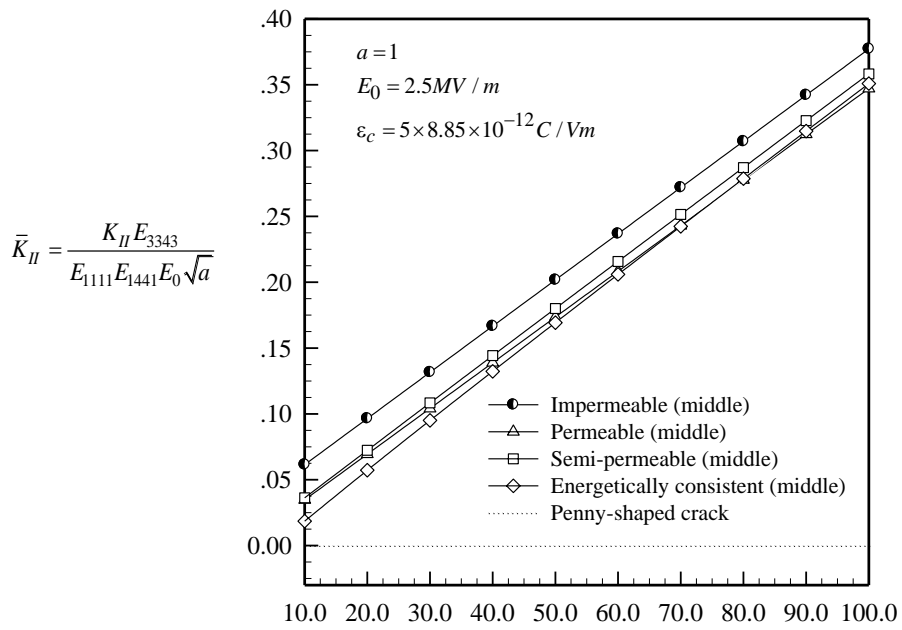
The results of a non-planar crack on the stress intensity factor K_{II} on four models (i.e., impermeable, permeable, semi-permeable and energetically consistent models) can be explained in figures 4.21 (b), (c) and (d). It can be found that when the applied mechanical load increases, the K_{II} have a tendency to increase the magnitude only at both middle and bottom points while the K_{II} at the top point decrease as the planar crack is clearly vanished. Furthermore, the stress intensity factor K_{II} of three different points under four models of electrical boundary conditions (i.e., impermeable, permeable, semi-permeable and energetically consistent models) are completely different. It can be observed further that the upper bounds of K_{II} at any points are formed as impermeable and, again, only the lower bound of the top bottom point are energetically consistent models. In contrast, the lower bounds of both the top and bottom points is switched of energetically consistent and permeable model corresponding to the turning point at $\sigma_0 = 30$ MPa and $\sigma_0 = 70$ MPa respectively. In addition, when the mechanical load is small, the permeable models strongly approach the energetically at the top and middle points, which is clearly distinct from the bottom point. It can be conclude that when the mechanical load increases, it has influence to the lower bounds of the top and bottom points and to the magnitude of K_{II} at three points.



(a)



(b)



(c)

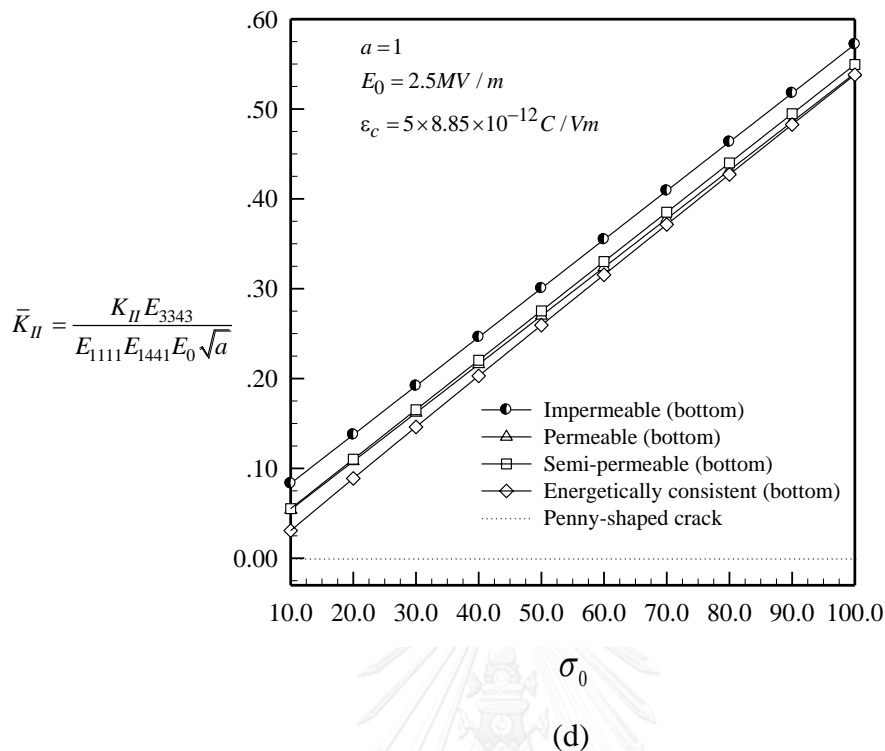


Figure 4.21 Dependent of normalized stress intensity factors $[K_{II}]$ on the mechanical load for cylindrical crack in infinite medium. Results are reported on (a) all points, (b) top, (c) middle and (d) bottom points

Next, the numerical results of a non-planar crack upon the maximum of the stress intensity factor K_{III} only at a middle point (a point along middle zone between the top and bottom point) under four models are obtained as reported in figure 4.22. It can be found that the increasing applied mechanical load leads to the decrease of the magnitude of the stress intensity factor K_{III} whereas the planar crack is vanished. Moreover, the stress intensity factor K_{III} under four models of electrical boundary conditions (i.e., impermeable, permeable, semi-permeable and energetically consistent models) is completely different. It can be investigated further that the upper bound is impermeable models while the permeable model serves as lower bound. Besides, as the mechanical load increase, the semi-permeable and energetically models share nearly identical trend. To be more precise, the semi-permeable model varies from the point near the permeable model at the beginning and approaches the energetically consistent model when the mechanical load is sufficiently large. It can be conclude that the increasing applied mechanical load has only the values of the stress intensity factors

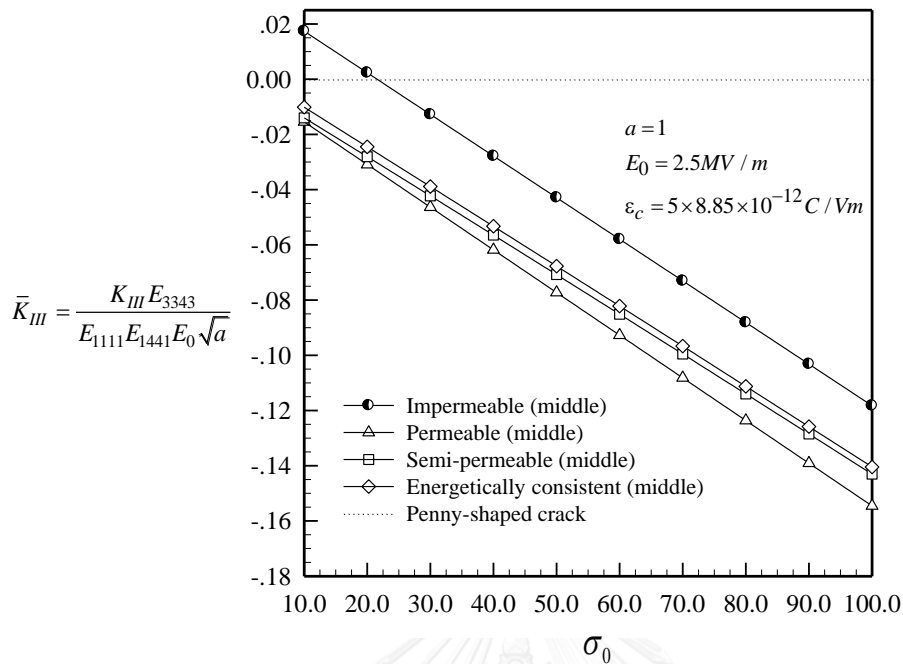
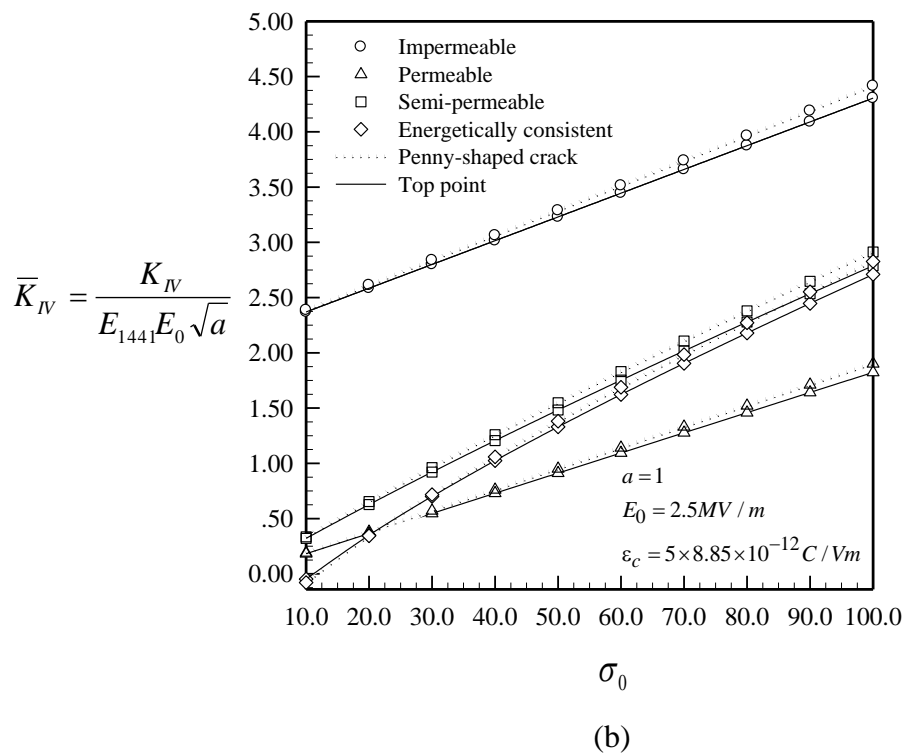
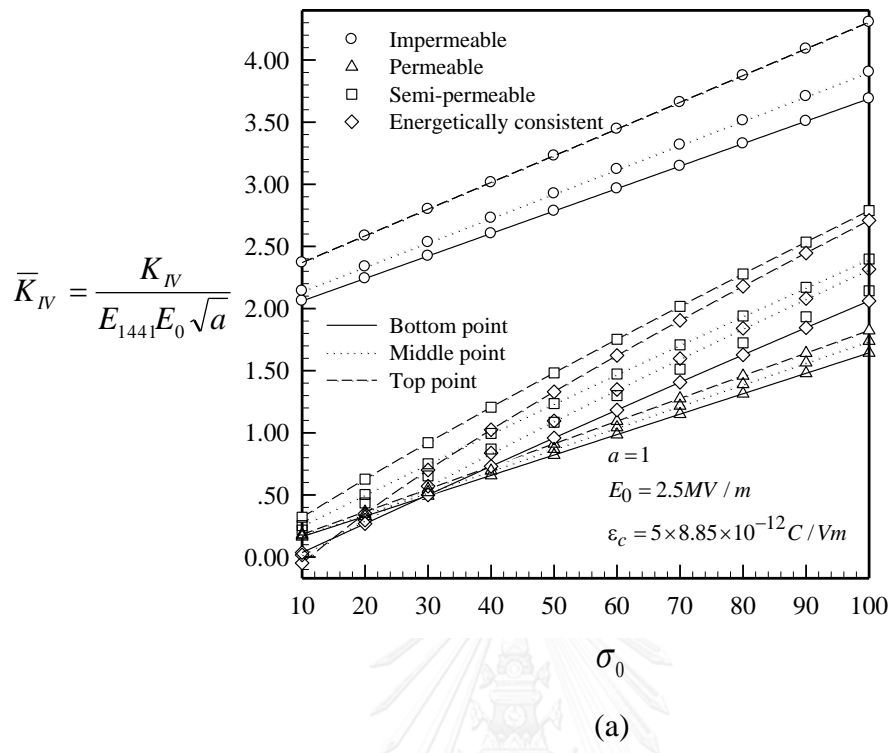


Figure 4.22 Dependent of normalized stress intensity factors $[K_{III}]$ on the mechanical load for cylindrical crack in infinite medium. Results are reported on the middle point

Finally, the effect of a non-planar crack on the electric intensity factor K_{IV} of three different points (i.e., top, middle and bottom points) under four models can be reported in figures 4.23 (c). It is found that when the applied mechanical load increases, the electrical intensity factors K_{IV} of three different points tends to increase but still significantly less than the magnitude of planar crack. Moreover, the impermeable models are upper bounds for the all points whereas the lower bound is switched of energetically consistent and permeable models corresponding to turning points such as at $\sigma_0 = 20 \text{ MPa}$, $\sigma_0 = 30 \text{ MPa}$ for the top and middle point respectively (as the turning point of planar crack occurs at $\sigma_0 = 20 \text{ MPa}$). In addition, when the applied mechanical is sufficiently large, K_{IV} at all points (i.e., top, middle and bottom points) of the semi-permeable and energetically consistent models share nearly identical trends and approach the impermeable model. It can be summarized that as the mechanical load increases, the turning points of lower bound of both planar and non-planar cracks are once again different at the middle and bottom points, except at the top point where the values remain the same.



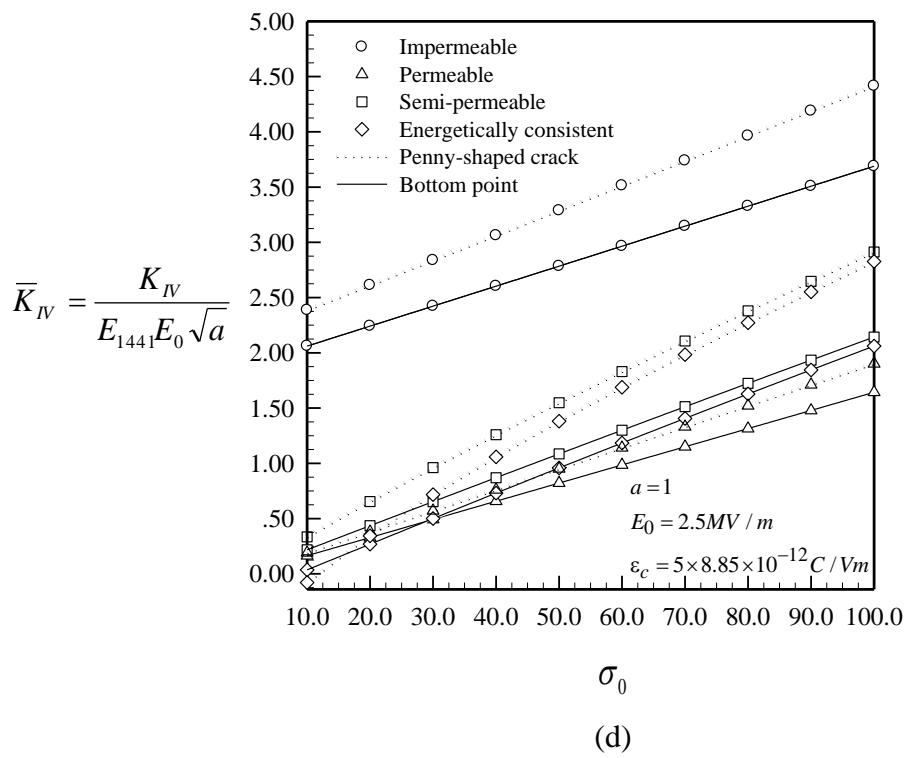
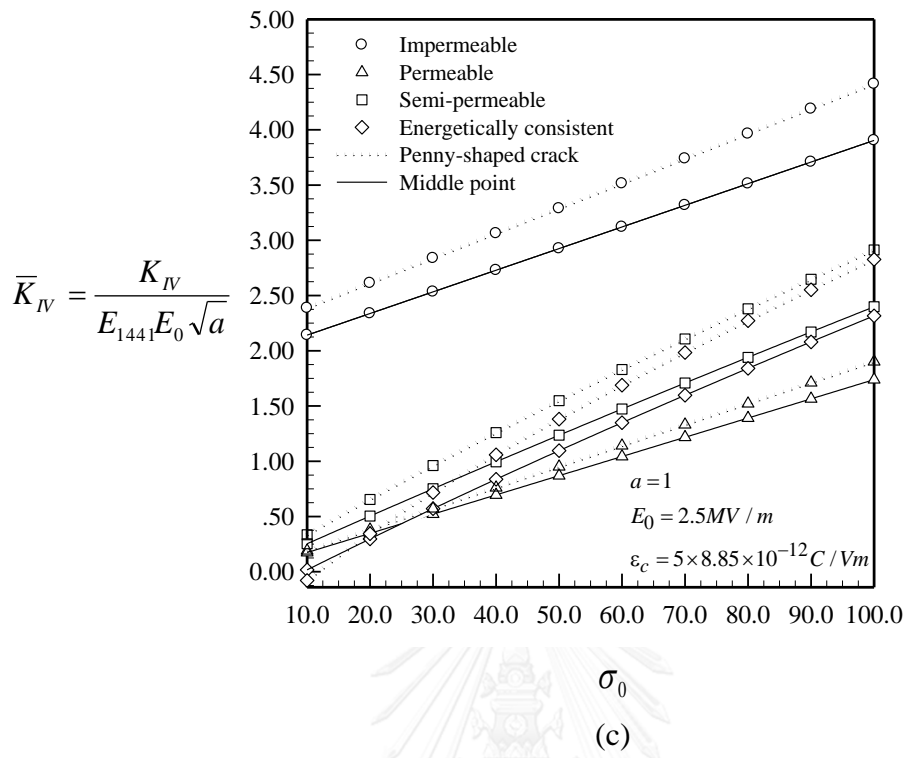


Figure 4.23 Dependent of normalized electric intensity factors $[K_{IV}]$ on the mechanical load for cylindrical crack in infinite medium. Results are reported on (a) all points, (b) top, (c) middle and (d) bottom points

4.2.1.3 Comparison between spherical cap crack and cylinder crack

From the above discussion, when the mechanical load increases from [10,20,30,.....,100] MPa, the difference and the similarity of the numerical results of intensity factor [$K_I, K_{II}, K_{III}, K_{IV}$] obtained from both spherical cap and cylindrical cracks can be concluded as follows:

The numerical results of the spherical cap crack utilized for investigations the influence of applied tensile mechanical load can be summarized as follow. It is seen that when the mechanical load increases, the magnitude of K_I on four crack models for spherical cap crack and the penny-shaped crack become different. While K_I of three models (i.e., impermeable, permeable and semi-permeable models) are identical for penny-shaped crack, the stress intensity factors K_I of three models are different for spherical cap crack. Accordingly, the curvature of non-planar crack indicates the dependent of electric field on stress intensity factor K_I . In contrast, the electric field has no influence to K_I for the penny-shaped crack in three models but has influence to the energetically consistent model. Given the stress intensity factors K_I obtained from other non-planar cracks (i.e., cylindrical crack) at three different points (i.e., top, middle and bottom points), it can be found that when the mechanical load increases, all the behaviors and trends are very identical analogous to the spherical cap crack only at the bottom points. In addition to this similarity of the both cracks (i.e., spherical cap and cylindrical cracks on the bottom point), the magnitude of K_I on four models at the top point are greater than the magnitude of K_I at the rest points. Moreover, the three models (i.e., impermeable, permeable and semi-permeable models) of cylindrical crack only at the top points are completely identical similar to those three models of penny-shaped crack. Nevertheless, the three models are still different at both middle and bottom point. It can be concluded that the three models become outstanding when the stress intensity factors are considered at bottom point, whereas the behavior of K_I is the same as penny-shaped crack at the bottom point.

The stress intensity factors K_{II} of spherical cap crack firstly illustrate results. It can be found that when the applied mechanical load increases, the magnitude of four models (i.e., impermeable, permeable, semi-permeable and energetically consistent models) also increases and depends on the mechanical load, whereas the planar crack is vanished. Furthermore, the stress intensity factor K_{II} under those four models is completely different. It can be further observed that the upper bound is impermeable model while the energetically consistent serves as lower bound. In addition, when the mechanical load is small, the semi-permeable and permeable models are nearly identical whereas they are converged to the energetically consistent models when the mechanical load is sufficiently large. Identically, the stress intensity factors K_{II} obtained from the cylindrical crack at three different points (i.e., top, middle and bottom points) are proposed to compare the K_{II} of spherical cap crack. When the mechanical load increases, the magnitude of K_{II} are completely different for all points. Furthermore, the stress intensity factor K_{II} of the bottom point under four models exhibits a strongly identical behavior to that of the spherical cap crack. Apart from the identical behavior of both cracks, the upper bounds of K_{II} at any points are formed as impermeable and, once again, only the lower bounds of the top bottom point are energetically consistent models. On the contrary, the lower bounds of both the top and bottom points are switched of energetically consistent and permeable model. In addition, it can be found that when the mechanical load is small, the permeable models strongly approach the

energetically at the top and middle points which is nevertheless clearly distinct from the bottom point.

The different point between spherical cap crack and cylindrical crack is the stress intensity factor K_{III} in which the cylindrical crack appears only the middle point (a point of the middle zone is located between the top and bottom points). It can be concluded that when the crack mechanical load increases, the magnitude of four models are completely different as they decrease the magnitude. Moreover, the semi-permeable model varies from permeable to energetically consistent model and their bounds, such as upper and lower bound serve as impermeable and permeable respectively.

Finally, the results of the spherical cap crack can be summarized as follows. When the applied mechanical load increases, the electrical intensity factors K_{IV} tends to increase, and the magnitude with higher slope of penny-shaped crack are greater than that of spherical cap crack. Moreover, the impermeable models of both cracks (i.e., planar and non-planar cracks) are always the upper bound whereas the lower bounds similarly are always switched of energetically consistent and permeable models for the entire range. Furthermore, when the applied mechanical increases, K_{IV} of the semi-permeable and energetically consistent models of both cracks, i.e., spherical cap and penny-shaped cracks, shares nearly identical trends. However, those two models approach to the impermeable model for penny-shaped crack whereas they are parallel to impermeable model. Identically, the electric intensity factor K_{IV} obtained from the cylindrical crack is offered to correlate the spherical cap crack and to be versus with planar crack. With the increasing mechanical load, the trend of electrical intensity factors K_{IV} of three different points are different by increasing the magnitude and are also less than the magnitude of penny-shaped crack. Moreover, the behaviors of spherical cap crack are identical to that of cylindrical crack at the top point. In addition to the parity of both cracks, the impermeable models are always upper bounds for the all points and analogous to both spherical cap and penny-shaped crack, whereas the lower bounds are the same for both cracks (i.e., spherical cap and penny-shaped cracks) by switching of energetically consistent and permeable models. In addition, as the crack subtended angle increases, the lower bound of the top point is permeable model which is different from the rest of the points. Besides, the convergence of both semi-permeable and energetically consistent of three different points is the strongest at the top point, which is similar to planar crack.

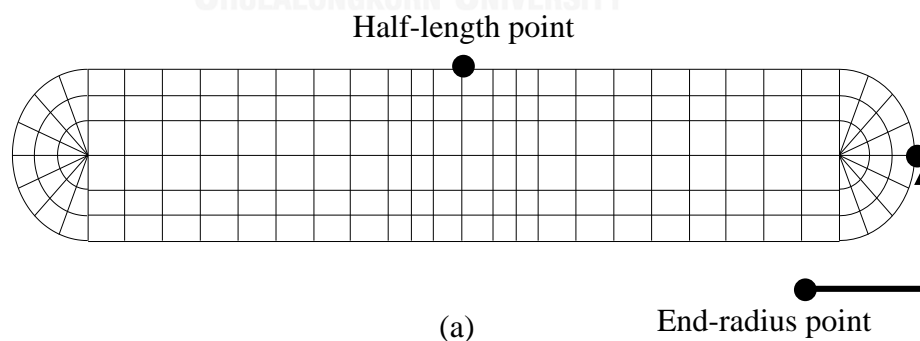
4.2.2 Influence of remote tensile mechanical load on tunnel crack

In this case, we consider a tunnel crack embedded in a transversely isotropic piezoelectric infinite medium. The crack geometry and the material properties of piezoelectric medium are analogous to the section 4.1.3. Nevertheless, the major differences from the previous case are that (i) the radius of end-radius and the half-length are fixed as 1 and 5, respectively (ii) the applied uniaxial remote stress is varied from [10,20,30,..., 100] MPa, (iii) the applied electric field E_0 is fixed at 2.5 MV/m which is similar to that of the previous section, and (iv) the dielectric permittivity inside the crack gap is fixed $\varepsilon_c = 5\varepsilon_0$ where $\varepsilon_0 = 8.85 \times 10^{-12}$ C/Vm is the permittivity of the air in the crack gap. Numerical results of non-zero intensity factors at two different points, i.e., at the end-radius and the half-length points (see figure 4.24 (a)), treated from the fine mesh 180 elements are reported in figures 4.24 (b) and (c) respectively. It

is found that the increasing mechanical load σ_0 has a tendency to increase the magnitude of the stress and electric intensity factors $[K_I, K_{IV}]$, for all crack models. In addition, the rate of increase of $[K_I, K_{IV}]$ at half-length point is more rapid than at the radius point and this can be discussed as follows:

Figure 4.24(b) indicates that, when the mechanical load increases, the stress intensity factor K_I of end-radius point are significantly less than the values of half-length point. Moreover, the K_I of three models (i.e., impermeable, permeable and semi-permeable models) are nearly identical for the all points and form as upper bound, whereas the lower bound is energetically consistent model. Moreover, the stress intensity factor K_I of the energetically consistent model approaches those three models. This can be concluded that as the mechanical load increases, it has influence only to the magnitude of stress intensity factors.

Finally, the numerical result of planar crack on the intensity factor K_{IV} on four models can be reported in figures 4.24 (c). It can be found that when the applied mechanical load increases, the electrical intensity factors K_{IV} of two different points (i.e., end-radius and half-length points) lead to the increase of the magnitude. For both points, the impermeable model is upper bound whereas the lower bound is switched of energetically consistent and permeable models corresponding to turning point at $\sigma_0 = 30 \text{ MPa}$. Once again, it can be found that when the applied mechanical is sufficiently large, K_{IV} of the semi-permeable and energetically consistent models share nearly identical trends for every point and approach the impermeable model. It can be summarized that the increasing mechanical loads has an influence to the magnitude and the lower bound of stress intensity factors K_{IV} .



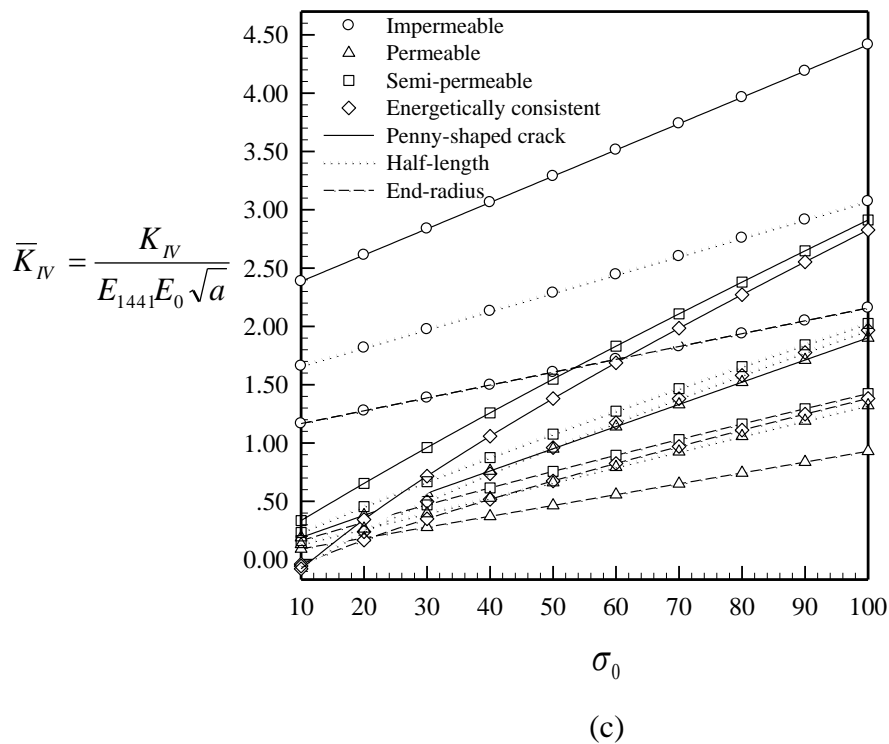
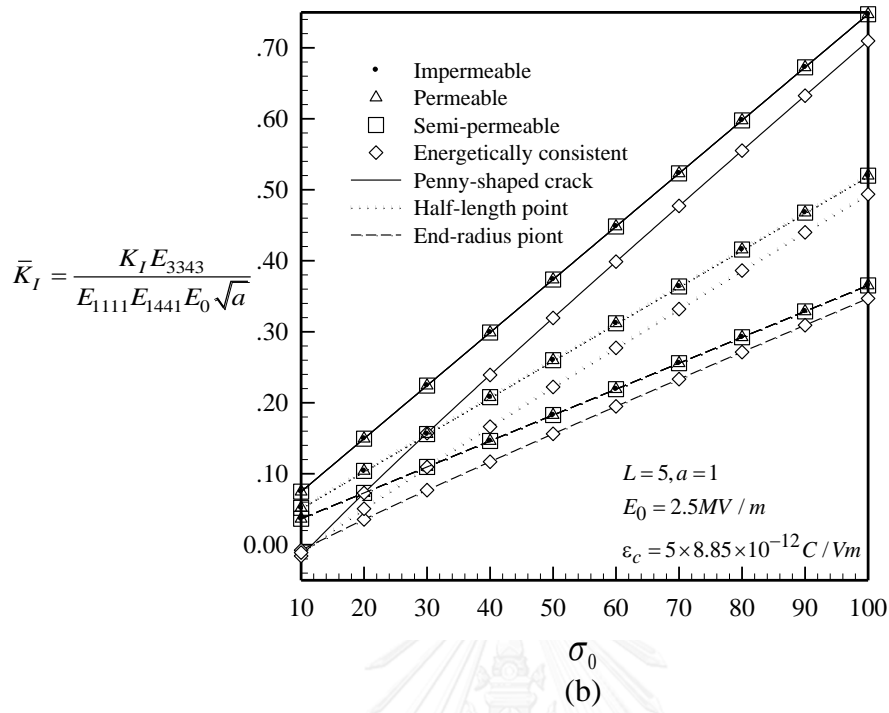


Figure 4.24 (a) the positions at end-radius and half-length points, (b) and (c) are dependent of normalized stress and electric intensity factors $[K_I, K_{IV}]$ on the mechanical load for a tunnel crack in infinite medium. Results are reported on the end-radius and half-length points

4.2.3 Influence of remote tensile mechanical load on a pair of penny-shaped crack

The two penny-shaped crack in vertical and horizontal directions are provided to conduct the influence of remote mechanical load which can be implement in the next sections.

4.2.3.1 Influence of remote tensile mechanical load on two penny-shaped crack in vertical direction

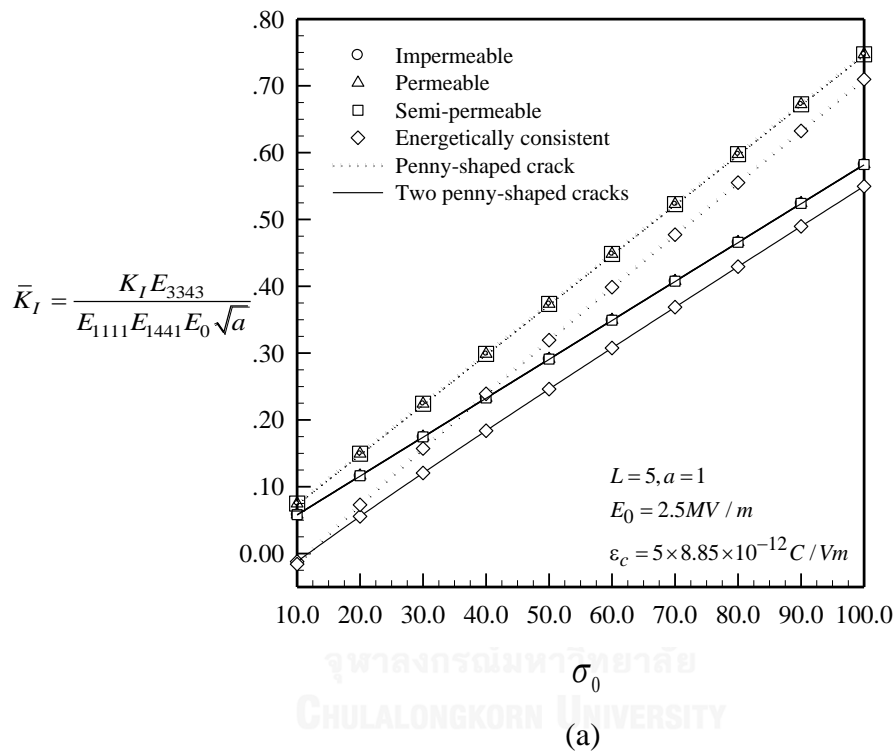
For the next investigation, we consider a two penny-shaped crack in vertical direction containing in a transversely isotropic piezoelectric infinite medium. The crack geometry and the material properties of piezoelectric medium are analogous to the section 4.1.4. The major differences of the parameter compared to that from the previous case are that (i) the radius and the vertical distance of two penny-shaped crack are fixed as 1 and 0.5 respectively (ii) the applied uniaxial remote stress is varied from [10,20,30,..., 100] MPa, (iii) the applied electric field E_0 is fixed at 2.5 MV/m which is similar to that of the previous section, and (iv) the dielectric permittivity inside the crack gap is fixed $\varepsilon_c = 5\varepsilon_0$ where $\varepsilon_0 = 8.85 \times 10^{-12}$ C/Vm is the permittivity of the air in the crack gap. The results of non-zero intensity factors along the crack front treated from the fine mesh 144 elements per crack are reported in figures. 4.25 (a) and (b) respectively. It can be found that as the mechanical load increases, σ_0 again tends to increase the magnitude of the stress and electric intensity factors [K_I , K_{IV}]. The rate of increase of [K_I , K_{IV}] can be discussed as follows:

Figure 4.25(a) shows that when the mechanical load increases, the stress intensity factor K_I under four crack models (i.e., impermeable, permeable, semi-permeable and energetically consistent models) also increases. Again, it is found that the trend of two penny-shaped cracks are nearly identical to that of the single penny-shaped crack but the slope of magnitude are less than one. Moreover, the K_I of three models (i.e., impermeable, permeable and semi-permeable models) are also nearly identical throughout the range of distribution and those three model serve as upper bound whereas the lower bound is expressly energetically consistent model. In addition, the stress intensity factor K_I of the energetically consistent model again approaches to those three models. This can be concluded that when the mechanical load increases, it has influence only to the magnitude of stress intensity factors.

Results from figure 4.25 (b) indicate that when the distance of the two cracks is small, the stress intensity factor K_{II} are appeared. It is manifested that when the mechanical load increase, the four models tend to decrease. Moreover, K_{II} of impermeable, permeable and semi-permeable models are nearly identical and serve as lower bound whereas the energetically consistent model approaches to those three models and also serve as upper bound at the entire range of distribution.

Eventually, the intensity factor K_{IV} on four models obtained from four models are shown in figures 4.25 (c). It is found that when the applied mechanical load increases, the magnitude and the trend of the electrical intensity factors K_{IV} are nearly identical but the behavior of four models are clearly different. Moreover, the

impermeable model serves as upper bound whereas the lower bound is switched of energetically consistent and permeable models corresponding to turning point at $\sigma_0 = 20$ MPa which is similar to other planar cracks. In addition, with the increase of the applied mechanical load, K_{IV} of the semi-permeable and energetically consistent models of two penny-shaped cracks are nearly identical behavior which is the same as the single penny-shaped crack, and those two models tend to approach the impermeable model. It can be summarized that the increasing mechanical load has an influence to both the magnitude and the lower bound of stress intensity factors K_{IV} , similar to other planar cracks.



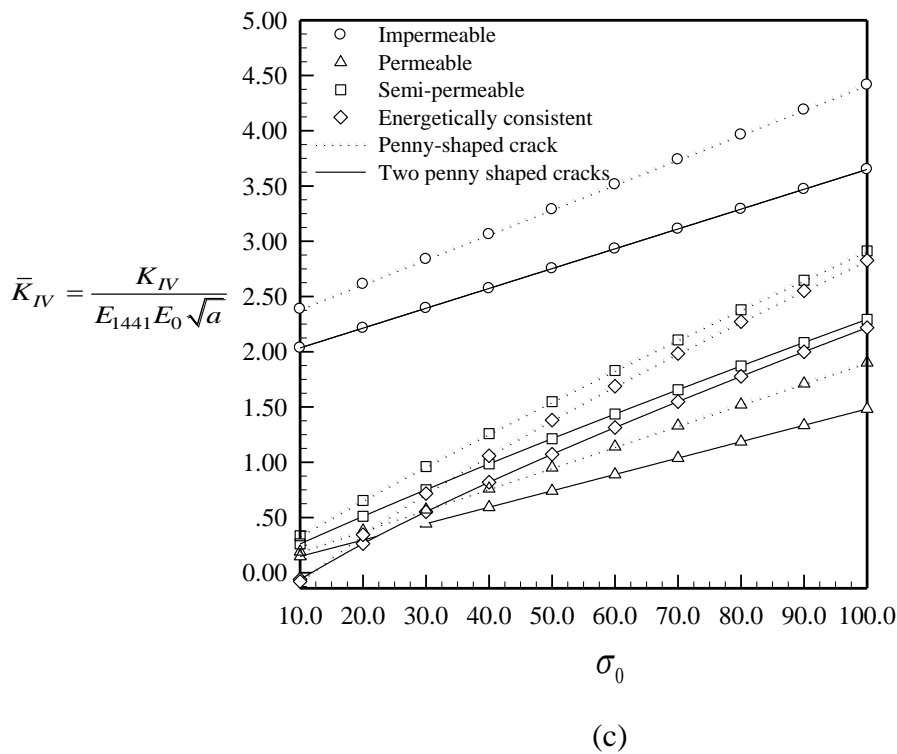
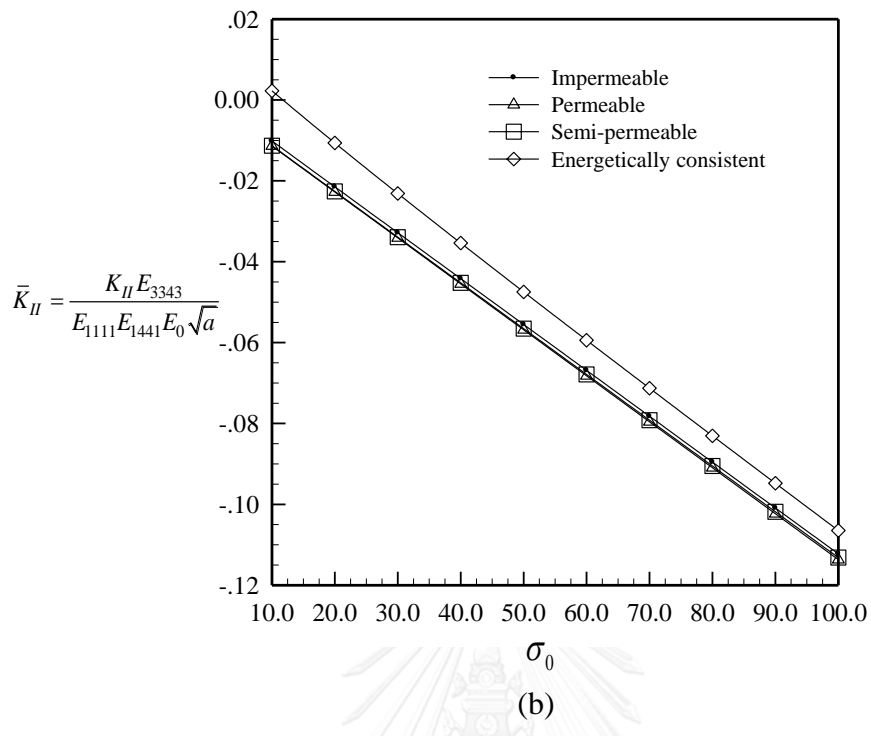


Figure 4.25 (a), (b) and (c) are dependent of normalized stress and electric intensity factors $[K_I, K_{IV}]$ on the mechanical load for a two penny-shaped crack in infinite medium. Results are reported on one penny-shaped crack

4.2.3.2 Influence of remote tensile mechanical load on two penny-shaped crack in horizontal direction

Finally, the last investigation for the mechanical load would be discussed by considering a two penny-shaped crack in horizontal direction containing in a transversely isotropic piezoelectric infinite medium. The crack geometry and the material properties of piezoelectric medium are analogous to the section 4.1.5. The major differences of the parameter compared to that of the previous case are that (i) the radius and the distance of two penny-shaped crack in horizontal direction are fixed as 1 and 2.25 respectively, (ii) the applied uniaxial remote stress is varied from [10,20,30,..., 100] MPa, (iii) the applied electric field E_0 is fixed at 2.5 MV/m which is similar to that of the previous section, and (iv) the dielectric permittivity inside the crack gap is fixed $\varepsilon_c = 5\varepsilon_0$ where $\varepsilon_0 = 8.85 \times 10^{-12}$ C/Vm is the permittivity of the air in the crack gap. The stress and electric intensity factors [K_I, K_{IV}] along the crack front at two different points (i.e., the maximum and minimum points, see figure 4.26) computed from the fine mesh 144 elements per crack are shown in figures. 4.26 (a) and (b) respectively. It is found that the increasing mechanical load σ_0 again tends to increase the magnitude analogous to the case of two penny-shaped cracks in vertical direction, which can be discussed as follows:

Figure 4.26 (a) indicates that when the mechanical load increases, the stress intensity factor K_I at two different points under four crack models (i.e., impermeable, permeable, semi-permeable and energetically consistent models) also increase, the trend of two penny-shaped cracks in horizontal direction at both points (i.e., maximum and minimum points) are nearly identical to that of the single penny-shaped crack; nevertheless, the magnitude K_I of both points are greater than single penny-shaped crack. Moreover, the K_I of three models (i.e., impermeable, permeable and semi-permeable models) of two and single penny-shaped cracks are identical at the entire range; Those three models also serve as upper bound whereas the lower bound is energetically consistent model similar to the discussion mentioned in the former case. Furthermore, the stress intensity factor K_I of the energetically consistent model identically approaches those three models for all cracks. This can be concluded that when the mechanical load increases, it influences only the magnitude of stress intensity factors.

Finally, the intensity factor K_{IV} of two penny-shaped cracks in horizontal direction on four models (i.e., impermeable, permeable, semi-permeable and energetically consistent models) obtained at both maximum and minimum points are shown in figures 4.26 (b). Similarly it can be summarized that when the applied mechanical load increases, the magnitude and the trend of the electrical intensity factors K_{IV} are nearly identical to the single penny-shaped crack and, once again, the four models are strongly different for all models of cracks. Moreover, at the two distinct points, the impermeable model serves as upper bound whereas the lower bound is switched of energetically consistent and permeable models corresponding to turning point at $\sigma_0 = 20$ MPa . This pattern is identical to the single penny-shaped crack. Besides, at both two points, K_{IV} of the semi-permeable and energetically consistent models are again identical, similar to the single penny-shaped crack. Those two models also approach the impermeable model. It can be concluded that, similar to other planer

crack, the increase of the applied mechanical load has influence to both the magnitude and the lower bound of stress intensity factors K_{IV} .

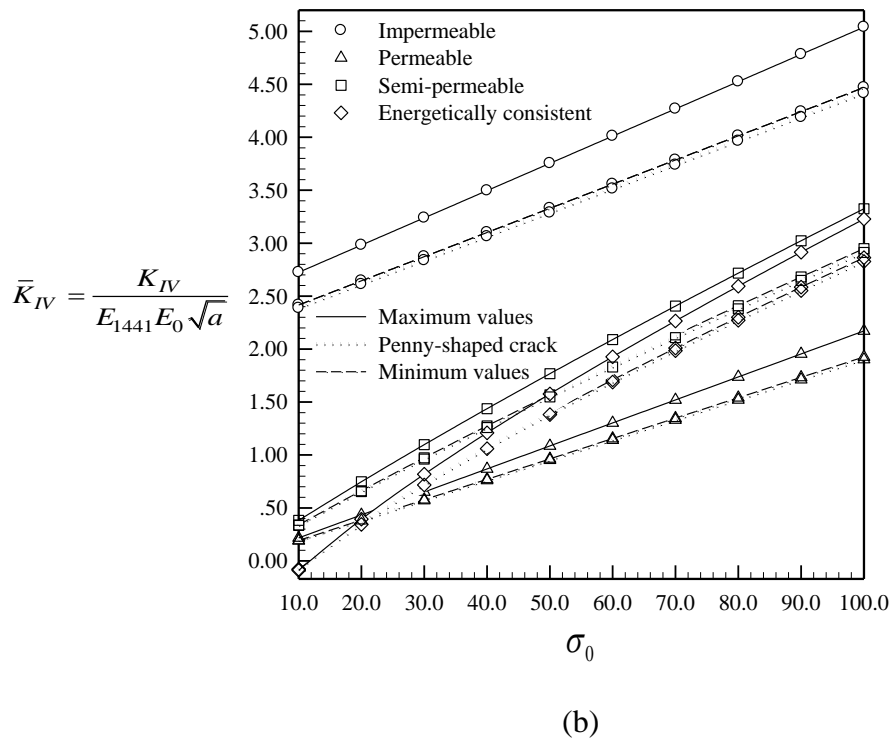
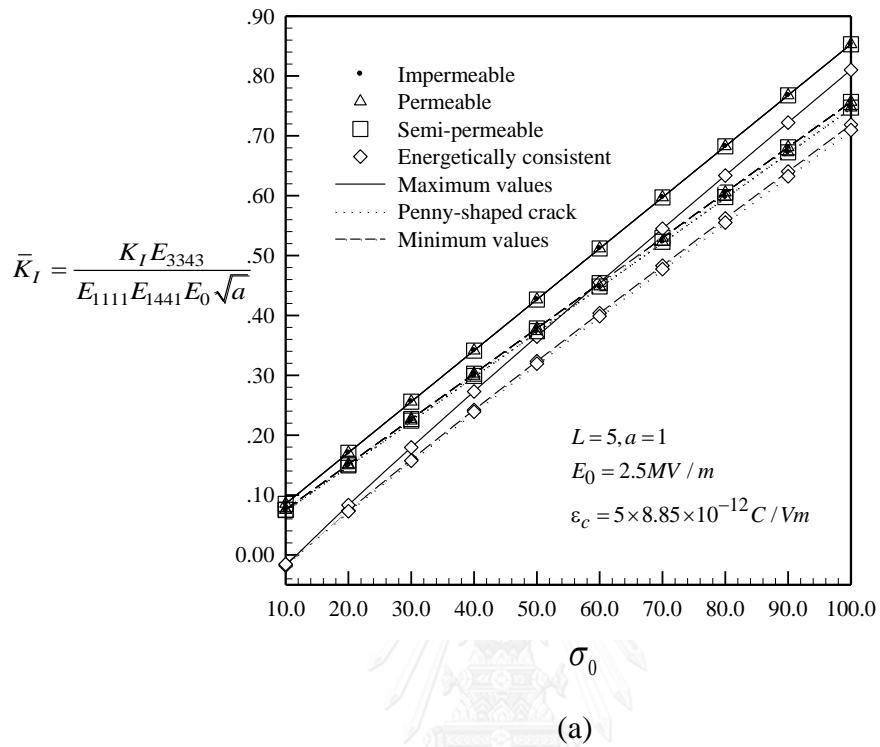


Figure 4.26 (a) and (b) are dependent of normalized stress and electric intensity factors $[K_I, K_{IV}]$ on the mechanical load for a two penny-shaped crack in infinite medium. Results are reported on the maximum and minimum values

4.3 Influence of remote electrical load on four crack-face boundary conditions

Influence of electric load (electric field) on stress and electric intensity factors is investigated. The several cracks are adopted for the exploration such as spherical cap crack, cylindrical crack, tunnel crack, two penny-shaped crack in vertical direction and the two penny-shaped cracks in horizontal direction. The effect of electric field will be revealed in the next section

4.3.1 Influence of remote electrical load on spherical cap and cylindrical crack

At the outset, the two non-planar cracks such as spherical cap and cylindrical cracks is employed to explore the stress and electric intensity factor on four crack-face model by varying the remote electric load. The influence of electrical field will be revealed in the following subsections.

4.3.1.1 Influence of remote electrical load on spherical cap crack

The first investigation for the influence of the electrical load is discussed by considering a spherical cap crack embed in a transversely isotropic piezoelectric infinite medium. The crack geometry, the mesh and the material properties of piezoelectric medium are analogous to those in the section 4.2.1. The key parameter differences from the previous case are that (i) the radius of spherical cap crack fixed as 1.2732395447352 corresponding to radius of penny-shaped crack as 1 ($a = 1$), (ii) the applied uniaxial remote stress is fixed as 50 MPa, (iii) the applied electric field E_0 is now varied from $[-4.5, -4, -3.5, \dots, 4.5]$ MV/m which is the key point of this section, and finally (iv) the dielectric permittivity inside the crack gap is fixed $\varepsilon_c = 5\varepsilon_0$ where $\varepsilon_0 = 8.85 \times 10^{-12}$ C/Vm is the permittivity of the air in the crack gap. The present numerical results shown in figures 4.27 (a) and (b) and (c) reveal that when the applied electric field increases from negative to positive values, the magnitude of the normalized stress and electric $[K_I, K_{II}, K_{IV}]$, particularly the magnitude of the three models (i.e., impermeable, semi-permeable and energetically consistent models), are extremely varied for the whole range of electric field. This can be discussed in detail as follows.

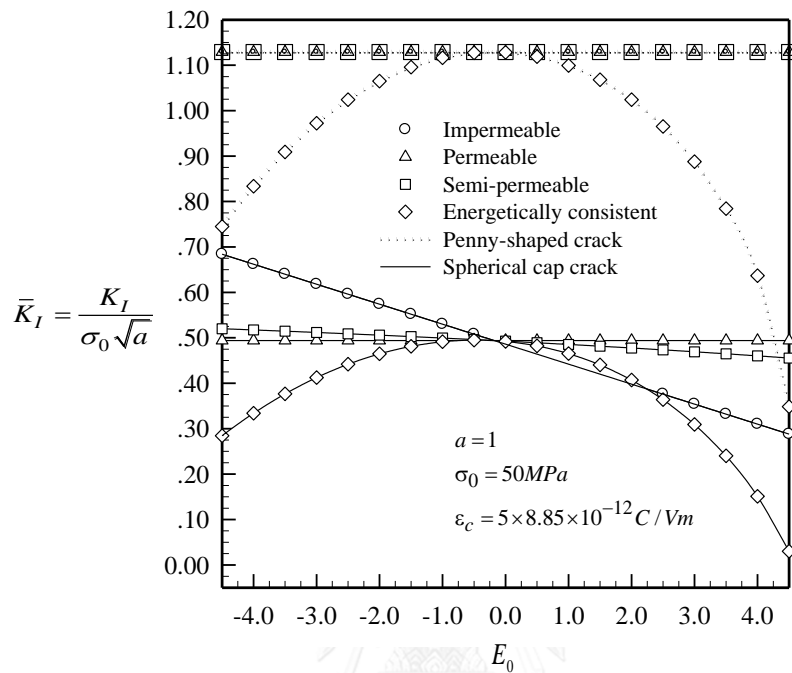
The stress intensity factors K_I upon four models reported in figures 4.27 (a) are obtained by comparing with the planar crack. It can be found that when the electric field varies, those three models (i.e., impermeable, semi-permeable and energetically consistent models) become different. For example, the energetically consistent models increases whereas for the impermeable and semi-permeable models decreases the magnitude at the range of negative electric field ($E_0 = -4.5$ to $E_0 = 0$ MV/m), and the behavior of those three models become opposite at the range of positive electric field ($E_0 = 0$ to $E_0 = 4.5$ MV/m). In contrast, the three models of penny-shaped crack are completely identical and the values of those models are obviously higher than the non-planar crack. Nevertheless, the trend of the energetically consistent models of both planar and non-planar crack are similar behaviors by presenting the large slope at both

sides of electric field range. Moreover, it is obvious that the bounds of planar and non-planar crack of the positive electric field range are significantly different. For example, the upper bound of spherical cap crack is permeable model whereas that of planar crack serves as three models (i.e., permeable, semi-permeable and impermeable models). Again, the lower bounds of both cracks slightly changed, for example the lower bound of planar crack serves as energetically consistent model while it is switched of impermeable and energetic consistent by showing the turning point at $E_0 = 2.5$ MV/m. In addition, one can see from figure 4.27 (a) that the permeable models of both planar and non-planar crack are independent of electric field. However, the semi-permeable and impermeable models are obviously dependent on electric field. This implies that the electric field has an influence not only to the magnitude but also to the four boundary conditions of both cracks.

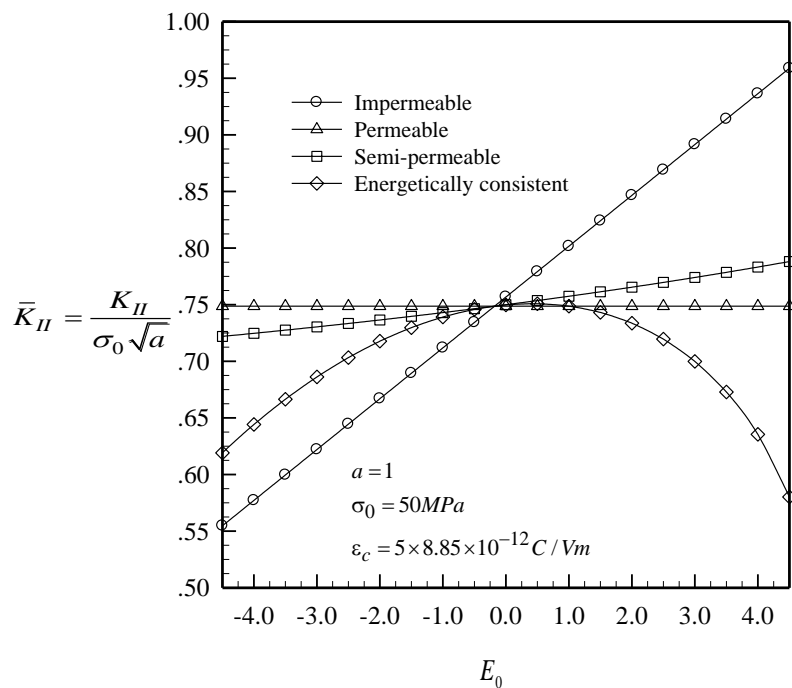
The results of stress intensity factor K_{II} on four models are presented in figure 4.27 (b). Results reveal that when the electric field varies from -4.5 to 4.5 MV/m the two models (i.e., impermeable and semi-permeable models) become opposite to the magnitude of K_I except the energetically consistent and permeable models. It can be explained further that those two models tend to increase the magnitudes at both negative and positive ranges of electric field, whereas the normalized stress K_{II} of planar crack vanishes. Figure 4.27 (b) also indicates that the energetically consistent model still has high slope compared to the other models. Furthermore, the upper bounds of positive range of electric field serve as impermeable model whereas the lower bound is again switched of permeable and energetically consistent models and this occurs at the turning point of $E_0 = 1$ MV/m. Throughout the range of electric field, the permeable model shows the behavior identical to the K_I , indicating the independence toward electric field. Similarly, the two models (i.e., impermeable and semi-permeable models) are strongly dependent of electric field. Finally, it can be summarized from above discussion that when the electric field varies from negative to positive values, it influences to both the magnitudes of the three models (i.e., impermeable, semi-permeable and energetically consistent models - except the permeable model) and lower bounds of four models at the positive range of electric field.

Finally, the electric intensity factor K_{IV} on four models (i.e., impermeable, permeable, semi-permeable and energetically consistent models) is shown in figure 4.27 (c). It can be seen that along with the increase of the electric field from the negative to the positive values of electric field, the magnitude of four models (i.e., impermeable, permeable, semi-permeable and energetically consistent models) are rather identical to the trend of planar crack (a penny-shaped crack). More specifically, the impermeable and semi-permeable models strongly depend on electric field. It can be observed further from the figure that the curve of the energetically consistent models is reduced compared with the stress K_I and K_{II} in the former discussion. It is nearly identical to semi-permeable models at the range $E_0 = -2$ to 1 MV/m but drops down when the electric field is sufficiently large. In addition, at the positive electric range of electric field, the upper bound is impermeable model whereas the lower bound is again switched between the permeable and the energetically consistent model which occurs at the turning point as $E_0 = 3.5$ MV/m. Besides, the permeable model of K_{IV} again is fully independent of electric field, similar to the normalized stress K_I and K_{II} in the previous discussion. This can be concluded that when the electric field varies, it affects both the

magnitude of three models (i.e., impermeable, semi-permeable and energetically consistent models) and the lower bound of those four models.



(a)



(b)

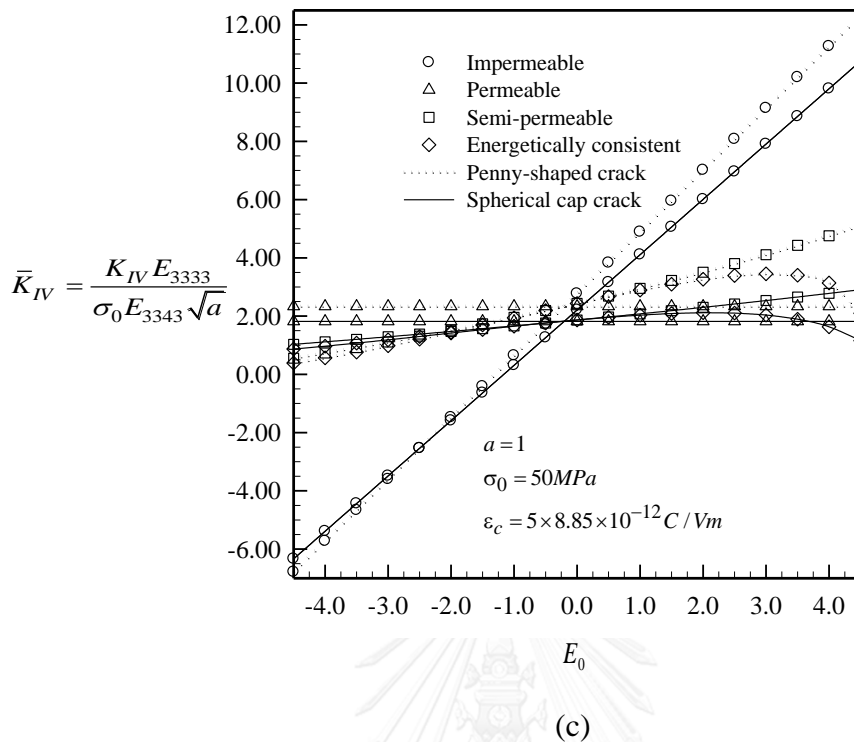


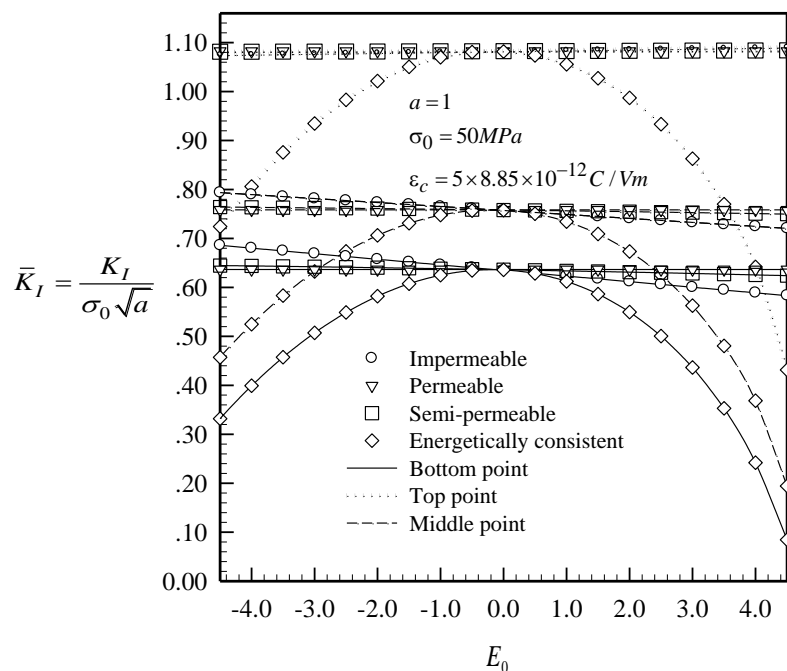
Figure 4.27 (a), (b) and (c) are dependent of normalized stress and electric intensity factors $[K_I, K_{II}, K_{IV}]$ on the electrical load for spherical cap crack in infinite medium. Results are reported as average values

4.3.1.2 Influence of remote electrical load on cylindrical crack

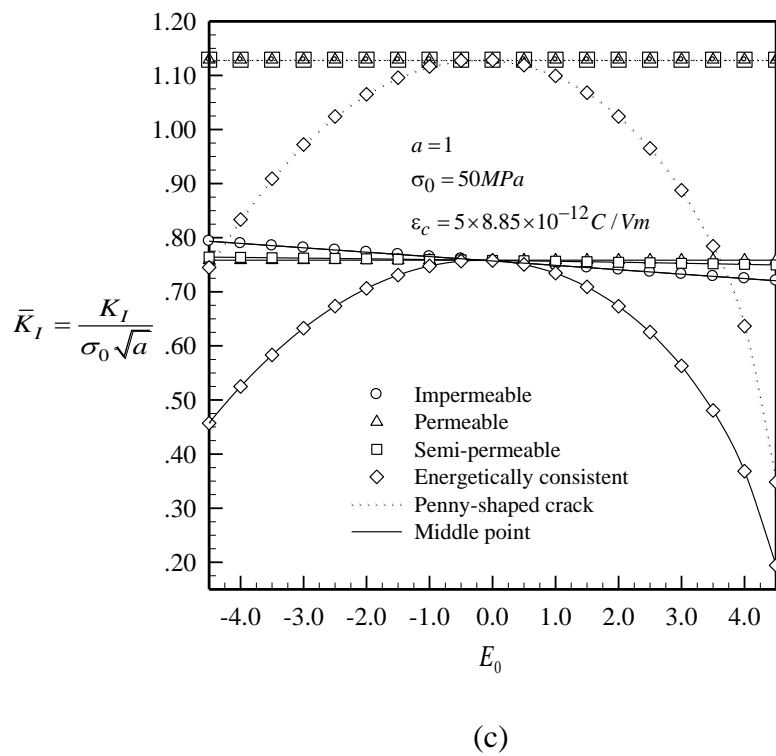
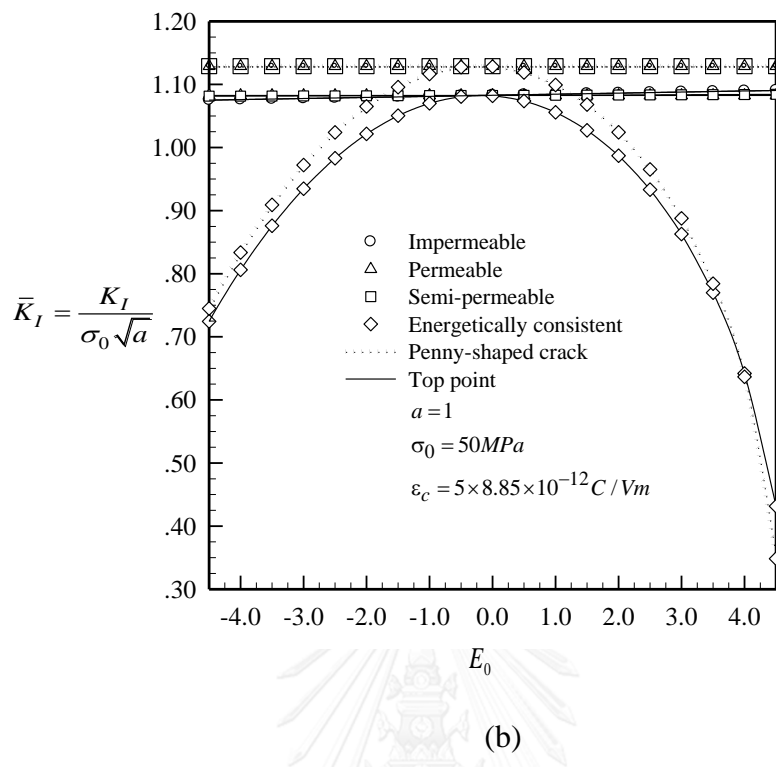
Next, we consider a cylindrical crack embed in a transversely isotropic piezoelectric infinite medium. The crack geometry, the mesh and the material properties of piezoelectric medium are similar to the section 4.2.2. The major distinctions from the previous research are that (i) the radius of cylindrical crack fixed as 1.2732395447352 corresponding to radius of penny-shaped crack as 1 ($a = 1$), (ii) the applied uniaxial remote stress is fixed as 50 MPa, (iii) The applied electric field E_0 now varies from $[-4.5, -4, -3.5, \dots, 4.5]$ MV/m which is similar to the spherical cap crack, and (iv) and the dielectric permittivity inside the crack gap is fixed $\epsilon_c = 5\epsilon_0$ where $\epsilon_0 = 8.85 \times 10^{-12}$ C/Vm is the permittivity of the air in the crack gap. The numerical results are presented in order to investigate the influence of electrical load on stress, and electric intensity factors at three different points (i.e., top, middle and bottom points as shown in figure 4.3) are displayed in figures 4.28 (a), 4.29 (a) and 4.30 (a). It can be found that when the applied electric field increases throughout the range $[-4.5$ to 4.5 MV/m], the trends of the normalized stress and electric $[K_I, K_{II}, K_{IV}]$ (only at the middle point) and K_{IV} are identical. However, the magnitude of those varies from positions (i.e., top, middle and bottom points) along the crack front which can be discussed in detail as follows:

The non-zero intensity factors K_I on four crack-face models (i.e., impermeable, permeable, semi-permeable and energetically consistent models) at three distinct points (i.e., top, middle and bottom points) reported in figure 4.28 (b), (c) and (d) are

investigated. It can be found that as the electric field increases from the negative to the positive values, the discrepancy of the magnitude depends on the positions (points) along the crack front, for example, the magnitude of the top point is greater than other two remaining points (i.e., middle and bottom points). Moreover, the three models (i.e., impermeable, semi-permeable and permeable models) are nearly identical which is very similar to the planar crack (penny-shaped crack) at the top point of cylindrical crack, and those three models gradually exhibit the distinctions when K_I is obtained from the middle and bottom points respectively. It should be noted that the behaviors of three points can be observed further from each figure, that the impermeable and semi-permeable models at three different points (i.e., top, middle and bottom points) strongly depend on the increasing electric field by exhibiting the slope of the magnitude, whereas the three models of planar crack are completely identical. Again, figures indicate that the permeable models are similarly independent of the electric field at all points which is identical to the planar crack. Furthermore, the upper and lower bound of all the three different points are permeable and energetically consistent models when the electric field is in the positive range. It should be remarked again that the magnitude of the energetically consistent models at three points of cylindrical crack are strongly dependent on the increasing electric field, and that is analogous to the planar crack. This can be implied that when the electric field varies from small to large values, it has an influence to the magnitude of three models of cylindrical crack and also to one model for planar crack, which is energetically consistent model.



(a)



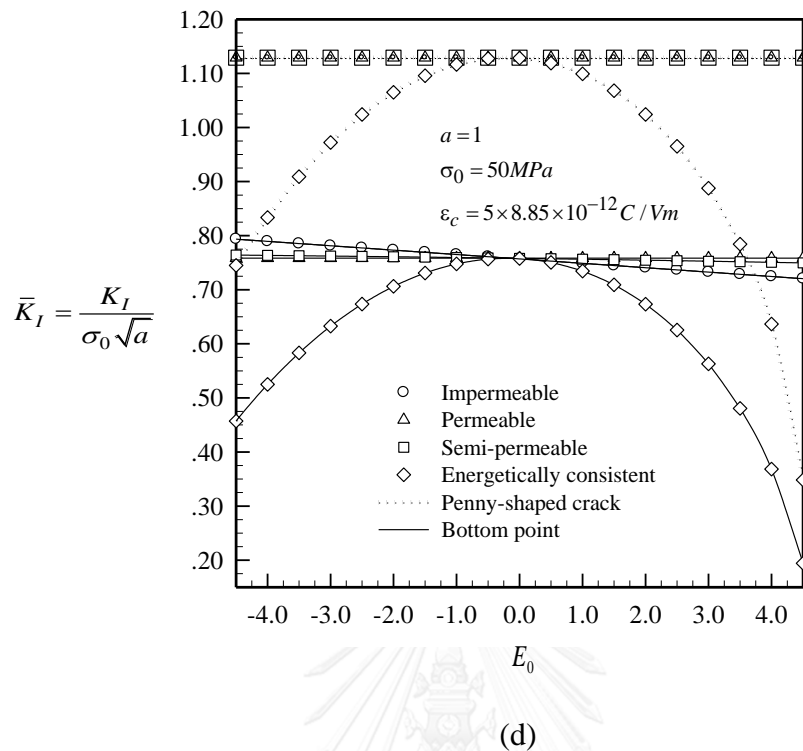
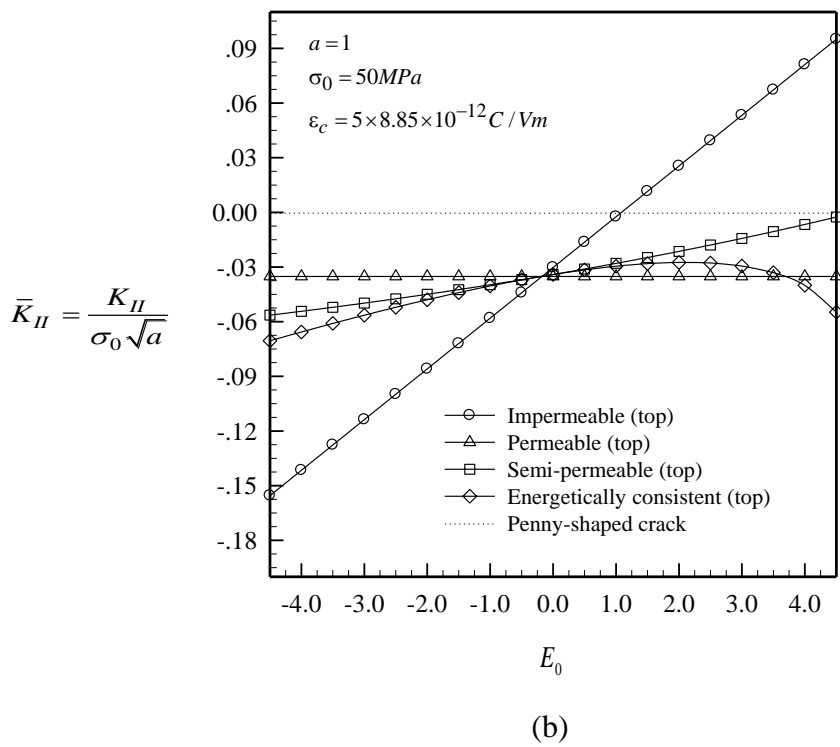
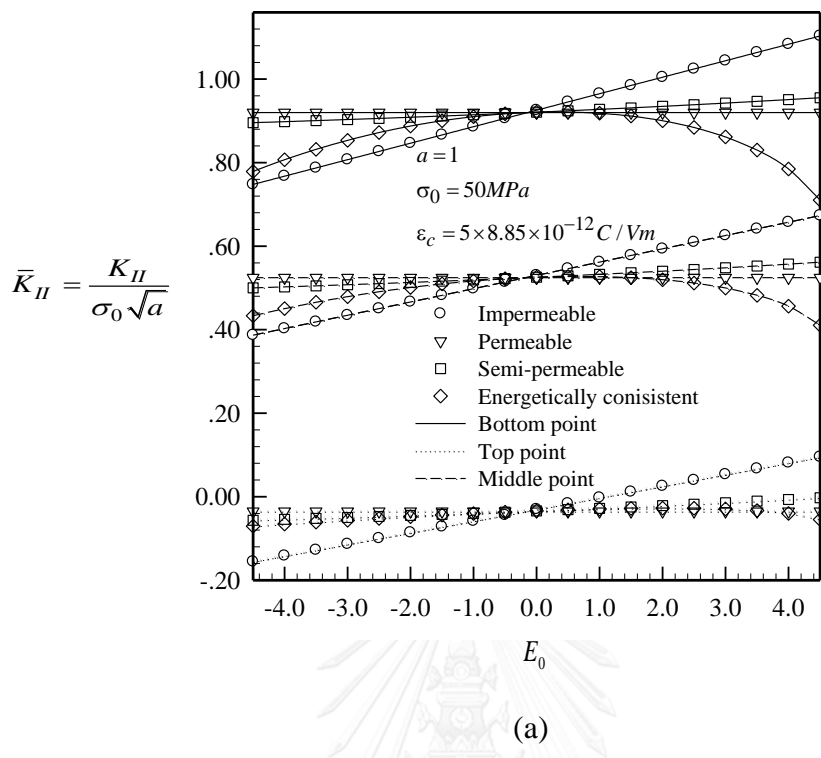


Figure 4.28 Dependent of normalized stress intensity factors [K_I] on the electrical load for cylindrical crack in infinite medium. Results are reported on (a) all points, (b) top, (c) middle and (d) bottom points

Next, the stress intensity factors K_{II} obtained from three distinct points (i.e., top, middle and bottom points) under four crack-face models (i.e., impermeable, permeable, semi-permeable and energetically consistent models) are studied as shown in figure 4.29(a), (b), (c) and (d). It can be found that when the electric field increases from small to the large values [-4.5 to 4.5 MV/m], the magnitude of the bottom point are significantly higher than other points (i.e., top and middle points), whereas the stress K_{II} of planar crack vanishes. However, the behaviors of three different points are rather different which can be observed further in detail. It can be found that the impermeable and semi-permeable models of three points again depend on the increasing electric field while the permeable models do not. Moreover, the bounds at the range of the positive electric field at three points are rather distinct, for example, the upper bounds of any points along the crack front of cylindrical crack are impermeable models whereas the lower bounds of those three points are switched of permeable and energetically consistent models corresponding to the turning point occurred at $E_0 = 3.5$, $E_0 = 1.5$ and $E_0 = 1$ MV/m for top, middle and bottom points respectively. In addition, the energetically consistent model at the top point are also different from both middle and bottom points by displaying the curve as a linear whereas at the remaining points exhibit as non-linear when the negative electric field is obtained. These can be summarized that the increasing electric field gives rise to affect not only the lower bound at any points but also to the magnitude of those positions.



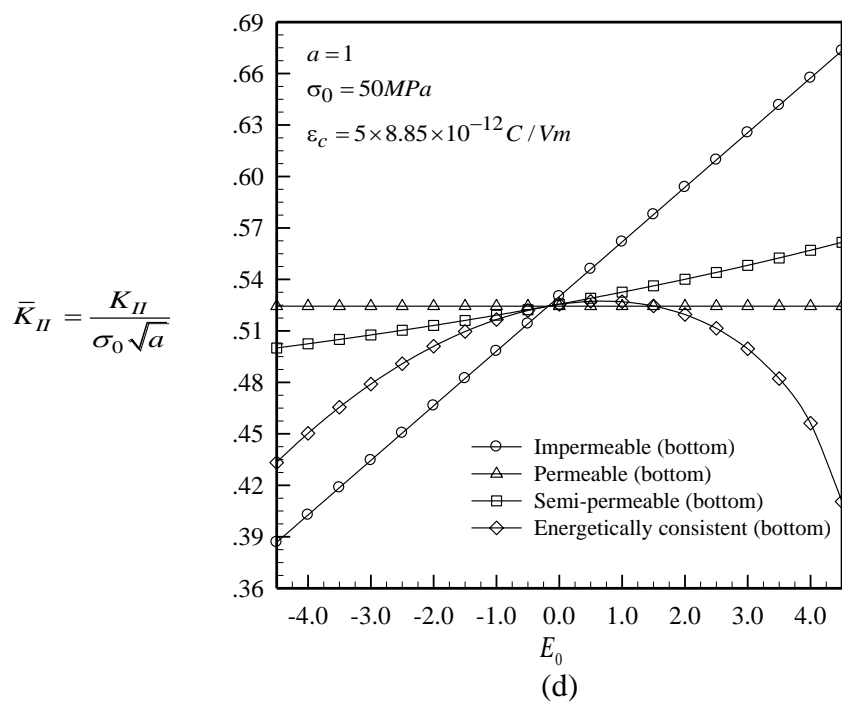
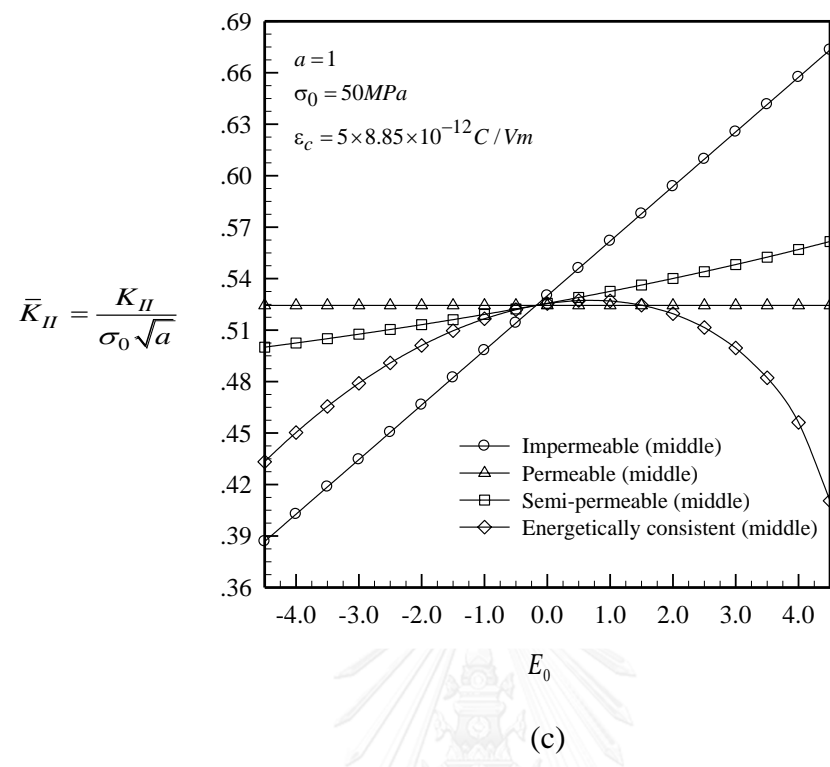


Figure 4.29 Dependent of normalized stress intensity factors [K_{II}] on the electrical load for cylindrical crack in infinite medium. Results are reported on (a) all points, (b) top, (c) middle and (d) bottom points

Next, we investigate the influence of stress intensity factors K_{III} on four crack-face models (i.e., impermeable, permeable, semi-permeable and energetically consistent models) only at the middle point along the crack front as reported in figure 4.30. It can be found that when the electric field increases from $[-4.5$ to 4.5 MV/m], the impermeable and semi-permeable models fully depend on the electric field, by exhibiting the increase of the magnitude. The slope of impermeable model, however, is greater than the semi-permeable model. It is also found that the permeable is perfectly independent of electric field by showing the constant magnitude. Furthermore, the energetically consistent model starts to increase at $E_0 = 0$ MV/m which is different from the behavior of $[K_I, K_{II}, K_{IV}]$ trends. Finally, results reveal that the upper bound at the range of positive electric field serves as impermeable model, whereas the lower bound is permeable model. This can be implied that when considering the negative and positive range of electric field, it has influence to both the magnitude of stress K_{III} and the bound of the four models.

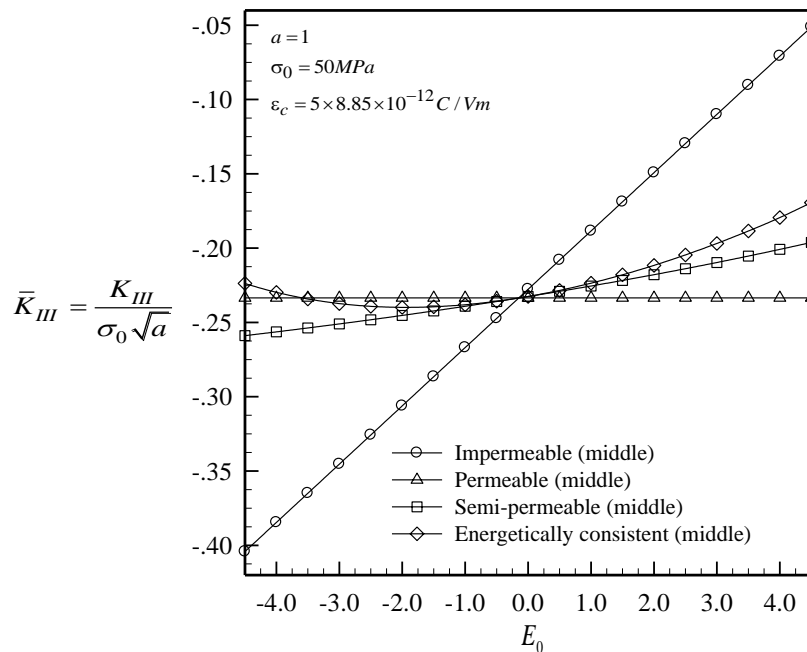
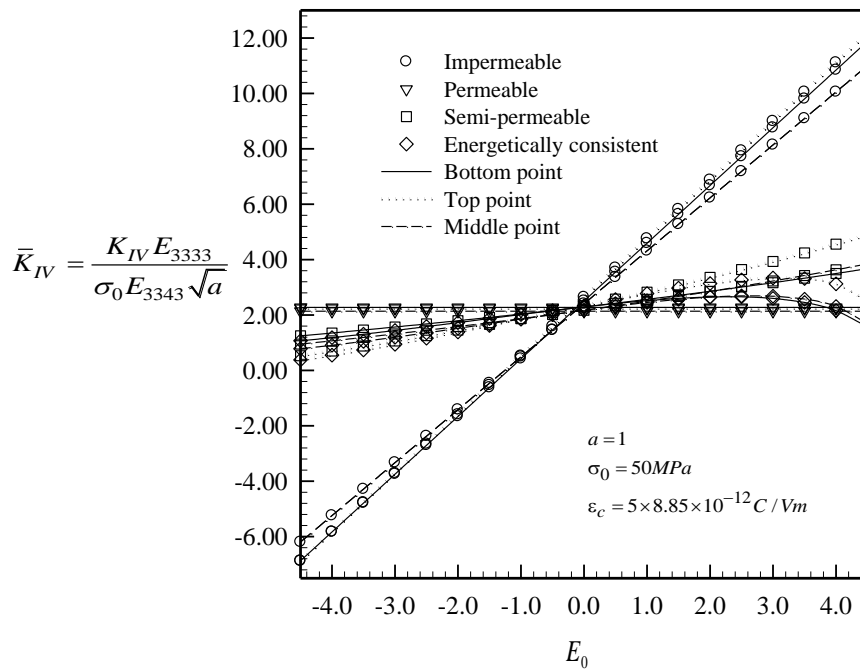


Figure 4.30 Dependent of normalized stress intensity factors $[K_{III}]$ on the electrical load for cylindrical crack in infinite medium. Results are reported on the middle point

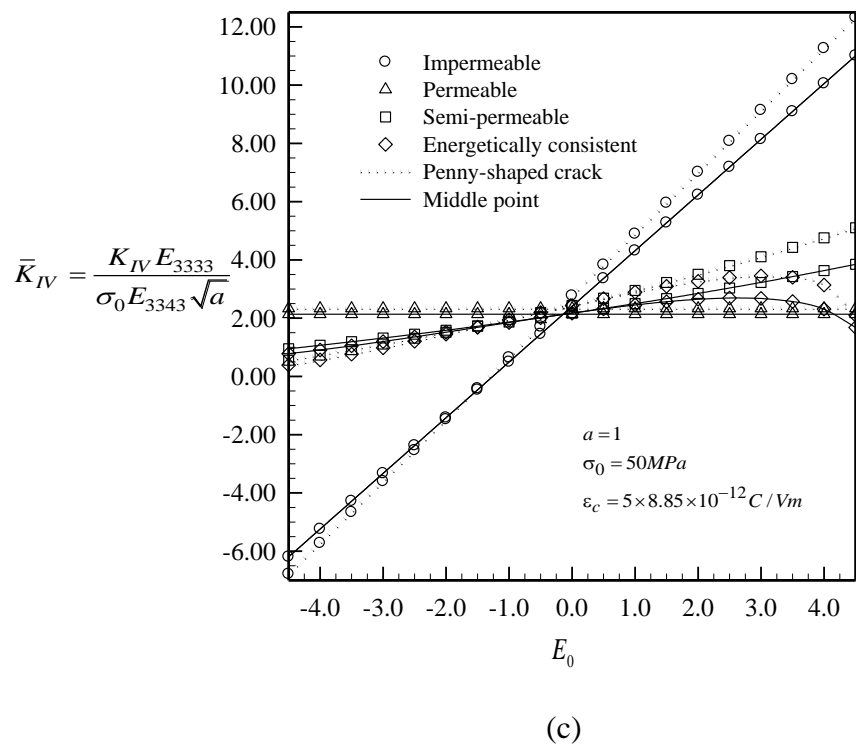
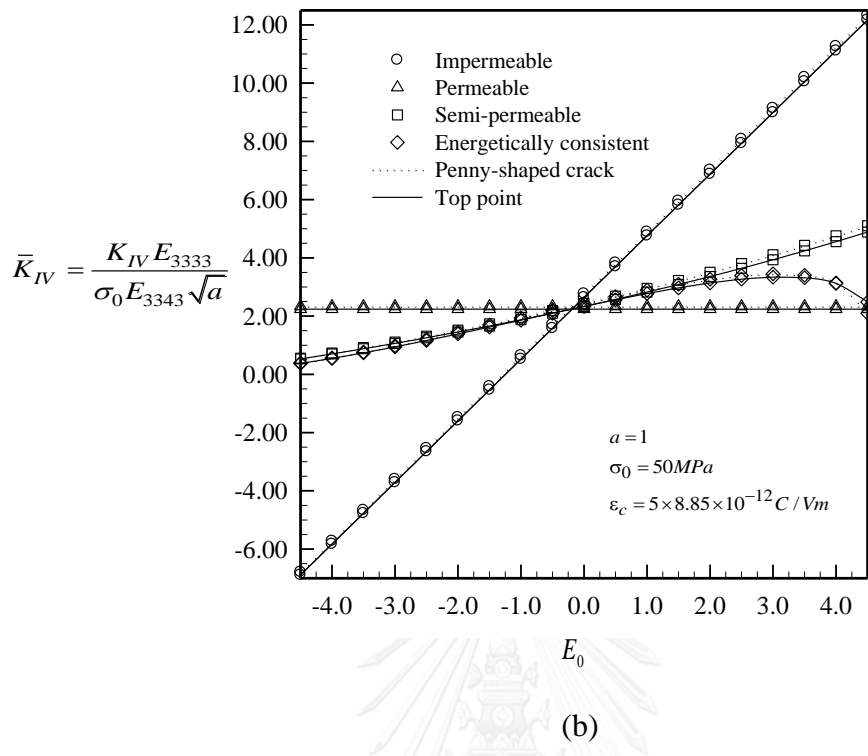
Eventually, the influence of electric intensity factors K_{IV} offered from three distinct points (i.e., top, middle and bottom points) on four models (i.e., impermeable, permeable and energetically consistent models) as illustrated in figure 4.31 (a), (b), (c) and (d) are investigated. As the electric field increases $[-4.5$ to 4.5 MV/m]. In addition, the magnitude of three different points slightly changes. However, the behaviors of four models are clearly distinct which would be investigated in detail.

From figure 4.31 (a), (b) and (c), it can be found that the semi-permeable and impermeable of three points along the crack front strongly depend on electric field. On the other hand, the permeable models are completely independent of electric field, and

that behaviors are identical to planar crack. Moreover, the energetically consistent models of three points (i.e., top, middle and bottom points) have similar trends by implying the linear curve at the range of negative electric field and by indicating the non-linear curve at the positive range of electric field which is similar to planar crack. Besides, it can be noticed that the upper bounds of three points serve as impermeable models while the lower bound varies from the three points at the range of positive electric field. For example, at the top point, the lower bounds are permeable model, whereas at both middle and bottom points they are switched of permeable and energetically consistent models. This leads to the turning points of the lower bounds at $E_0 = 4$ MV/m for both points. These can be implied that when the electric field is changed, it affects to both the magnitude and the lower bound of four crack models.



(a)



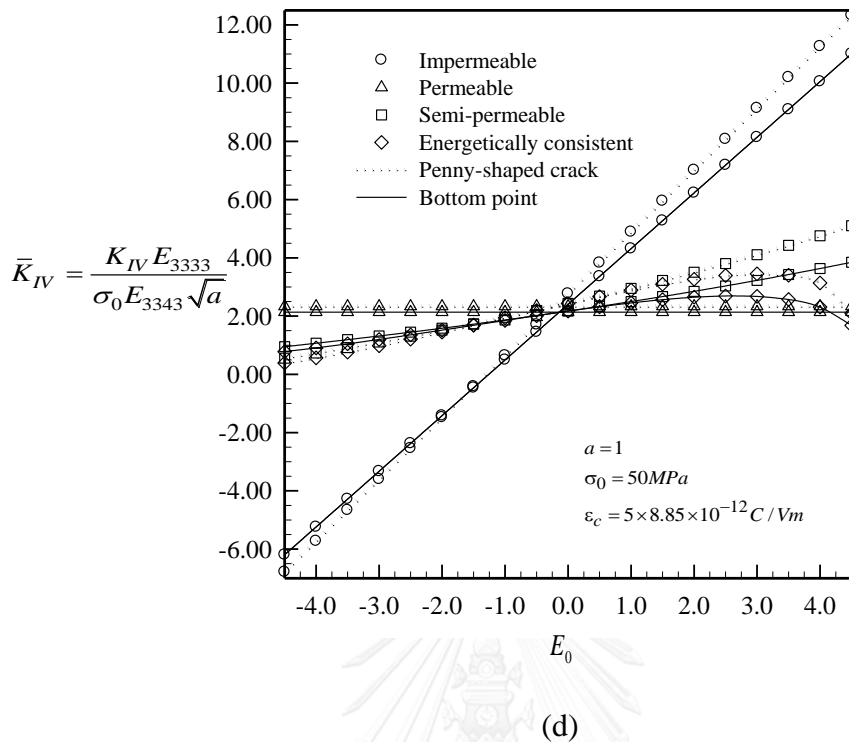


Figure 4.31 Dependent of normalized electric intensity factors $[K_{IV}]$ on the electrical load for cylindrical crack in infinite medium. Results are reported on (a) all points, (b) top, (c) middle and (d) bottom points

4.3.1.3 Comparison between spherical cap crack and cylinder crack

From the above discussion, the stress and electric intensity factors $[K_I, K_{II}, K_{IV}]$ offered from both spherical cap crack and the top point of cylindrical crack on four models (i.e., impermeable, permeable, semi-permeable and energetically consistent models) have major points which can be compared as follows.

Results of the spherical cap crack can be summarized as follows. When the electric field varies, the two models (i.e., impermeable, semi-permeable models) are distinct and are strongly dependent of electric field which is completely different from the penny-shaped crack, whereas both permeable and energetically consistent models of both cracks (i.e., penny-shaped and spherical cap crack) exhibit clearly identical trends. However, the magnitude of penny-shaped crack on four models is higher than the spherical cap crack. It can be found that the bounds of planar and non-planar crack of the positive electric field range are significantly different. For example, the upper bound of spherical cap crack is pure permeable model whereas one is three models (i.e., permeable, semi-permeable and impermeable models) for the planar crack. Again, the lower bounds of both cracks slightly change. For example, the lower bound of planar crack serves as pure energetically consistent model while it is switched of impermeable and energetic consistent. In addition, the permeable models of both planar and non-planar cracks are independent of electric field. The semi-permeable and impermeable models, on the contrary, are obviously dependent on electric field. Similarly, the stress intensity factors K_I obtained from cylindrical crack at three different points (i.e., top,

middle and bottom points) are compared with the previous cracks (i.e., spherical cap and penny-shaped cracks). It is found that the magnitudes of three different points are completely different depending on the point along the crack front. The behavior of spherical cap crack is also very identical to K_I at the bottom point of cylindrical crack. Apart from the similarity of spherical cap crack, we can also indicate that the dependent of electric field of K_I at the top point along the crack front of cylindrical crack are weaker than at the rest of the point (i.e., middle and bottom points). The dependent of electric field for energetically consistent model at any points and penny-shaped crack is still strong. Moreover, the upper and lower bound of both cylindrical crack (at any points) and penny-shaped crack are identical but those lower bounds are different from spherical cap crack.

For the stress intensity factor K_{II} obtained from spherical cap crack, it can be found that with the increasing electric field, the three models (i.e., impermeable, semi-permeable and energetically consistent models) are strongly dependent of electric field at the entire range of electric field. Furthermore, the upper bounds of positive range of electric field serve as impermeable whereas the lower bound is again switched of permeable and energetically consistent models. Throughout the range of electric field, it manifests that the permeable model shows similar behavior to the K_I . Identically, the stress intensity factor K_{II} obtained from cylindrical crack at top, middle and bottom points are considered to compare with spherical cap crack. It can be found that the magnitudes of all points are completely different. In addition, the dependent and independent of both three models (i.e., impermeable, semi-permeable and energetically consistent models) and permeable model exhibit very identical behaviors. The switching point of the lower bound of cylindrical crack at all points, however, is varied depending on the point along the crack front. Those varying are also different from the lower point of spherical cap crack.

For the stress intensity factors K_{III} obtained only at the middle point of cylindrical crack can be conclude that, the three models (i.e., impermeable, semi-permeable and energetically consistent models) are similarly dependent on increasing the electric field; however, the permeable model is not dependent of electric field similar to K_I and K_{II} in previous discussion. Moreover, the upper and lower bounds of K_{III} on four models serve as impermeable and permeable models at the positive range of electric field respectively.

Finally, from the electric intensity factors K_{IV} on four models (i.e., impermeable, permeable, semi-permeable and energetically consistent models) of spherical cap crack, it can be concluded that the magnitude of penny-shaped crack on four models are greater than that of spherical cap crack. Moreover, the behavior of both spherical cap and penny-shaped cracks exhibit very identical trends. For example, the dependent of electric field of three models (i.e., impermeable, semi-permeable and energetically consistent models) of both planar and non-planar crack are also identical. In addition, the permeable models of both cracks similarly are independent of electric field at the entire range but the lower bounds of penny-shaped crack is different from spherical cap crack - the lower bounds of spherical cap crack is switched of permeable and energetically consistent models. On the other hand, results of stress intensity factors K_{IV} obtained from top, middle and bottom points of cylindrical crack indicate that the magnitude of top point is greater than the rest point. The behavior of K_{IV} at bottom point of cylindrical crack are very identical to that of spherical cap crack. In addition to the

similarity of both spherical and top point of cylindrical crack, it is also seen that the lower bound of K_{IV} at three points of cylindrical crack depends on the obtained electric intensity factors K_{IV} along the crack front. In addition, the behavior of K_{IV} at the top point is very identical to the penny-shaped crack.

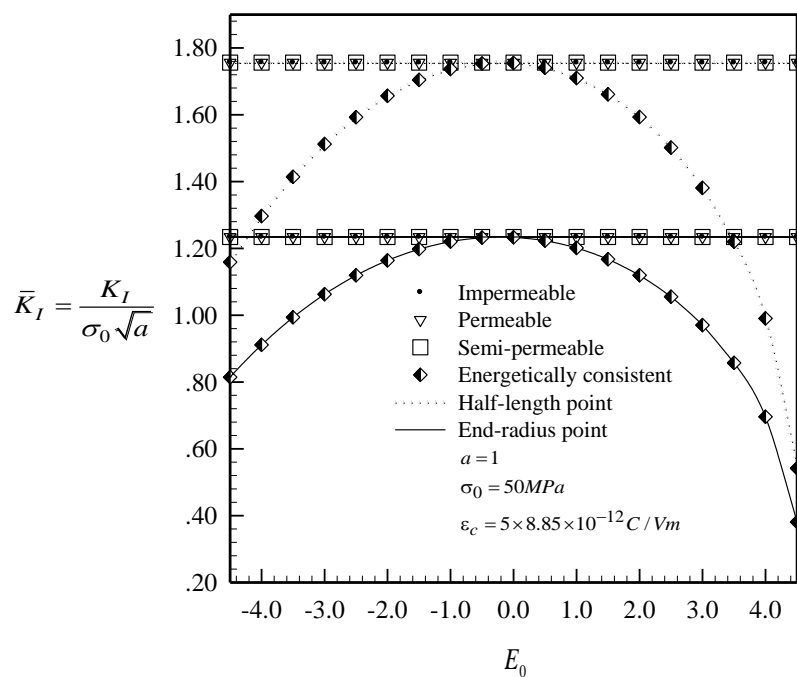
4.3.2 Influence of remote electrical load on tunnel crack

In this case, the influence of electrical load is investigated by considering a tunnel crack containing in a transversely isotropic piezoelectric infinite medium. The crack geometry, the mesh and the material properties of piezoelectric medium are analogous to those applied in section 4.2.3. The essential distinctions from the previous investigation are that (i) the end-radius and the half-length of tunnel crack are fixed as 1 and 5 respectively (ii) the applied uniaxial remote stress is fixed as 50 MPa, (iii) the applied electric field E_0 is now varied from [-4.5, -4, -3.5, ..., 4.5] MV/m which is similar to the other cracks, and (iv) and the dielectric permittivity inside the crack gap is fixed $\varepsilon_c = 5\varepsilon_0$ where $\varepsilon_0 = 8.85 \times 10^{-12}$ C/Vm is the permittivity of the air in the crack gap. The effect are offered to explore the influence of electrical load on stress and electric intensity factors at two different points (i.e., the end-radius and half-length points as illustrated in figure 4.23a) are reported in figures 4.32 (a),(b),(c) and (d). It can be found that when the range of the applied electric field increases [-4.5 to 4.5 MV/m], the magnitude of the normalized stress and electric K_I and K_{IV} of both points (i.e., the end-radius and the half-length points) are rather different. For example, the magnitude of the half-length point is completely greater than that of both the end-radius point and the penny-shaped crack as shown in figure 4.32(b) and (d). However, the trends of both points and the penny-shaped crack are very almost identical along the crack front which can be discussed in detail as follows:

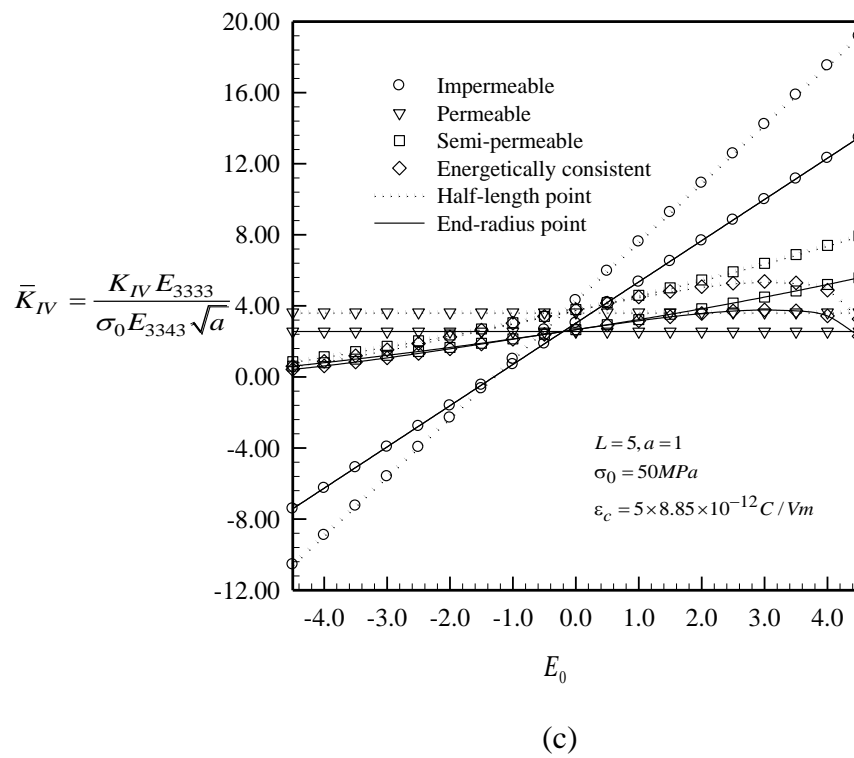
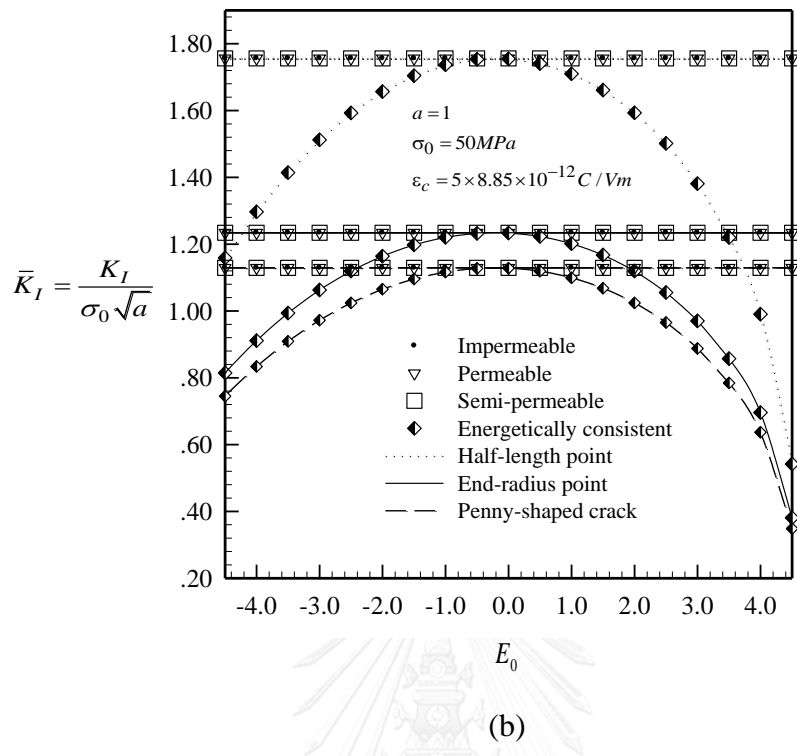
At the outset, the numerical results of stress intensity factors K_I at two different points (i.e., the end-radius and the half-length points) on four crack-face models (i.e., impermeable, permeable, semi-permeable and energetically consistent models) reported in figure 4.32 (a) and (b) are investigated. It is found that when the range of the electric field increase from small to large values [-4.5 to 4.5 MV/m], the magnitude of both points are completely different and also different from that of the penny-shaped crack. The trends of all points, however, are obviously identical similar to that of the penny-shaped crack. More specifically, the three models of both point (i.e., the end-radius and the half-length points) are also completely identical and independent of electric field. In addition, those three models (i.e., impermeable, permeable and semi-permeable models) serve as upper bounds, whereas the energetically consistent models of both points strongly depend on the electric field and serve as the lower bound in range of the positive electric field of which all behaviors are analogous to the behaviors of penny-shaped crack. It can be observed further from the figure that the turning points between the positive and negative ranges of the electric field are always generated at $E_0 = 0$ MV/m. Accordingly. From this investigation, one can thoroughly understand the behaviors of the three models (i.e., impermeable, permeable, semi-permeable and energetically consistent models).

Finally, the influence of electric intensity factors K_{IV} on four crack models (i.e., impermeable, permeable, semi-permeable and energetically consistent models) obtained from two distinct points (i.e., end-radius and the half-length points) are reported in figure 4.32 (c) and (d). It can be found that when the electric field increases

[-4.5 to 4.5MV/m], the magnitude of K_{IV} at two points are rather different, i.e., the magnitude of end-radius point is obviously less than that of the half-length points. More specifically, the slopes of K_{IV} for the half-length points are also higher than the other point. Not only these behaviors but also the magnitude is identical to that of the planar crack. For example, the impermeable and semi-permeable models extremely depend on the electric field and the permeable models are independent of increasing of the electric field. Moreover, the behaviors of energetically consistent models are linear curve at the negative range of electric field whereas they change to the non-linear curve in the positive range of electric field. In addition, the turning points of the negative and positive electric field ranges again occur at $E_0 = 0$ MV/m which is similar to those of the planar crack. From the positive range of electric field, it can be indicated from figure again that the upper bound is impermeable models whereas the lower bound us is permeable model. It can be said that the behavior of the tunnel crack is similar to that of the penny-shaped crack. The only difference is the magnitude.



(a)



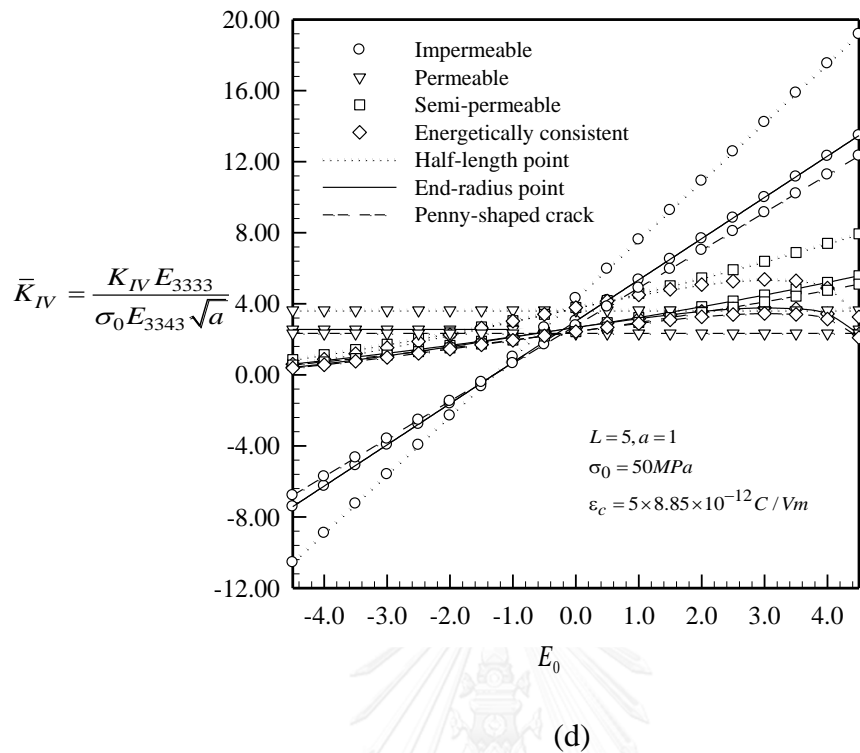


Figure 4.32 (a), (b), (c) and (d) are dependent of normalized electric intensity factors $[K_I, K_{IV}]$ on the electrical load for tunnel crack in infinite medium. Results are reported on the end-radius and half-length points

4.3.3 Influence of remote electrical load on two pair of penny-shaped cracks

In this section, two pair of two penny-shaped cracks (e.g., two penny-shaped cracks in both vertical and horizontal directions) are studied of stress and electric intensity factor on four crack-face models. Each crack will be implemented in subsection follow.

4.3.3.1 Influence of remote electrical load on two penny-shaped crack in vertical direction

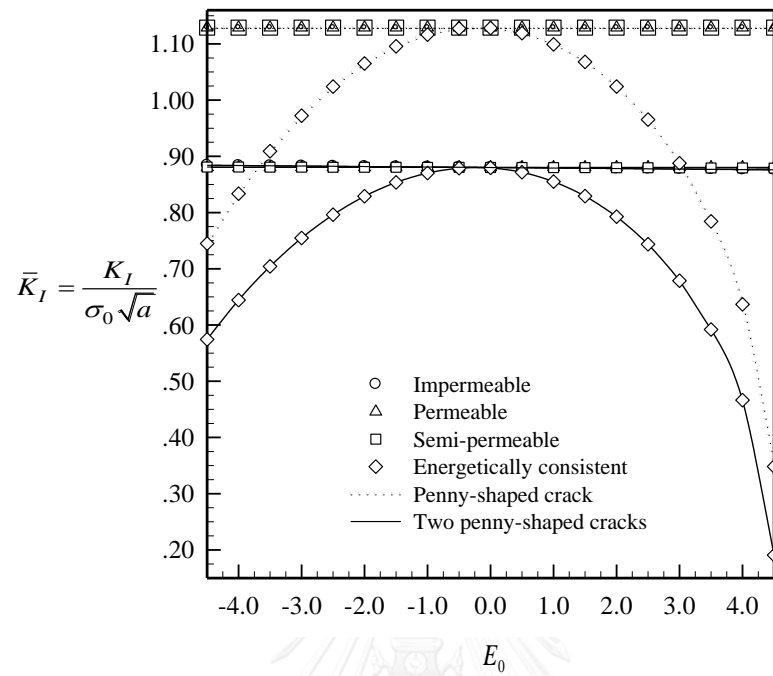
In this special case, we aim to consider the influence of electric field by discussing a two penny-shaped cracks in vertical direction embed in a transversely isotropic piezoelectric infinite medium. The geometry, the mesh and the material properties of piezoelectric medium of the two penny-shaped cracks are analogous to section 4.2.3.1. The major difference from the previous investigation are that (i) the radius a the distance L of a two penny-shaped cracks are fixed as 1 and 0.5 respectively (ii) the applied uniaxial remote stress is fixed as 50 MPa, (iii) The applied electric field E_0 is now varied from $[-4.5, -4, -3.5, \dots, 4.5]$ MV/m which is similar to the other cracks, and (iv) the dielectric permittivity inside the crack gap is fixed $\epsilon_c = 5\epsilon_0$ where $\epsilon_0 = 8.85 \times 10^{-12}$ C/Vm is the permittivity of the air in the crack gap. The numerical results reported in figures 4.33 (a) and (b) are obtained from the point along the crack front of a penny-shaped crack. It is seen that as the applied electric field increases $[-4.5$ to 4.5 MV/m],

the magnitude of the normalized stress and electric K_I and K_{IV} along the crack front is slightly discrepant from the single penny shaped crack. For example, the magnitude of the two penny-shaped crack is clearly less than that of the penny-shaped crack of both K_I and K_{IV} . Moreover, the behaviors of both cracks (i.e., the two penny-shaped crack and the penny-shaped crack) are completely identical which can be observed in detail as follows.

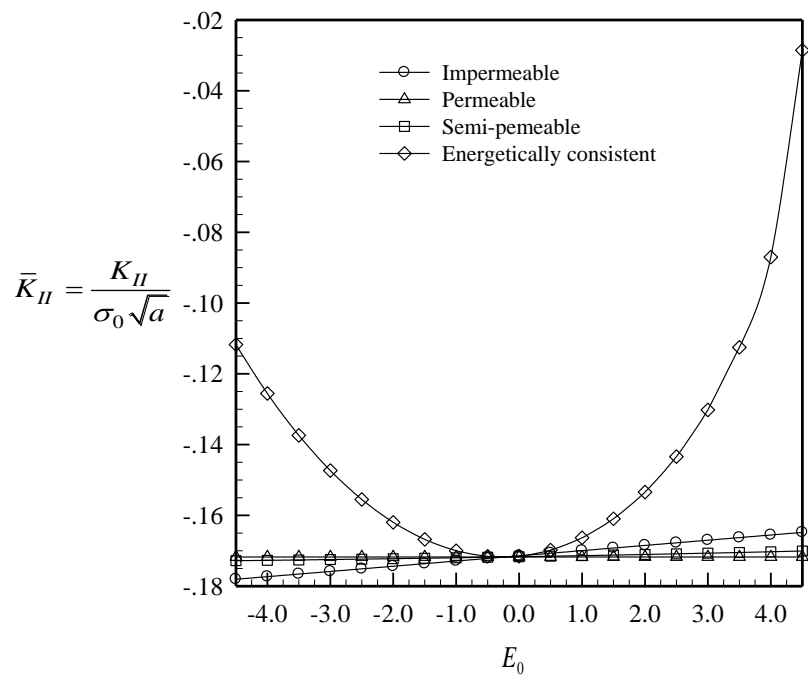
First, the numerical results of stress intensity factors K_I on four crack-face models (i.e., impermeable, permeable, semi-permeable and energetically consistent models) reported in figure 4.33 (a) are obtained. It can be found that when the electric field varies from $[-4.5$ to 4.5 MV/m], the three models (i.e., impermeable, permeable and semi-permeable models) are nearly identical and are weak dependent of the increase of the electric field which is similar to the behavior of planar cracks (i.e., the penny-shaped crack). Moreover, as the electric field increases, the energetically consistent model analogous to penny-shaped crack strongly depends on the electric field. The figures 4.33(a) also reveal that the turning point of the negative and positive range occurs at $E_0 = 0$ MV/m. This can be implied that as the electric field increases, the trend of stress intensity factor K_I on four models of the two penny-shaped cracks with the distance of both cracks $L=0.5$ are very similar to those of penny-shaped crack or the general planar cracks.

In this special case, the stress intensity factor K_{II} obtained from two penny-shaped crack in vertical direction under four models (i.e., impermeable, permeable, semi-permeable and energetically consistent models) are proposed. It is found that increasing the electric field, K_{II} of impermeable, semi-permeable and energetically consistent models are significantly dependent of electric field whereas the permeable model is independent of electric field at the entire range. However, the distribution of four models are negative values. Similarly the electric field $E_0 = 0$ MV/m is the point that the energetically consistent model start to decrease the magnitude. This reveal that when the distance of the two crack is relative small, it give rise to appear K_{II} and it influences to impermeable, semi-permeable and energetically consistent models

Eventually, the influence of numerical result on intensity factor obtained from four crack-face models (i.e., impermeable, permeable, semi-permeable and energetically consistent models) are proposed. It reveal that with the increase of the electric field from $[-4.5$ to 4.5 MV/m], the trends of the normalized electric K_{IV} of both two penny-shaped cracks and penny-shaped crack are very identical; nevertheless, the magnitude of the two penny-shaped cracks is less than the single penny-shaped crack. It can be observed from figure 4.33 (b) again that the lower bound on the range of the positive electric is permeable model, whereas the upper bound is still impermeable model. Moreover, it is similar to penny-shaped crack that the permeable models are clearly independent of the increasing electric field. On the other hand, the two models (i.e., impermeable and semi-permeable models) extremely depend on the increasing electric field and the results reveal in the figure that the turning point of the electric field range is at $E_0 = 0$ MV/m. This can be implied that the K_{IV} of the two penny-shaped crack in vertical direction on four models exhibits the same behaviors as those of the penny-shaped crack.



(a)



(b)

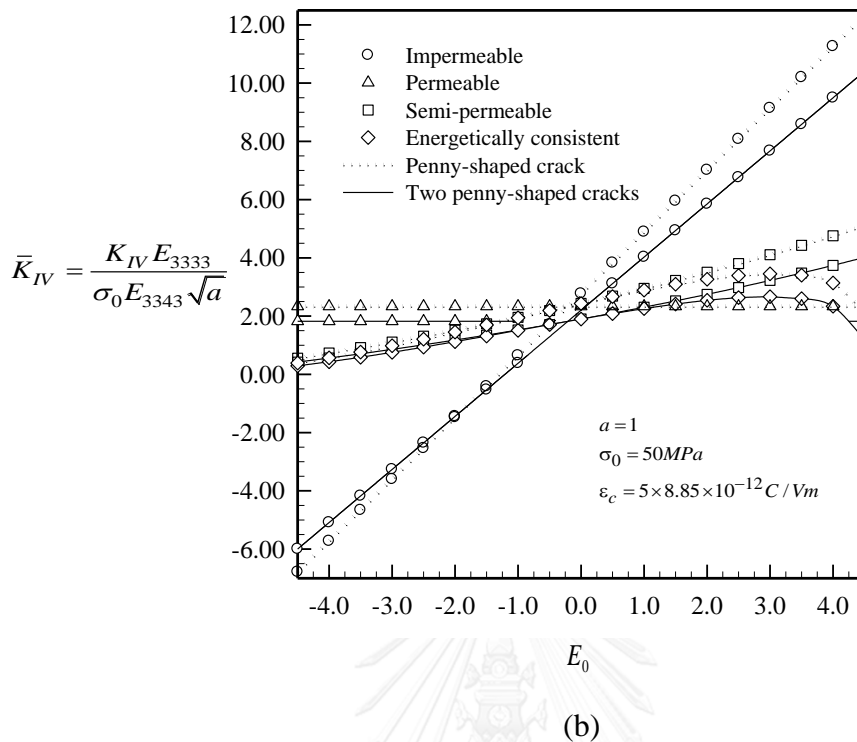


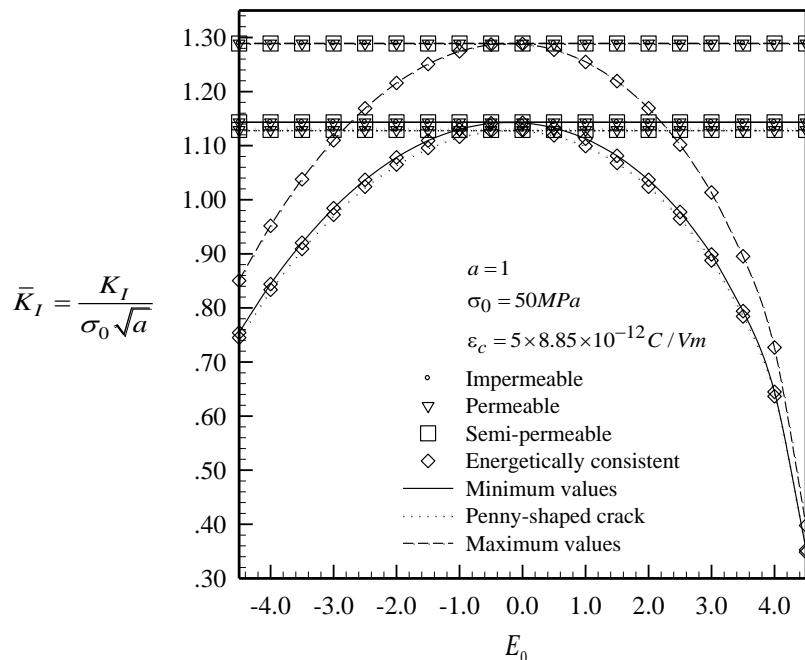
Figure 4.33 (a), (b) and (c) are dependent of normalized stress and electric intensity factors $[K_I, K_{II}, K_{IV}]$ on the electrical load for two penny-shaped cracks in infinite medium. Results are reported on one penny-shaped crack

4.3.3.2 Influence of remote electrical load on two penny-shaped crack in horizontal direction

For final investigation, we again focus on the influence of electric field by considering a two penny-shaped cracks in horizontal direction containing in a transversely isotropic piezoelectric infinite medium. The geometry of the crack, the mesh and the material properties of piezoelectric medium of the two penny-shaped cracks are analogous to the section 4.2.3.2. The major difference from the previous research are that (i) the radius a the distance L of a two penny-shaped cracks are fixed as 1 and 2.25 (horizontal direction) respectively, (ii) the applied uniaxial remote stress is fixed as 50 MPa, (iii) the applied electric field E_0 is now varied from $[-4.5, -4, -3.5, \dots, 4.5]$ MV/m which is similar to the previous cracks, and (iv) the dielectric permittivity inside the crack gap is fixed $\epsilon_c = 5\epsilon_0$ where $\epsilon_0 = 8.85 \times 10^{-12}$ C/Vm is the permittivity of the air in the crack gap. The effects illustrated in figures 4.34 (a) and (b) are gained from the two different points (i.e., maximum and minimum values) along the crack front of a penny-shaped crack. From the influence the increasing applied electric field from -4.5 to 4.5 MV/m, it can be found that the magnitude of the normalized stress and electric K_I and K_{IV} of two points along the crack front are the same as those of the pure penny shaped crack. However, the behaviors of the both cracks (i.e., the two penny-shaped crack in horizontal direction and the penny-shaped crack) are completely identical which is similar to the previous section. This can be concluded in detail as follows.

Figure 4.34 (a) shows that as the electric field increases from negative to positive values [-4.5 to 4.5 MV/m], the stress intensity factors K_I obtained from both points (i.e., maximum and minimum points) on four models are exactly identical to penny-shaped crack. There are a few identical points exhibited in this investigation. First, the three modes (i.e., impermeable, permeable and semi-permeable models) are independent of the electric field. Second, the energetically consistent models depend on increasing the electric field as discussed in previous sections. In addition, as the electric field increases, at the large distance of the two penny-shaped cracks the electric field does not affect the four models as penny-shaped crack should be.

Finally, the result in figure 4.34 (b) obtained from the maximum and minimum points of the two penny-shaped cracks are investigated. It is found that as the electric field increases, both the trends and the behaviors of the electric intensity factors K_{IV} are very identical to the penny-shaped crack. Again, the trends of two penny-shaped crack in horizontal direction can be concluded similarly to those mentioned in the previous discussion, e.g., the strong dependent on three models (i.e., impermeable, semi-permeable and energetically consistent models) of the electric field, the obvious independent of electric field on the permeable model. Besides, it should be noted that when the distance of the two penny-shaped crack is large, the influence of the increasing electric field is independent, and does not differ from the four boundary conditions as the penny-shaped crack should be.



(a)

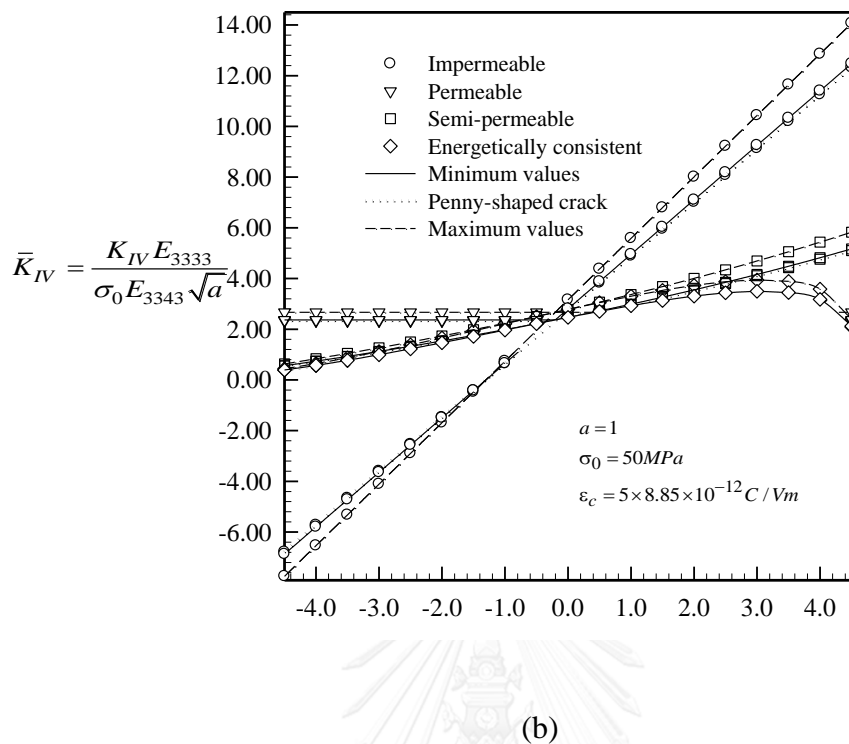


Figure 4.34 (a) and (b) are dependent of normalized stress and electric intensity factors $[K_I, K_{IV}]$ on the electrical load for two penny-shaped cracks in infinite medium. Results are reported on the maximum and minimum values

4.4 Influence of permittivity on four crack-face boundary conditions

In this section, the influence of permittivity inside the crack gap are investigate on stress and electric intensity factors along the crack front are investigated on four crack-face models (e.g., impermeable, permeable, semi-permeable and energetically consistent models). The multiple cracks including planar and non-planar are adopted for this study are utilized such as the non-planar cracks (e.g., spherical cap and cylindrical cracks), the planar cracks (e.g., the tunnel crack and two pair of penny-shaped cracks in both vertical and horizontal directions) which can discuss in the following sections.

4.4.1 Influence of permittivity on spherical cap and cylindrical crack

First, the non-planar cracks such as spherical cap and cylindrical cracks are utilized to investigate the influence of permittivity inside the crack gap on stress and electric intensity factors. The investigation will be carried out in subsection follow.

4.4.1.1 Influence of permittivity on spherical cap crack

In this special case, we investigate the influence of the permittivity ϵ_c of a medium inside the crack gap by considering the spherical cap cracks with radius R embedded

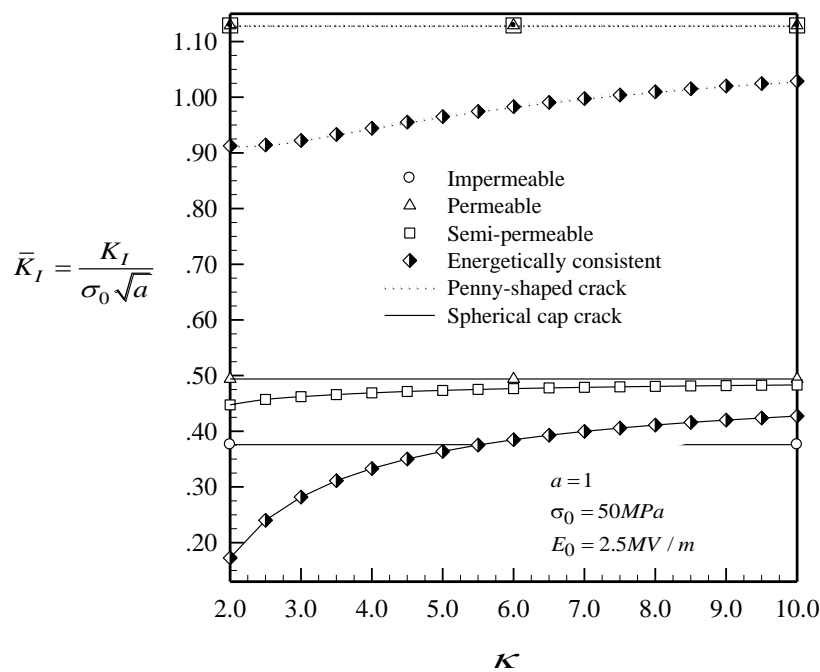
a piezoelectric infinite medium which is made of PZT-4 similar to the previous case. The key information different from the previous case are that (i) the permittivity of a medium inside the crack gap which is determined by $\varepsilon_c = \kappa\varepsilon_0$ where κ is termed the relative permittivity and $\varepsilon_0 = 8.85 \times 10^{-12} \text{ C/(Vm)}$ is the permittivity of the air that can be varied [$\kappa = 2, 2.5, 3, 3.5, \dots, 10$], (ii) the half subtended angle and the radius R of the spherical cap crack are defined as $\theta = 45$ degree and $R = 1.2732395447352$, and (iii) the uniform remote tension σ_0 is determined to be 50 MPa whereas the electric field E_0 still remains at 2.5 MV/m, and (iv) only the finest meshes (144 elements) of crack configuration are utilized in the investigation. The numerical results of stress and electric intensity factors [K_I, K_{II}, K_{IV}] obtained from the average points along the crack front on four crack-face models (i.e., impermeable, permeable, semi-permeable and energetically consistent models) are investigated as shown in figures 4.35 (a),(b) and (c) which can be discussed in detail as follows.

The results reported in figure 4.35 (a) are obtained from the research on four crack-face models. It can be found that the stress intensity factor K_I of three models (i.e., impermeable, permeable and semi-permeable models) is not identical and the results of semi-permeable models depend on permittivity of the medium inside the crack gap. Accordingly, the magnitude increases from impermeable to the permeable modes when the values of permittivity increase. This is in contrast to the stress intensity factors K_I on the penny-shaped crack, in which those three models are identical and independent of the permittivity of the medium inside the crack gap. This follows the works of previous investigators (i.e., Li and Lee, 2004; Chen et al, 2000 and Chen and Lim, 2005) who specify that the three models (i.e., impermeable, permeable and semi-permeable models) are identical and independent of medium inside the crack gap and depend only on the mechanical loading. It can be found again from figure 4.32 (a) that the K_I of energetically consistent model strongly depends on the permittivity of medium inside the crack. In addition, the upper bound is permeable model whereas the lower bound is switched of energetically consistent and impermeable models. This finding is in contrast with the solution for penny-shaped cracks, in which the energetically consistent model is less than the other three models (i.e., impermeable, permeable and semi-permeable models) in the entire range of ε_c which is analogous to the prediction of Li et al, 2011. This can be implied that the non-planar crack plays a significant role on K_I for three crack model.

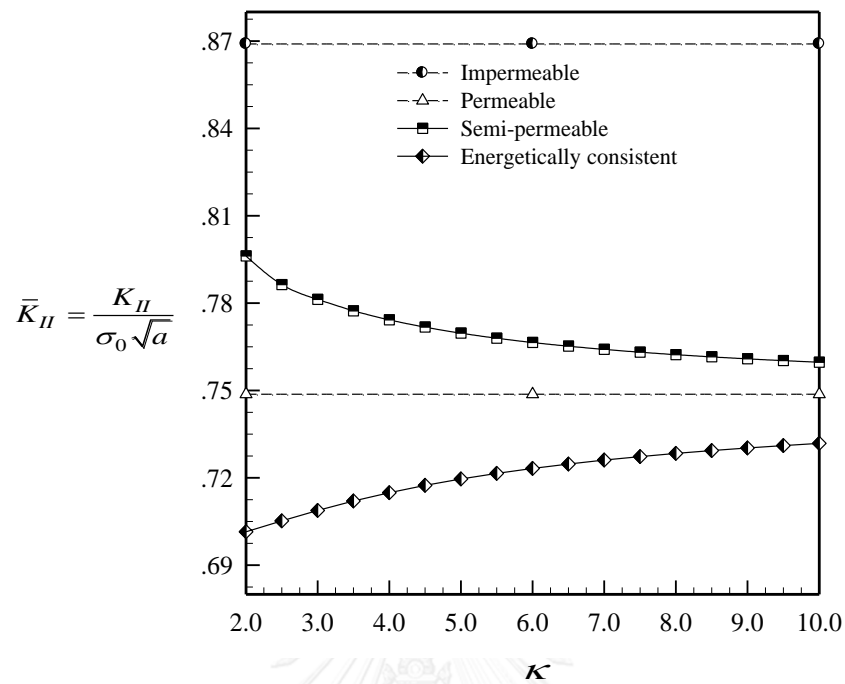
Next, the numerical results stress intensity factors K_{II} obtained from the average points along the crack front are studied as reported in figure 4.35 (b). It is found that when the permittivity of medium inside the crack gap increase, the magnitude of three models (e.g., impermeable, permeable and semi-permeable models) are strongly different. It can be observed further from figure that the semi-permeable model is varied from the impermeable to permeable model which is in contrast with the semi-permeable model of stress intensity factors K_I . Moreover, it is again seen that the upper bound is completely impermeable model whereas the lower bound still remains the energetically consistent model. Besides, results also reveal that the energetically consistent model varies from lower bound and that one approaches to the permeable model when the permittivity of the medium increase. This indicates that increasing the permittivity of non-planar crack has essentially influence to the behavior of semi-permeable model.

Finally, the electric intensity factors K_{IV} gained from four models (i.e., impermeable, permeable, semi-permeable and energetically consistent models) are

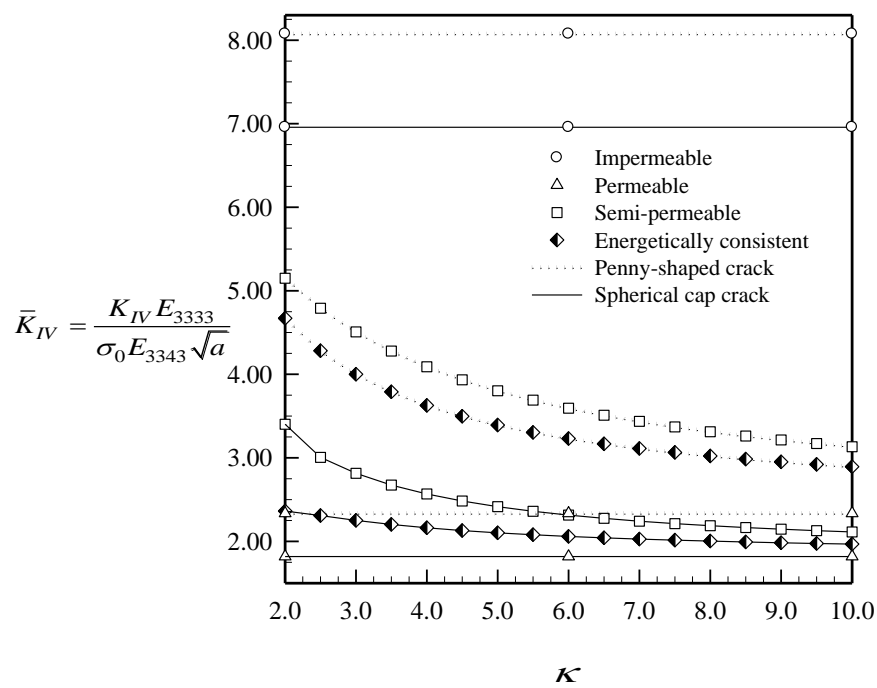
investigated as reported in figure 4.35 (c). It is manifested that as the permittivity ϵ_0 of medium inside the crack gap increase, the two models (i.e., semi-permeable and energetically consistent models) are decreased and are strongly dependent on the medium inside the crack gap. This behavior is similar to that of the penny-shaped crack which is different to the stress intensity factors K_I . It is also found that the semi-permeable model varies from impermeable to permeable model, and that the upper bound is impermeable models whereas the lower bound still remains permeable model. This indicates that the influence of permittivity inside the crack gap affects the magnitude of two models (i.e., semi-permeable and energetically consistent models).



(a)



(b)



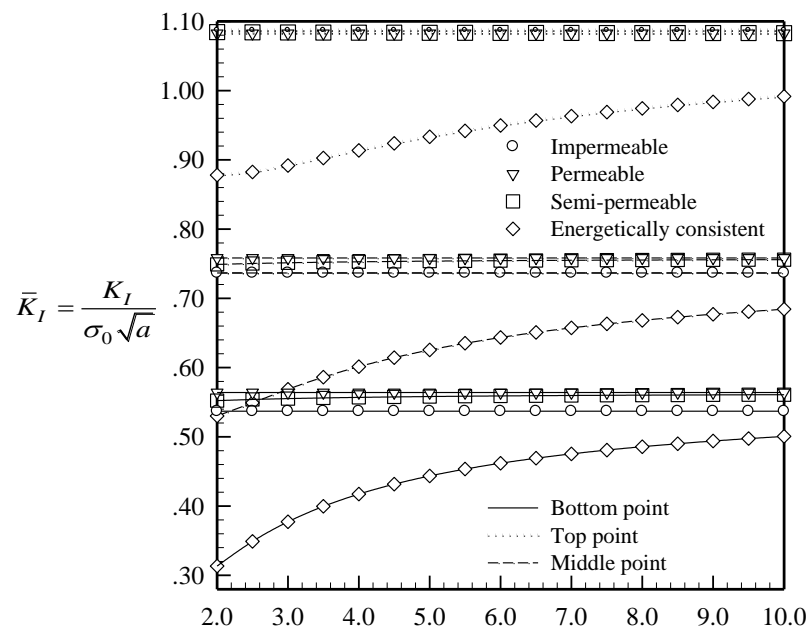
(c)

Figure 4.35 (a), (b) and (c) are dependent of normalized stress and electric intensity factors $[K_I, K_{II}, K_{IV}]$ on the permittivity for spherical cap cracks in infinite medium. Results are reported as average values

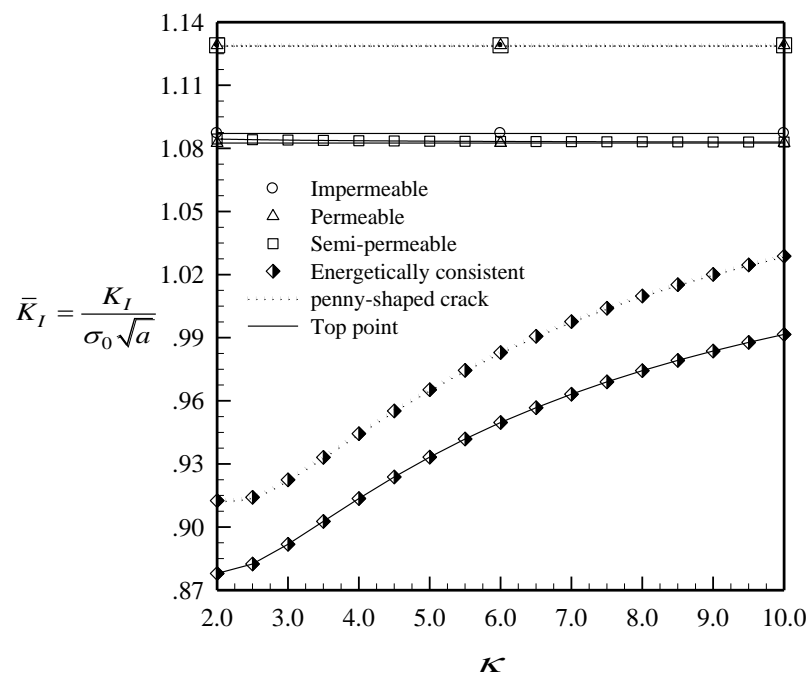
4.4.1.2 Influence of permittivity on cylindrical crack

Next, we consider the influence of the permittivity ε_c of a medium inside the crack gap for a cylindrical cracks with radius R embed in a piezoelectric infinite medium which is made of PZT-4 analogous to the previous section. The main distinction from the previous section are that (i) the permittivity of a medium inside the crack gap which is determined by $\varepsilon_c = \kappa\varepsilon_0$ where $\varepsilon_c = \kappa\varepsilon_0$ is termed the relative permittivity and $\varepsilon_0 = 8.85 \times 10^{-12}$ C/(Vm) is the permittivity of the air which can be varied [$\kappa = 2, 2.5, 3, 3.5, \dots, 10$], (ii) the half subtended angle and the radius R of the cylindrical crack are determined as $\theta = 45$ degree and $R = 1.2732395447352$, (iii) the uniform remote tension σ_0 is determined as 50 MPa whereas the electric field E_0 is fixed as 2.5 MV/m, and (iv) only the finest meshes (144 elements) similar to previous section are employed in the study. In this special case, the numerical results of stress and electric intensity factors [K_I, K_{II}, K_{IV}] and K_{III} (only middle point) obtained from the three distinct points (i.e., top, middle and bottom points) of a quarter [1/4] along the crack front on four crack-face models (i.e., impermeable, permeable, semi-permeable and energetically consistent models) are explored as shown in figures 4.36 (a) to (d), 4.37 (a) to (d), 4.38 and 4.39(a) to (d). This would be discussed in detail as follows.

The effects reported in figure 4.36 (a), (b), (c) and (d) are obtained on four crack-face models. It can be found that as the permittivity ε_c increases, the stress intensity factor K_I at three points (i.e., top, middle and bottom points) of three models (i.e., impermeable, permeable and semi-permeable models) are clearly different. Such differences depend on the three points. For example, at the top point, the discrepancy of the three models is small but will be large at the lower points (e.g., middle and bottom points). It can be observed further that the three points of semi-permeable models are dependent on permittivity of the medium inside the crack gap and that the semi-permeable model varies from impermeable to permeable models which is different from the solutions of three models for penny-shaped crack found in the works of many investigators (e.g., Li and Lee, 2004; Chen et al., 2000 and Chen and Lim, 2005). Figure 4.36 (b),(c) and (d) show that the predicted K_I of energetically consistent models of the three points (i.e., top, middle and bottom points) increase and strongly depend on the permittivity of medium inside the crack gap, and that the energetically consistent model approaches to permeable model analogous to penny-shaped crack. Similarly, the bounds of the obtained stress intensity factors K_I at the three points are identical, i.e., the upper bounds at the top, the middle and the bottom points are impermeable whereas the lower bound is energetically consistent and model. This behavior is in agreement with the solution for penny-shaped cracks in which energetically consistent is less than the three models (i.e., impermeable, permeable and semi-permeable models). This is also similar to the work of Li et al., 2011 with the increase of the permittivity as mentioned in the previous Section. This can be implied that the cylindrical crack is distinct for three crack models at all points.



(a)



(b)

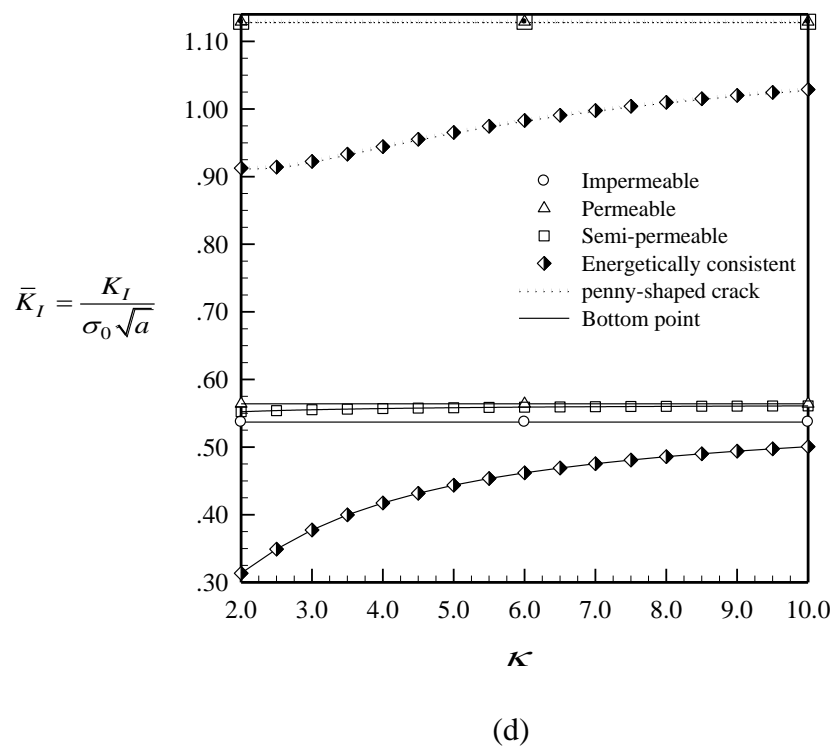
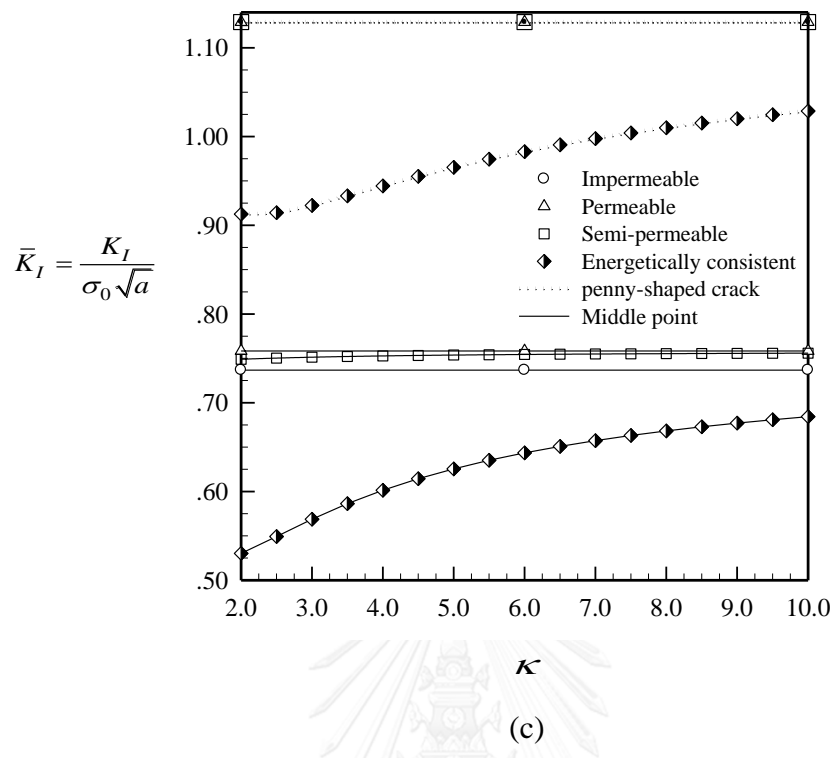
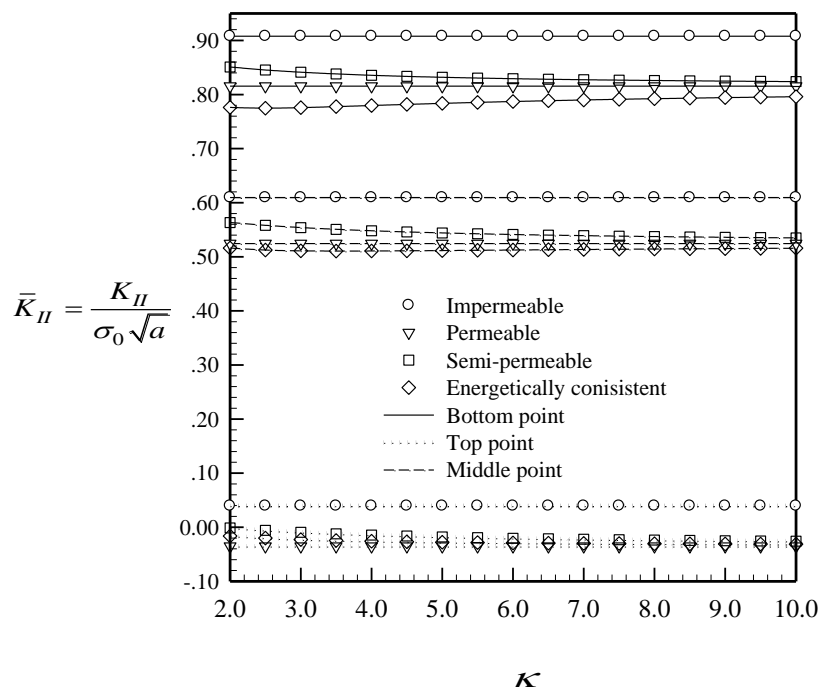
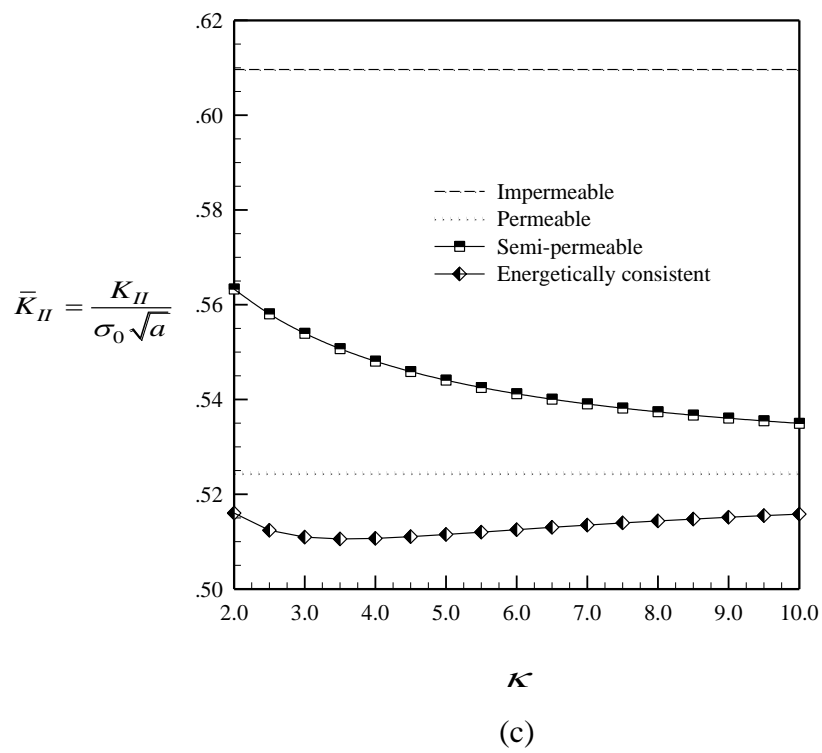
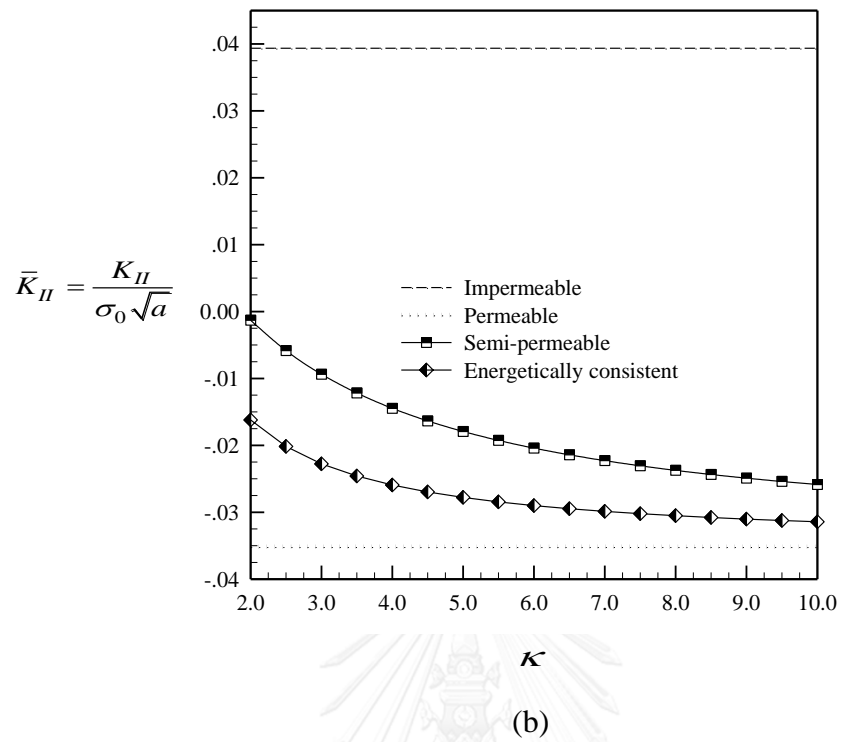


Figure 4.36 (a), (b), (c) and (d) are dependent of normalized stress intensity factors $[K_I]$ on the permittivity for a cylindrical cracks in infinite medium. Results are reported on all points, the top, middle and bottom points

Here we investigate the influence of permittivity on stress intensity factors K_{II} at three points along the crack front, on four crack-face models (i.e., impermeable, permeable, semi-permeable and energetically consistent models) as shown in figure 4.37 (a), (b), (c) and (d). It can be found that as the permittivity ε_c increases, the magnitude of stress intensity factor K_{II} at the bottom point is greater than at the middle and the top points respectively. Moreover, the bottom point exhibits the discrepancy of the magnitude which is greater than the remaining points for instance, the three models (i.e., impermeable, permeable and semi-permeable models) at any points are completely different. More specifically, the semi-permeable at three points also decreases and approaches to permeable model which depends on the three points. Clearly, the upper bounds at the all points are impermeable model whereas the lower bounds of the top point are permeable model, and energetically consistent model for the two remaining points (i.e., middle and bottom points). This can be concluded that when the permittivity increases, it has an influence on the lower bound of three different points which is not identical.



(a)



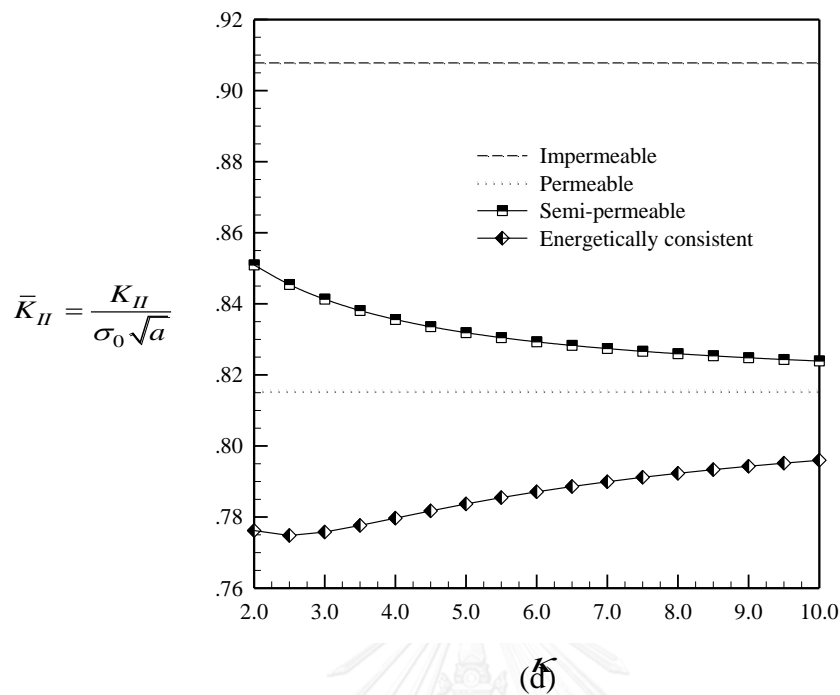


Figure 4.37 Dependent of normalized stress intensity factors $[K_{II}]$ on the permittivity for a cylindrical cracks in infinite medium. Results are reported on (a) all points, (b) top, (c) middle and (d) bottom points

Results shown in figure 4.38 gained from normalized stress intensity factors K_{III} only at the middle point on four models along the crack front are investigated. It can be found that with the increasing permittivity, the upper bound and lower bound of predicted solutions of both semi-permeable and energetically consistent models are impermeable and permeable respectively. Moreover, the three models (i.e., impermeable, permeable and semi-permeable models) are different and are dependent of permittivity which is similar to the stress intensity factors $[K_I, K_{II}]$ as discussed in prior discussion. In addition, it can be observed further that the semi-permeable and energetically consistent models share similar trends, and that those two models vary from impermeable to permeable model when the permittivity increases. In conclusion, it can be summarized that the permittivity has influence to magnitude of the semi-permeable model and the energetically models.

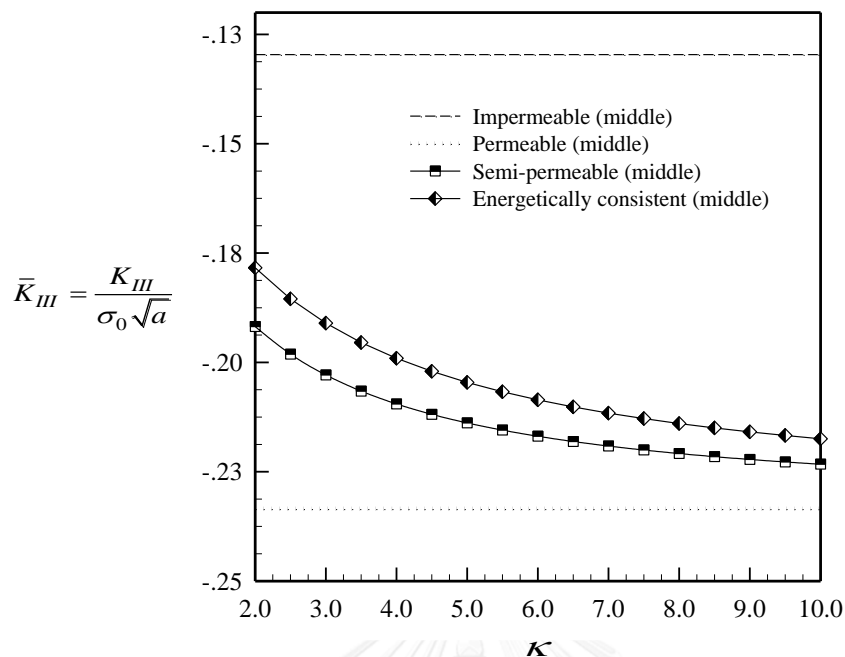
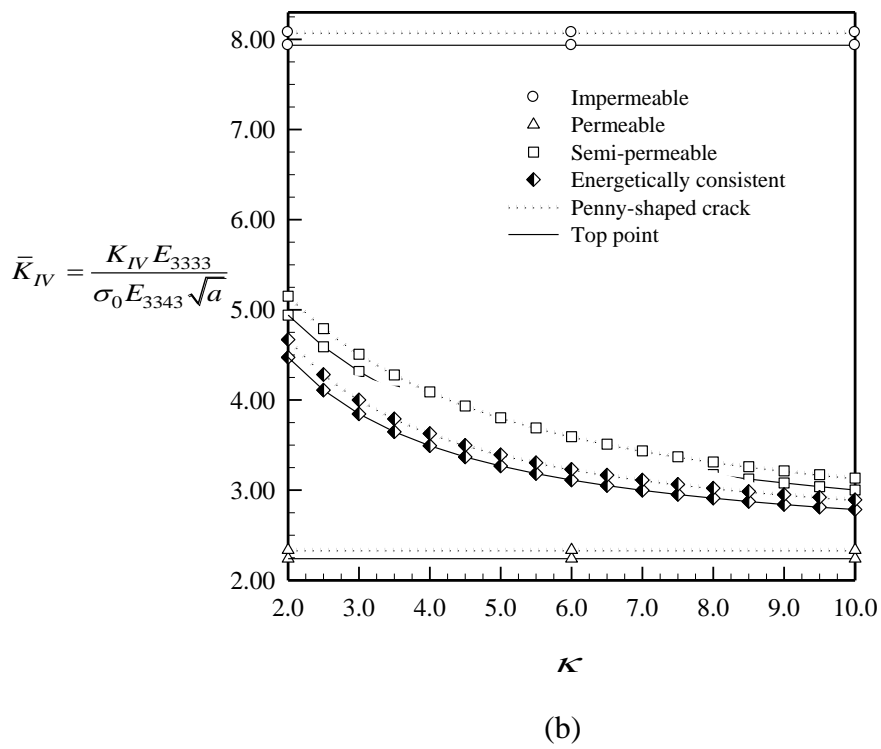
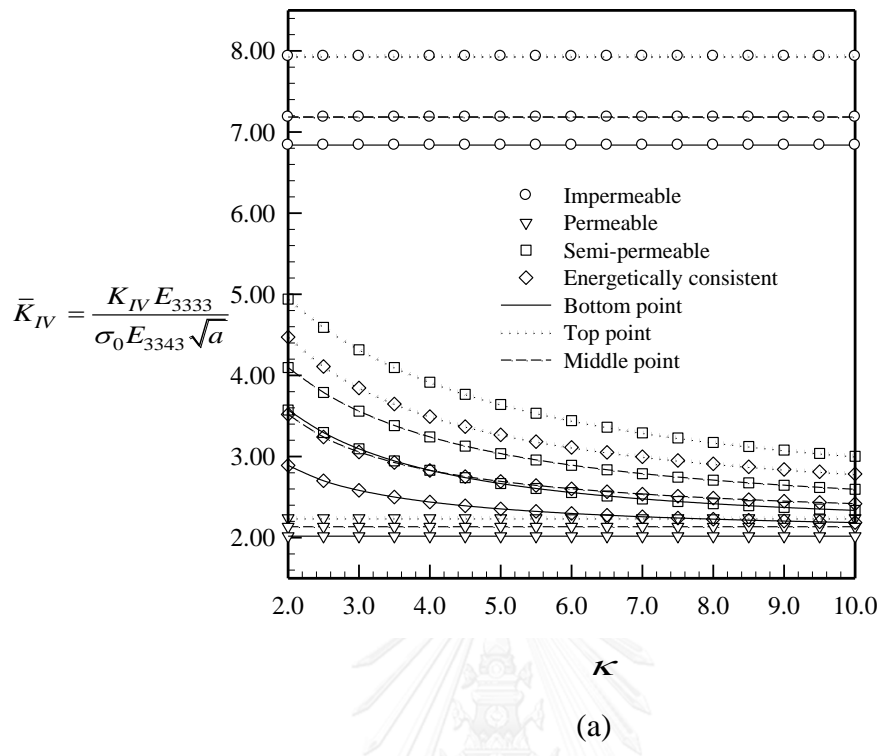


Figure 4.38 Dependent of normalized stress intensity factors $[K_{III}]$ on the permittivity for a cylindrical cracks in infinite medium. Results are reported on the middle point

Finally, the influence of permittivity on the electric intensity factors K_{IV} on four models (i.e., impermeable, permeable, semi-permeable and energetically consistent models) at three different points (i.e., top, middle and bottom points) are illustrated in figure 4.39 (a), (b), (c) and (d). It can be found that as the permittivity increases, the magnitude of top point is greater than that of other points (i.e., middle and energetically consistent). The trends of K_{IV} at those three points, however, are identical. For example, the three models (i.e., impermeable, permeable, semi-permeable models) are also not identical and the two models including the semi-permeable and energetically consistent models share rather similar trends and are strongly dependent of permittivity inside the crack gap. Moreover, those two models again varies from impermeable to permeable models. Besides, it is seen again from the figures that at three different points, the upper bound and lower bound still remain impermeable and permeable respectively. In short, it can conclude that the increasing permittivity affects only the magnitude of semi-permeable and energetically consistent models respectively.



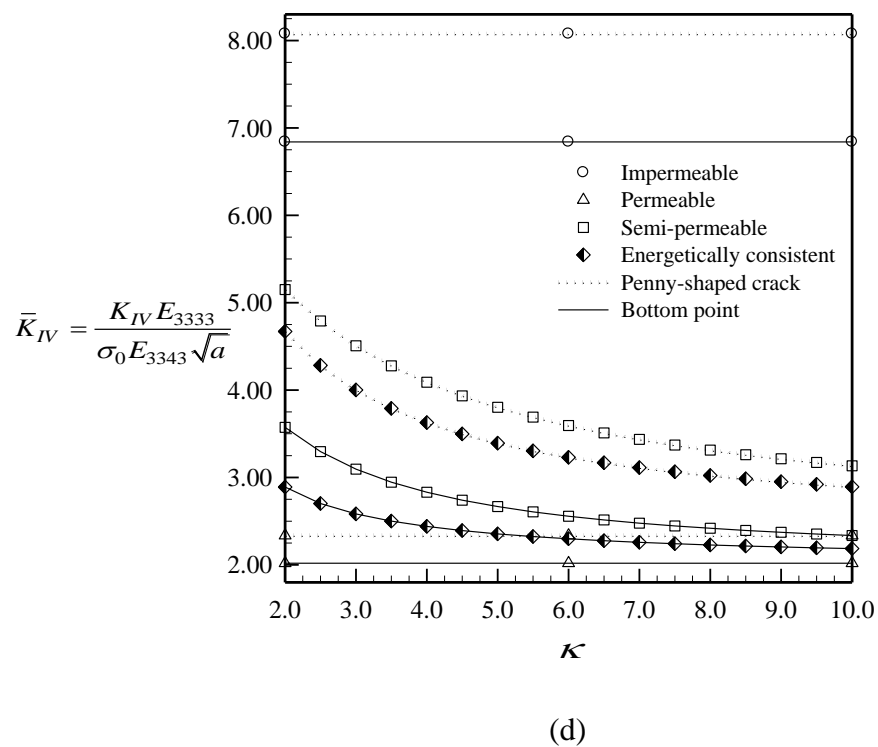
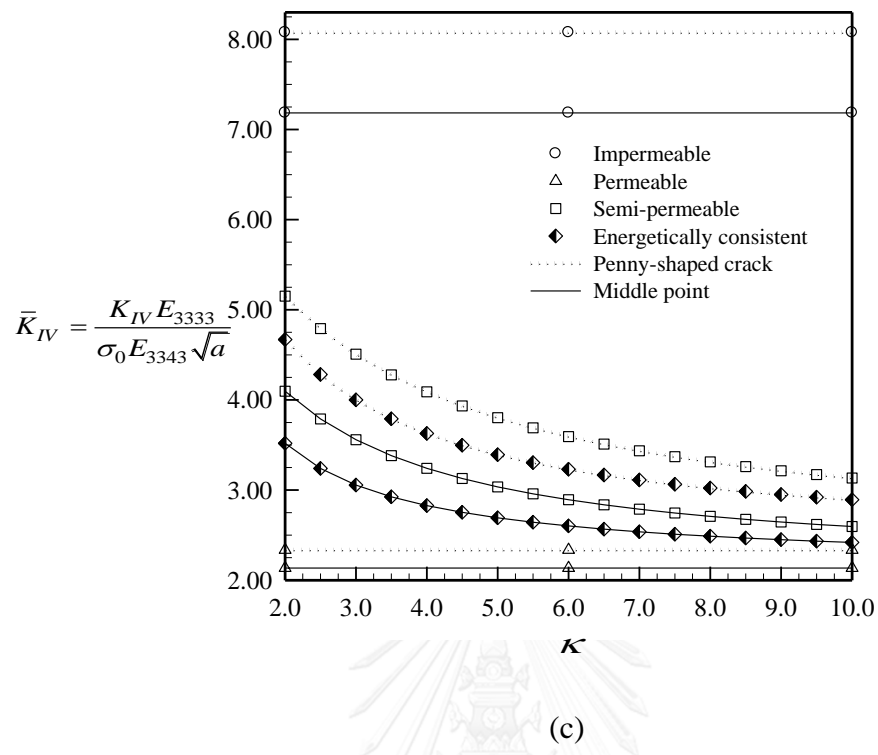


Figure 4.39 Dependent of normalized electric intensity factors [K_{IV}] on the permittivity for a cylindrical cracks in infinite medium. Results are reported on (a) all points, (b) top, (c) middle and (d) bottom points

4.4.1.3 Comparison between spherical cap and cylinder cracks

Throughout the discussion, for the influence of permittivity above on the stress and electric intensity factors [K_I, K_{II}, K_{IV}] obtained from both spherical cap crack and the top point of cylindrical crack on four models (i.e., impermeable, permeable, semi-permeable and energetically consistent models) there are a few important points which can be compared as follows.

Results of the spherical cap crack can be predicated as follow. It is found that the stress intensity factor K_I of three models are not identical and the results of semi-permeable models are dependent on permittivity of the medium inside the crack gap. In contrast with the stress intensity factors K_I on the penny-shaped crack, those three models are identical and are independent of the permittivity of the medium inside the crack gap. Moreover, It is seen again that the K_I of energetically consistent model of both cracks (i.e., spherical cap and penny-shaped crack) strongly depends on the permittivity of medium inside the crack gap and the results also reveal that the upper bound is permeable models whereas the lower bound is switched of energetically consistent and impermeable models. This finding is in contrast with the solution for penny-shaped cracks that one is less than the three models (e.g., impermeable, permeable and semi-permeable models) in the entire range of ε_c . For the cylindrical crack, the stress intensity factors K_I obtained from the top, middle and bottom points can be compared with other cracks that increasing the permittivity, the magnitude K_I of penny-shaped crack are greater than the magnitude of K_I obtained from three points. It is also found that the behaviors of spherical cap crack of four models are very similar to K_I of cylindrical crack at the bottom point; in contrast, the behavior of penny-shaped crack on four models are very identical to K_I of cylindrical crack at the top point. In addition to the similarity of those crack behaviors, it is also found that the dependent of three crack models (i.e., impermeable, permeable and energetically consistent models) of increasing the permittivity strongly depend on the points along the crack front for example at the top and bottom points of cylindrical crack along the crack front, it is found that the three models are nearly identical at the top point whereas the three models of K_I at bottom point can clearly see the distinct of the three models ; moreover, the energetically consistent model of cylindrical (at all points) and penny-shaped crack is strongly still dependent on increasing the permittivity at the entire range

Next, the stress intensity factor K_{II} harvested from spherical cap crack is found that increasing the permittivity, the three models (i.e., impermeable, semi-permeable and energetically consistent models). It is found that when the permittivity of medium inside the crack gap increase, the magnitude of three models (e.g., impermeable, permeable and semi-permeable models) are strongly different whereas the penny-shaped crack have zero intensity factor K_{II} . Moreover, it is again seen that the upper bound is impermeable model whereas the lower bound still remains the energetically consistent model. Besides, results also reveal that the energetically consistent and semi-permeable models are strongly dependent of increasing the permittivity. Parallel to spherical cap crack is cylindrical crack. The stress intensity factors K_{II} at three different points (i.e., top, middle and bottom points) are harvested to compare the spherical cap crack. It is found that the magnitude of three points of cylindrical crack are completely different; however, the behavior at the top point of cylindrical crack are very identical to spherical cap crack. Again, a part from the similarity of both cracks, it is found that

the lower bound of three point of cylindrical crack strongly depend on the points along the crack front for example at top point, lower bound is permeable whereas the lower bound is energetically consistent model at the middle and bottom points

For the stress intensity factors K_{III} gained only at the middle point of cylindrical crack can be conclude that, the three models (i.e., impermeable, permeable, semi-permeable and energetically consistent models) are completely different when the permittivity increase; more specifically, the semi-permeable and energetically consistent models are identical and are dependent of increasing permittivity

Finally, the electric intensity factors K_{IV} on four models (i.e., impermeable, permeable, semi-permeable and energetically consistent models) of spherical cap crack can be concluded that the magnitude of penny-shaped crack on four models are greater than magnitude of spherical cap crack when the permittivity increase. It is found that the two models (e.g., semi-permeable and energetically consistent models) are decreased and are strongly dependent on the medium inside the crack gap similar behavior to the penny-shaped crack. It is also seen that the semi-permeable and energetically consistent models varies from impermeable to permeable models and results show that the upper bound is impermeable models whereas the lower bound still remains permeable model, for both spherical and penny-shaped crack. Identically, the results from cylindrical crack are obtained on four crack models. It is found that the magnitude of three different points are completely different. Moreover, result also reveal that the K_{IV} of spherical cap crack are very identical to the bottom point of cylindrical; in contrast, K_{IV} of penny-shaped crack are very identical to the top point of cylindrical crack.

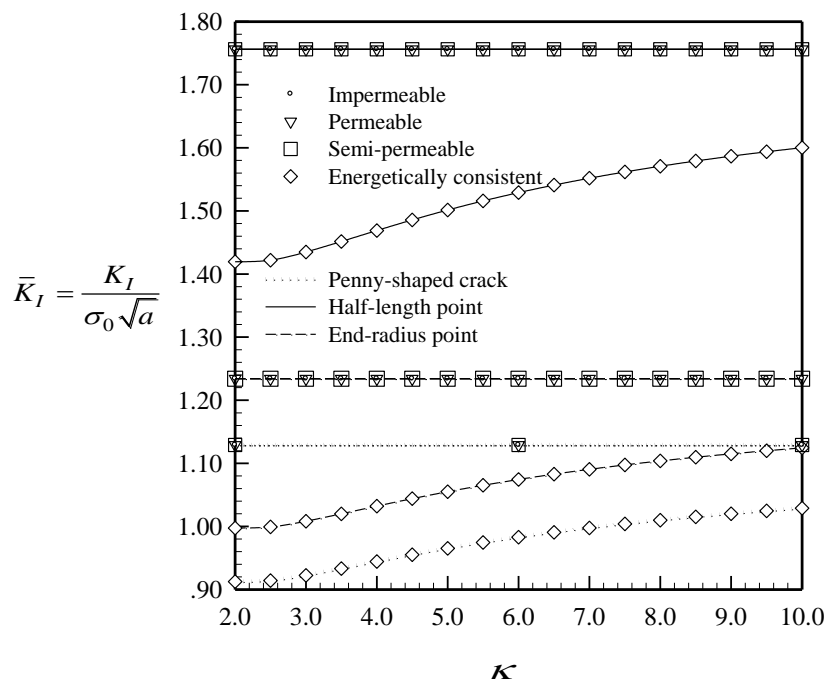
4.4.2 Influence of permittivity of tunnel crack

In this case, the influence of the permittivity ε_c of a medium inside the crack gap is considered for a tunnel cracks with end-radius a and the half-length L containing in a piezoelectric infinite medium which is made of PZT-4 similar to the previous section. The main parameter difference from the previous section are that (i) the permittivity of a medium inside the crack gap which is determined by $\varepsilon_c = \kappa\varepsilon_0$ where κ is termed the relative permittivity and $\varepsilon_0 = 8.85 \times 10^{-12} \text{ C/(Vm)}$ is the permittivity of the air which can be varied [$\kappa = 2, 2.5, 3, 3.5, \dots, 10$], (ii) the end-radius and the half-length of the crack are defined as 1 and 5, (iii) the uniform remote tension σ_0 is determined as 50 MPa whereas the electric field E_0 is fixed as 2.5 MV/m, and (iv) only the finest meshes (180 elements) similar to the non-planar section are utilized in the investigation. The numerical results of stress and electric intensity factors [K_I, K_{IV}] offered from the two different points (i.e., end-radius and half-length points) along the crack front on four crack-face models (i.e., impermeable, permeable, semi-permeable and energetically consistent models) are investigated as displayed in figures 4.40 (a) and (b). This would be discussed in detail as follows.

From results illustrated in figure 4.40 (a) on stress intensity factor K_I of four models, (i.e., impermeable, permeable, semi-permeable and energetically consistent models), it is found that that as the permittivity increases $\varepsilon_c = \kappa\varepsilon_0$ from [2 to 10], the magnitude of both points (i.e., end-radius and half-length points) become greater than that of penny-shaped crack. The trend and behaviors of both cracks, however, is nearly identical. For example, the three models (i.e., impermeable, permeable and semi-

permeable models) of both points of tunnel crack are again the same as penny-shaped crack and those three models serve as upper bound analogous to the work of many researchers (e.g., Li and Lee, 2004; Chen et al, 2000 and Chen and Lim, 2005). In addition, the energetically consistent models of both point are still dependent of the increase of the permittivity inside the crack gap, and serve as the lower bound and approaches to the upper bound similar to the solutions of Li et al, 2011. This can be implied that the increasing permittivity has influence only to the magnitude of the stress intensity factor K_I of both points which is not different to penny-shaped crack

Finally, the influence of electric intensity factors K_{IV} of two different points on four models are investigated as illustrated in figures 4.40 (b). As the permittivity varies from [2 to 10], the magnitude of electric intensity factors K_{IV} of both points between the end-radius and the half-length points are again greater than that of the penny-shaped crack. The experiment shows that the semi-permeable and energetically consistent models are strongly dependent of permittivity and are identical to the two models of penny-shaped crack. In addition, the upper and lower bound serves as the impermeable and permeable models. Such result is again similar to the planar crack. This can be concluded that as the permittivity increases with the half-length as 5, only the magnitude is greater than penny-shaped crack. Nevertheless, the trends on electric intensity factor of both points (i.e., end-radius and half-length points) are identical.



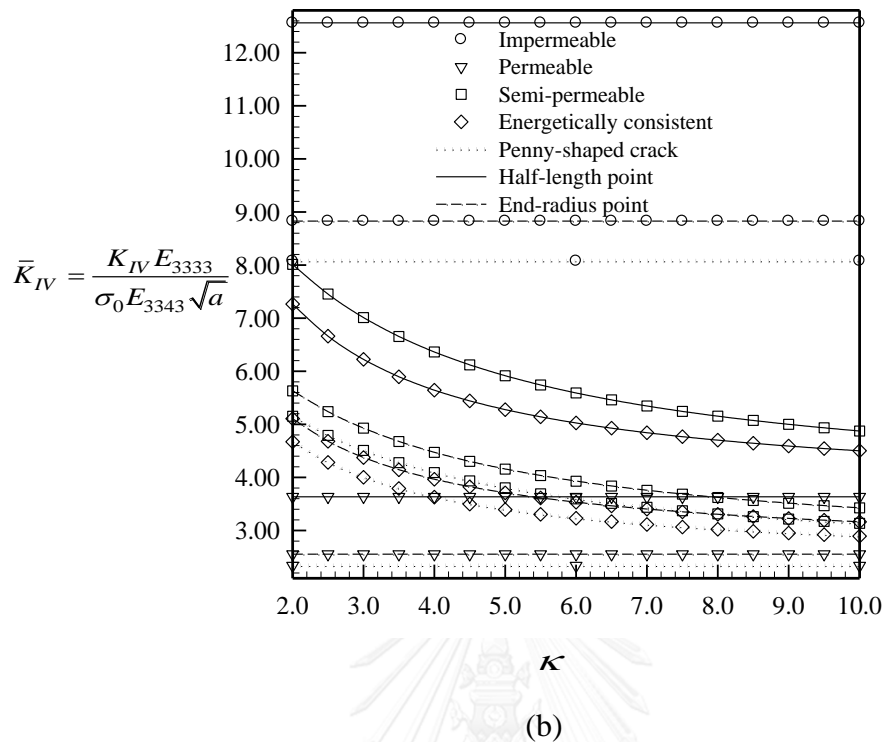


Figure 4.40 (a) and (b) are dependent of normalized electric intensity factors $[K_I, K_{IV}]$ on the permittivity for a tunnel crack in infinite medium. Results are reported on the end-radius and half-length points

4.4.3 Influence of permittivity of two penny-shaped crack in vertical direction

For this part, we investigate the influence of the permittivity ε_c of a medium inside the crack gap by applying the two-penny-shaped cracks in vertical direction with radius a and the distance of the two cracks L containing in a piezoelectric infinite medium which is made of PZT-4 similar to the previous sections. The main differences from the previous section are that (i) the permittivity of a medium inside the crack gap which is defined by $\varepsilon_c = \kappa \varepsilon_0$ where κ is termed the relative permittivity and $\varepsilon_0 = 8.85 \times 10^{-12} \text{C}/(\text{Vm})$ is the permittivity of the air that can be varied $[\kappa = 2, 2.5, 3, 3.5, \dots, 10]$, (ii) the radius and the vertical distance of the crack are defined as 1 and 5 respectively, (iii) the uniform remote tension σ_0 is determined as 50 MPa whereas the electric field E_0 is fixed as 2.5 MV/m, and (iv) only the finest meshes (144 elements per a penny-shaped crack) similar to the penny-shaped crack are employed in this study.

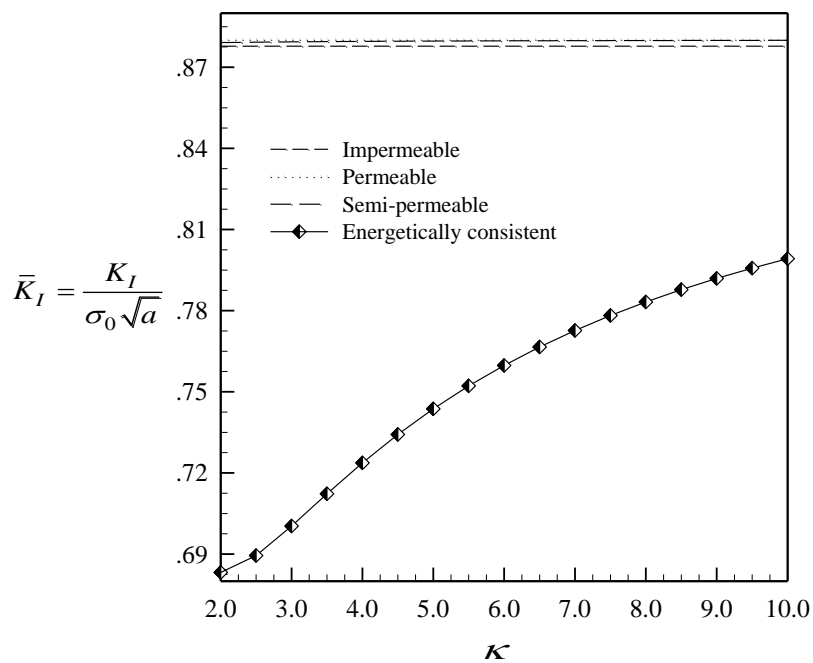
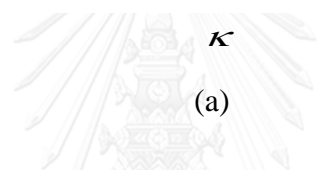
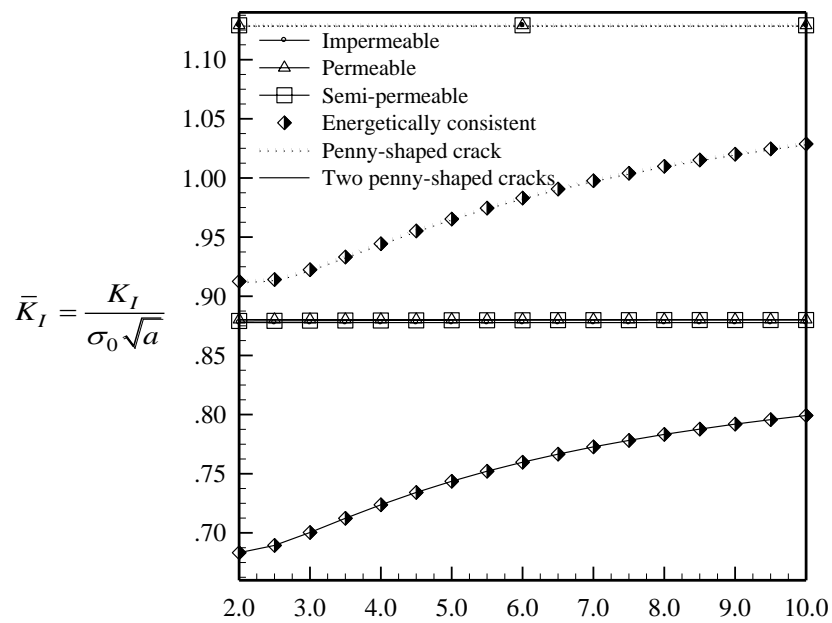
The numerical results of stress and electric intensity factors $[K_I, K_{II}, K_{IV}]$ obtained from the average values in one of two penny-shaped cracks along the crack front under four crack-face models (i.e., impermeable, permeable, semi-permeable and energetically consistent models) are illustrated in figures 4.41 (a) and (b) which can be discussed in detail as follows.

Figure 4.41 (a) shows the numerical results of stress intensity factors K_I on four models (i.e., impermeable, permeable, semi-permeable and energetically consistent

models). The figure shows that, under the same condition, as the permittivity inside the crack gap increases [2 to 10], the magnitude of normalized stress intensity factors K_I of the two penny-shaped cracks on four models are expressly less than the penny-shaped crack. Nevertheless, the trends of both cracks are a little bit different. More specifically, the identical and independent of permittivity for penny-shaped crack on three models (i.e., impermeable, permeable, and semi-permeable models) which is analogous to the work of many researchers (e.g., Li and Lee, 2004; Chen et al, 2000 and Chen and Lim, 2005) as discussed in previous cases, but those three models of two penny-shaped cracks are weak dependent of permittivity as indicated in figure 4.41(a.1). Moreover, the dependent of the energetically consistent models of both two and one penny-shaped cracks are again very identical and that one tend to increase and approach to the three models (i.e., impermeable, permeable, semi-permeable models). This can be concluded that as the permittivity increases, it affects not only the magnitude of stress intensity factor K_I but also the three crack-face models (i.e., impermeable, permeable, semi-permeable models)

Another results vanished from penny-shaped crack is the stress intensity factor K_{II} as shown in figure 4.41 (b). It is found that when the permittivity increase, the four models (i.e., impermeable, permeable, semi-permeable and energetically consistent models) are different and negative values. Moreover, the semi-permeable model are dependent of permittivity inside the crack gap and that one tend to decrease the magnitude at the entire range. Results also reveal that the energetically consistent model is dependent of permittivity and tend to decrease at the entire range. It should be remarked that the upper bound of this case is energetically consistent model whereas the lower bound is permeable model. It can be summarized that increasing the permittivity, it influences to the magnitude K_{II} of four models; more specifically, the semi-permeable and energetically consistent models

Eventually, the electric intensity factors K_{IV} obtained on four crack models are investigated as illustrated in figures 4.41 (c). It can be found that as the permittivity increases, the upper and lower bounds of predicted solutions including semi-permeable and energetically consistent models are impermeable and permeable models respectively. Moreover, the magnitude K_{IV} predicted from the two penny-shaped cracks is clearly less than that of the penny-shaped crack. The two models (i.e., semi-permeable and energetically consistent models) are the same behaviors and are dependent of permittivity by varying from the impermeable to permeable models. This implies again that, with a small distance L , the influence of the increasing permittivity only affects the magnitude of stress intensity factors which is not different from other planar crack



(a.1)

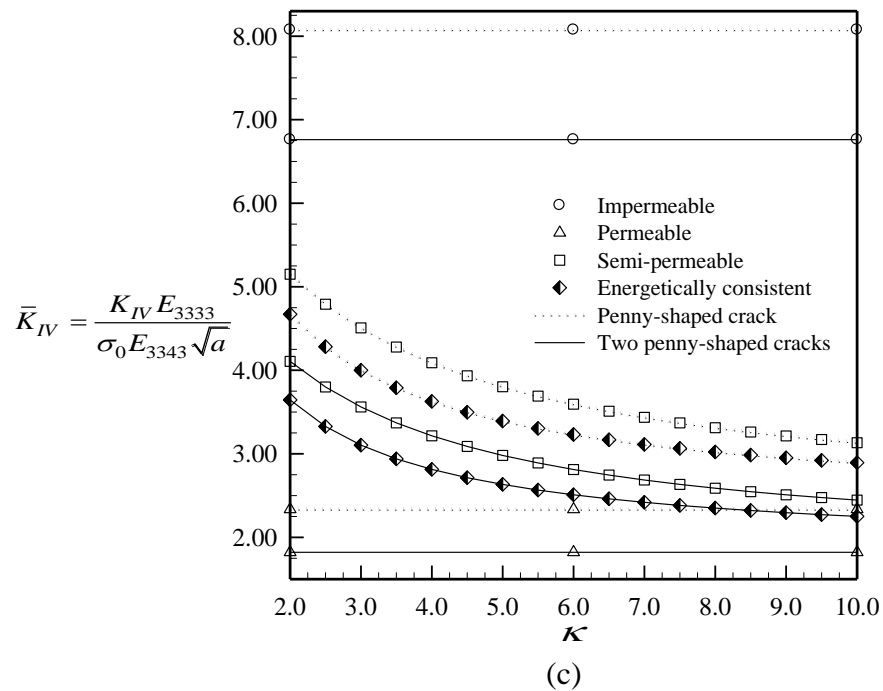
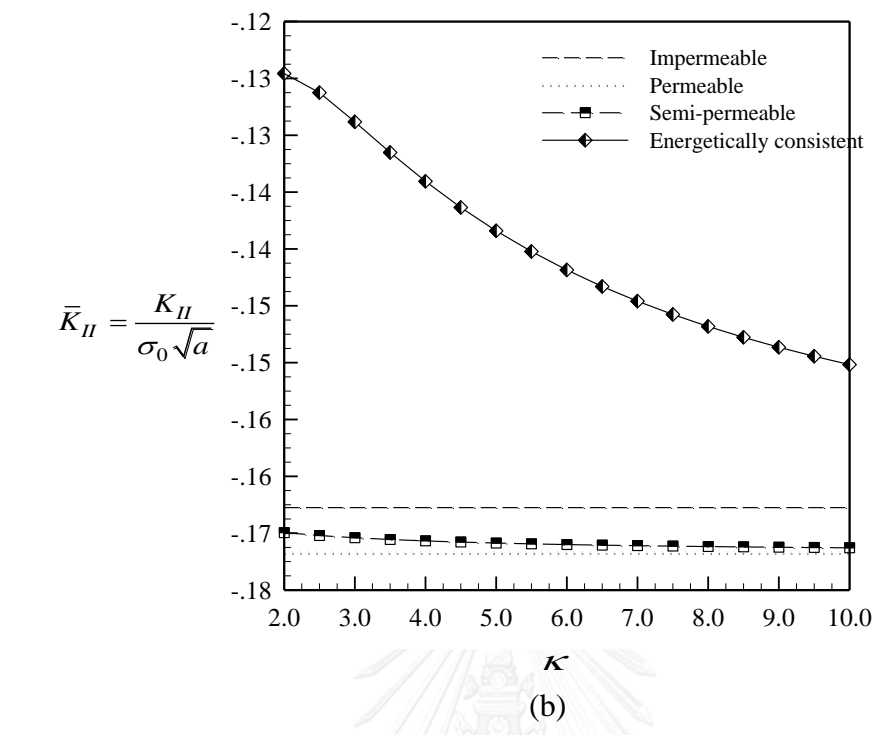


Figure 4.41 (a, a.1) (b) and (c) dependent of normalized stress and electric intensity factors [K_I , K_{II} , K_{IV}] on the permittivity for a two penny-shaped cracks in vertical direction in infinite medium. Results are reported on one penny-shaped crack

4.4.4 Influence of permittivity of two penny-shaped crack in horizontal direction

Finally, the influence of the permittivity ε_c of a medium inside the crack gap is investigated for the two-penny-shaped cracks in horizontal direction with radius a and the distance of the two cracks L containing in a piezoelectric infinite medium which is made of PZT-4 analogous to the previous section. The main differences from the previous section are that (i) the permittivity of a medium inside the crack gap is assigned by $\varepsilon_c = \kappa\varepsilon_0$ where κ is termed the relative permittivity and $\varepsilon_0 = 8.85 \times 10^{-12}$ C/(Vm) is the permittivity of the air that can be varied [$\kappa = 2, 2.5, 3, 3.5, \dots, 10$], (ii) the radius and the horizontal distance of the two cracks are imposed as 1 and 2.25 respectively, (iii) the uniform remote tension σ_0 is fixed as 50 MPa whereas the electric field E_0 is defined as 2.5 MV/m, and (iv) only the finest meshes (144 elements per a penny-shaped crack) similar to the penny-shaped crack are utilized in this exploration. The numerical results of stress and electric intensity factors [K_I, K_{IV}] obtained from the two different points (i.e., maximum and minimum values) for one of the two penny-shaped cracks, under four crack-face models (i.e., impermeable, permeable, semi-permeable and energetically consistent models) are obtained as shown in figures 4.42 (a) and (b). This would be discussed in detail as follows.

Results of stress intensity factors K_I of two different points (i.e., maximum and minimum points) on four crack-face models (i.e., impermeable, permeable, semi-permeable and energetically consistent models) are illustrated in figure 4.42 (a). Results show that as the permittivity increases, the magnitude of K_I at the maximum point for two penny-shaped cracks in horizontal direction is expressly greater than both the minimum and the penny-shaped crack, respectively. In this case, the three models (i.e., impermeable, permeable and energetically consistent models) are again completely identical and are independent of permittivity, for the two different typed cracks. Furthermore, the energetically consistent models of the two points are dependent on the permittivity analogous to that of penny-shaped crack. It is seen that the upper bounds of the two points serve as those three models whereas the lower bounds are the energetically consistent models. This can be concluded that the increasing permittivity has effect only the magnitude K_I on four model and the trends of stress intensity factor K_I on four models is selfsame to K_I other planar cracks

Finally, the above discussion obviously shows that the three models (i.e., impermeable, permeable, semi-permeable models) of the stress intensity factors K_I are identical while the electric intensity factors K_{IV} on four crack models at the two points (i.e., maximum and minimum points) are not identical, which is analogous to penny-shaped crack and other planar cracks. Besides, from conclusion of the previous sections, it is found that the two models (i.e., semi-permeable and energetically consistent models) are strongly dependent of permittivity and those two models vary from impermeable to permeable models, respectively. Similarly, the impermeable model is upper bound whereas the lower bound is permeable. This implies that as the permittivity increases, the trends of both two penny-shaped cracks in horizontal direction with the distance 2.25 and of one penny-shaped crack are identical.

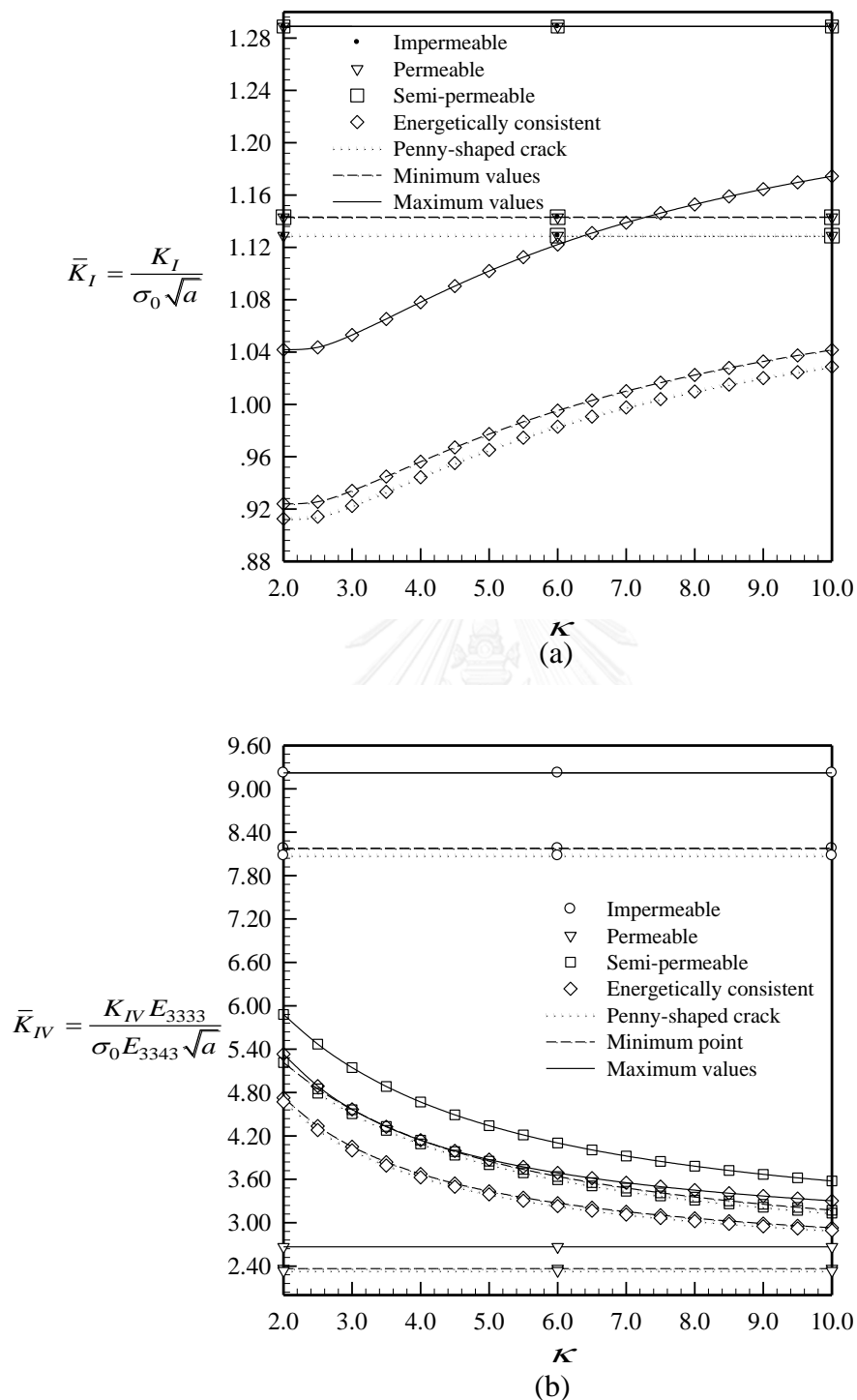


Figure 4.42 (a) and (b) are dependent of normalized electric intensity factors [K_I , K_{IV}] on the permittivity for two penny-shaped cracks in horizontal direction in infinite medium. Results are reported on the maximum and minimum values along the crack front

CHAPTER 5

CONCLUSIONS

This thesis mainly discussed the stress and electric intensity factors of cracks in piezoelectric media for various crack configurations under various crack-face and loading conditions. The boundary value problem is formulated based on a classical theory of linear piezoelectricity. A method of boundary integral equations is utilized to obtain the final governing integral equation. An existing numerical technique based on a weakly singular symmetric Galerkin boundary element method (SGBEM) proposed by Rungamornrat and Mear (2008) and Phongtinnaboot et al. (2011) is utilized to determine the unknown crack-face data such as the relative crack-face generalized displacement. The stress and electric intensity factors along the crack front are post-processed from the relative crack-face generalized displacement using the existing formula proposed by Rungamornrat and Mear (2008).

The verification of this method is insisted with the existing benchmark solution. The convergence of numerical results are implemented in order to verify the finest meshes with different levels of mesh refinement by utilizing the impermeable scheme. The finest meshes of each problem are then chosen in the influence study of various parameters. The first convergence solution are for the non-planar cracks (i.e., a spherical cap and cylindrical cracks). The second ones are for the planar cracks (i.e., the tunnel crack, two pair of two penny-shaped cracks in both vertical and horizontal directions) containing in a piezoelectric infinite domain. The numerical results from convergence solutions manifest that the predicted stress and electric intensity factors are well accepted by using the impermeable scheme. Finally, those finest meshes of each crack problems are imposed and utilized in the influence study of various parameters in the next step.

In the influence study of cracks with various parameters under four boundary conditions is investigated to obtain the numerical results on stress and electric intensity factors along the crack front by using the weakly singular SGBEM. The main study are the influence of geometries (i.e., the crack subtended angle, the curvature of non-planar cracks, the aspect ratio of tunnel crack and the interaction of two penny-shaped cracks in both vertical and horizontal directions), the influence of both mechanical and electrical loads of all planar and non-planar cracks and the influence of dielectric permittivity inside the crack gap for all planar and non-planar cracks. Eventually, the numerical results of various parameters in 3D cracks under four crack-face models can be concluded in the following sections.

5.1 Influence of geometry on intensity factors

Influence of half-subtended angle for non-planar cracks (i.e., spherical cap and cylinder cracks) under four crack-face models (i.e., impermeable, permeable, semi-permeable and energetically consistent models) can be concluded in two main points. first, they introduces the peak magnitude of K_I , K_{II} and K_{IV} on four crack-face models in the entire range of increasing the crack subtended angle whereas K_{III} on four models of cylinder crack produce the minimum values in the negative stress intensity factors. Second, the

crack-subtended angle at the entire range also affect to the bounds of all non-planar cracks under four crack-face models which can be briefly summarized as follow: in the entire range, the crack-subtended angle obviously does not affect to the upper bounds of all stress and electric intensity factors [K_I , K_{II} , K_{III} and K_{IV}] for all non-planar cracks such as the upper bound of K_I are permeable models, and the upper bounds of K_{II} , K_{III} and K_{IV} are impermeable models. Similarly, at the small crack subtended angle also has no influence to lower bounds of all stress and electric intensity factors [K_I , K_{II} , K_{III} and K_{IV}] for all non-planar cracks. Nevertheless, at the large crack subtended angle, it influences to the lower bound of K_I and K_{IV} such as the lower bound of K_I for all non-planar crack are switched of energetically consistent and impermeable models and the lower bound of K_{IV} for all non-planar cracks are switched of permeable and energetically consistent models. However, it should be noted that the lower bounds of non-symmetric curve crack (e.g., cylindrical crack) have different behavior of upper and lower bounds depending on the position along the crack front which is different from the symmetric curve crack (e.g., spherical cap crack).

Influence of curvature for non-planar cracks (i.e., spherical cap and cylindrical cracks) on four crack-face models can be summarized in three main points. First, it inhibits the crack opening indicated by the negative magnitude of K_I on four crack face models. Second, in the large curvature, K_{II} of all non-planar cracks produce the maximum values on four crack face models; Moreover, K_{III} produces the negative value on four crack face models. Finally, the large curvature influences to the bounds on four crack-face models which can shortly concluded as follow: in the entire range, the curvature explicitly does not influence to or do not change the upper bounds of all stress and electric intensity factors [K_I , K_{II} , K_{III} and K_{IV}] for all non-planar cracks such as the upper bound of K_I are permeable models whereas upper bound of penny-shaped crack serve as three models, and the upper bounds of K_{II} , K_{III} and K_{IV} are impermeable models (the upper bound of K_{IV} is identical to penny-shaped crack). Similarly, at the range of the near-flat curvature, it also has no influence to lower bounds of all stress and electric intensity factors [K_I , K_{II} , K_{III} and K_{IV}] for all non-planar cracks (lower bounds of K_I and K_{IV} are now identical to penny-shaped crack). Nevertheless, at the large curvature, it influences to the lower bound of K_I and K_{IV} such as the lower bound of K_I for all non-planar crack are switched of impermeable and energetically consistent models whereas the lower bound of penny-shaped crack is energetically consistent model. The lower bounds of K_{IV} for all non-planar cracks at the large curvature are switched of energetically consistent and permeable models whereas lower bound of penny-shaped crack is permeable model). However, it should be noted that the behavior of non-symmetric curve crack (e.g., cylindrical crack) have different behavior depending on the position along the crack front which is different from the symmetric curve crack (e.g., spherical cap crack).

The influence of aspect ratio on intensity factors K_I and K_{IV} obtained from tunnel crack can be concluded that when the aspect ratio is small, upper bounds of K_I and K_{IV} are the three models (i.e., impermeable, permeable and semi-permeable models) and impermeable models (similar to penny-shaped crack), respectively, whereas the lower bounds of K_I and K_{IV} are energetically consistent and permeable models (similar to penny-shaped crack), respectively

The influence of vertical interaction on intensity factor K_I , K_{II} and K_{IV} obtained from two penny-shaped cracks in vertical direction can be concluded that when the

distance of the two cracks is relative small, the upper bounds of K_I , K_{II} and K_{IV} are respectively the three models (i.e., impermeable, permeable and semi-permeable models), energetically consistent and impermeable models, respectively (K_{II} of penny-shaped crack vanishes), whereas the lower bounds of K_I , K_{IV} and K_{II} are energetically consistent, permeable and the three models (i.e., permeable, semi-permeable and energetically consistent models), respectively. It is obvious that the magnitude of K_{II} are negative value.

The influence of horizontal interaction on intensity factor K_I and K_{IV} obtained from two penny in horizontal direction, it can be summarized that when the horizontal interaction is small, the upper bounds of K_I and K_{IV} of four crack-face models are the three models (i.e., impermeable, permeable and semi-permeable models) and impermeable models, respectively, whereas the lower bounds of K_I and K_{IV} are energetically consistent and permeable models, respectively, which is identical to upper bound and lower bound of K_I and K_{IV} for penny-shaped crack

5.2 Influence of mechanical loading on intensity factors

For the planar cracks (i.e., tunnel crack, penny shaped cracks, two penny-shaped cracks in vertical and horizontal directions), the influence of mechanical loading on the stress intensity factors K_I , K_{IV} and K_{II} (K_{II} only for the case of two penny-shaped cracks in vertical direction) of four models can be summarized that at the entire range of increasing the mechanical loading, the upper bounds of K_{II} , K_{IV} and K_I on four models are energetically consistent, impermeable models and the three models (i.e., impermeable, permeable and semi-permeable models), respectively, whereas the lower bounds of K_I , K_{II} and K_{IV} are identically energetically consistent, permeable models and the switching models between energetically consistent and permeable models, respectively.

For non-planar cracks (i.e., spherical and cylinder cracks), influence of mechanical load can be summarized that at the entire range of increasing mechanical load, the upper bounds of K_I and K_{IV} for all non-planar cracks under four models are permeable and energetically consistent models, respectively, whereas the upper bound of K_{II} for all non-planar cracks and the upper bound of K_{III} (only at the middle point of cylinder crack) are permeable models. The lower bound of K_I for all non-planar cracks, the lower bound of K_{II} for spherical cap crack and the lower bound of K_{II} at the bottom points of cylindrical crack are energetically consistent models. Moreover, the lower bounds of K_{IV} for all non-planar cracks and the lower bound K_{II} at the top and middle points of cylinder crack are switched of energetically consistent and permeable models. However, the lower bound of K_{III} only at the middle point is permeable model at the entire range.

5.3 Influence of electrical loading (electric field) on intensity factors

For the planar cracks (i.e., penny-shaped crack, tunnel crack, two penny-shaped crack in vertical and horizontal directions), the influence of electrical loading on the stress intensity factors K_I , K_{IV} and K_{II} (only for the case of two penny-shaped cracks in vertical direction) on four models can be summarized that at the positive range of electric field, the upper bounds of K_{IV} , K_{II} and K_I on four crack models are impermeable and energetically consistent and three models (i.e., impermeable, permeable and semi-

permeable models), respectively, whereas the lower bound of K_I , K_{II} and K_{IV} are energetically consistent, permeable and the switching models (the switching models between permeable and energetically consistent models), respectively.

For the non-planar cracks (i.e., spherical cap and cylinder cracks), the stress intensity factors K_I , K_{II} , K_{IV} and K_{III} (only at the middle point of cylinder crack) of four models can be concluded that at the positive range of electric field, the upper bounds (K_I) of spherical cap crack, the upper bound (K_I) of middle and bottom points of cylinder crack are permeable models. The upper bounds of K_{II} and K_{IV} for all non-planar cracks, the upper bound of K_I at the top point and upper bound of K_{III} at the middle of cylinder crack are impermeable models. However, the lower bounds (K_I) of spherical cap crack is switched of impermeable and energetically consistent models. The lower bounds of K_I at all points of cylinder crack are energetically consistent models. Similarly, the lower bounds (K_{II} and K_{IV}) of for spherical cap crack, lower bound of K_{II} at all points and lower bound of K_{IV} at the middle and bottom points of cylinder crack are switched of permeable and energetically consistent models. Nevertheless, the lower bounds of K_{III} at the middle point and the lower bound of K_{IV} at the top point of cylinder crack serve as permeable models.

5.4 Influence of permittivity inside the crack gap on intensity factors

For the planar cracks (i.e., penny-shaped crack, tunnel crack, two penny-shaped crack in vertical and horizontal directions), the influence of permittivity inside the crack gap on stress intensity factors K_I , K_{IV} and K_{II} (only for the case of two penny-shaped cracks in vertical direction) can be concluded that the upper bounds of K_{II} , K_{IV} and K_I (K_I of all planar cracks; except, two penny-shaped crack in vertical direction) on four models are energetically consistent, impermeable and three models (i.e., impermeable, permeable and semi-permeable models), respectively. The upper bound of K_I for two penny-shaped crack in vertical direction is permeable models. However, the lower bounds of K_I and K_{IV} for all planar cracks are energetically consistent and permeable models, respectively, which is analogous to the lower bounds of K_{II} only for two penny-shaped cracks in vertical direction also permeable model.

Finally, the influence of permittivity inside the crack gap of non-planar cracks (i.e., spherical cap and cylinder cracks) on electric intensity factors K_I , K_{II} , K_{IV} and K_{III} (only at the middle point of cylinder crack) under four models can be concluded that the upper bounds (K_I) of spherical cap crack, the upper bound of K_I at the middle and bottom points of cylinder crack are permeable models. The upper bounds (K_{II} and K_{IV}) of spherical cap crack, the upper bound of K_{II} and K_{IV} at all points of cylinder crack, the upper bound of K_I at the top point and the upper bound of K_{III} only at the middle point of cylinder crack are impermeable models. Vice versa, the lower bounds of K_I for spherical cap crack is switched of energetically consistent and impermeable models. Identically, the lower bound of K_I at all points of cylindrical crack, the lower bound of K_{II} for spherical cap crack and the lower bound of K_{II} at the middle and bottom points of cylindrical crack are energetically consistent models. Finally, the lower bound of K_{II} at the top point, the lower bound of K_{III} at the middle point of cylinder crack and the lower bound of K_{IV} for all non-planar crack are permeable models.

REFERENCES

- Chen, H. s., Wei, W. y., Liu, J. x., & Fang, D. n. (2014). *Propagation of a semi-infinite conducting crack in piezoelectric materials: Mode-I problem*. Paper presented at the Journal of the Mechanics and Physics of Solids.
- Chen, W., & Lim, C. (2005). 3D point force solution for a permeable penny-shaped crack embedded in an infinite transversely isotropic piezoelectric medium. *International Journal of Fracture*, 131(3), 231-246.
- Chen, W., & Shioya, T. (2000). Complete and exact solutions of a penny-shaped crack in a piezoelectric solid: antisymmetric shear loadings. *International Journal of Solids and Structures*, 37(18), 2603-2619.
- Chiang, C.-R., & Weng, G. J. (2007). Nonlinear behavior and critical state of a penny-shaped dielectric crack in a piezoelectric solid. *Journal of Applied Mechanics*, 74(5), 852-860.
- Curie, J., & Curie, P. (1880). Développement, par pression, de l'électricité polaire dans les cristaux hémiedres à faces inclinées. *Comptes Rendus*, 91, 294-295.
- Davi, G., & Milazzo, A. (2001). Multidomain boundary integral formulation for piezoelectric materials fracture mechanics. *International Journal of Solids and Structures*, 38(40), 7065-7078.
- Denda, M., & Mansukh, M. (2005). Upper and lower bounds analysis of electric induction intensity factors for multiple piezoelectric cracks by the BEM. *Engineering analysis with boundary elements*, 29(6), 533-550.
- Fang, Q., Feng, H., Liu, Y., & Jiang, C. (2011). Energy density and release rate study of an elliptic-arc interface crack in piezoelectric solid under anti-plane shear. *Theoretical and Applied Fracture Mechanics*, 55(1), 20-30.
- Gao, C.-F., & Fan, W.-X. (1999). Exact solutions for the plane problem in piezoelectric materials with an elliptic or a crack. *International Journal of Solids and Structures*, 36(17), 2527-2540.
- Groh, U., & Kuna, M. (2005). Efficient boundary element analysis of cracks in 2D piezoelectric structures. *International Journal of Solids and Structures*, 42(8), 2399-2416.
- Gruebner, O., Kamlah, M., & Munz, D. (2003). Finite element analysis of cracks in piezoelectric materials taking into account the permittivity of the crack medium. *Engineering fracture mechanics*, 70(11), 1399-1413.
- Hu, K., & Chen, Z. (2013). Size effect on crack kinking in a piezoelectric strip under impact loading. *Mechanics of Materials*, 61, 60-72.
- Jiang, L., & Sun, C. (2001). Analysis of indentation cracking in piezoceramics. *International Journal of Solids and Structures*, 38(10), 1903-1918.
- Kogan, L., Hui, C.-Y., & Molkov, V. (1996). Stress and induction field of a spheroidal inclusion or a penny-shaped crack in a transversely isotropic piezoelectric material. *International Journal of Solids and Structures*, 33(19), 2719-2737.
- Kuna, M. (2010). Fracture mechanics of piezoelectric materials—Where are we right now? *Engineering fracture mechanics*, 77(2), 309-326.
- Landis, C. M. (2004). Energetically consistent boundary conditions for electromechanical fracture. *International Journal of Solids and Structures*, 41(22), 6291-6315.

- Li, C., Man, H., Song, C., & Gao, W. (2013). Fracture analysis of piezoelectric materials using the scaled boundary finite element method. *Engineering fracture mechanics*, 97, 52-71.
- Lippmann, G. (1881). Principe de la conservation de l'électricité, ou second principe de la théorie des phénomènes électriques. *J. Phys. Theor. Appl.*, 10(1), 381-394.
- McMeeking, R. M. (2004). The energy release rate for a Griffith crack in a piezoelectric material. *Engineering fracture mechanics*, 71(7), 1149-1163.
- Nam, B.-G., & Watanabe, K. (2008). Effect of electric boundary conditions on crack energy density and its derivatives for piezoelectric material. *Engineering fracture mechanics*, 75(2), 207-222.
- Nan, H., & Wang, B. (2013). Effect of crack face residual surface stress on nanoscale fracture of piezoelectric materials. *Engineering fracture mechanics*, 110, 68-80.
- Ou, Z.-C., & Chen, Y.-H. (2007). Re-examination of the PKHS crack model in piezoelectric materials. *European Journal of Mechanics-A/Solids*, 26(4), 659-675.
- Park, S., & Sun, C. (1993). Effect of electric field on fracture of piezoelectric ceramics. *International Journal of Fracture*, 70(3), 203-216.
- Phongtinnaboot, W., Rungamornrat, J., & Chintanapakdee, C. (2011). Modeling of cracks in 3D piezoelectric finite media by weakly singular SGBEM. *Engineering analysis with boundary elements*, 35(3), 319-329.
- Qin, T., Yu, Y., & Noda, N. (2007). Finite-part integral and boundary element method to solve three-dimensional crack problems in piezoelectric materials. *International Journal of Solids and Structures*, 44(14), 4770-4783.
- Rungamornrat, J., & Mear, M. E. (2008). Analysis of fractures in 3D piezoelectric media by a weakly singular integral equation method. *International Journal of Fracture*, 151(1), 1-27.
- Sladek, J., Sladek, V., Wünsche, M., & Zhang, C. (2012). Analysis of an interface crack between two dissimilar piezoelectric solids. *Engineering fracture mechanics*, 89, 114-127.
- Solis, M., Sanz, J., Ariza, M., & Dominguez, J. (2009). Analysis of cracked piezoelectric solids by a mixed three-dimensional BE approach. *Engineering analysis with boundary elements*, 33(3), 271-282.
- Stroh, A. (1958). The cleavage of metal single crystals. *Philosophical Magazine*, 3(30), 597-606.
- Tran, H. D., & Mear, M. E. (2014). A weakly singular SGBEM for analysis of two-dimensional crack problems in multi-field media. *Engineering analysis with boundary elements*, 41, 60-73.
- Wang, X., & Jiang, L. (2002). *Fracture behaviour of cracks in piezoelectric media with electromechanically coupled boundary conditions*. Paper presented at the Proceedings of the Royal Society of London A: Mathematical, Physical and Engineering Sciences.
- Xu, X.-L., & Rajapakse, R. (2001). On a plane crack in piezoelectric solids. *International Journal of Solids and Structures*, 38(42), 7643-7658.
- Yang, J. H., & Lee, K. Y. (2002). Three-dimensional non-axisymmetric behavior of a penny shaped crack in a piezoelectric strip subjected to in-plane loads. *European Journal of Mechanics-A/Solids*, 21(2), 223-237.

- Zhao, M., Zhang, R., Fan, C., & Pan, E. (2012). Three-dimensional extended displacement discontinuity method for vertical cracks in transversely isotropic piezoelectric media. *Engineering analysis with boundary elements*, 36(9), 1406-1415.
- Zhou, Z.-G., Zhang, P.-W., & Wu, L.-Z. (2012). Basic solutions of a 3D rectangular limited-permeable crack or two 3D rectangular limited-permeable cracks in the piezoelectric/piezomagnetic composite materials. *Applied Mathematical Modelling*, 36(6), 2404-2428.



VITA

Bounsana Chansavang was born in Luangprabang, Laos on August 8, 1986, the son of Mrs. Bounthieng Chansavang. He received his Bachelor of Engineering degree in Civil Engineering from National University of Laos in 2009. Later, he become a teacher in Souphanouvong University until May of 2013 and continued his Master Degree in Civil Engineering, under the supervision of Associate Professor Dr. Jaroon Rungamornrat and Dr. Weeraporn Phongtinnaboot in June of 2013 under the Asian Country Scholarship 2013.

